REMOTE SENSING OF ATMOSPHERIC WINDS BY UTILIZING SPECKLE-TURBULENCE INTERACTION AND OPTICAL HETERODYNE DETECTION

Farzin Amzajerdian

B.S., Electrical Engineering, Portland State University, 1980
M.S., Electrical Engineering, Portland State University, 1982
B.S., Mathematics, Portland State University, 1982

A dissertation submitted to the faculty
of the Oregon Graduate Center
in partial fulfillment of the
requirements for the degree
Doctor of Philosophy
in
Electrical Engineering

June, 1988

The dissertation *"Remote Sensing of Atmospheric Winds by Utilizing Speckle-Turbulence Interaction and Optical Heterodyne Detection"* by Farzin Amzajerdian has been examined and approved by the following Examination Committee:

J. Fred Holmes, Thesis Advisor
Professor

Richard A. Elliott
Professor

V. S. Rao Gudimetla
Assistant Professor

M. Aslam K. Khalil
Professor

ACKNOWLEDGMENTS

I would like to express my deepest gratitude to my research advisor, Dr. J. Fred Holmes for his support and encouragement throughout this work. Also, for the many discussions in which I have greatly benefited from his vast knowledge and ingenuity. I am also grateful to Dr. Rao Gudimetla for allowing me to benefit from his scientific insight and for his friendship. Thanks are due to Dr. Richard Elliott for his thoughtful attention in this work and useful suggestions. I would like to acknowledge Drs. Holmes, Elliott, Gudimetla and Khalil for serving in my dissertation examination committee.

I wish to thank John Hunt for his many contributions in development of the experimental apparatus and making his engineering skills available to me whenever needed. I also appreciate Carl Miller for his help in maintaining the laser propagation field site facilities. To my fellow students Douglas Draper and Dr. Paolo Dobrilla go many thanks for their friendship and interest in my work.

Finally, I wish to thank Dr. Pieter Frick, my advisor at Portland State University, for his advice and encouragement in pursuing my academic career.

This work was supported in part by the U.S. Army Research Office.

CONTENTS

LIST OF TABLES

LIST OF FIGURES

ABSTRACT

REMOTE SENSING OF ATMOSPHERIC WINDS BY UTILIZING SPECKLE-TURBULENCE INTERACTION AND OPTICAL HETERODYNE DETECTION

Farzin Amzajerdian, Ph.D.

Oregon Graduate Center, 1988

Supervising Professor: J. Fred Holmes

Speckle-turbulence interaction can be utilized in single-ended remote sensing of path averaged atmospheric crosswinds. If a laser transmitter is used to illuminate a target, the resultant speckle field generated by the target is randomly perturbed by atmospheric turbulence as it propagate back to the transmitter-receiver. When a crosswind is present, this scintillation pattern will move with time across the field of view of the receiver. As a result, the averaged vector wind velocity along the path perpendicular to the direction of propagation can be obtained by using the time-delayed statistics of the speckle field at the receiver.

The theoretical basis of the speckle propagation through the turbulent atmosphere is provided along with the analytical formulations of the time-delayed statistics of the return intensity. Several windsensing techniques using these statistics are described and their performance evaluated. The

turbulence-induced correlation between the outgoing and return paths was considered and the analytical formulations of the dependence effect of the two paths on the time-delayed statistics and the performance of remote measurements of atmospheric parameters using optical heterodyne detection are presented.

A continuous wave laser transmitter of modest power in conjunction with optical heterodyne detection can exploit the speckle-turbulence interaction to measure the crosswinds. Several optical heterodyne transmitter-receiver systems, using a CO_2 waveguide laser as the source, were designed and built. The major difficulty to design an optical heterodyne system is to obtain sufficient optical isolation between the transmitter and local oscillator beams. The novel techniques developed to improve the isolation are described. It was also shown that an optimum local oscillator level exists when photoconductors are used as optical heterodyne detectors.

Considerable amount of data were obtained over three different target ranges of 500m, 1000m and 1300m. The experimental data taken under different atmospheric conditions are represented and discussed.

An analysis was performed to predict the measurement errors associated with the statistical parameters required to determine the wind velocity. Then, the optimum system parameters for which the estimation of wind velocity is most accurate were obtained.

CHAPTER 1

INTRODUCTION

The possibility of the remote probing of the atmospheric turbulence and crosswind by measuring the effects produced by the atmosphere on optical propagation[1,2] was recognized in the late 1960's[3-5]. The ability to measure the spatial average turbulence strength (represented by the index of refractive structure constant C_n^2) and wind velocity made optical remote sensing very attractive to many applications, since widely spaced point measurements do not represent the true spatial average. The feasibility of an optical sensor which requires a laser source at one end of the path and a receiver at the other end had been demonstrated during the early 1970's[6-9] and has proven to be reliable over the years. However, the use of these sensors are limited to applications where both ends of the path are accessible. The objective of this work is the development of an optical remote sensor with both the transmitter and the receiver at the same end of the path.

The effect of turbulence on the target generated speckle pattern in conjunction with the heterodyne detection can be utilized in single-ended optical remote sensing of atmospheric crosswind. As shown in figure (1.1), a speckle pattern is generated when the target is illuminated by a laser beam[10,11]. The resultant speckle pattern is perturbed by the atmosphere as it propagates

back to the transmitter end. This creates a scintillation pattern at the receiver which will move across the field of view of the receiver in the presence of a crosswind. As a result, the average vector crosswind along a horizontal path perpendicular to the direction of propagation can be obtained by using the time-delayed statistics of the speckle field at the receiver.

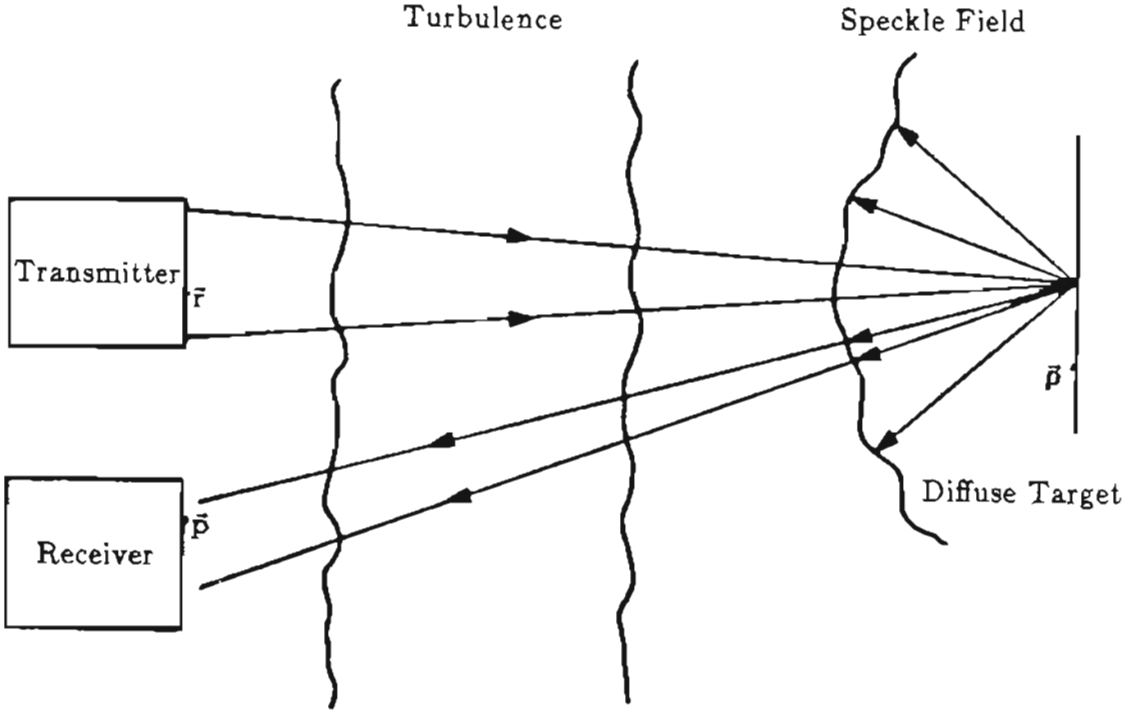

Figure 1.1 Transmitter-Receiver Configuration.

In the past, some work was accomplished in developing a pulsed laser system that utilizes the speckle-turbulence interaction and direct detection[12–16]. The experimental results indicated the potential of the speckle-turbulence technique. However, such a system is inadequate for the purpose of windsensing with present pulsed laser technology as limited pulse repetition rate restricts the processing techniques requiring a priori knowledge of the strength of turbulence for wind measurements. Furthermore, a pulsed laser remote sensor requires a complicated and expensive transmitter and a complex electronic receiver which suffers from the additional problems of beam alignment, beam jitter and stability.

The single-ended remote sensing of the atmospheric crosswind is also possible by the application of passive techniques. There had been substantial effort in developing passive systems for which the scintillation of the visible light reflected from a target surface or the natural infrared background radiation was used to measure the crosswind[17–20]. Even though a passive system may benefit from the simplicity of the optics, it suffers from large variations in the received radiation and poor signal to noise ratio.

Another technique that should be noted is doppler lidar remote wind sensing[21,22]. This technique uses the aerosols in the atmosphere to scatter some of the transmitted energy from a pulsed laser back to a receiver where the doppler shift is used to measure the magnitude of the wind velocity along the line of sight. The advantage of the doppler systems is the ability to easily obtain the wind profile along the path. Furthermore, since the movement of the aerosols is used to measure the wind speed and not the

turbulence eddies, the nonuniformities of the turbulence is of no concern. For these reasons, the doppler systems are very well suited for global measurements from the earth's orbit.

The major disadvantage of the doppler technique is the need for an elaborate transmitter-receiver system while many applications require a simple, compact and inexpensive system. In addition to that, certain applications require measuring the path averaged vector wind in a plane perpendicular to the line of sight. This can be accomplished by a speckle-turbulence system while a doppler system measures the component of the wind along the line of sight.

The body of the material in this thesis is divided into five chapters. In chapter 2, first the theory of the speckle propagation through the turbulent atmosphere is described and the formulations for the statistics required for wind measurements are provided. Then, several windsensing techniques, including the ones developed in the course of this work, are described. Some theoretical work was performed showing the effect of the turbulence-induced correlation between the outgoing and return paths on the statistics of the return intensity. In section 2.3, the analytical formulations of the dependence effect of the two paths on the time-delayed statistics and the performance of coherent lidars are presented.

A great deal of effort was devoted to the construction and development of the coherent lidars used in gathering data. In chapter 3, the experimental procedure is outlined and each experimental set-up is described and their

performance discussed in detail. Experimental set-ups include two novel techniques developed to improve the local oscillator isolation. In section 3.4, the use of photoconductors as optical heterodyne detection is described followed by the analytical formulation of optimum detection parameters.

The experimental results are presented in chapter 4, including the statistical parameters required for wind and strength of turbulence measurements. The results of the wind measurements are reported for various atmospheric conditions over three different path lengths. Comparisons are made between the wind measurements using different experimental set-ups and processing techniques followed by some discussion.

In chapter 5, analytical expressions for the estimation errors associated with the statistical parameters are derived. The effect of these errors on the wind measurements is shown and optimum system parameters are obtained for which the measurements are most accurate.

In chapter 6, final conclusions for the analytical and experimental work in this thesis are given. That chapter summerizes the preceding pages and provides the future directions in which this work can be extended.

The appendices include the listings of the computer source programs used for various numerical evaluations and processing the collected data. In addition, the schematics of the electronic circuits designed and built for this work are provided.

CHAPTER 2

SPECKLE-TURBULENCE INTERACTION AND ITS APPLICATION IN REMOTE WIND SENSING

Heterodyne detection is most efficient when the transmitter beam is focused on the target and the receiving aperture is of the order of the speckle size [23]. As a result, the speckle effect cannot be averaged at the detector and its statistics must be included along with that of the turbulence. In order to establish sufficient background, the statistics of the speckle propagation through the turbulent atmosphere is first reviewed in this chapter and the region of validity of the simplified formulation is described. Then, several windsensing techniques that utilize these statistics are described and their reliabilities evaluated.

Some work was accomplished on the bistatic heterodyne lidars which included the dependence effect of the turbulence on the outgoing and returning paths[24]. Analytical expressions have been derived describing the time-delayed statistics of the lidar return and the heterodyne signal power as a function of the separation between the transmitter and the receiver. It is shown that the correlation between the two paths can have a significant effect on the the performance of coherent lidars in general and the wind and strength of turbulence measurements in particular.

2.1 Statistics Of The Returned Intensity

Analytical formulations for the first and second order statistics of the returned intensity have been derived when a diffuse target is illuminated by a laser beam[25,26]. The exact formulations of the statistics are quite complex and difficult to interpret. However, Lee *et al.* [25] by applying the jointly gaussian assumption obtained simple, closed form expressions describing the second order, time-delayed statistics. Both exact and simplified formulations are described here and the region of validity of the later is discussed.

Referring to figure (1.1) and by applying the extended Huygen-Fresnel principle[27], the field at the target is written as

$$U(\rho)=\frac{ke^{ikL}}{2\pi iL}\int dr U(r)\exp\left(\frac{ik}{2L}(\rho-r)^2+\psi_1(\rho,r)\right) \tag{2.1}$$

where $\psi_1(\rho,r)$ is the complex phase factor describing the effect of the refractive turbulence on a spherical wave traveling from r to ρ , L is the path length and U(r) is the source amplitude distribution which, for a single-mode laser beam, is given by

$$U(r)=U_0\exp(-r^2/2\alpha_0^2-ikr^2/2F) \tag{2.2}$$

where α_0 ,F and k are the transmitter beam radius, focal length and wave number, respectively. Denoting the turbulence effect from the target to the receiver by $\psi_2(p,\rho)$, the field at the receiver is

$$U(p)=\frac{ke^{ikL}}{2\pi iL}\int d\rho T(\rho)U(\rho)\exp\left(\frac{ik}{2L}(p-\rho)^2+\psi_2(p,\rho)\right) \tag{2.3}$$

where $T(\rho)$ is the complex reflectivity function of the target. If the transverse coherence length of the incident wave is much greater than the surface correlation distance [22] then

$$<T(\rho_1)T^*(\rho_2)>=\frac{4\pi}{k^2}T_0^2\delta(\rho_1-\rho_2) \tag{2.4}$$

where $<\ >$ denotes an ensemble average over the target statistics and T_0^2 is the target reflectivity coefficient.

The mutual intensity function is then given by

$$\Gamma(p_1,p_2)=<U(p_1)U^*(p_2)>$$

$$=(\frac{k}{2\pi L})^2\int\int d\rho_1 d\rho_2 <T(\rho_1)T^*(\rho_2)><U(\rho_1)U^*(\rho_2)$$

$$\exp\left[\frac{ik}{2L}\left((p_1-\rho_1)^2-(p_2-\rho_2)^2\right)+\psi_2(p_1,\rho_1)+\psi_2^*(p_2,\rho_2)\right]> \tag{2.5}$$

Using equations (2.1), (2.2) and (2.4), the expression above reduces to

$$\Gamma(p_1,p_2)=\frac{T_0^2U_0^2}{\pi L^2}(\frac{k}{2\pi L})^2 e^{i\frac{k}{2L}(p_1^2-p_2^2)}\int\int\int d\rho dr_1 dr_2$$

$$\exp\left[-\frac{r_1^2+r_2^2}{2\alpha_0^2}+i\frac{k}{2L}(1-L/F)(r_1^2-r_2^2)-\frac{ik}{L}\left(\rho.(r_1-r_2)+\rho.p\right)\right]$$

$$<\exp\left(\psi_1(\rho,r_1)+\psi_1^*(\rho,r_2)\right)><\exp\left(\psi_2(p_1,\rho)+\psi_2^*(p_2,\rho)\right)> \tag{2.6}$$

It should be noted that the incident and reflected waves have been assumed

to be independent. The ensemble averages can be written in terms of the wave structure functions defined as

$$<\exp\left(\psi_1(\rho,r_1)+\psi_1^*(\rho,r_2)\right)>=e^{-\frac{1}{2}D_\psi(r_1-r_2)} \tag{2.7}$$

The integrations of Eq. (2.6) can be performed, giving

$$\Gamma(p_1,p_2)=\frac{T_0^2U_0^2\alpha_0^2}{L^2}e^{\frac{ik}{2L}(p_1^2-p_2^2)}$$

$$\exp\left[-p^2\left(\frac{1}{4\alpha_0^2}+\frac{k^2\alpha_0^2}{4L^2}(1-\frac{L}{F})^2\right)-2(\frac{p}{\rho_0})^{5/3}\right] \tag{2.8}$$

Where $D_\psi(p)=2(p/\rho_0)^{5/3}$ is the wave structure function[28], $\rho_0=\left(0.546Lk^2\int_0^1 C_n^2(w)dw\right)^{-3/5}$ is the turbulence coherence length, C_n^2 is the structure constant of the index of refraction and p_1-p_2 is defined as p .

The time-delayed mutual intensity function is defined by

$$\Gamma(p_1,p_2,\tau)=<U(p_1,t_1)U^*(p_2,t_2)> \tag{2.9}$$

where $\tau=t_1-t_2$. Including the time-delay τ in Eq. (2.6), the last term must be replaced by

$$<\exp\left(\psi_1(\rho,r_1,t_1)+\psi_1^*(\rho,r_2,t_2)\right)><\exp\left(\psi_2(p_1,\rho,t_1)+\psi_2^*(p_2,\rho,t_2)\right)>$$

$$=\exp\left[-\frac{1}{2}D_{\psi_1}(0,r,V\tau)-\frac{1}{2}D_{\psi_2}(p,0,V\tau)\right] \tag{2.10}$$

where the time-delayed wave structure function is given by

$$D_{\psi_2}(\mathbf{p},0,V\tau)=2.91Lk^2\int_0^1 C_n^2(w)\,|(1-w)\mathbf{p}-V\tau|^{5/3}dw \tag{2.11}$$

where w is the normalized path length from the transmitter-receiver to the target and V is the vector wind velocity. Applying the principle of reciprocity[29] which implies $D_{\psi_1}(0,\mathbf{r},V\tau)=D_{\psi_2}(-\mathbf{r},0,V\tau)$ and performing the integrations the time-delayed mutual intensity function can be obtained

$$\Gamma(\mathbf{p}_1,\mathbf{p}_2,\tau)=\frac{T_0^2U_0^2\alpha_0^2}{L^2}e^{\frac{ik}{2L}(p_1^2-p_2^2)}\exp\left[-p^2\left(\frac{1}{4\alpha_0^2}+\frac{k^2\alpha_0^2}{4L^2}(1-\frac{L}{F})^2\right)\right.$$
$$\left.-2.91Lk^2\int_0^1 dw C_n^2(w)\,|(1-w)\mathbf{p}-V\tau|^{5/3}\right] \tag{2.12}$$

The only restriction on Eq. (2.12) is that the transverse coherence length of the incident wave (ρ_0) is much greater than the correlation distance of the target surface. This condition easily holds in the real world in the infrared region and is usually true in the visible region.

The fields are gaussian and incoherent after scattering from the target and in the absence of turbulence, the fields are jointly gaussian at the receiver end[11,30] . It has been shown in the past that for most atmospheric conditions operating at longer wavelengths, the fields at the receiver can be assumed to be jointly gaussian[25,31] for which the time-delayed (T-D) covariance function can be written as

$$C(\rho_1,\rho_2,\tau)=<I(\rho_1,t_1)I(\rho_2,t_2)>-<I(\rho_1,t_1)><I(\rho_2,t_2)>$$

$$=<U(\rho_1,t_1)U^*(\rho_1,t_1)U(\rho_2,t_2)U^*(\rho_2,t_2)>-<I(\rho_1,t_1)><I(\rho_2,t_2)>$$

$$=<U(\rho_1,t_1)U^*(\rho_2,t_2)><U^*(\rho_1,t_1)U(\rho_2,t_2)>=|\Gamma(\rho_1,\rho_2,\tau)|^2 \quad (2.13)$$

Using Eqs. (2.12) and (2.13), the T-D covariance function normalized by the mean intensity squared for the focused beam case can simply be written as

$$C_N(\rho,\tau)=\exp\left[-\frac{\rho^2}{2\alpha_0^2}-\frac{32}{3\rho_0^{5/3}}\int_0^1 dw\,|(1-w)\rho-V\tau|^{5/3}\right] \quad (2.14)$$

It can be seen from Eq. (2.14) that the normalized variance is unity by setting ρ and τ equal to zero.

The simplicity of Eq. (2.14) makes it very attractive for remote sensing purposes. To derive exact formulations of the statistics, the time-delayed correlation function needs to be initially developed.

$$B_I(\rho_1,\rho_2,\tau)=<U(\rho_1,t_1)U^*(\rho_1,t_1)U(\rho_2,t_2)U^*(\rho_2,t_2)>$$

$$=\left(\frac{k}{2\pi L}\right)^4\int\int\int\int d\rho_1 d\rho_2 d\rho_3 d\rho_4$$

$$<U'(\rho_1,t_1)U'^*(\rho_2,t_1)U'(\rho_3,t_2)U'^*(\rho_4,t_2)>H(\rho_1,\rho_2,\rho_3,\rho_4;\rho_1,\rho_2;\tau)$$

$$\exp\left[\frac{ik}{2L}\left(\rho_1^2-\rho_2^2+\rho_3^2-\rho_4^2-2\rho_1\cdot(\rho_1-\rho_2)-2\rho_2\cdot(\rho_3-\rho_4)\right)\right] \quad (2.15)$$

where the fields after scattering from the target are denoted by $U'(\rho)$ and

$$H = <\exp\left[\psi(p_1,\rho_1,t_1)+\psi^*(p_1,\rho_2,t_1)+\psi(p_2,\rho_3,t_2)+\psi^*(p_2,\rho_4,t_2)\right]>$$

$$=\exp\left[-1/2(D_{12}-D_{13}+D_{14}+D_{23}-D_{24}+D_{34})+2C_{\chi_{13}}+2C_{\chi_{24}}\right] \qquad (2.16)$$

The generalized wave structure and the log-amplitude covariance functions are given by[28,32]

$$D_{ij}=2.91Lk^2\int_0^1 dtC_n^2(t)\left|\, t(p_i-p_j)+(1-t)(\rho_i-\rho_j)-V(t_i-t_j)\right|^{5/3} \qquad (2.17)$$

and

$$C_{\chi_{ij}}=0.132\pi^2Lk^2\int_0^1 C_n^2(t)\int_0^\infty dKK^{-8/3}\sin^2\left(\frac{K^2t(1-t)L}{2k}\right)$$

$$J_0\left[K\left|\, t(p_i-p_j)+(1-t)(\rho_i-\rho_j)-V(t_i-t_j)\right|^{5/3}\right] \qquad (2.18)$$

where $p_2=p_1$, $p_3=p_2$, $p_4=p_2$; $t_1=t_2=0$, $t_3=t_4=\tau$ and t is the normalized path length from the source to the field point. For the problem considered here, t represents the path from the target to the receiver (*i.e.*, t=1-w).

The fields, after scattering from the diffuse target, are jointly gaussian and delta correlated. For such a case, the following relationship holds[28]

$$<U'(\rho_1,t_1)U'^*(\rho_2,t_1)U'(\rho_3,t_2)U'^*(\rho_4,t_2)>=$$
$$\left(\frac{4\pi}{k^2}\right)^2<I'(\rho_2,t_1)><I'(\rho_4,t_2)>\delta(\rho_1-\rho_2)\delta(\rho_3-\rho_4)$$
$$+\left(\frac{4\pi}{k^2}\right)^2<U'(\rho_4,t_1)U'^*(\rho_4,t_2)><U'^*(\rho_2,t_2)U'(\rho_2,t_1)>$$
$$\delta(\rho_1-\rho_4)\delta(\rho_3-\rho_2) \qquad (2.19)$$

The T-D covariance function is related to the T-D correlation function by

$$C_I(\rho_1,\rho_2,\tau)=B_I(\rho_1,\rho_2,\tau)-<I(\rho_1,t_1)><I(\rho_2,t_2)> \tag{2.20}$$

Using Eq. (2.19) in Eq. (2.15) and performing the integrations over $d\rho_1$ and $d\rho_2$, the T-D covariance function becomes

$$\begin{aligned} C_I(\rho_1,\rho_2,\tau)=&\frac{1}{\pi^2L^4}\int\int d\rho_2 d\rho_4 (e^{4C_\chi(\rho,\rho,\tau)}-1)<I(\rho_2)><I(\rho_4)> \\ &+\frac{1}{\pi^2L^4}\int\int d\rho_2 d\rho_4 e^{i\frac{k}{L}\rho\cdot\rho} H(\rho_4,\rho_2,\rho_2,\rho_4;\rho_1,\rho_2;\tau) \\ &<U'(\rho_4,t_1)U'^*(\rho_4,t_2)><U'(\rho_2,t_2)U'^*(\rho_2,t_1)> \end{aligned} \tag{2.21}$$

The ensemble averages over the fields can be obtained by using Eq. (2.1)

$$\begin{aligned} <U'(\rho_4,t_1)U'^*(\rho_4,t_2)>=&T_0^2U_0^2(\frac{k}{2\pi L})^2\int\int dr_1 dr_2 \\ &<\exp\left[\psi_1(\rho_4,r_1,t_1)+\psi_1^*(\rho_4,r_2,t_2)\right]> \\ &\exp\left[-\frac{r_1^2+r_2^2}{2\alpha_0^2}+\frac{ik}{2L}(1-L/F)(r_1^2-r_2^2)-\frac{ik}{L}\rho_4\cdot(r_1-r_2)\right] \end{aligned} \tag{2.22}$$

After some mathematical manipulation, the expression above reduces to

$$\begin{aligned} <U'(\rho_4,t_1)U'^*(\rho_4,t_2)>=&\frac{T_0^2U_0^2\alpha_0^2k^2}{4\pi L^2}\int dr \exp\left[-\frac{r^2}{4\alpha_0^2}-\frac{ik}{L}\rho_4\cdot r\right. \\ &\left.-\left(\frac{\alpha_0 k}{2L}(1-L/F)\right)^2 r^2-\frac{1}{2}D_\psi(0,r,\tau)\right] \end{aligned} \tag{2.23}$$

Holmes *et al* [28] performed some of the integration of Eq. (2.21) analytically and the rest numerically for the zero time-delayed case. Their result for the normalized variance, obtained from Eq. (2.21) by setting p and τ equal to zero, is shown in figure (2.1) as a function of log-amplitude variance (Rytov variance[1], $\sigma_\chi^2=0.124C_n^2k^{7/6}L^{11/6}$). Figure (2.1) shows that for $\sigma_\chi^2<0.02$ the normalized variance is very close to unity which results from the jointly gausssian fields. The covariance function has also been shown in excellent agreement with the jointly gaussian assumption under the same condition.

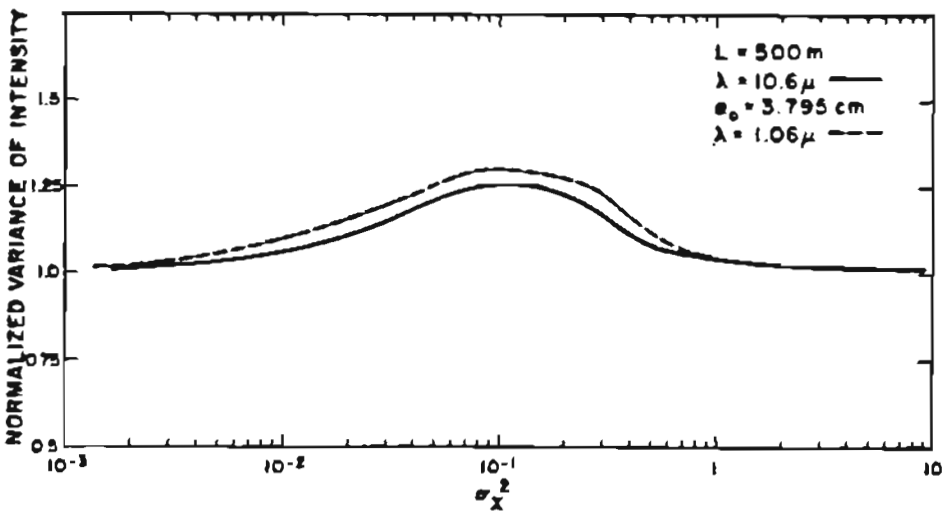

Figure 2.1 Normalized variance of the received intensity versus the log-amplitude variance for the focused beam (F=L).

The formulation of Eq. (2.21) can be somewhat simplified by neglecting the log-amplitude covariance function (C_χ) as shown by Lee *et al* [25]. Nevertheless, the formulations that follow are still too complex for useful interpretation and only the normalized variance can be evaluated analytically, giving a numerical value of one.

The validity of the jointly gaussian assumption was later verified experimentally[31]. The measured normalized variance and spatial covariance function have been shown to be in excellent agreement with the jointly gaussian predictions when $\sigma_\chi^2 < 0.02$ and $\rho_0 > \alpha_0$, respectively.

These conditions are not difficult to satisfy especially in the infrared region of operation and path lengths of the order of kilometers. This is one of the reasons for using a CO_2 laser operating at 10.6μm for this work. As an example, consider an intermediate turbulence strength of $C_n^2 = 10^{-14}\ m^{-2/3}$, a path length of 1 km and a transmitter beam radius of 3 cm. Operating at 10.6 μm, the log-amplitude variance and the coherence length are equal to

$$\sigma_\chi^2 = 2.13 \times 10^{-3} < 0.02$$

$$\rho_0 = 0.68 > 0.03$$

2.2 Wind Sensing Techniques

There are several techniques that utilize the T-D covariance function given by Eq. (2.14) to measure the crosswind velocity. Most processing techniques developed for the line of sight case[33] are applicable to the speckle-turbulence interaction, possibly with some modifications. In addition to these techniques, a new method was developed[34] which proved to be most suitable for processing the quantity of Eq. (2.14). Each method is described in this section and evaluated individually.

Some of the windsensing techniques are illustrated in figure (2.2). Perhaps the most common method in the line of sight case is the slope of the T-D covariance function at the zero time delay[5] . The T-D covariance function is rewritten in a form that is more convenient for our intentions.

$$C_I(\mathbf{p},\tau)=<I>^2\exp\left[-\frac{p^2}{2\alpha_0^2}-5.82Lk^2\int_0^1 dw C_n^2(w)\left\{(1-w)^2p^2-2(1-w)pV(w)\tau\cos\theta+(V(w)\tau)^2\right\}^{5/6}\right] \quad (2.24)$$

where θ is the angle between $\mathbf{p}$ and $\mathbf{V}$. The slope of the Eq. (2.24) is given by

$$S_I=\frac{\partial C_I(\mathbf{p},\tau)}{\partial\tau}\Big|_{\tau=0}$$

$$=C_I(\mathbf{p},0)(5/3)5.82Lk^2p^{2/3}\int_0^1 dw C_n^2(w)V(w)(1-w)^{2/3}\cos\theta \quad (2.25)$$

It can be seen from Eq. (2.25) that the wind weighting function is equal to $(1-w)^{2/3}$ and the slope is sensitive only to the component of wind along p . When the wind and the turbulence are uniform along the path, Eq. (2.25) reduces to

$$S_I=(32/3)C_I(p,0)\frac{p^{2/3}}{\rho_0^{5/3}}V_p \tag{2.26}$$

where V_p is the wind component along p and can be obtained when ρ_0 is known. This implies that the slope method must be used in conjunction with one of the other methods in order to be useful.

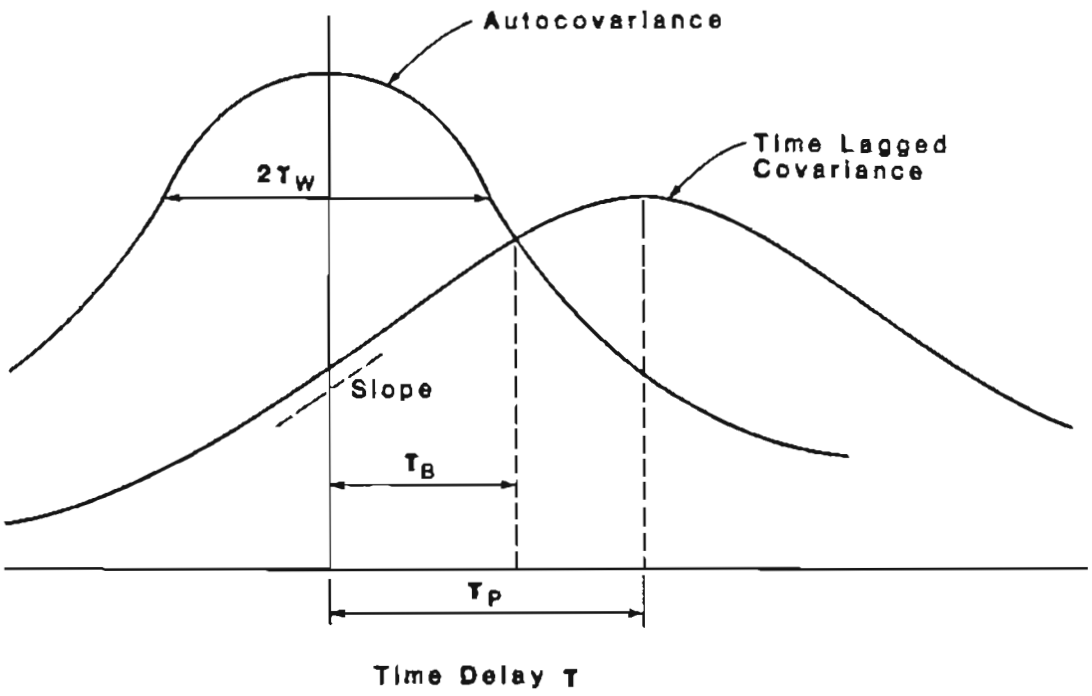

Figure 2.2 Wind Sensing Techniques.

Some numerical analysis has been performed to demonstrate the sensitivity of the various methods to nonuniformities of the wind and the turbulence. This is done by using a 60% sinusoidally modulated wind and structure constant of the index of refraction C_n^2 in Eq. (2.24). As illustrated in figures (2.3) and (2.4), the slope method is insensitive to the nonuniformities of the wind and the turbulence along the path. However, the use of a different method with a different weighting function to eliminate ρ_0 can cause considerable error in the wind measurement.

The method that is usually used in conjunction with the slope method is the width of the autocovariance. In this method, the time delay, τ_w, at which the autocovariance falls to 67% of its peak value is measured[33]. The slope of the autocovariance curve is a maximum at this time delay. Letting Eq. (2.24) be equal to 0.67 with p=0 and $\tau=\tau_w$, we have

$$5.82Lk^2\int_0^1 dw C_n^2(w)\,|\,V(w)\tau_w\,|^{5/3} = 0.4 \tag{2.27}$$

For uniform wind and turbulence, Eq. (2.27) reduces to

$$V=\frac{0.1395\rho_0}{\tau_w} \tag{2.28}$$

This method is best utilized with the slope method in determination of both the wind velocity and turbulence coherence length (ρ_0) which is related to the strength of the turbulence.

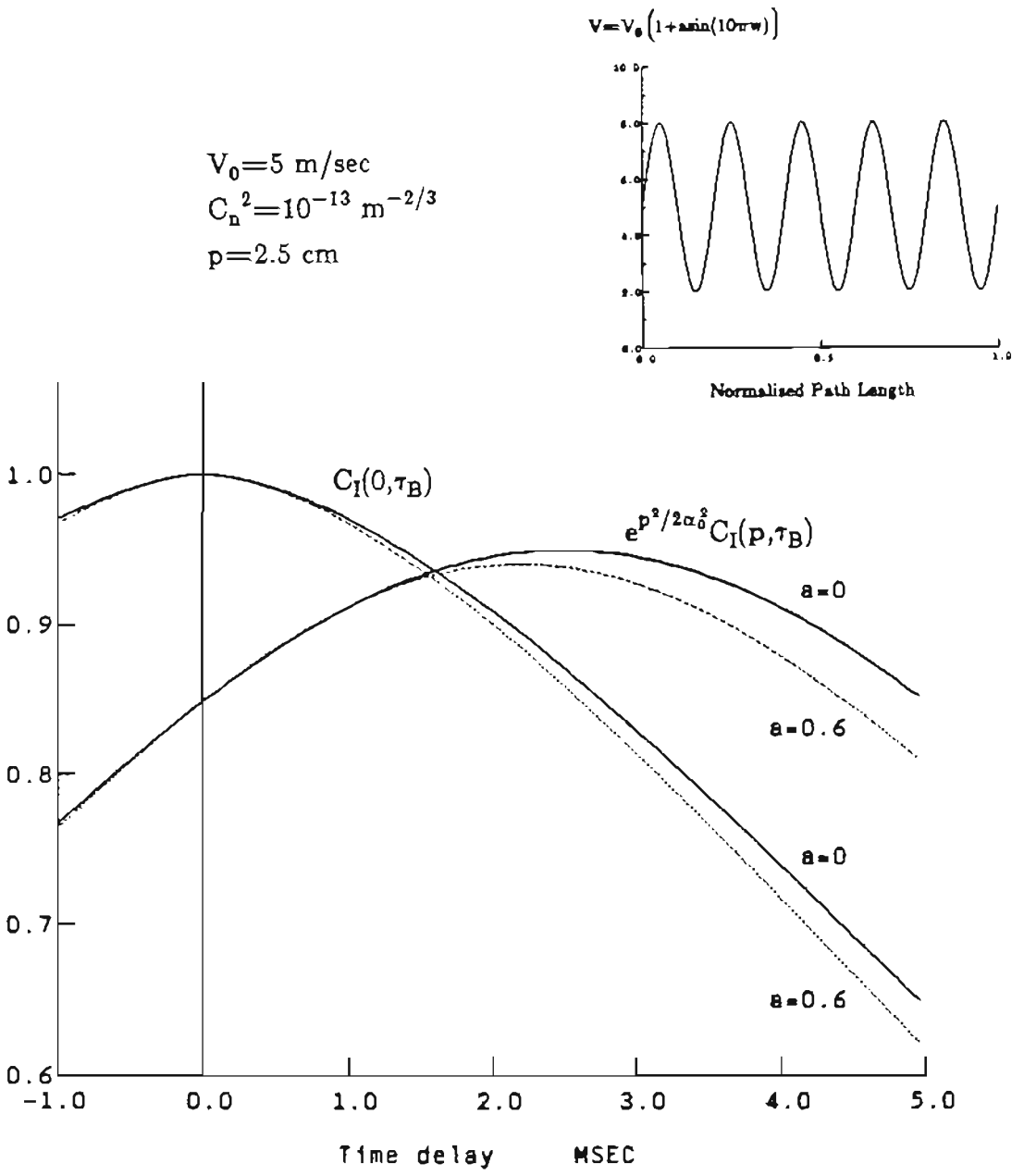

Figure 2.3 The effect of nonuniform wind on processing techniques.

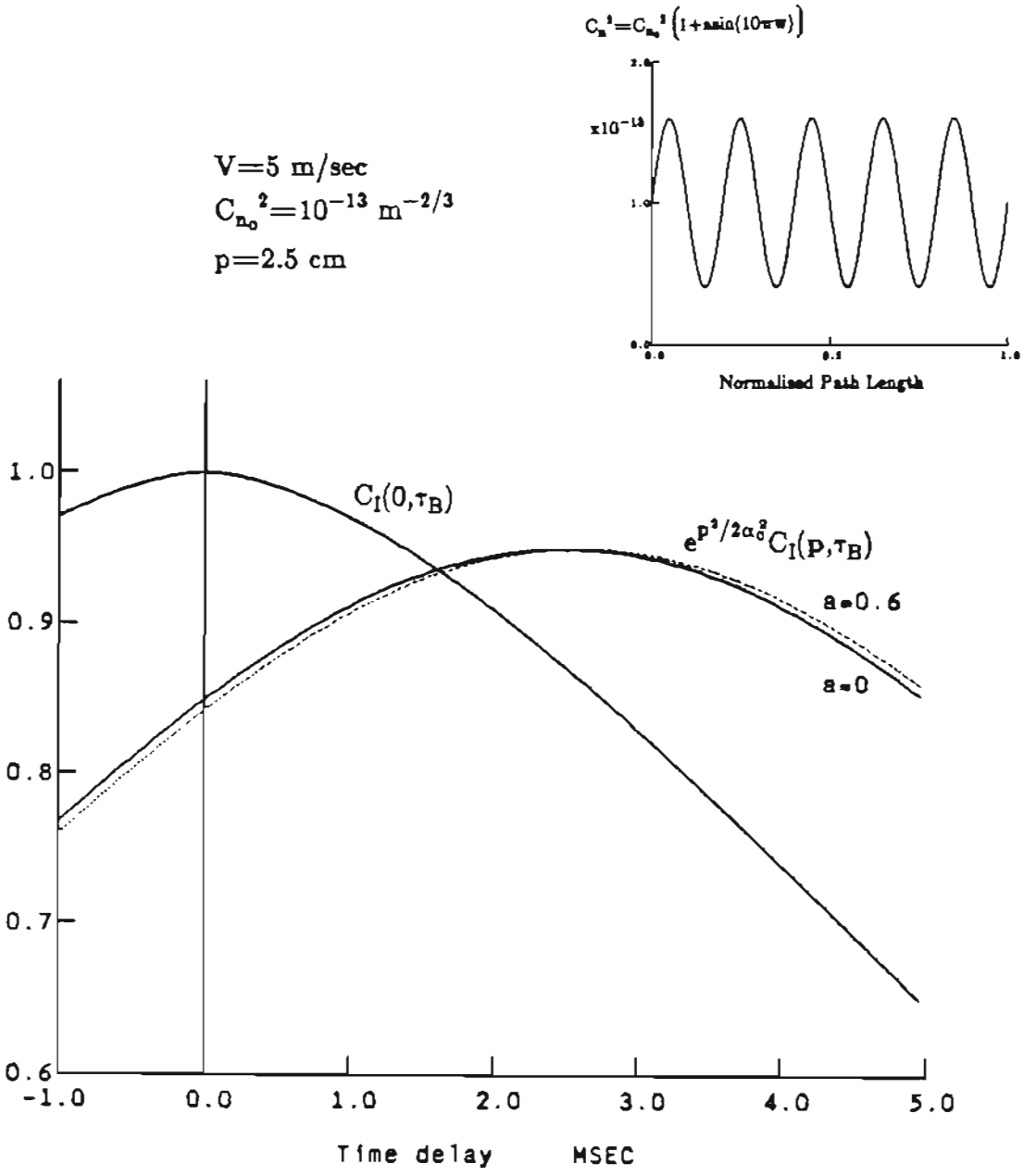

Figure 2.4 The effect of nonuniform turbulence on processing techniques.

It should be noted that, this method has no sensitivity to the direction of the wind. From Eq. (2.27), the relative sensitivity functions of the wind are obtained to be uniform. Figures (2.3) and (2.4) illustrate the sensitivity of this method to the nonuniformities along the path

It is also possible to obtain ρ_0 from the covariance function. From Eq. (2.24), we can obtain

$$\rho_0^{5/3} = -\frac{4p^{5/3}}{\ln C_I(p,0) + p^2/2\alpha_0^2} \tag{2.29}$$

This has the advantage of determining ρ_0 independent of the wind velocity. However, it is relatively sensitive to the nonuniformities of the turbulence.

Another method of interest is the delay to peak for which the time delay, τ_p, corresponding with the peak of the T-D covariance curve is measured[3,5] (see figure (2.2)). This requires the estimation of several points of the T-D covariance curve in order to determine τ_p. The accuracy of this method is very much limited to the number of T-D covariance points estimated, the sampling period and the spacing between the detectors. Therefore, it may require a great deal of processing time to obtain reasonable accuracy. The major advantage of this method is that it does not require any knowledge of the strength of turbulence.

The time delay corresponding to the peak is obtained by differentiating Eq. (2.24) with respect to τ and setting the result equal to zero. That is

$$\int_0^1 dw C_n^2(w) V(w) \left((1-w)p\cos\theta - V(w)\tau_p\right)$$

$$\left((1-w)^2p^2 - 2(1-w)pV(w)\tau_p\cos\theta + (V(w)\tau_p)^2\right)^{-1/6} = 0 \quad (2.30)$$

For the case where V and p are colinear and V is uniform along the path, Eq. (2.30) can be solved analytically, giving $\tau_p = \frac{p}{2V}$, or $V = \frac{p}{2\tau_p}$.

For the case where V and p are orthogonal, the solution to Eq. (2.30) is $\tau_p = 0$. This means that there is no shift of the peak of the T-D covariance function from the component of wind along the direction of propagation and no sensitivity to that component of the wind.

The relative weighting function on τ_p can be found by letting $V(w) = V(w')\delta(w-w')$ in Eq. (2.30) giving $\tau_p = \frac{(1-w')p\cos\theta}{V(w')}$. Consequently, the relative sensitivity function on the measured wind velocity along p is $1/(1-w')$. The distinction between the relative wind sensitivity function and the conventional wind weighting function should be noted here. Because Eq. (2.30) is not a linear function of the wind, a linear wind weighting function cannot be defined. However, the relative sensitivity function does give the relative contribution of each part of the path.

The delay to peak method is quite sensitive to the nonuniformities of the wind along the path[5] (see figure (2.3)). However, as can be seen in figure (2.4), it is not sensitive in any form to the nonuniformities of the turbulence.

The other method that is often used in the line of sight case for wind measurements is the Briggs method[33] that measures the time delay at which the autocovariance and T-D covariance curves cross. A slight modification is made for the speckle-turbulence interaction as illustrated by the following

$$e^{p^2/2\alpha_\delta^2} C_I(p,\tau_B) = C_I(0,\tau_B) \tag{2.31}$$

Using Eqs. (2.24) and (2.31), we have

$$\int_0^1 dw C_n^2(w) \left[(1-w)^2 p^2 - 2(1-w) p V \tau_B \cos\theta + (V\tau_B)^2\right]^{5/6}$$

$$= \int_0^1 dw C_n^2(w) | V(w)\tau_B |^{5/3} \tag{2.32}$$

Solving Eq. (2.32) numerically for V, gives the component of the wind velocity along p as

$$V = \frac{p}{3.1056\tau_B} \tag{2.33}$$

The Briggs method like the delay to peak method does not require knowledge of the turbulence strength but it suffers from long processing time. The relative sensitivity function of the wind using the Briggs method is not known, however, numerical analysis of figures (2.3) and (2.4) shows that the effect of the nonuniformities along the path is insignificant.

All the methods described above were used to process the collected data by the experimental apparatus with less than acceptable results. The major

reason for the poor performance of these methods was concluded to be the rather small effect of the turbulence on the T-D covariance curve at the 10.6μm wavelength. As an example, at 10.6μm for a 1000 meter path and $C_n^2=10^{-13}m^{-2/3}$, the peak of the T-D covariance curve rises only 2.5% above the value at zero time delay. These small changes coupled with having to find them in a fully developed speckle patterns makes processing difficult. However, it should be noted that these techniques should be usable at shorter wavelengths where the speckle-turbulence interaction is stronger. The result of the work accomplished in the past using a pulsed laser and direct detection in the near infrared region tends to confirm that conclusion[35].

To overcome these difficulties, an effort was made to develop a new processing technique. Considerable success was gained using the new technique which is referred to as the Z-Log Ratio (ZLR) method[34]. The ZLR method uses the measured values of the covariance and the autocovariance of an arbitrary time delay. The quantity to be estimated is the parameter Z defined as

$$Z=\frac{\ln(C_I(0,\tau)/\sigma_I^2)}{\ln(C_I(p,0)/\sigma_I^2)+p^2/2\alpha_0^2} \tag{2.34}$$

Using Eq. (2.24) in Eq. (2.34), gives

$$Z=\frac{\int_0^1 dw C_n^2(w)\,|\,V(w)\tau\,|^{5/3}}{\int_0^1 dw C_n^2(w)\,|\,(1-w)p\,|^{5/3}} \tag{2.35}$$

For uniform atmospheric conditions, the wind velocity is obtained from Eq. (2.35) to be

$$V=(3/8)^{3/5}\frac{p}{|\tau|}Z^{3/5} \tag{2.36}$$

The only system parameters needed to obtain the wind velocity are the spacing between the detectors and the transmitter beam radius. The ZLR method does not provide the direction of the wind for which the sign of the measured slope of the T-D covariance can be used. From Eq. (2.35) the wind sensitivity function is obtained to be uniform and the numerical simulation showed some sensitivity to nonuniform winds. The structure constant of the index of refraction cancels out by taking the ratio in Eq. (2.35). The numerator and the denominator have different weighting functions for C_n^2, however, the numerical analysis showed little effect on this method due to nonuniformities of the turbulence.

In order to reduce the measurements error, Z is measured at several time delays. That is

$$V=(3/8)^{3/5}\frac{p}{N}\sum_{n=1}^{N}\frac{Z_n^{3/5}}{|\tau_n|} \tag{2.37}$$

where Z_n is the measured value at time delay τ_n. Eq. (2.37) was used to process most of the wind data presented in ch. 4 where the results are usually averaged over five terms.

The mean square error associated with this measurement is given by

$$\mathrm{MSE}=\frac{1}{N}\sum_{n=1}^{N}\left[Z_n-(8/3)\left(\frac{V^2\tau_n^2}{p^2}\right)^{5/6}\right]^2 \tag{2.38}$$

In an attempt to further improve the ZLR method, the error given by Eq. (2.38) was minimized by modifying Eq. (2.37). Taking the derivative of Eq. (2.38) with respect to V and setting it equal to zero, we obtain

$$\frac{\partial \mathrm{MSE}}{\partial V}=\frac{2}{N}\sum_{n=1}^{N}-(40/9)\left(\frac{\tau_n^2}{p^2}\right)^{5/6}(V^2)^{1/3}\left[Z_n-(8/3)\left(\frac{V^2\tau_n^2}{p^2}\right)^{5/6}\right]^2=0 \tag{2.39}$$

Now, solving for the wind velocity

$$V_{\mathrm{MMSE}}=p\left[(3/8)\sum_{n=1}^{N}Z_n|\tau_n|^{5/3}/\sum_{n=1}^{N}|\tau_n|^{10/3}\right]^{3/5} \tag{2.40}$$

Using Eq. (2.40) in Eq. (2.38), the minimum mean square error is obtained.

$$\mathrm{MMSE}=\frac{1}{N}\left[\sum_{n=1}^{N}Z_n^2-\left(\sum_{n=1}^{N}Z_n|\tau_n|^{5/3}\right)^2/\sum_{n=1}^{N}|\tau_n|^{10/3}\right] \tag{2.41}$$

The results of the experimental measurements obtained using Eq. (2.40) showed slight improvement over that of the Eq. (2.37). It is proposed that Eqs. (2.38) and (2.41) might be used as a measure of reliability of the data.

The preprocessing of the samples showed some improvement in reducing the statistical fluctuation in the measurements. This is accomplished by generating one bit per sample which is equal to zero or one depending on whether the received intensity is greater than or less than the received mean intensity, respectively. This technique is referred to as Binary-Z Log Ratio

(B-ZLR) method. B-ZLR method reduces the processing time and allows for much less complex processing instrumentation.

It should be noted that the component of the wind aligned with $\mathbf{p}$ has been considered here. In order to determine the vector wind, the use of three or more detectors have been proposed where the two vector spacings $\mathbf{p}_1$ and $\mathbf{p}_2$ are not colinear.

2.3 Statistics Of The Bistatic Lidar Returns

The analysis of section 2.1 included the assumption of independent effects of the turbulence on the outgoing and return paths. However, it has been shown that the statistical dependence of the two paths can significantly influence time-delayed statistics of the lidar returns[24] .

The effect of correlation between incident and reflected waves has been considered by Aksenov *et al* [36] for the two asymptotic cases of spherical and plane waves reflected from a diffuse target. This showed that an increase in intensity fluctuations occurs with decreasing separation between the source and the receiver. However, their results cannot directly be applied to lidar returns where the source is of finite size.

In this section, the general bistatic case is considered by including the time-delayed statistical dependence of the outgoing and return paths. Analytical expressions have been obtained describing the time-delayed statistics as a function of the separation between the transmitter and receiver.

Discarding the independence assumption of the incident and reflected waves, the two ensemble averages of Eq. (2.6) are replaced by a single average given by

$$<\exp\left(\psi_1(\rho,r_1)+\psi_1^*(\rho,r_2)+\psi_2(p_1,\rho)+\psi_2^*(p_2,\rho)\right)>$$

Making use of the principle of reciprocity ($\psi_2(p,\rho)=\psi_1(\rho,p)$) and the equality of Eq. (2.16), the ensemble average above can be written in terms of the wave structure function.

$$< >=\exp\left[-\frac{1}{2}\left(D_\psi(r_1-r_2)+D_\psi(p_1-p_2)+D_\psi(r_1-p_2)+D_\psi(r_2-p_1)\right.\right.$$
$$\left.\left.-D_\psi(r_1-p_1)-D_\psi(r_2-p_2)\right)\right] \qquad (2.42)$$

where the wave structure function is defined as $D_\psi(x)=2(x/\rho_0)^{5/3}$. The log-amplitude covariance function C_χ has not been included in Eq. (2.42), since its effects are negligible for low path integrated turbulence as discussed earlier. Making the following change of variables

$$r=r_1-r_2 \qquad 2R=r_1+r_2$$
$$p=p_1-p_2 \qquad 2q=p_1+p_2$$

and using Eq. (2.42) in Eq. (2.6), we can write

$$\Gamma(p_1,p_2)=\frac{T_0^2U_0^2}{\pi L^2}\left(\frac{k}{2\pi L}\right)^2 e^{i\frac{k}{L}p\cdot q}\int\int dr\,dR\; H(r,p,R,q)$$
$$\exp\left(-\frac{r^2}{4\alpha_0^2}-\frac{R^2}{\alpha_0^2}+i\frac{k}{L}(1-L/F)r\cdot R\right)\int d\rho\, e^{-i\frac{k}{L}\rho\cdot(r+p)} \qquad (2.43)$$

where H is defined as

$$H(\mathbf{r},\mathbf{p},\mathbf{R},\mathbf{q})=\exp\left[-\frac{1}{2}\left(D_\psi(\mathbf{r})+D_\psi(\mathbf{p})+D_\psi(\mathbf{R}+\frac{\mathbf{r}}{2}-\mathbf{q}+\frac{\mathbf{p}}{2})+D_\psi(\mathbf{R}-\frac{\mathbf{r}}{2}-\mathbf{q}-\frac{\mathbf{p}}{2})\right.\right.$$
$$\left.\left.-D_\psi(\mathbf{R}+\frac{\mathbf{r}}{2}-\mathbf{q}-\frac{\mathbf{p}}{2})-D_\psi(\mathbf{R}-\frac{\mathbf{r}}{2}-\mathbf{q}+\frac{\mathbf{p}}{2})\right)\right] \qquad (2.44)$$

The vector $\mathbf{p}$ specifies the spacing between the receivers and $\mathbf{q}$ the spacing between the transmitter and receivers. The integration over ρ and $\mathbf{r}$ can be performed by making use of the identity

$$\int d\rho e^{-i\frac{k}{L}\rho\cdot(\mathbf{r}+\mathbf{p})}=(\frac{2\pi L}{k})^2\delta(\mathbf{r}+\mathbf{p})$$

Hence, the mutual intensity function reduces to

$$\Gamma(\mathbf{p}_1,\mathbf{p}_2)=\frac{T_0^2U_0^2}{\pi L^2}e^{i\frac{k}{L}\mathbf{p}\cdot\mathbf{q}}e^{-p^2/4\alpha_\delta^2}\int d\mathbf{R}\exp\left(-\frac{R^2}{\alpha_0^2}-i\frac{k}{L}(1-L/F)\mathbf{p}.\mathbf{R}\right)$$
$$\exp\left[-\frac{1}{\rho_0^{5/3}}\left(2p^{5/3}+2|\mathbf{R}-\mathbf{q}|^{5/3}-|\mathbf{R}-\mathbf{q}-\mathbf{p}|^{5/3}-|\mathbf{R}-\mathbf{q}+\mathbf{p}|^{5/3}\right)\right] \qquad (2.45)$$

It can be seen from the expression above that as the transmitter-receiver spacing increases, the correlation between the two paths becomes less significant compared to the correlation between any two points along each path. Consequently, Eq. (2.45) reduces to the one with independent paths assumption when the spacing between the transmitter and the receiver (q) is much greater than α_0 and p, regardless of the turbulence coherence length ρ_0. This might be easier to see by letting q be much larger than R and p in Eq. (2.45) for which the quantity involving the last three terms in the

exponent tends to zero.

Now, including the time-delay τ in Eq. (2.6), the ensemble average must be replaced by

$$<\exp\left(\psi_1(\rho,r_1,t_1)+\psi_1^*(\rho,r_2,t_2)+\psi_2(\rho_1,\rho,t_1)+\psi_2^*(\rho_2,\rho,t_2)\right)> \qquad (2.46)$$

However, the atmospheric eddies along one path drift through the other path with the crosswind (see figure (2.5)).

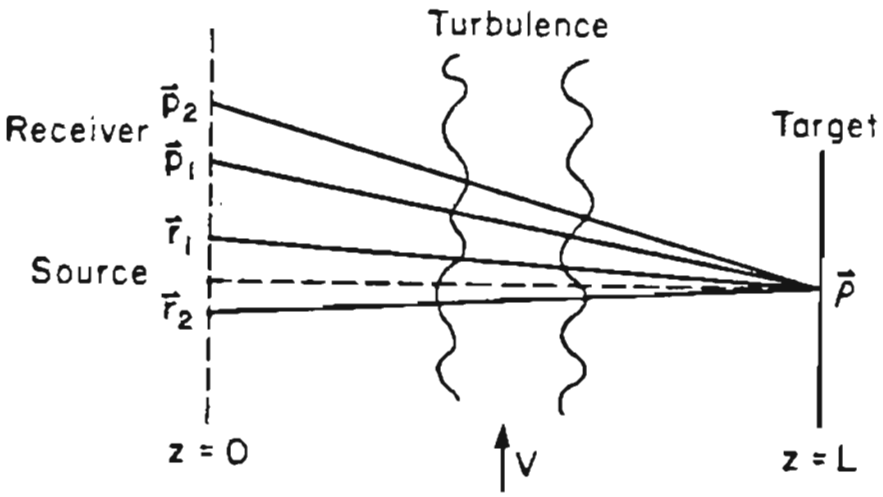

Figure 2.5 The turbulent eddies drift with the wind through both outgoing and return paths.

From figure (2.5) and the application of the principle of reciprocity, the ensemble average of Eq. (2.46) can be written as

$$\exp\left[-\frac{1}{2}\left(D_\psi(-\mathbf{r},0,V\tau)+D_\psi(\mathbf{p},0,V\tau)+D_\psi(\mathbf{r}_1-\mathbf{p}_2,0,V\tau)+D_\psi(\mathbf{r}_2-\mathbf{p}_1,0,-V\tau)\right.\right.$$
$$\left.\left.-D_\psi(\mathbf{r}_1-\mathbf{p}_1,0,0)-D_\psi(\mathbf{r}_2-\mathbf{p}_2,0,0)\right)\right] \qquad (2.47)$$

The first two terms of Eq. (2.47) describe the individual paths and the remaining terms describe the dependency of the two paths. Following the same steps as before and integrating over $d\rho$ and dr, the time delayed mutual intensity can be written as

$$\Gamma(\mathbf{p}_1,\mathbf{p}_2,\tau)=\frac{T_0^2U_0^2}{\pi L^2}e^{i\frac{k}{L}\mathbf{p}\cdot\mathbf{q}}e^{-p^2/4\alpha_0^2}\int d\mathbf{R}\exp\left(-\frac{R^2}{\alpha_0^2}-i\frac{k}{L}(1-L/F)\mathbf{p}.\mathbf{R}\right)$$
$$\exp\left[\frac{1}{\rho_0^{5/3}}\left(|\mathbf{q}-\mathbf{R}+\mathbf{p}|^{5/3}+|\mathbf{q}-\mathbf{R}-\mathbf{p}|^{5/3}\right)\right.$$
$$\left.-2.91Lk^2\int_0^1 dw C_n^2(w)\left(|(1-w)\mathbf{p}-V\tau|^{5/3}+\frac{1}{2}|(1-w)(\mathbf{q}-\mathbf{R})-V\tau|^{5/3}\right.\right.$$
$$\left.\left.+\frac{1}{2}|(1-w)(\mathbf{q}-\mathbf{R})+V\tau|^{5/3}\right)\right] \qquad (2.48)$$

Applying the jointly gaussian assumption, the normalized time-delayed covariance function for the focused beam case can be written as

$$C_N(\mathbf{p},\tau)=\left\{\frac{e^{-p^2/4\alpha_0^2}}{\pi\alpha_0^2}\int d\mathbf{R}e^{-R/\alpha_0^2}\exp\left[\frac{1}{\rho_0^{5/3}}\left(|\mathbf{q}-\mathbf{R}+\mathbf{p}|^{5/3}+|\mathbf{q}-\mathbf{R}-\mathbf{p}|^{5/3}\right)\right.\right.$$

$$-2.91Lk^2\int_0^1 dw C_n^2(w)\left(|(1-w)\mathbf{p}-\mathbf{V}_\tau|^{5/3}\right.$$

$$\left.\left.\left.+\frac{1}{2}|(1-w)(\mathbf{q}-\mathbf{R})-\mathbf{V}_\tau|^{5/3}+\frac{1}{2}|(1-w)(\mathbf{q}-\mathbf{R})+\mathbf{V}_\tau|^{5/3}\right)\right]\right\}^2 \quad (2.49)$$

Eq. (2.49) has been numerically evaluated (see appendix A) and the result is plotted in figures (2.6) and (2.7) assuming uniform atmospheric turbulence and wind velocity for two cases: coaxial paths (q=0) and finite transmitter-receiver spacing. The independent paths case, described by Eq. (2.14), is also shown for comparison. It can be seen that as the spacing between the transmitter and receiver increases, Eq. (2.49) approaches the T-D covariance function obtained with the independent paths assumption.

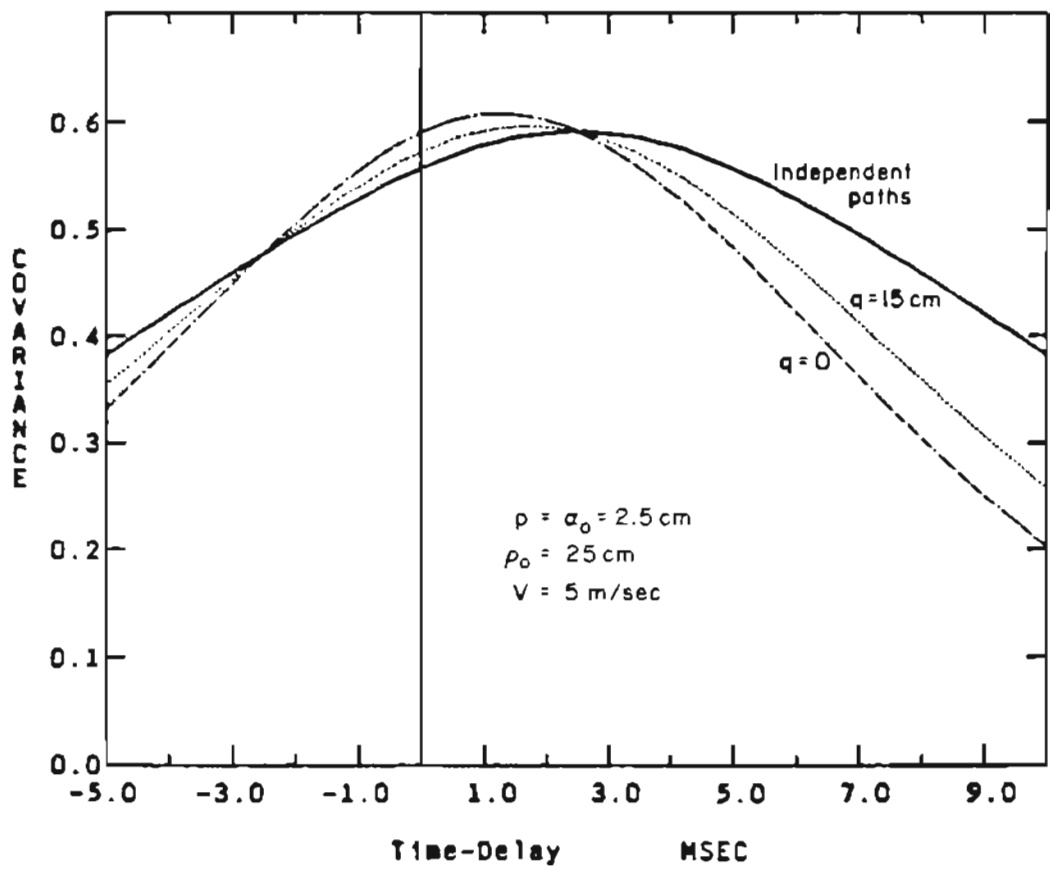

Figure 2.6 The Time-Delayed Covariance for three cases of independent paths (solid line), bistatic (dotted line) and monostatic (dot-dashed line).

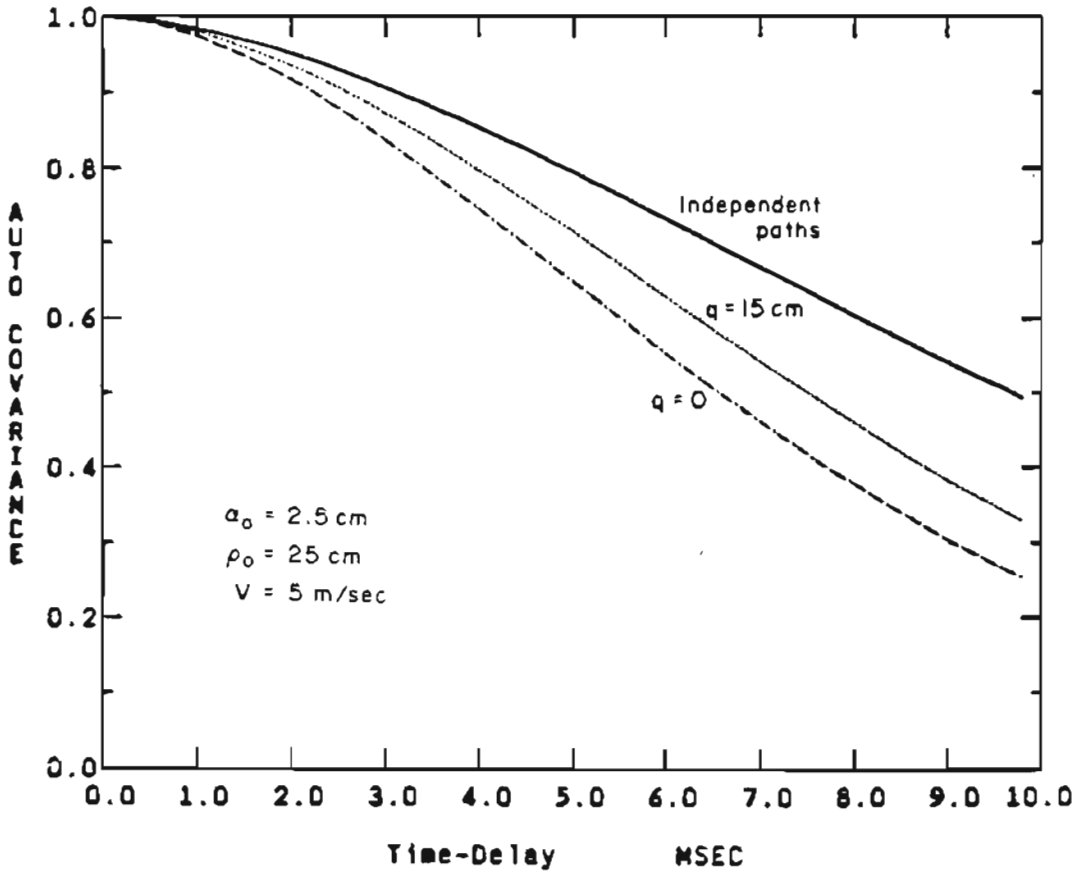

Figure 2.7 The Autocovariance for three cases of independent paths (solid line), bistatic (dotted line) and monostatic (dot-dashed line).

It should be noted that the turbulence outer scale size has not been considered here and has been taken to be infinite[28]. Therefore, the time-delayed statistics may approach its asymptotic form of independent paths more rapidly with q than shown in figures (2.6) and (2.7) when q is larger than the outer scale size.

The increase in covariance (τ=0) with decreasing q (see figure (2.6)), reflects the fact of higher correlation between the two paths with smaller separation. As can be seen from figure (2.6), the peak of T-D covariance function moves toward zero time delay and figure (2.7) shows that the auto-covariance falls faster with time as the transmitter-receiver spacing decreases. These effects can be quite significant for many applications including the remote sensing of the atmospheric turbulence and crosswinds.

The extent of the error that can result by applying the processing techniques described previously is obvious from figures (2.6) and (2.7), when the transmitter and receiver are not spaced far enough from each other. The higher covariance implies weaker turbulence while faster decorrelation means stronger turbulence or higher wind velocity than the true quantities. The shift of the peak of the T-D covariance curve also gives rise to higher wind velocity.

The other application that is worth noting is the coherent DIAL (differential-absorption lidar) measurements which can be affected by the time-delayed statistical dependence of the outgoing and return paths. The DIAL systems deduce the concentration of the molecular species by measur-

ing the returned radiation at two distinct frequencies[37]. The frequencies are chosen such that the corresponding absorption coefficients of the molecule being monitored are substantially different. However, in many practical cases the level of the concentration is very low. For this reason, the measurements accuracy is of great importance which improves with higher temporal correlation[38–40] of the returned intensity. The faster decorrelation resulting from smaller transmitter-receiver spacing can increase the error associated with coherent DIAL measurements[41] .

2.4 Heterodyne Signal Power

It is clear from the analysis above that the spacing between the transmitter and receiver can play a significant role on the performance of a heterodyne detection system. The work by Clifford and Wandzura[42] takes the dependence effect of the turbulence on both paths into account and analyzes the performance of a monostatic heterodyne lidar where the paths are coaxial. They have demonstrated that the signal degradation due to the presence of atmospheric turbulence is less severe for the monostatic lidar than previously predicted by independent paths assumption.

The analytical formulation describing the heterodyne signal power for the general bistatic case as a function of the transmitter-receiver spacing is presented here. It has been shown that the results approach those of the monostatic and the independent paths cases in the limit[24].

The heterodyne signal power is given by

$$<i_s^2>=<|\int U(p)U_{LO}^*(p)dp|^2> \tag{2.50}$$

where $U_{LO}(p)$ is the local oscillator field distribution. The signal power can be written in terms of the mutual intensity function as

$$<i_s^2>=\int\int dp_1 dp_2 U_{LO}^*(p_1)U_{LO}(p_2)\Gamma(p_1,p_2) \tag{2.51}$$

where $\Gamma(p_1,p_2)$ is given by Eq. (2.45). It can be assumed that the local oscillator is an untruncated gaussian beam centered at $\mathbf{a}$, as expressed below

$$U_{LO}(p)=e^{-(p-a)^2/2\beta_0^2-ikp.s} \tag{2.52}$$

where the phasefront angle is specified by the aiming vector $\mathbf{s}$. Using Eq. (2.45) with F=L and Eq. (2.52) in (2.51), the signal power can be expressed as

$$<i_s^2>=\frac{T_0^2U_0^2}{\pi L^2}\int\int dpdq\, e^{-(q-a)^2/\beta_0^2}e^{i\frac{k}{L}p.q}e^{-p^2/4\beta_0^2-p^2/4\alpha_0^2}\int dR e^{-R^2/\alpha_0^2}$$
$$\exp\left[-\frac{1}{\rho_0^{5/3}}\left(2p^{5/3}+2|R-q|^{5/3}-|R-q-p|^{5/3}-|R-q+p|^{5/3}\right)\right] \tag{2.53}$$

where the integration variables are changed to $\mathbf{p}$ and $\mathbf{q}$. The vector $\mathbf{a}$ specifies the location of the center of the receiver aperture and the transmitter is centered at the origin of the coordinate system.

Once again, making the change of variables $\xi=R-q$, $2\eta=R+q$ and setting $\alpha_0=\beta_0$ for simplicity reasons, gives

$$<i_s^2>=\frac{T_0^2U_0^2}{\pi L^2}\int dp\ e^{-p^2/2\alpha_0^2}\int\int d\xi d\eta\ e^{i\frac{k}{L}p\cdot(\eta-\frac{\xi}{2})}\ e^{-2(\eta-\frac{a}{2})^2/\alpha_0^2}\ e^{-(\xi+a)^2/2\alpha_0^2}$$
$$\exp\left[-\frac{1}{\rho_0^{5/3}}\left(2p^{5/3}+2\xi^{5/3}-|\xi-p|^{5/3}-|\xi+p|^{5/3}\right)\right] \qquad (2.54)$$

The complex phase factor in the expression above can be simplified, since $L>>k\alpha_0^2$ which is the far field assumption and true for most practical applications[23], therefore

$$e^{i\frac{k}{L}p\cdot(\eta-\frac{\xi}{2})}=e^{i\frac{k}{L}p\cdot q}\simeq e^{i\frac{k}{L}p\cdot a}$$

It should be noted that, the usual case of heterodyne detection has been considered here, for which the transmitter beam is focused on the target and the receiving aperture is of the order of the speckle size. The integration over η can easily be performed resulting in

$$<i_s^2>=\frac{T_0^2U_0^2\alpha_0^2}{2L^2}\int dp\ e^{-p^2/2\alpha_0^2}\ e^{ikp\cdot(\frac{a}{L}-s)}\int d\xi\ e^{-(\xi+a)^2/2\alpha_0^2}$$
$$\exp\left[-\frac{1}{\rho_0^{5/3}}\left(2p^{5/3}+2\xi^{5/3}-|\xi-p|^{5/3}-|\xi+p|^{5/3}\right)\right] \qquad (2.55)$$

For the wavefronts of the signal and the local oscillator to be superimposed, the aiming vector **s** must lineup with the vector connecting point **a** to the origin of the coordinate system in the target plane (i.e., to make an angle equal to a/L with respect to the transmitter plane), in which case the complex phase factor in Eq. (2.55) cancels out.

Expressing the integrand in terms of new variables $\mathbf{p}'=\mathbf{p}/\alpha_0$ and

$\xi' = \xi/\alpha_0$, the resultant signal power can be written in a more convenient form

$$<i_s^2> = \frac{2\pi^2 T_0^2 U_0^2 \alpha_0^6}{L^2} F_0(a_0, r_0) \tag{2.56}$$

where $a_0 = \frac{a}{\alpha_0}$, $r_0 = \frac{\alpha_0}{\rho_0}$ and F_0 is the SNR reduction factor due to the atmospheric turbulence, given by

$$F_0(a_0, r_0) = \frac{1}{(2\pi)^2} \int dp' \, e^{-p'^2/2} \int d\xi' \, e^{-(\xi' + a_0)^2/2}$$
$$\exp\left[-r_0^{5/3} \left(2p'^{5/3} + 2\xi'^{5/3} - |\xi' - p'|^{5/3} - |\xi' + p'|^{5/3} \right) \right] \tag{2.57}$$

The integration is performed numerically and the result is shown in figures (2.8) for different values of a_0 as a function of r_0. The reduction factor for $a_0 = 0$ corresponds with Clifford's result[42] for the monostatic case. It is shown that the reduction factor approaches the independent paths assumption as a_0 increases.

The effect of the misalignment on the SNR can be quite significant. This effect can be examined by including the complex phase factor in Eq. (2.55) which depends on the laser wavenumber, path length and the receiver aperture size as well as the angle between the return and local oscillator wavefronts.

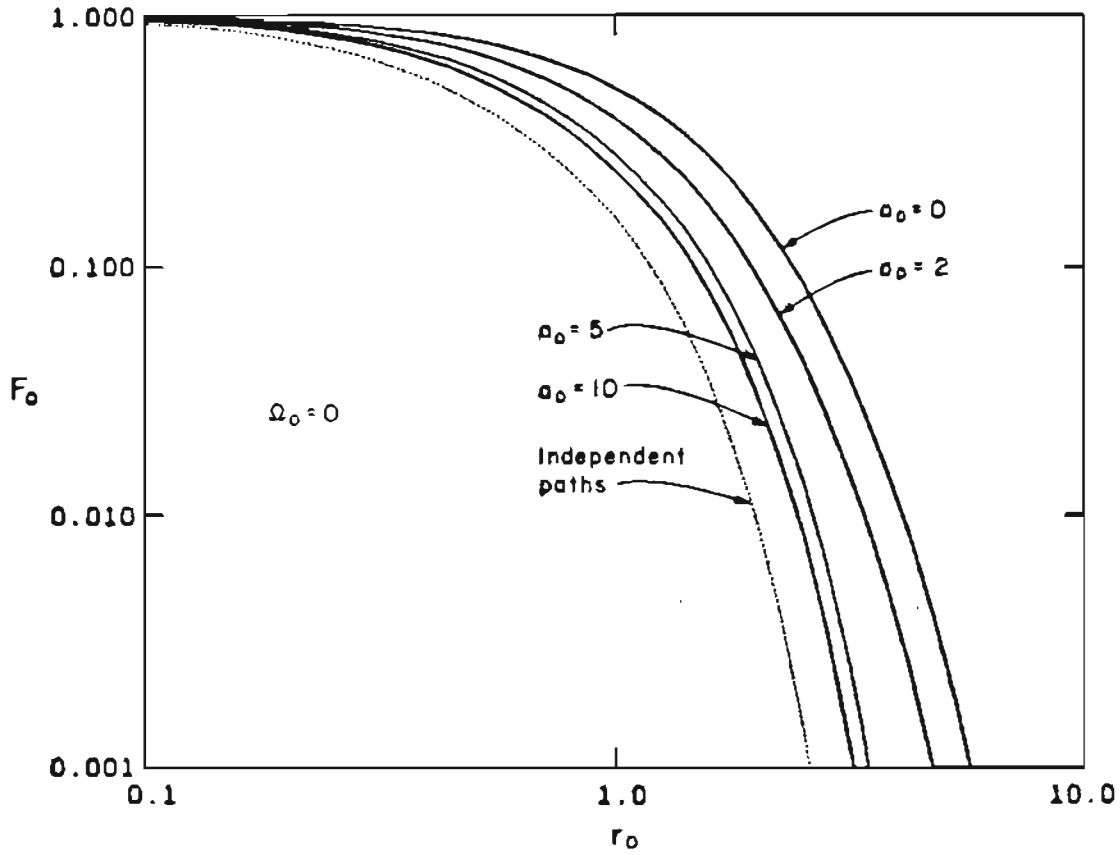

Figure 2.8 The heterodyne SNR reduction factor versus receiving aperture radius for various transmitter-receiver spacings compared with the independent paths assumption.

CHAPTER 3

EXPERIMENTAL PROCEDURE

Several optical heterodyne transmitter-receiver systems were constructed to exploit the speckle-turbulence interaction. The heterodyne detection[43–46] allowed for the use of a continuous wave (cw) CO_2 waveguide laser of moderate power operating at 10.6 μm which has many advantages over pulsed visible or near infrared transmitters. The longer wavelength allows for better penetration of smoke, dust and fog; and the continuous transmission translates into stable output, low beam pointing jitter[47] and reduced complexity of the receiver electronics[34]. In addition, such a laser has the advantage of being compact, inexpensive, reliable and eye safe.

The major challenge in devising the optical heterodyne system was to acquire adequate isolation between the local oscillator and the transmitter beams. The original experimental layout is first described in this chapter, with the problem of insufficient isolation discussed in detail. Next, the synchronous heterodyne detection and the dual acoustooptic modulators systems are described, these improved the local oscillator isolation by about 27 db and 100 db respectively. In the last section, the use of photoconductive (PC) in place of photovoltaic (PV) detectors is described. The PC detectors were used because of availability in larger sizes (with lower cost) which is required

in conjunction with lower optical magnification to suppress the possible effects of the angle of arrival fluctuations. An attempt was made to maximize the SNR, interesting findings were obtained regarding the photoconductors when used as optical heterodyne detectors. The theoretical analysis leading to expressions for the SNR are presented.

The selected experimental results are presented for each system for various atmospheric parameters and path lengths in the next chapter.

3.1 Optical Heterodyne System

The transmitter-receiver optics are shown in figure (3.1). The CO_2 waveguide laser used as the source radiates about 6.0 watts of power continuously and has a beam radius of about 1.2 mm. Part of the laser radiation is split from the main beam to be used as an optical local oscillator and the remaining part of the beam is transmitted. A half-wave plate rotates the polarization of the beam to be transmitted from vertical to horizontal to match the acoustooptic (AO) modulator which shifts the optical frequency by 37.5 MHz. The output of the AO modulator is circularly polarized by a quarter-wave plate and then passed through a 40X beam expander (giving $\alpha_0 \simeq 34$ mm) that is focused on the target.

The local oscillator portion of the laser beam is circularly polarized by a quarter-wave plate and collimated by a 5X beam expander to prevent the beam from diverging.

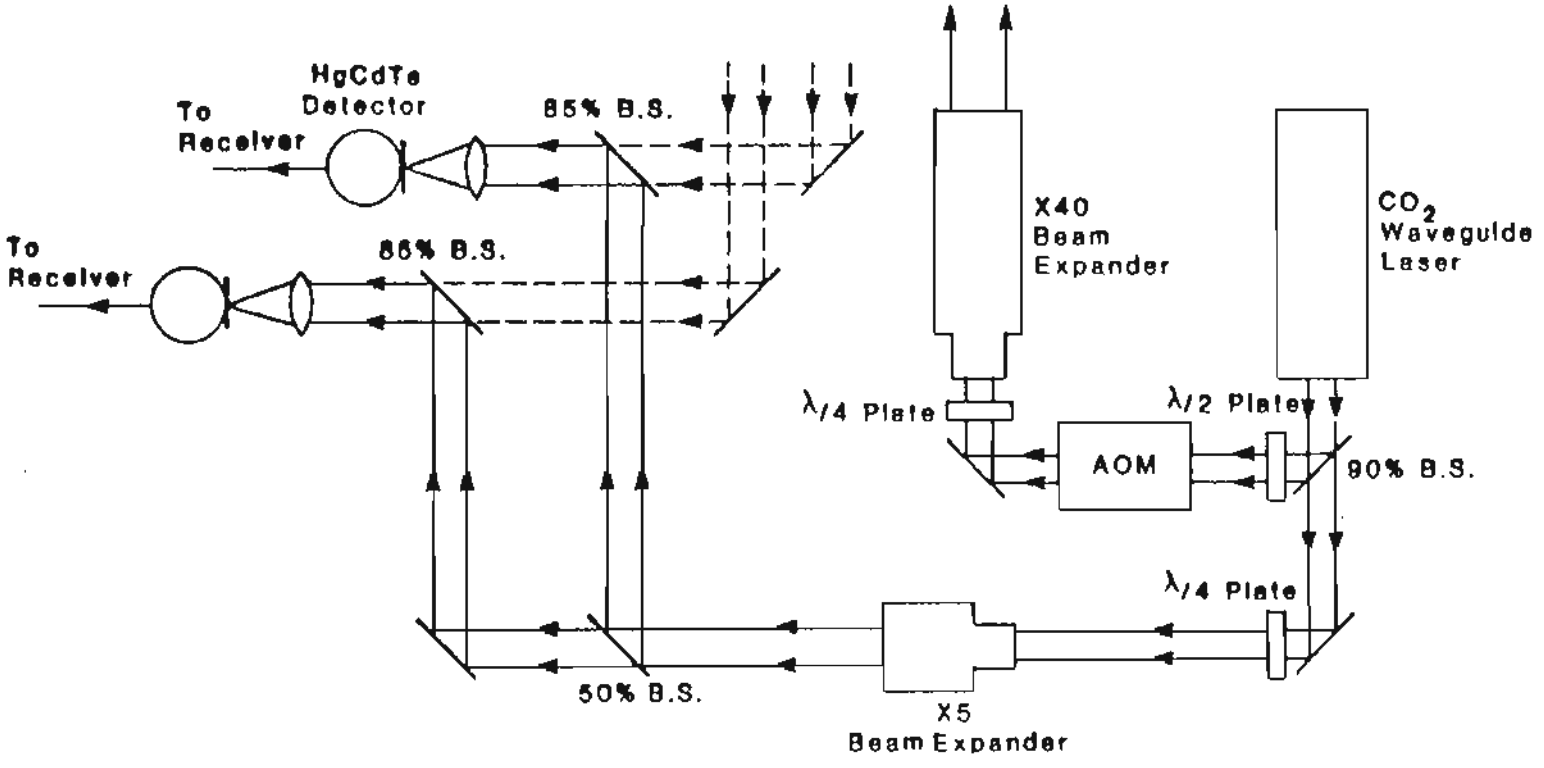

Figure 3.1 Transmitter-Receiver Optics.

The circular polarization of the local oscillator eliminates any depolarization effect caused by the target. The collimated beam is then split into two beams to be focused onto two photovoltaic HgCdTe detectors operating in the reverse biased mode.

The transmitter beam, after propagating through the atmosphere, is scattered off a diffuse target of sandblasted aluminum. The returned radiation is directed by two one-inch mirrors set at 45 degrees onto lenses that focus it on the detectors. The wavefronts of the signals and the local oscillators are superimposed by two 85% beam splitters. The frequency of the heterodyne signal is equal to the difference in the transmitted and the local oscillator frequencies (37.5 MHz).

The focal length of the lenses and the area of the detectors are 12.7 cm and $4x10^{-4}$ cm^2 respectively, giving a field of view of $4x10^{-4}/(12.7)^2=2.48x10^{-6}$ steradian. The transmitted power is about one watt and the local oscillator power is about $2.5x10^{-4}$ watt per channel. The average received power from the target is of the order of 10^{-13} watt. The detectors are placed in separate dewars giving some freedom in selecting the transverse spacing between them and simplifying the optical design.

The laser is a product of Laakmann Electro-Optic Inc., model RF 44 and the detectors are made by New England Research Center, Inc. with a responsivity of about 5 A/W. The AO modulator is Isomet model 1207B-06 made of Germanium crystal; it is designed for 10.6 μm wavelength and has a deflection efficiency of about 80% when driven with full power at the center

frequency (40 MHz). The RF and video bandwidths of the AO modulator are 20 MHz and 500 KHz, respectively.

A block diagram of the receiver is shown in figure (3.2). The output of each detector is amplified and band pass filtered before being mixed by the 37.4 MHz local oscillator to obtain a 100 KHz intermediate frequency (IF) signal. An envelope detector demodulates the signal and its amplified output is recorded. The received intensities are recovered by squaring the measured amplitudes in a computer. The receivers have stable outputs with linearities of better than 0.1%. These are required because of the small interaction with the turbulence in the infrared region. The complete schematic of the receiver electronics is given in appendix B.

The main problem of this optical heterodyne system was insufficient optical isolation between the transmitter and the local oscillator beams. The back-scattering of the frequency-shifted light by the AO modulator crystal, due to its imperfection, contaminates the local oscillator[48,49]. Even though, the level of contamination (i.e., $10\log\frac{P_c}{P_{LO}}$) was measured to be about -70 db, it was sufficient to affect the heterodyne signal making the processing for the statistics difficult. The presence of the frequency-shifted light on the local oscillator path creates a DC offset when it is detected, it also mixes with the actual signal from the target which generates large amplitude homodyne beats.

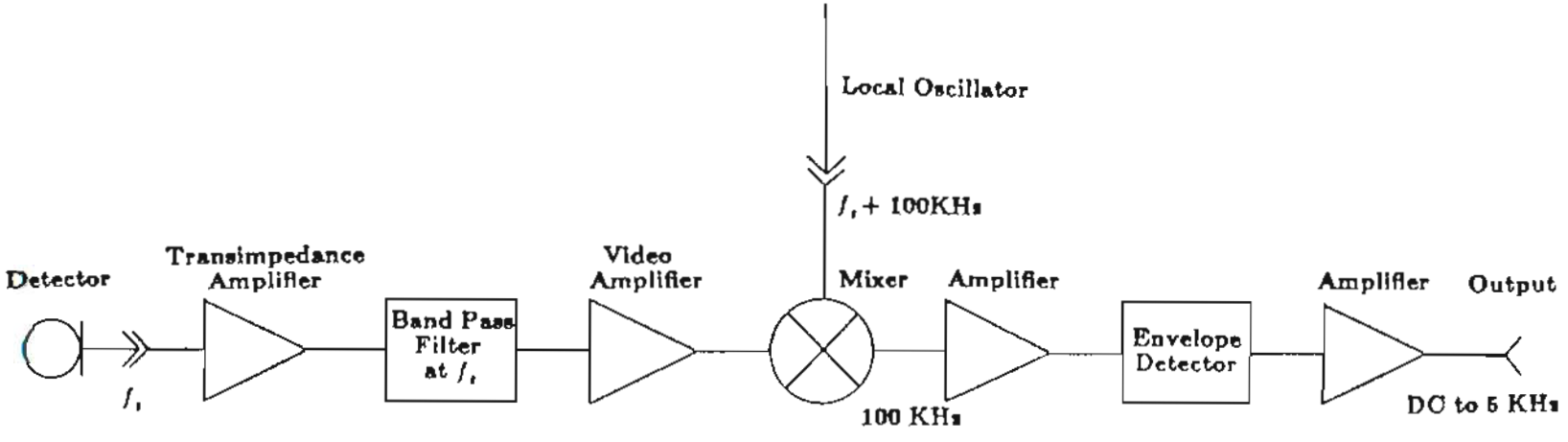

Figure 3.2 Receiver Electronics.

It was possible to reduce the amount of the optical feedback (contamination) by using quarter-wave plates and Brewster angle polarizers at the output of the laser. However, the polarization of the optical feedback was not stable resulting in a variable degree of isolation with time. By frequent readjustment of the quarter-wave and Brewster plates some useful but still contaminated data was obtained (see chapter 4).

It should be noted that proper alignment is crucial to the performance of this set-up as well as the ones to be described in the later sections. Heterodyne detection requires precision alignment of the local oscillator and receiver optics[43,44]. The precise alignment of the transmitter beam that must be focused on the target is also important. The invisibility of the light made the problem even more involved, making the use of certain novel techniques necessary. The description of these techniques are not in the scope of this text. However, some of these techniques can be found in the literture[50,51].

3.2 Synchronous Heterodyne Detection System

In order to overcome the optical feedback problem, a gated transmitter-receiver scheme was proposed[52]. In such a system, the transmitter and receiver are synchronously turned on and off out of phase so that the optical feedback is not present on the receiver at the same time as the signal from the target.

The gating of the transmitter is performed by the acoustooptic modulator so the laser can be run continuously for the reason of stability. The receiver is gated by switching the local oscillator input to the mixer. Figures (3.3) and (3.4) summarize the principle of this system. While transmitting, the receiver is turned off allowing sufficient time for the beam to travel to the target and back. At this time the transmitter is turned off and the receiver turned on to receive the signal. It should be noted that, the time required for the acoustic waves to travel across the AO modulator crystal must be taken into account for the proper timing of the transmitter-receiver switching. This time delay is not included in figure (3.3), for reasons of simplicity. The schematics of the logic and switching circuits can be found in appendix B along with the receiver electronics.

Ideally, there should be no optical feedback when the receiver is on and infinite isolation between the local oscillator and the transmitter beams should have been achieved. Unfortunately, this was not the case.

An improvement of only 27 db was achieved due to the existence of echoes in the acoustooptic modulator. Even when the RF drive to the AO modulator is turned off, the acoustic waves travel between the faces of the crystal for a relatively long time generating frequency-shifted light[53].

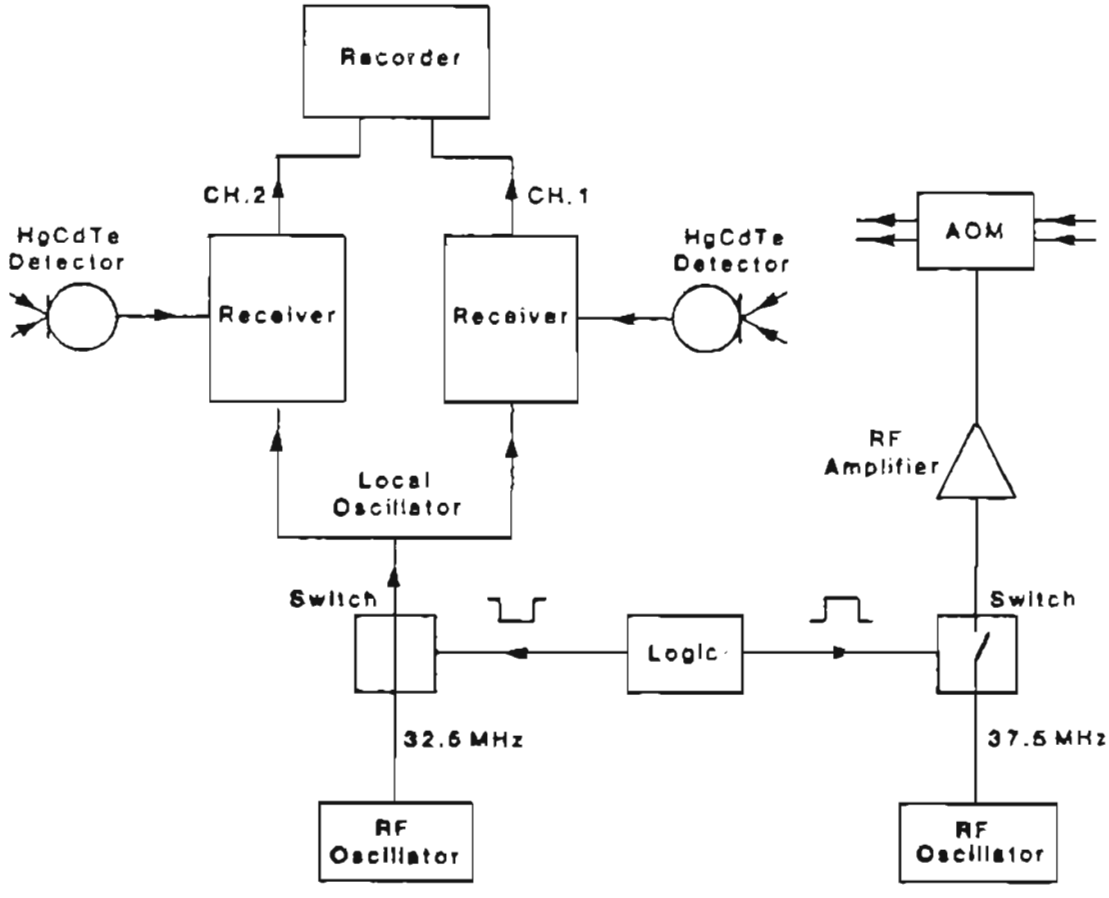

Figure 3.3 Transmitter-Receiver Electronics For The Synchronous Heterodyne Detection System.

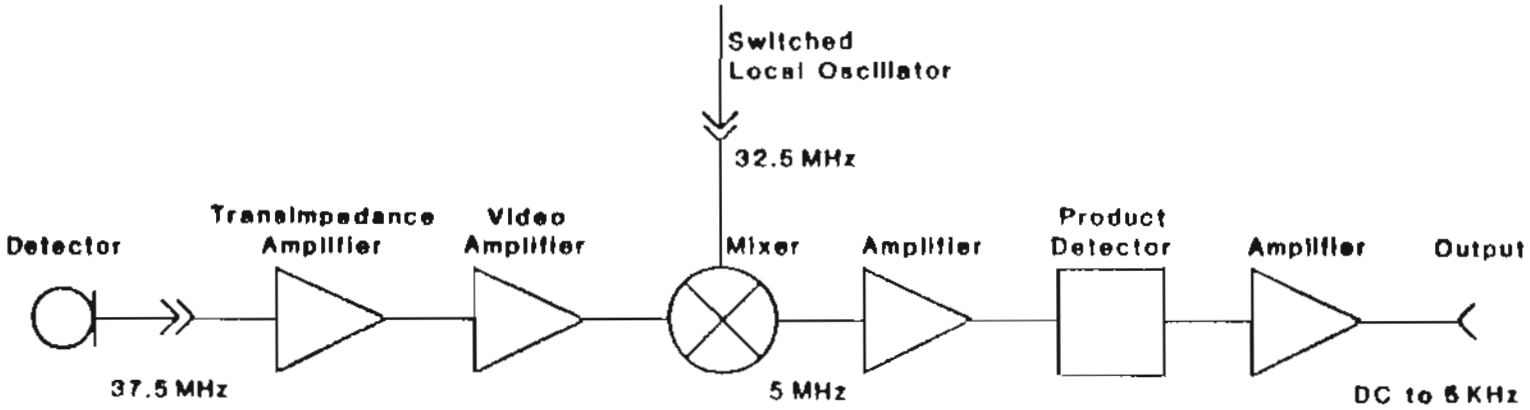

Figure 3.4 Receiver Electronics For The Synchronous Heterodyne Detection System.

The relative amount of optical feedback during ON and OFF periods is shown in figure (3.5). The velocity of acoustic waves traveling in the crystal is 5.5 mm/μsec and the interactive acoustic path length is 49 mm . This gives a total traveling time of $2\text{x}49\ \frac{\text{mm}}{5.5\ \text{mm}/\mu\text{sec}} = 17.82\ \mu\text{sec}$ which is in agreement with the experimental result of figure (3.5).

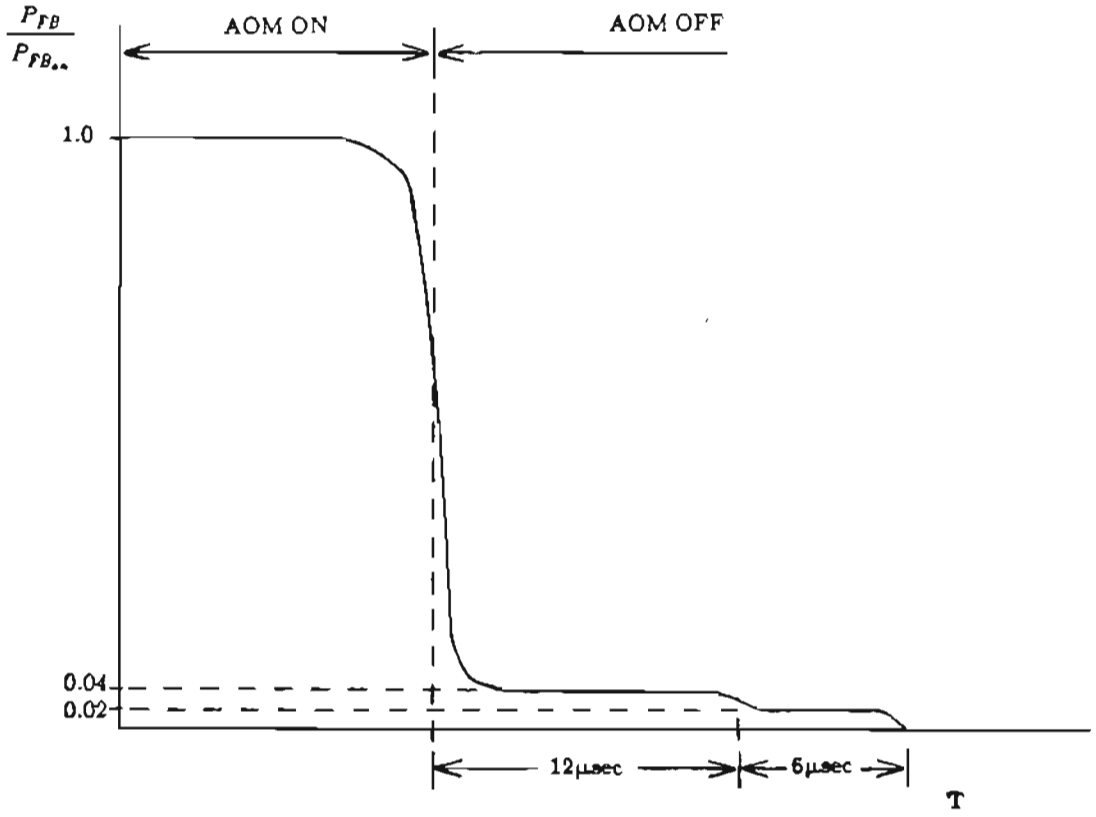

Figure 3.5 Relative optical feedback power during ON and OFF periods of the AO modulator.

3.3 Dual Acoustooptic Modulators System

A heterodyne system using two acoustooptic modulators was devised[53] which resulted in a degree of isolation of over 200 db. The basic difference between the dual AO modulators system and the system described in section 3.1, is the addition of the second modulator on the local oscillator (LO) path (see figure (3.6)).

As shown in figure (3.6), a 3X beam expander is now placed at the output of the laser to expand both the transmitter and the LO beams followed by the half-wave plate to change the polarization of them to match the requirements of the AO modulators. A 10X beam expander focuses the transmitter beam on the target giving a total of 30X expansion of the laser beam and a beam radius α_0 of about 25 mm.

The optical frequencies of the transmitter and LO beams are up-shifted by 37.5 MHz (f1) and 42.5 MHz (f2) by the AO modulators. The frequency of the detectable signal is equal to the difference in the transmitter and LO frequencies (*i.e.*, 5 MHz). The electronic receiver shown in figure (3.2) was used by setting f_s equal to 5 MHz.

The scattering of light by AO modulators contaminates the local oscillator as described in section 3.1. Consequently, besides the optical frequency of the local oscillator (i.e., f_0+42.5 MHz), there would be other frequency components present from which f_0 and f_0+37.5 MHz are significant.

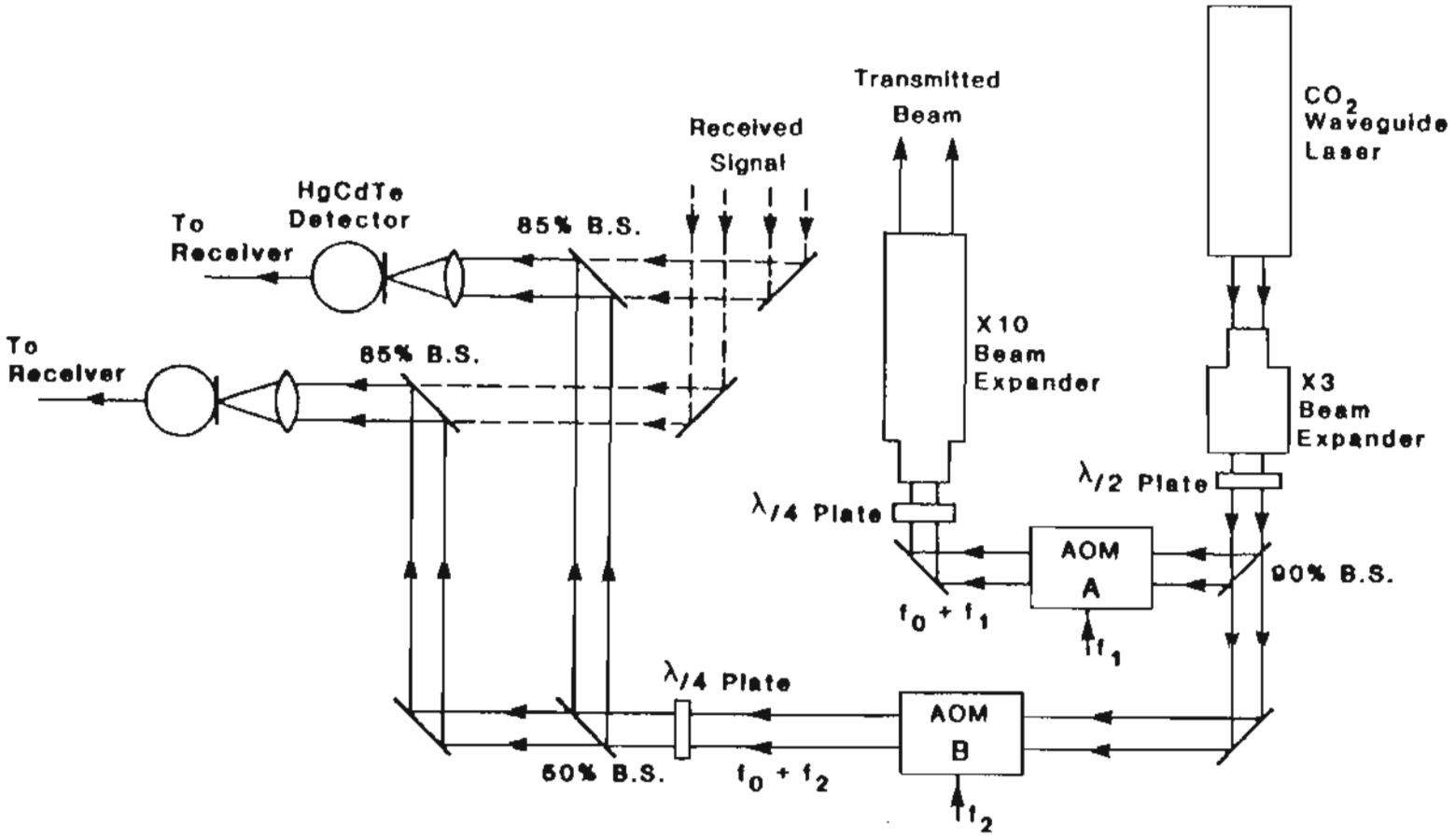

Figure 3.6 Dual Modulators Optics.

These components mix at the detector resulting in signals at 37.5, 42.5 and 5 MHz. The first two components are removed by the electronic filter and the following shows the last component to be insignificant.

An experimental procedure was devised to measure the level of contamination and to verify the improved isolation[53]. The system shown in figure (3.6) was utilized in conjunction with the electronic set-up illustrated in figure (3.7). The output voltage is related to the input current and in turn to the optical power by the the following expressions

$$V_{out}=K(f)i_{in} \tag{3.1}$$

$$i_{in}=\rho P \tag{3.2}$$

where K(f) is the actual gain of the set-up that was determined for each frequency present at the output of the detector and ρ is the responsivity of the detector. The quantities of interest are the local oscillator signal, the real signal, contamination other than at the signal frequency and contamination at the signal frequency

$$i_{LO}=\rho P_{LO} \qquad (DC) \tag{3.3}$$

$$i_s=2\rho\sqrt{P_{LO}P_s} \qquad (f_2-f_1 \text{ or } f_2+f_1) \tag{3.4}$$

$$i_{cj}=2\rho\sqrt{P_{LO}P_{cj}} \qquad j=1,2 \qquad (f_1,f_2) \tag{3.5}$$

$$i_{cs}=2\rho\sqrt{P_{c1}P_{c2}} \qquad (f_2-f_1 \text{ or } f_2+f_1) \tag{3.6}$$

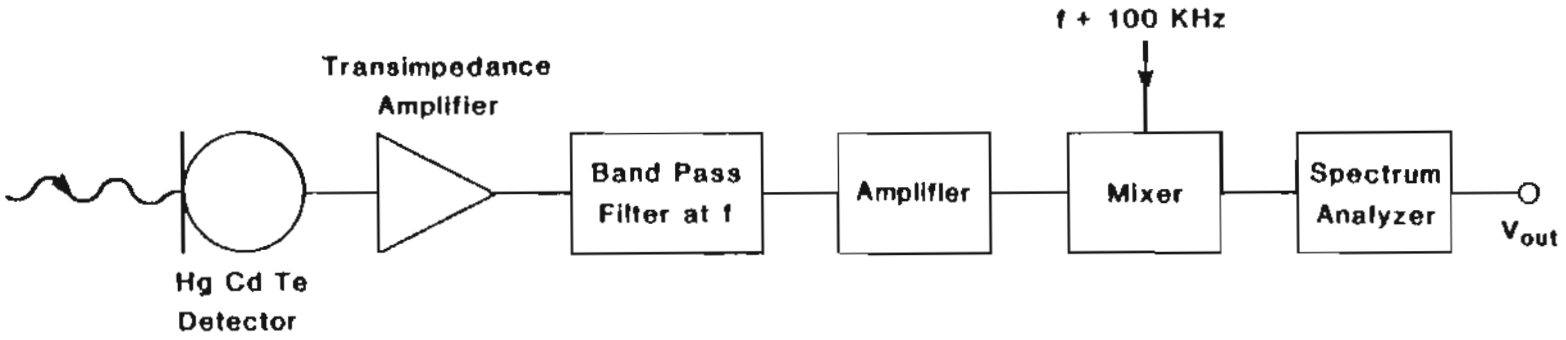

Figure 3.7 Experimental setup for the local oscillator isolation measurements.

Experimental data was obtained for each of the two modulators operated in both the transmitter path and local oscillator path, one at a time; the results are summarized in table (3.1). The transmitter modulator was driven at full power resulting in an actual transmitted power of about one watt. The local oscillator modulator was driven at about 60% of its full power yielding 2.5×10^{-4} watt of effective LO power incident on each detector. The best result was obtained when modulator A is used on the LO path and modulator B on the transmitter path.

The minimum detectable signal power to the LO power ratio given by

$$10\log\left(\frac{P_{s_{min}}}{P_{LO}}\right) = 10\log\left(\frac{P_{c1}}{P_{LO}}\right) + 10\log\left(\frac{P_{c2}}{P_{LO}}\right) \tag{3.7}$$

was found to be -170 db for channel one with both modulators in their best location. This is equivalent to an isolation of 206 db between the transmitter and the local oscillator and minimum detectable signal power of 2.5×10^{-21} watt, which is significantly below the measured noise equivalent power of 7.9×10^{-18} watt. Similar results were obtained for channel two as indicated in table (3.1).

$10Log\frac{P_s}{P_{LO}}$	Acoustooptic Modulator A only		Acoustooptic Modulator B only		Both Modulators	
	In LO Leg f2=42.5 MHz	In Transmit Leg f1=37.5 MHz	In LO Leg f2=42.5 MHz	In Transmit Leg f1=37.5 MHz	LO= f_0 +42.5 MHz Difference (5 MHz)	LO= f_0 -42.5 MHz Sum (80 MHz)
CH. 1	-76 db	-69 db	-85 db	-94 db	< -135 db	< -119 db
CH. 2	-76 db	-69 db	-78 db	-92 db	< -135 db	< -117 db

Table 3.1 Local oscillator isolation measurements.

One other advantage of the dual modulator system is the ability to extend the operational range of signal frequency. Depending on the orientation of AO modulators, the optical frequency can be either up-shifted (f_0+f) or down-shifted (f_0-f). If both modulators have the same orientation, the signal frequency is equal to f_2-f_1 (figure (3.8a)) and with different orientation the signal frequency would be f_2+f_1 (figure (3.8b)). For modulators with 40 MHz center frequency and 20 MHz bandwidth, the signal frequency range can be extended from 0 to 20 MHz and from 60 MHz to 100 MHz.

The optical feedback is independent of the orientation of the modulators resulting in the same amount of isolation for the sum of the frequency case. This was experimentally verified where the noise equivalent power was measured to be 3.15×10^{-16} watt at the sum frequency (see table (3.1)) and no optical feedback could be detected.

Even though there was no experimental data obtained for verification, it is expected to gain the same level of isolation by placing the modulators in series on the transmitter (or the local oscillator) leg as shown in figure (3.8c,d).

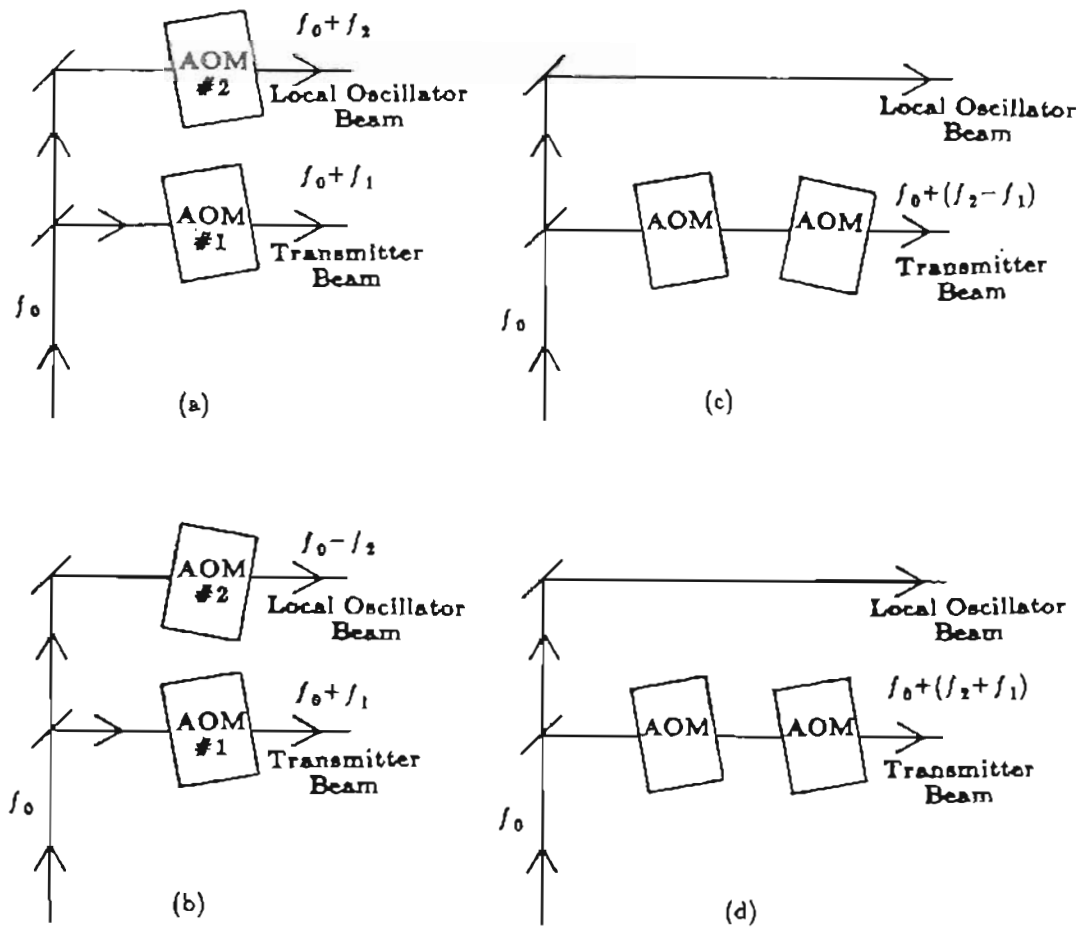

Figure 3.8 Parallel (a,b) and Series (c,d) configurations for two modulators systems.

3.4 Heterodyne Detection Using Photoconductors

The possible effect of the angle of arrival fluctuations on the accuracy of the wind measurements was of some concern. These fluctuations are the result of the continuous deflection of the phasefront of the propagating wave caused by the moving turbulent eddies[2,54].

The optical receiver of the dual modulator system of section 3.3 was modified to eliminate any possible effect that may result from the angle of arrival fluctuations. Figure (3.9) shows the optical design of the receiver. A two-inch mirror is used to direct the returning radiation through an afocal telescope onto a pair of detectors. The telescope consists of two lenses of focal lengths 25.4 and 6.2 centimeters giving a magnification of 4.1. The low optical magnification is necessary to suppress the angle of arrival fluctuations[15] which in return demands larger size detectors. The detectors are positioned close to the focal plane of the imaging lens where the image is least dependent on the incident angle. The detectors are HgCdTe photoconductors which have the advantage of larger size and lower cost. They are 2 mmX 2 mm in dimension placed side by side 0.1 mm apart in a single dewar. This gives an effective spacing of 8.6 mm between the detectors.

The drive frequency of the LO modulator was changed from 42.5 Mhz to 37.6 MHz to reduce the heterodyne signal frequency from 5 MHz to 100 KHz. This accommodates the bandwidth requirements of the detectors and makes the receiver's electronics much simpler. Each receiver simply consists of a preamplifier followed by an envelope detector and an amplifier (see App. B).

The addition of a 5X beam expander on the LO path provides a collimated beam that is several times larger than the detectors, resembling a plane wave over the surface of the detectors. A pinhole is placed at the common focus of the lenses to limit the field of view of the detectors and at the same time to cancel the spherical aberration. The 83% beam splitter combines the LO and the returned signal to produce the heterodyne signal at the detectors.

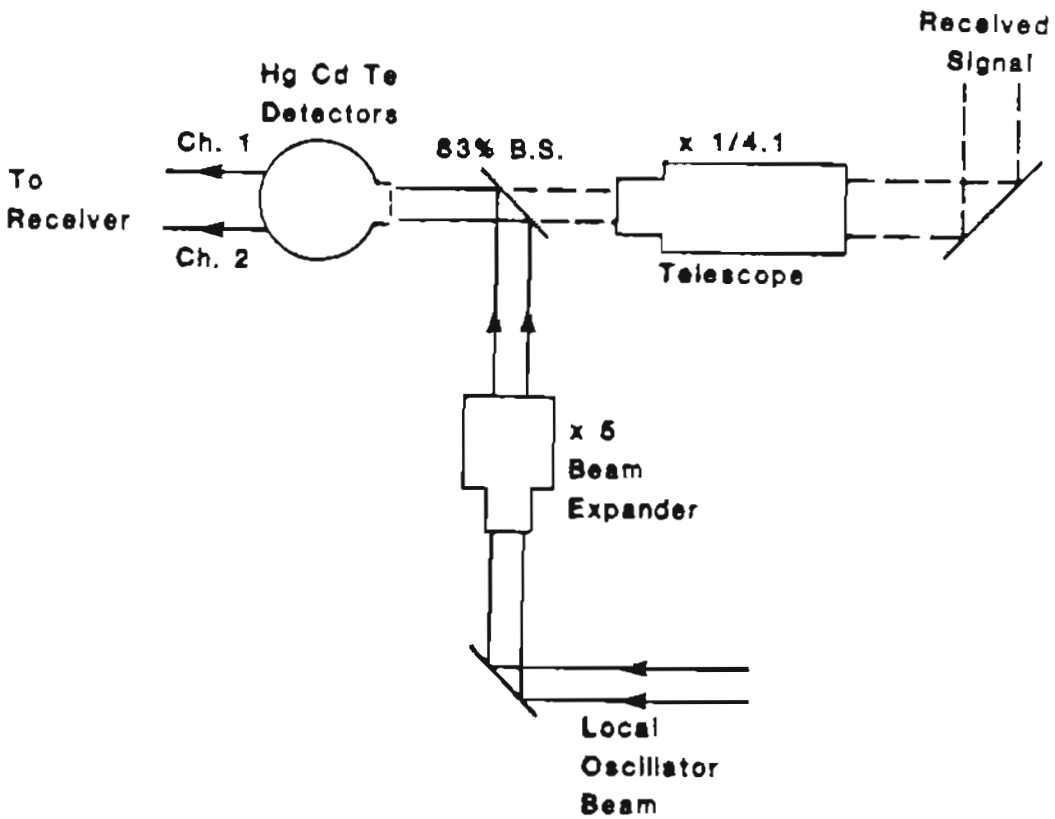

Figure 3.9 Receiver optics using photoconductive detectors.

The theoretical analysis that follows, helped specify the optimum detection parameters in accordance with the photoconductors parameters. A constant bias current of 40 mA is applied to each detector that is large enough to make the detector generation-recombination (g-r) noise dominate. In this case, the best SNR can be obtained with a preamplifier input impedance much greater than the detector dark impedance. The preamplifier input impedance was chosen to be about 1 kΩ as opposed to the detector dark impedance of about 40 Ω. Each detector is illuminated by about 1 mW of local oscillator power providing the optimum SNR.

In optimizing the SNR, the change in the conductance of a photoconductor with the application of the local oscillator is of major concern. This is due to the considerable effect the conductance has on the effective responsivity of the detector and its interaction with the external circuit. Most literature considers the ideal case where the circuit connected to the detector has no effect on the response of the detector[44,55,56]. For direct detection when the signal is very small and the external circuit is designed for minimum interaction, these results are satisfactory. The work by Penin *et al* [57] includes the LO induced interaction with the circuit in the derivation of the noise factor of a PC detector as a function of LO power for a constant voltage bias. Their result is nevertheless incorrect, since the problem is nonlinear in nature and the equivalent source term is also modified by the local oscillator.

Consequently, an analytical approach was made including both effects to formulate the SNR[58]. The results are presented here in terms of the device

parameters that can be easily measured for both constant voltage bias and constant current bias cases. First, the linear region of the photoconductor operation is considered and then the more exact results are obtained by including the second order term to express the conductance of a detector.

In the linear region, the conductance can be written as

$$G_{detector}=G+G'P_{in} \tag{3.8}$$

where G is the dark conductance, G′ is a constant (at a given frequency) and P_{in} is the optical power applied to the detector.

G and G′ can be easily obtained by applying a known voltage across the detector and measuring the current, or vice versa, for at least two different known optical powers. However, that should not be necessary because G and ρ_v, the detector voltage responsivity at a specific bias current, are usually supplied by the manufacturer; and G′ can be expressed in terms of G and ρ_v. When a bias current I_B and an optical power P_{in} are applied to the detector and there is no loading by an external circuit, the voltage generated is given by

$$V=\frac{I_B}{G+G'P_{in}} \tag{3.9}$$

The voltage responsivity is defined by

$$\rho_v=\frac{\partial V}{\partial P_{in}}\Big|_{P_{in}=0} \tag{3.10}$$

Using Eq. (3.9) in the definition above, the responsivity is equal to

$$\rho_v = \frac{I_B G'}{G^2} \tag{3.11}$$

which can be solved for G′ in terms of the device parameters as

$$G' = \frac{G^2 \rho_v}{I_B} \tag{3.12}$$

The other parameter of interest is the photoconductive gain g that is obtained as follows. If a bias voltage V_B is applied across the detector, the photo current that flows is given by

$$i = V_B G' P_{in} = \frac{\eta e g P_{in}}{h\nu} \tag{3.13}$$

and consequently,

$$g = \frac{V_B G' h\nu}{\eta e} \tag{3.14}$$

where h is Planck's constant, ν is the optical frequency, e is the electric charge and η is the quantum efficiency of the detector.

3.4.1 Voltage Bias Case

Figure (3.10) shows the configuration of the bias voltage case, where the direct current bias voltage V_B is applied only across the detector, because of the inductor. Even though the circuit is nonlinear, it can be solved by linearizing the problem about an operating point established by the local oscillator. This will yield correct results, since the local oscillator is much larger than the signal or the noise sources.

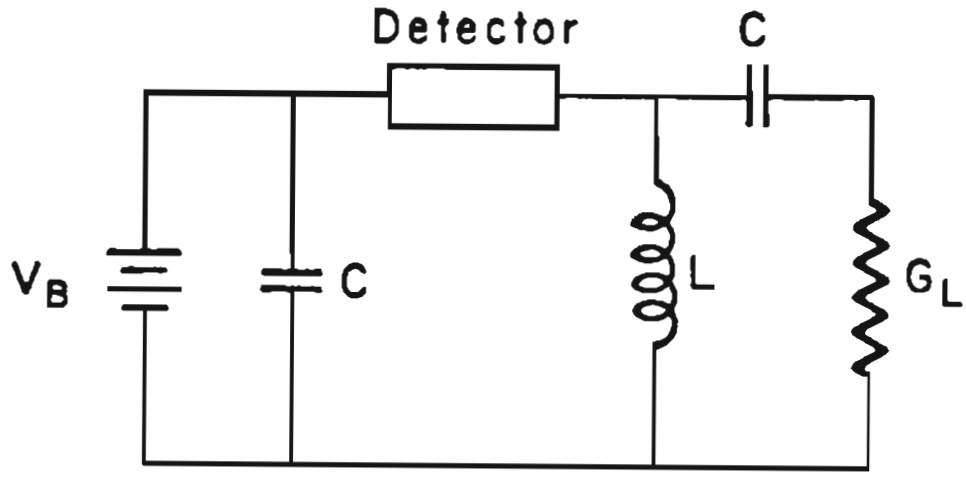

Figure 3.10 Constant Voltage Bias Circuit

The current that flows through the detector is given by

$$i=V_B G_T(\omega,P_{in})=I_{DC}+i_{het}+i_n+\text{ higher order terms} \tag{3.15}$$

where

$$P_{in}=P_{LO}+P_{het}+P_{nLO}=P_{LO}+2\sqrt{P_{LO}P_S}+\alpha(\omega)P_{LO} \tag{3.16}$$

$$G_T=G+G'P_{LO} \qquad \text{for } \omega=0 \tag{3.17}$$

$$G_T=\frac{G_L(G+G'P_{in})}{(G+G_L+G'P_{in})} \qquad \text{for } \omega=\omega_{het} \tag{3.18}$$

i_n is the noise current and i_{het} is the current at the heterodyne frequency.

P_{LO} is the applied local oscillator power that establishes the DC operating point about which there will be small fluctuations due to the signal power P_s. $\alpha(\omega)P_{LO}$ represents the local oscillator noise which is also small compared to P_{LO} . It is assumed that L and C are chosen such that Eqs. (3.17) and (3.18) are substantially correct. Making use of the Taylor series expansion established by P_{LO} as indicated by Eq. (3.15) and neglecting the higher order terms, we obtain

$$I_{DC}+i_{het}=V_B(G+G'P_{LO})+2V_BG'\sqrt{P_{LO}P_S}\frac{G_L^2}{(G+G_L+G'P_{LO})^2} \qquad (3.19)$$

where use was made of

$$i_{het}=V_B\left[\frac{\partial G_T(\omega,P_{in})}{\partial P_{in}}\right]_{P_{in}=P_{in,0}}\frac{\partial P_{in}}{\partial P_{het}}P_{het} \qquad (3.20)$$

The first term in Eq. (3.19) is the DC bias current that flows through the detector and the second term is the heterodyne signal current that flows through both the detector and the AC coupled load. From Eq. (3.19), the small signal equivalent circuit can be constructed as shown in figure (3.11), where

$$i_s=2V_BG'\sqrt{P_{LO}P_S}\frac{G_L}{(G+G_L+G'P_{LO})} \qquad (3.21)$$

The heterodyne signal current can be displayed graphically in a more convenient form when it is normalized as follows

$$i_{het_N} = \frac{i_{het}}{2V_B\sqrt{GG'P_S}}$$

$$= \frac{x^{1/2}y^2}{(1+x+y)^2} \tag{3.22}$$

where $x = G'P_{LO}/G$ and $y = G_L/G$. i_{het_N} is plotted versus x, the normalized local oscillator power, for several values of the normalized load conductance in figure (3.12). As can be seen, the loading has a significant effect on the heterodyne signal current. The LO power yielding maximum signal can be easily obtained from Eq. (3.22) to be

$$P_{LO} = \frac{G+G_L}{3G'} \tag{3.23}$$

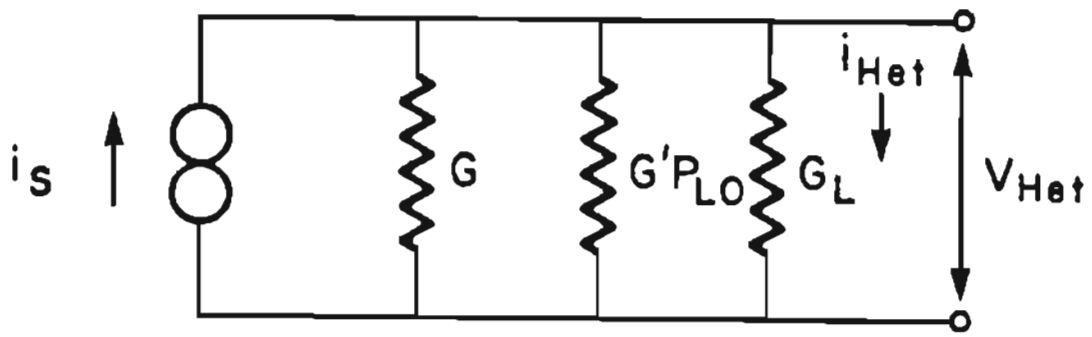

Figure 3.11 Small Signal Equivalent Circuit.

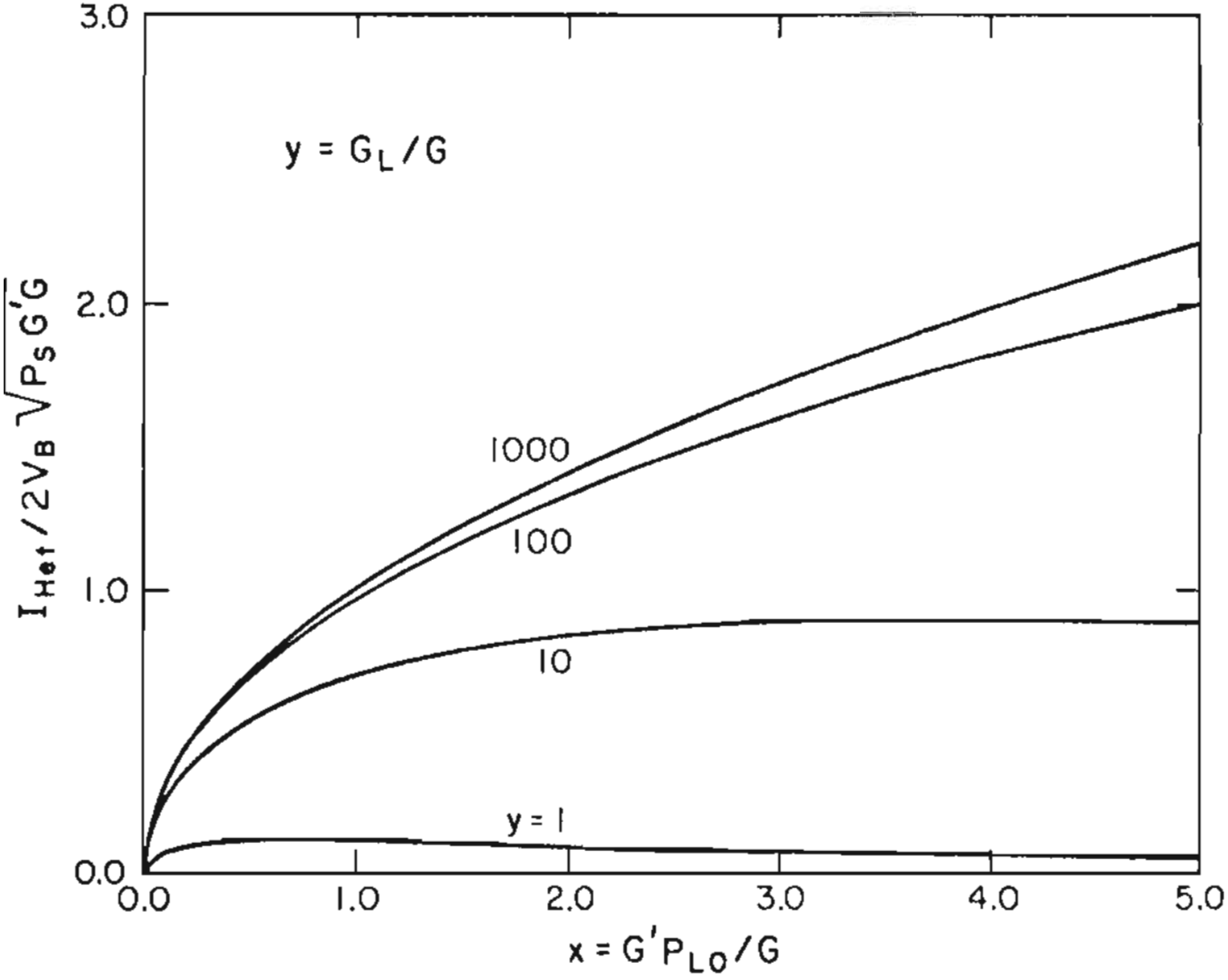

Figure 3.12 Normalized heterodyne signal current, voltage bias case.

The noise sources are generation-recombination (g-r) noise due to the bias, local oscillator noise, and Johnson noise from the conductances. The equivalent circuit for the noise is the same as for the signal. The g-r noise power is given by

$$\text{g-r noise} = 4egI_{DC}B$$

$$= 4BV_B^2(G+G'P_{LO})h\nu G'/\eta \tag{3.24}$$

where g and I_{DC} are given by Eqs. (3.14) and (3.19), respectively, and B is the bandwidth.

The LO noise current can be found using the same technique that was used for the heterodyne signal current.

$$i_{nLO} = V_B \left[\frac{\partial G_T(\omega, P_{in})}{\partial P_{in}} \right]_{P_{in}=P_{LO}} \frac{\partial P_{in}}{\partial P_{nLO}} P_{nLO}$$

$$= V_B \alpha(\omega) G' P_{LO} \frac{G_L^2}{(G+G_L+G'P_{LO})^2} \tag{3.25}$$

The same equivalent circuit used for the signal applies to the LO noise current source.

$$i_{snLO} = V_B \alpha(\omega) G' P_{LO} \frac{G_L}{(G+G_L+G'P_{LO})} \tag{3.26}$$

Using Eqs. (3.24) and (3.26), and incorporating the Johnson noise the total mean square noise current through the load is given by

$$<i_n^2> = \left[\frac{BV_B^2 G'^2 G_L^2 P_{LO}^2 <\alpha^2(\omega)>}{(G+G_L+G'P_{LO})^2} + 4BV_B^2(G+G'P_{LO})\frac{h\nu G'}{\eta} \right.$$

$$\left. + 4BKT_D(G+G'P_{LO}) + 4BKT_e G_L \right] \frac{G_L^2}{(G+G_L+G'P_{LO})^2} \qquad (3.27)$$

where T_D is the temperature of the detector, T_e is the equivalent noise temperature of the terminating conductance and any amplifier that follows, and K is Boltzmann's constant. The SNR can readily be obtained from Eqs. (3.22) and (3.27). For the usual case where the g-r noise is dominant, the SNR is given by

$$\frac{S}{N} = \frac{G' G_L^2 P_{LO} P_S}{(G+G'P_{LO})(G+G_L+G'P_{LO})^2 Bh\nu/\eta} \qquad (3.28)$$

The SNR can be expressed more conveniently when it is normalized by $\eta P_S/Bh\nu$ and written in terms of x and y

$$\left(\frac{S}{N}\right)_N = \frac{xy^2}{(1+x)(1+x+y)^2} \qquad (3.29)$$

The expression above is plotted in figure (3.13) as a function of x for various values of y. It can be seen that the SNR increases with G_L and there is an optimum P_{LO} that produces a maximum SNR, given by

$$P_{LO} = \frac{G}{4G'}\left(\sqrt{9+8G_L/G}-1\right) \qquad (3.30)$$

A family of curves describing the optimum P_{LO} is shown in figure (3.14).

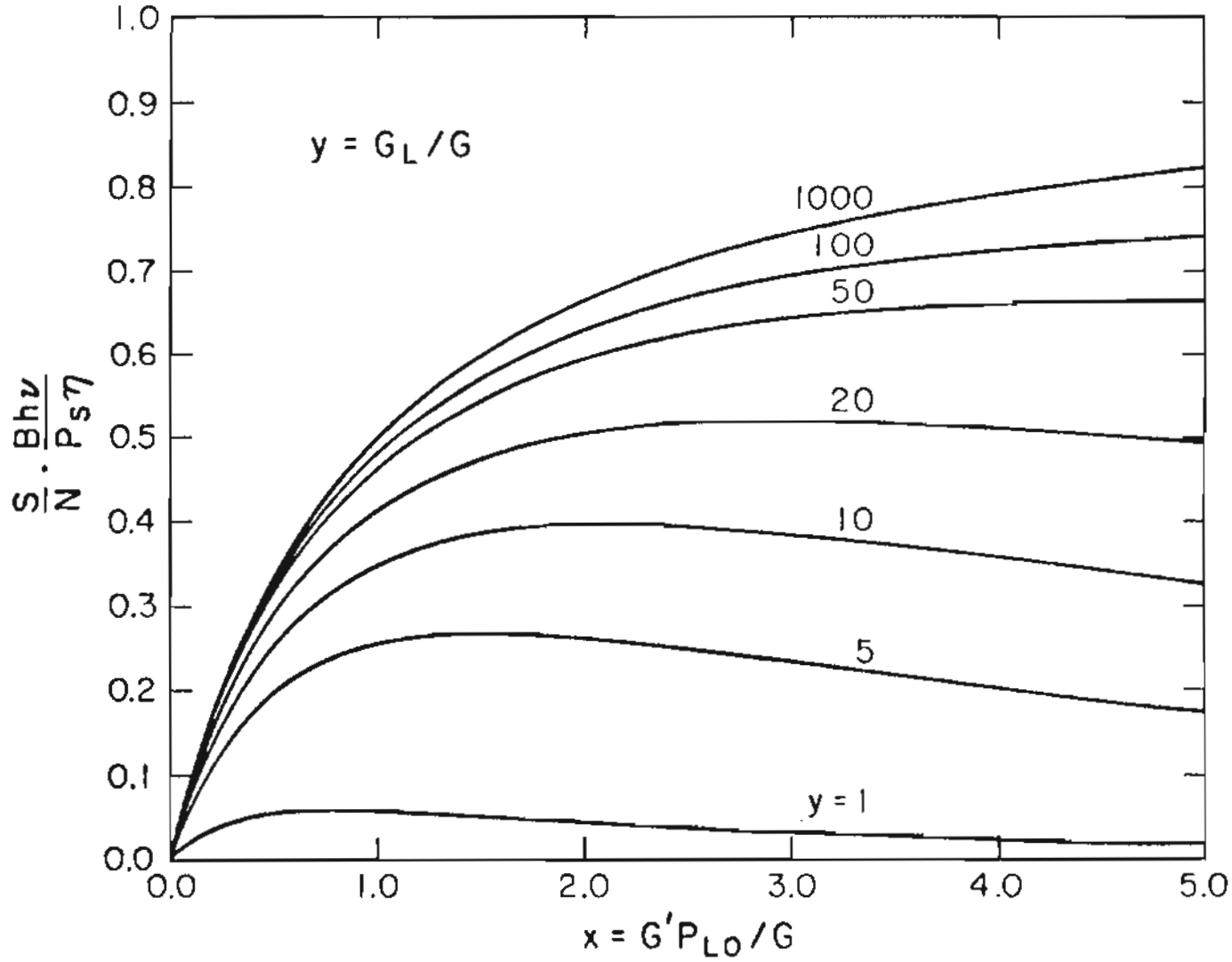

Figure 3.13 Normalized signal to noise ratio, voltage bias case.

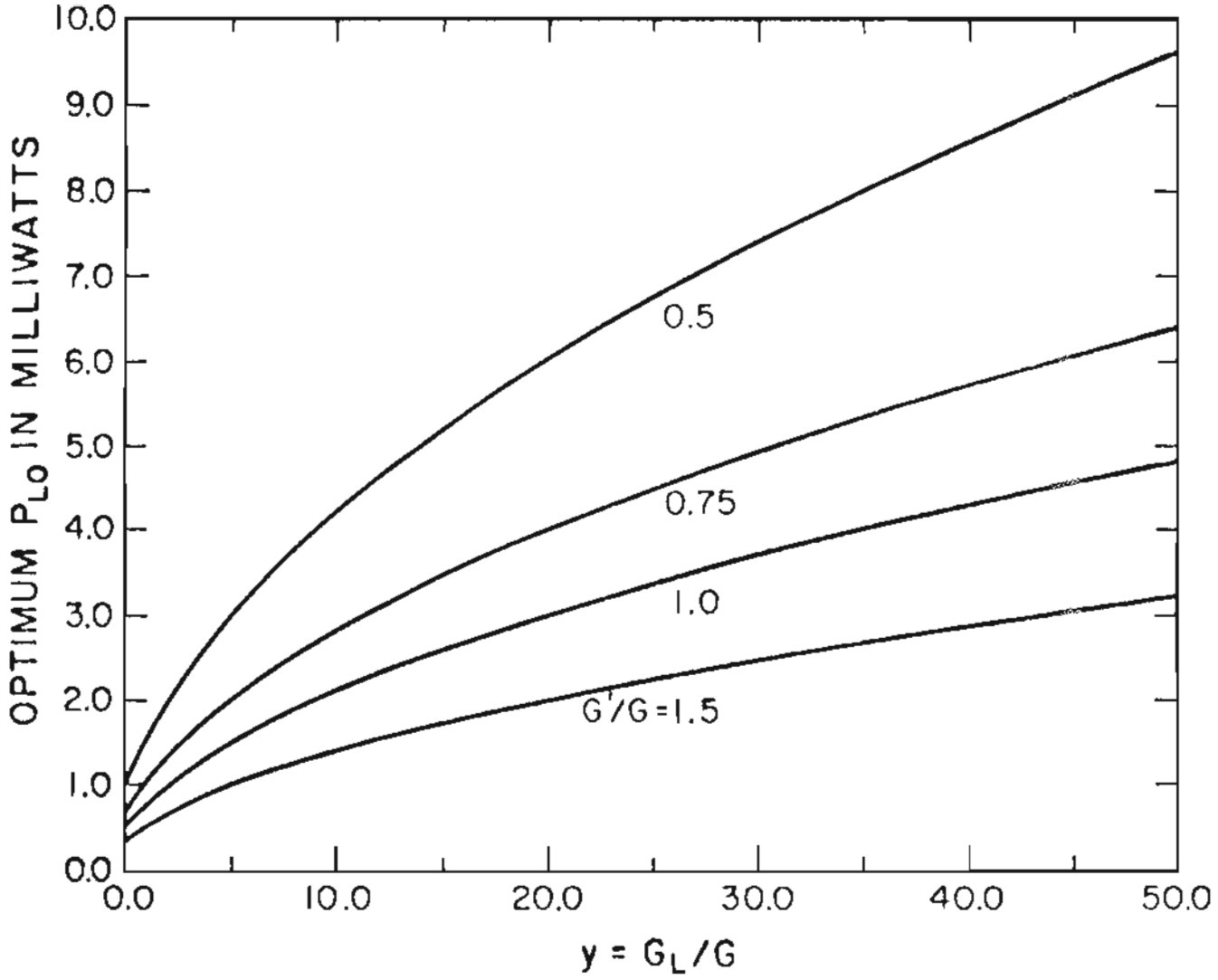

Figure 3.14 Optimum local oscillator level, voltage bias case.

It should be remembered that G′ is a function of frequency given by

$$G'(\omega)=\frac{G'(0)}{\sqrt{1+\omega^2\tau^2}} \tag{3.31}$$

where τ is the carrier lifetime.

3.4.2 Current Bias Case

The biasing of the detector can be accomplished by use of a constant current source as shown in figure (3.15). The SNR for this method of biasing can be obtained in a similar fashion as for the voltage bias case.

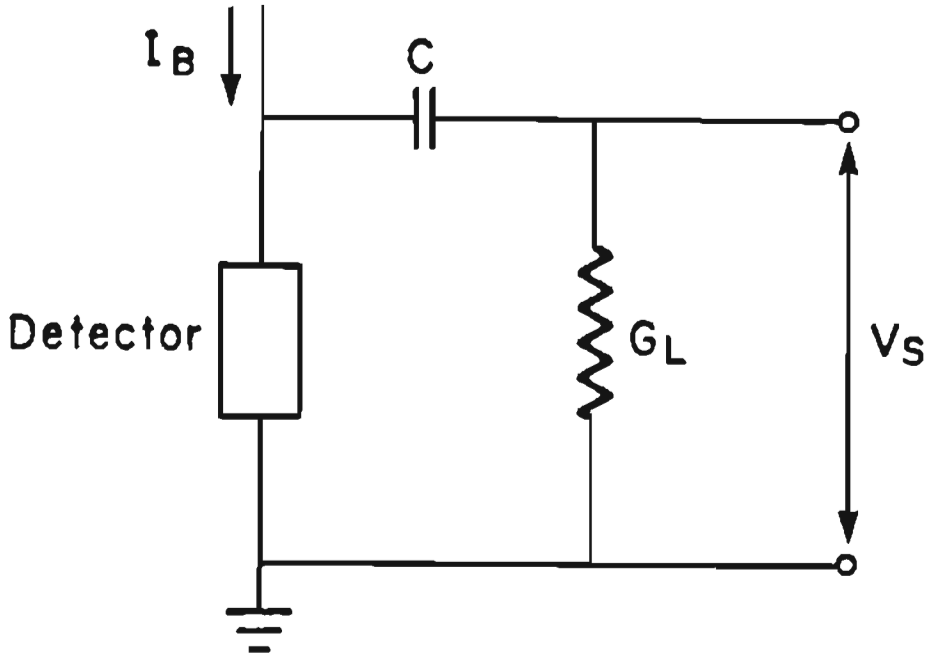

Figure 3.15 Constant Current Bias Circuit.

The voltage across the detector is given by

$$v=\frac{I_B}{G_T(\omega,P_{in})}=V_{DC}+v_{het}+v_n+\text{ higher order terms} \tag{3.32}$$

Using the Taylor series expansion

$$V_{DC}+v_{het}=\frac{I_B}{G+G'P_{LO}}+\frac{2I_BG'\sqrt{P_{LO}P_S}}{(G+G_L+G'P_{LO})^2} \tag{3.33}$$

It is obvious from the expression above that the small signal equivalent circuit for the current bias case is identical to that of the voltage bias case shown in figure (3.11). The equivalent current source is given by

$$i_s=\frac{2I_BG'\sqrt{P_{LO}P_S}}{(G+G_L+G'P_{LO})} \tag{3.34}$$

and the normalized v_{het} is given by

$$v_{het_N}=\frac{v_{het}}{2I_B\sqrt{G'P_s/G^3}}$$

$$=\frac{x^{1/2}}{(1+x+y)^2} \tag{3.35}$$

where x and y are defined earlier. As shown in figure (3.16), the heterodyne voltage in addition to being greatly effected by the terminating load, is highly non-uniform with a sharply peaked maximum occurring at $P_{LO}=\frac{(G+G_L)}{3G'}$.

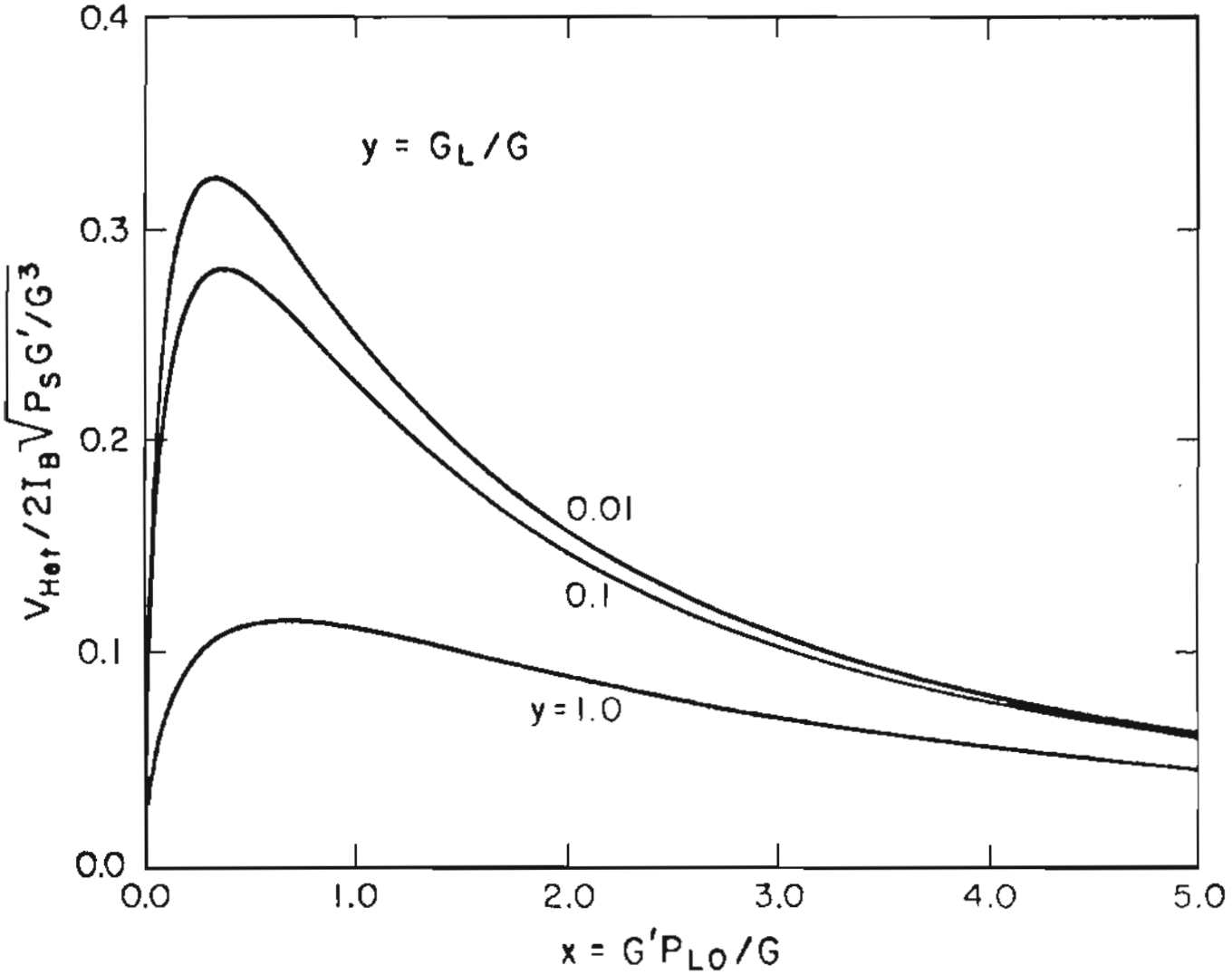

Figure 3.16 Normalized heterodyne signal voltage, current bias case.

The noise sources are the same as for the voltage bias case. Using the same approach, the total voltage noise variance is given by

$$<v_n^2> = \left[\frac{BI_B^2 G'^2 P_{LO}^2 <\alpha^2(\omega)>}{(G+G_L+G'P_{LO})^2} + \frac{4BI_B^2 G' h\nu}{\eta(G+G'P_{LO})} \right.$$

$$\left. +4BKT_D(G+G'P_{LO})+4BKT_e G_L \right] \frac{1}{(G+G_L+G'P_{LO})^2} \qquad (3.36)$$

Once again, considering the case where the g-r noise is dominant, using Eqs. (3.33) and (3.36), the SNR can be written as

$$\frac{S}{N} = \frac{G'(G+G'P_{LO})P_{LO}P_S}{(G+G_L+G'P_{LO})^2 Bh\nu/\eta} \qquad (3.37)$$

Normalizing the SNR by the same factor as before and rewritting in terms of x and y, we have

$$\left(\frac{S}{N}\right)_N = \frac{S}{N}\cdot\frac{Bh\nu}{\eta P_S} = \frac{x(1+x)}{(1+x+y)^2} \qquad (3.38)$$

Figure (3.17) shows a family of curves of the SNR for several values of y. As can be seen from figure (3.17), the SNR increases as x increases and y decreases. The SNR is a monotonic increasing function of x as it approaches a saturation level. This is due to the fact that the noise falls off faster than the signal past its peak value as P_{LO} increases.

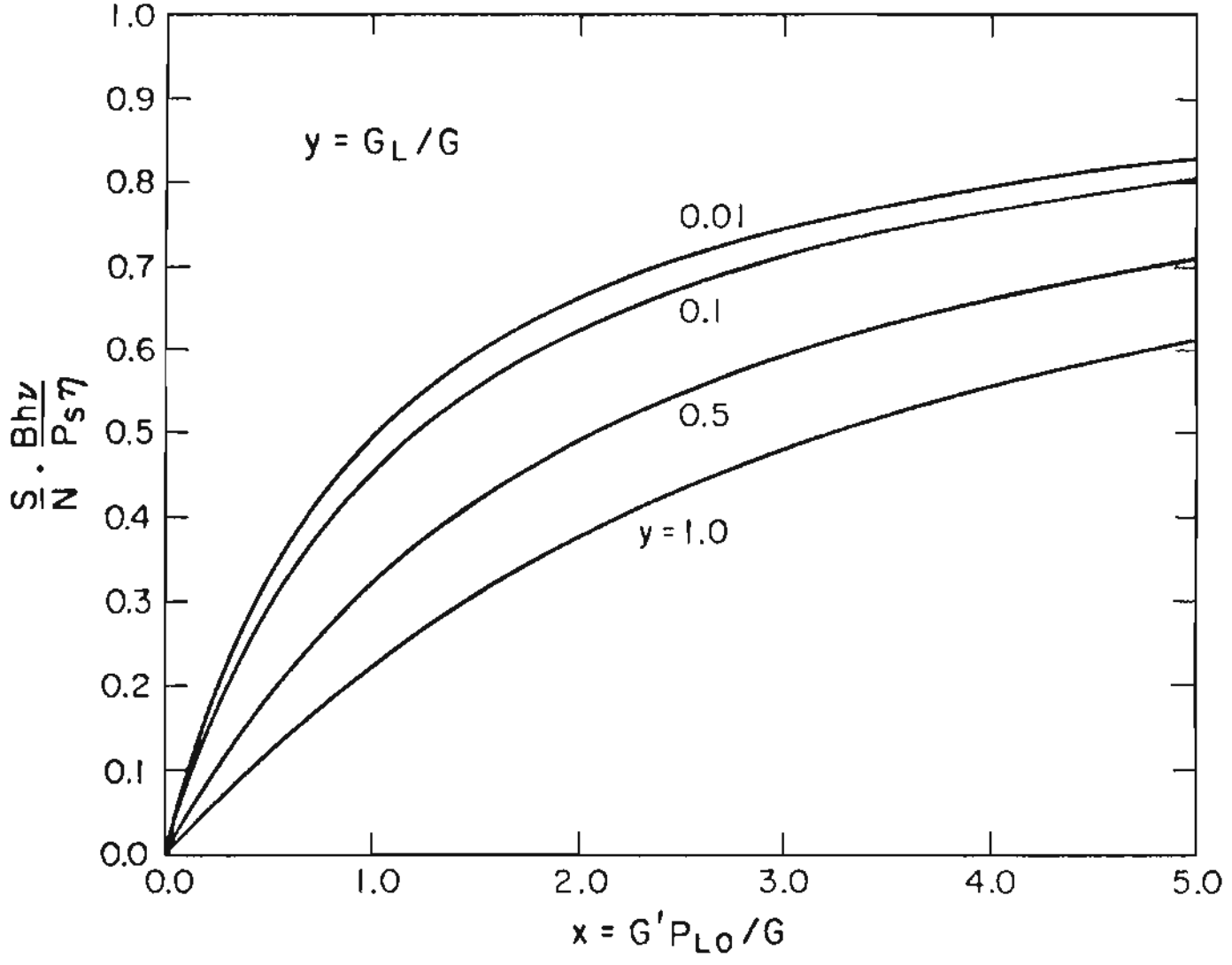

Figure 3.17 Normalized signal to noise ratio, current bias case.

3.4.3 Quadratic Region

The preceding formulations of the SNR's were restricted to the linear region of the photoconductor operation. However, as the local oscillator power increases, the detector response will become nonlinear. In this section, the operation region is extended to the quadratic region where the conductance can be modeled as

$$G_{detector}=G+G'P_{in}+G''P_{in}^2 \tag{3.39}$$

The previous results are still valid if the following substitutions are made

$$G+G'P_{LO} \rightarrow G+G'P_{LO}+G''P_{LO}^2 \tag{3.40}$$

$$G' \rightarrow G'+2G''P_{LO} \tag{3.41}$$

For the voltage bias case, the heterodyne signal current and SNR for the usual case of the g-r noise limited are given by

$$i_{het}=2V_B(G'+2G''P_{LO})\sqrt{P_{LO}P_S}\frac{G_L^2}{(G+G_L+G'P_{LO}+G''P_{LO}^2)^2} \tag{3.42}$$

$$\frac{S}{N}=\frac{(G+2G''P_{LO})G_L^2P_{LO}P_S}{(G+G'P_{LO}+G''P_{LO}^2)(G+G_L+G'P_{LO}+G''P_{LO}^2)^2Bh\nu/\eta} \tag{3.43}$$

For the current bias case, we get

$$v_{het}=\frac{2I_B(G'+G''P_{LO})\sqrt{P_{LO}P_S}}{(G+G_L+G'P_{LO}+G''P_{LO}^2)^2} \tag{3.44}$$

$$\frac{S}{N}=\frac{(G'+2G''P_{LO})(G+G'P_{LO}+G''P_{LO}^2)P_{LO}P_S}{(G+G_L+G'P_{LO}+G''P_{LO}^2)^2Bh\nu/\eta} \tag{3.45}$$

3.4.4 Results

The conductance of the PC detectors described earlier were measured versus P_{LO} . Figure (3.18) shows these results and a least squares fit made to the data for one of the detectors. From figure (3.18), the detector conductance is given by

$$G_{detector}=0.0276+0.0175P_{LO}-0.003P_{LO}^2 \tag{3.46}$$

where P_{LO} is expressed in milliwatts. The SNR's provided by Eqs. (3.43) and (3.45) are plotted in figures (3.19) and (3.20) using the actual conductance given by Eq. (3.46). It can be seen that for both biasing techniques, the SNR's have a true maximum for a finite value P_{LO} . It can be inferred from these figures that for this particular device, the current biasing gives the better SNR for realistic values of G_L . The results of figure (3.20) were used to determine the detection parameters previously given.

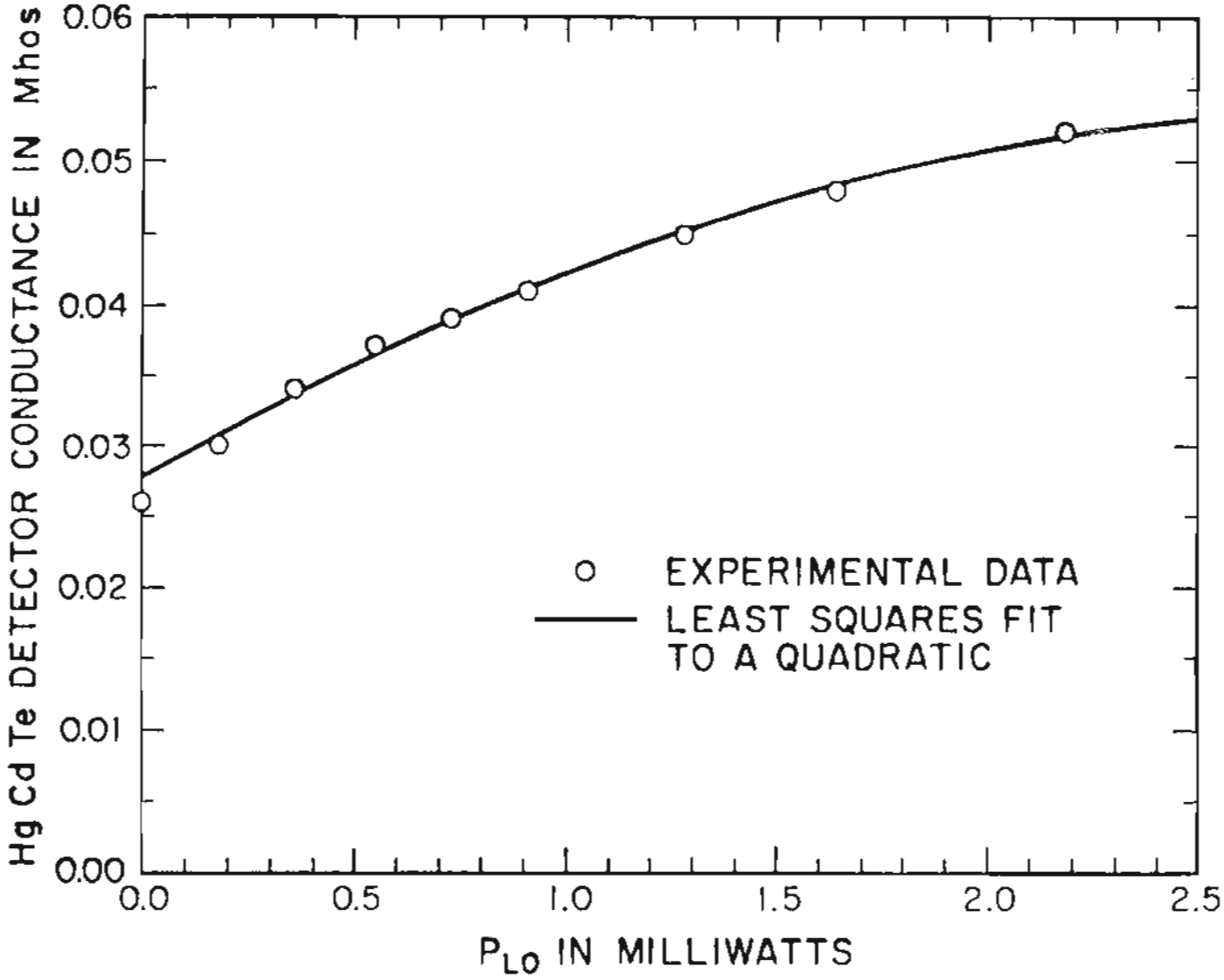

Figure 3.18 Conductance as a function of local oscillator power.

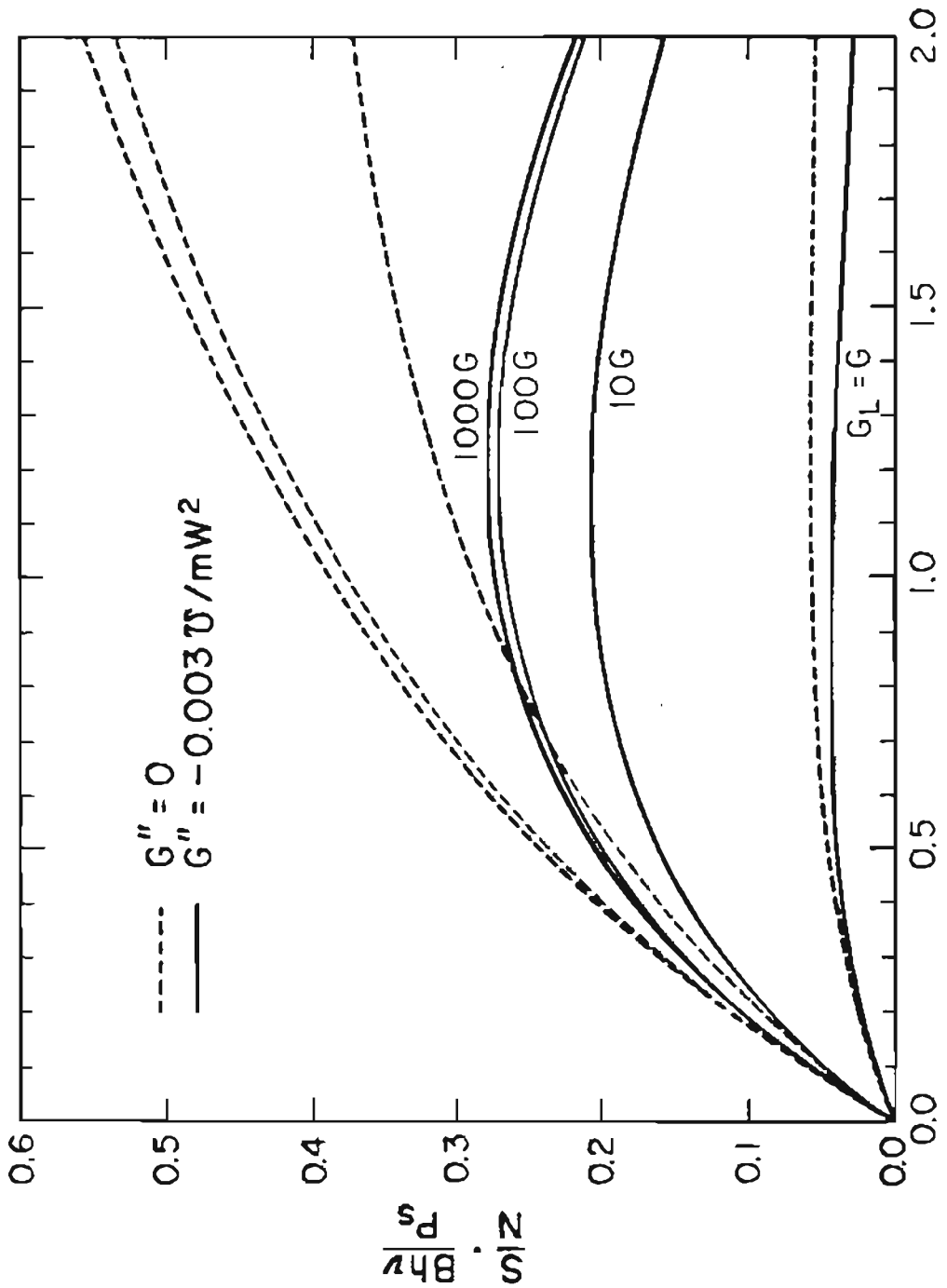

Figure 3.19 Signal to noise ratio for the voltage bias case.

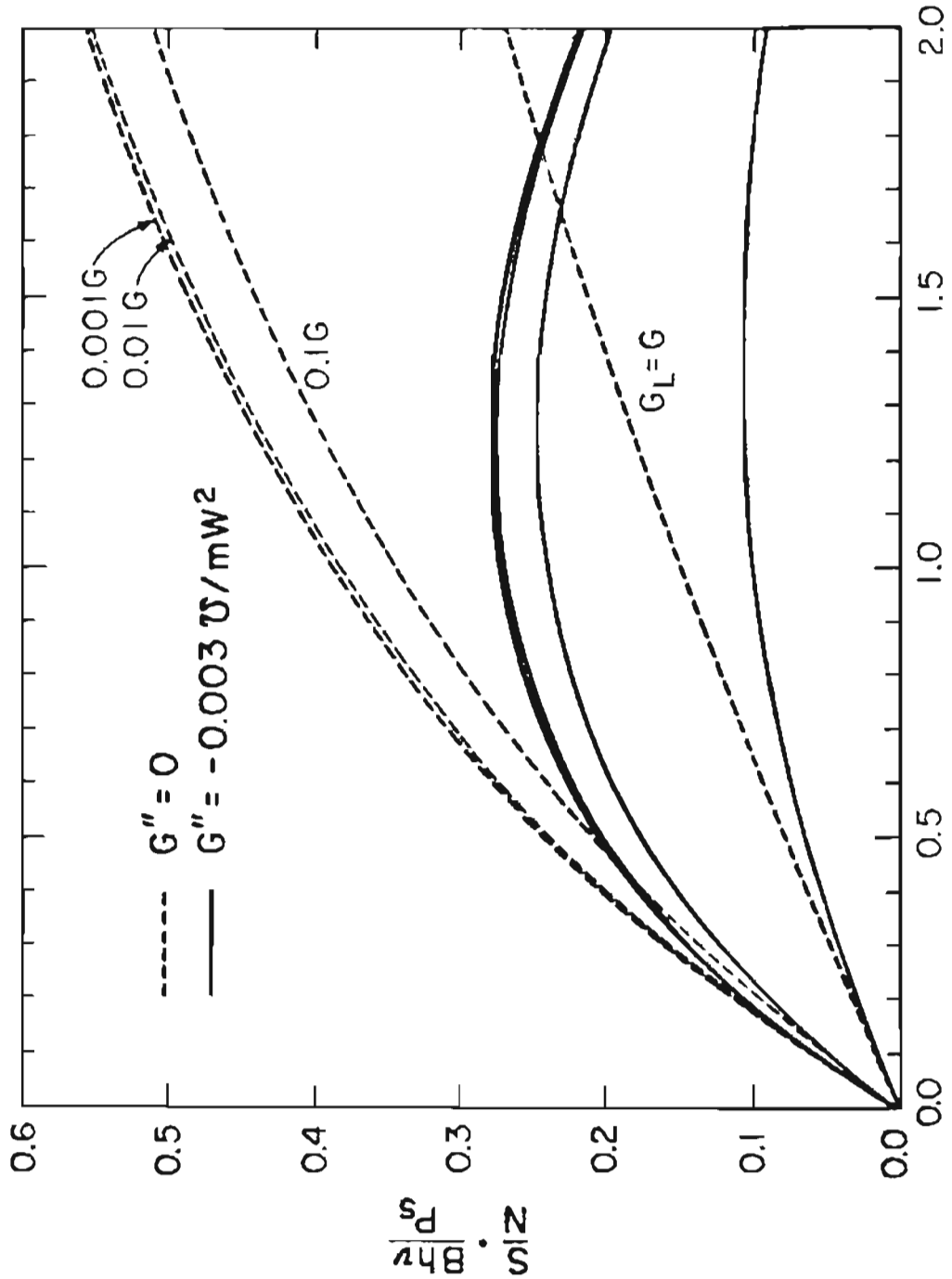

Figure 3.20 Signal to noise ratio for the current bias case.

CHAPTER 4

EXPERIMENTAL RESULTS

Each of the systems described in the previous chapter was first tested over a propagation path of about 200 meters in the vicinity of the Oregon Graduate Center (OGC). Then, the measurements were made at the OGC laser propagation field site where horizontal paths up to several kilometers over featureless farm land are available for which the turbulence is expected to be quite uniform.

Considerable amounts of data were collected over path lengths of 500 m, 1000 m and 1300 m at about two meters above the ground and a variety of atmospheric conditions. The locations of the targets were chosen to be accessible so that the in situ measurement over the same path could be made. It should be noted that the systems described in sections 3.3 and 3.4 have demonstrated the capability of operating over longer path lengths, with a possibility of up to 10 Km.

An example of the wind measurements is shown in figure (4.1) where the dual modulators system of section 3.4 is used over a 1000 m path. The results of figure (4.1) was obtained by using the B-ZLR technique of processing with an averaging time of 2.5 seconds. The in situ data was obtained by using a Campbell Scientific CA-9 path averaging scintillometer and crosswind

sensor.

The Campbell unit is a double ended unit with a 5 mW HeNe laser as transmitter at one end and a receiver at the other. The Campbell unit operates on the principle that the slope of the time-delayed covariance function for the log-intensity from a point source in a turbulent atmosphere is proportional to the path averaged crosswind. This type of sensor has been extensively tested using propeller anenometers[5,8] and found to be accurate to around 0.5 m/s.

The turbulence level measured by the Campbell unit during this measurement was intermediate at $C_n^2=2.37\text{x}10^{-14}\ m^{-2/3}$. The mean wind velocity averaged over the forty measurements is 2.01 m/s which is in good agreement with the in situ measurement of 2.09 m/s. The RMS error is 0.33 m/s which has been computed by using the following expression

$$\text{RMS error} = \left[\frac{1}{N}\sum_{i=1}^{N}(V_{het_i}-V_{Insitu_i})^2\right]^{1/2} \tag{4.1}$$

where V_{het_i} and V_{Insitu_i} are the individual heterodyne system and in situ measurements and N is the total number of measurements. Additional results of the wind measurements using different heterodyne systems and processing techniques will be presented in section 4.2.

The remote windsensing utilizing the speckle-turbulence interaction requires the measurements of certain statistical parameters. These statistical parameters include the variance, time delayed covariance and autocovariance of the received intensity.

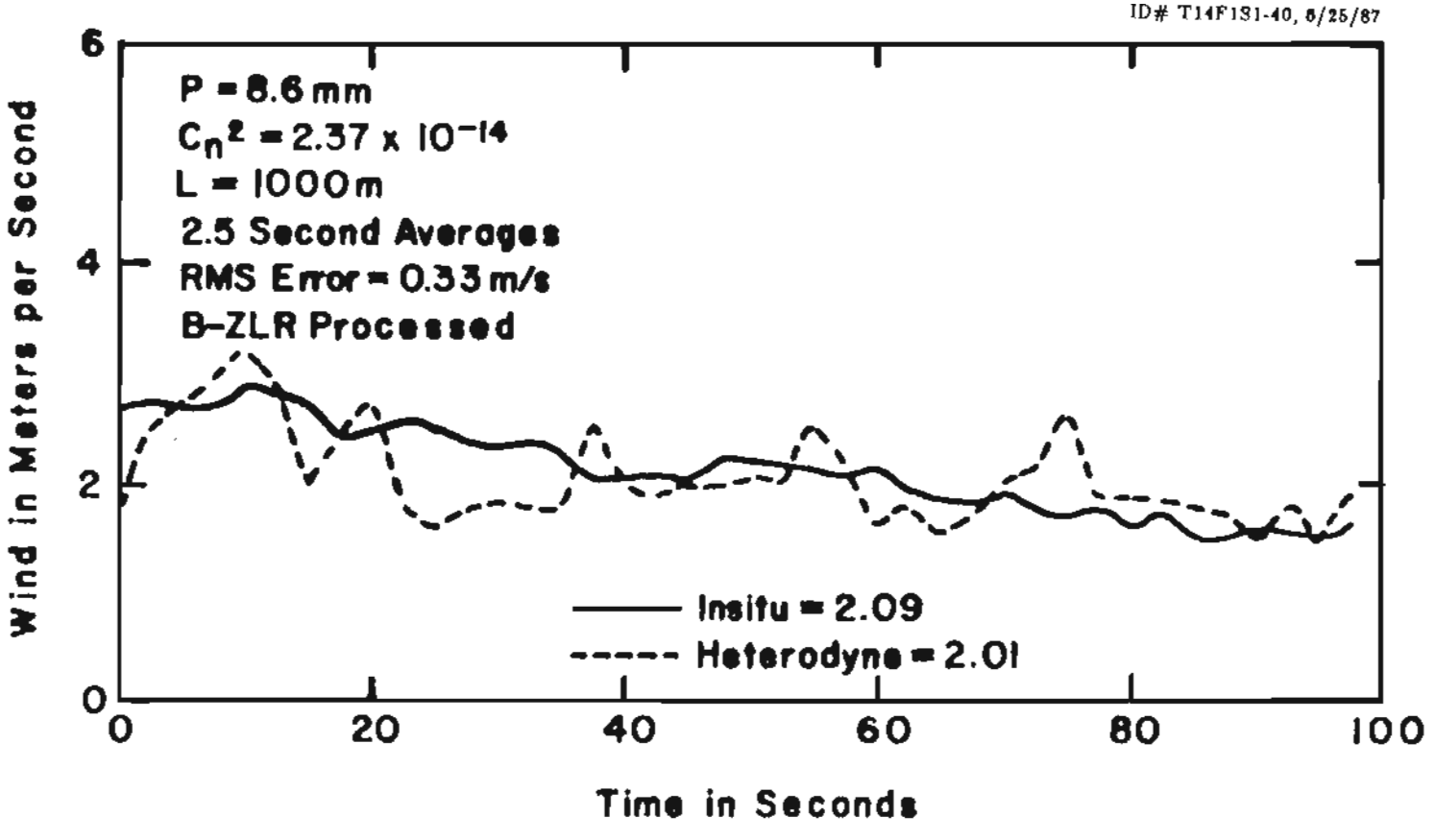

Figure 4.1 Wind Measurement.

In the next section some of the results of these measurements are presented and compared with the theoretical predictions. The processing program used to generate the results presented in this chapter is listed in appendix C.

4.1 Measurements Of The Statistical Parameters

The wind sensing techniques utilize the theoretical formulations obtained by the application of the independent paths and jointly gaussian assumptions. Therefore, any deviation of the measured parameters from these formulations can result in inaccurate wind measurements. Samples of measured statistical parameters are presented and discussed in this section.

The analytical formulations of the estimation errors associated with the statistics have been derived and will be presented in the next chapter as a function of the number of samples and the sampling period.

The normalized variance of the received intensity was measured over a wide range of atmospheric conditions and different path lengths. The results of these measurements are represented in tables (4.1), (4.2) and (4.3) for which the dual modulators systems were used over a 1000 m target range. The dual modulators system with the focusing receiver optics (see figure (3.6)) was utilized to obtain the data of tables (4.1) and (4.2), and the system with the imaging receiver optics (see figure (3.9)) was used for the data of table (4.3). The measurements are averaged over 5000 samples with a 0.5 millisecond period, and separated in time by about 4 seconds.

ID# T9F8S1-40, 10/10/86

Set #	Normalized Variance		Normalized Covariance	Wind Velocity Using ZLR (m/s)	In Situ Data	
	Channel #1	Channel #2			σ_χ at λ=632.8nm	Wind (m/s)
1	1.281	1.161	0.504	4.62	0.313	5.29
2	1.152	1.112	0.449	5.40	0.327	4.65
3	1.085	1.085	0.484	5.82	0.327	4.87
4	1.234	1.161	0.485	5.82	0.338	4.78
5	1.207	1.275	0.459	4.89	0.322	4.87
6	1.409	1.233	0.537	5.51	0.327	4.96
7	1.214	1.146	0.475	5.92	0.328	5.08
8	1.225	1.192	0.499	6.47	0.329	5.02
9	1.102	0.973	0.428	4.08	0.310	5.01
10	1.132	1.130	0.474	5.70	0.322	4.96
11	1.139	1.061	0.424	4.50	0.325	5.11
12	1.058	1.174	0.395	3.98	0.326	5.23
13	1.128	1.074	0.437	4.99	0.328	4.88
14	1.141	1.198	0.519	5.20	0.323	4.94
15	1.110	1.086	0.521	5.77	0.315	4.96
16	1.155	1.199	0.513	6.55	0.313	4.78
17	1.367	1.185	0.521	2.95	0.319	5.04
18	1.408	1.120	0.464	2.93	0.320	4.64
19	1.148	1.041	0.426	2.55	0.321	4.74
20	1.105	1.040	0.443	5.37	0.309	4.51
21	1.131	1.070	0.441	5.29	0.326	5.16
22	1.122	1.121	0.455	6.08	0.320	4.57
23	1.231	1.158	0.479	3.72	0.314	4.57
24	1.447	1.176	0.540	4.26	0.331	4.81
25	1.151	1.094	0.454	5.58	0.323	4.86
26	1.390	1.212	0.483	5.10	0.300	4.76
27	1.320	1.136	0.461	6.35	0.310	4.50
28	1.081	1.146	0.366	3.65	0.322	4.37
29	1.199	1.274	0.478	4.51	0.306	4.70
30	1.460	1.249	0.462	3.39	0.311	4.61
31	1.355	1.291	0.455	5.12	0.311	4.69
32	1.287	1.251	0.274	3.82	0.328	4.41
33	1.363	1.243	0.402	5.79	0.321	4.64
34	1.409	1.326	0.371	3.74	0.332	4.58
35	1.269	1.195	0.369	4.52	0.330	4.40
36	1.280	1.307	0.372	2.85	0.311	4.49
37	1.612	1.216	0.437	4.21	0.321	4.67
38	1.418	1.291	0.380	4.45	0.328	4.41
39	1.275	1.316	0.336	3.27	0.326	4.31
40	1.488	1.478	0.376	4.19	0.317	4.69
Mean	1.252	1.180	0.446	4.72	0.321	4.76
S.D.	0.135	0.096	0.058			

Table 4.1 Experimental Results; 2.5 second averages;

α_0=25mm , p=16mm, L=1000m.

ID# T7F3S1-80, 4/8/86

Set #	Normalized Variance		Normalized Covariance	Wind Velocity Using ZLR (m/s)	In Situ Data	
	Channel #1	Channel #2			σ_χ at λ=632.8nm	Wind (m/s)
1	1.042	1.109	0.127	1.37	0.063	1.92
2	0.861	1.008	0.059	1.05	0.062	1.93
3	1.318	1.671	0.075	1.31	0.054	1.85
4	1.327	0.983	0.148	1.15	0.065	2.02
5	1.211	1.024	0.030	2.78	0.066	1.87
6	1.137	1.390	0.077	1.58	0.063	1.91
7	1.020	1.023	0.153	2.48	0.061	1.94
8	1.107	1.067	0.130	1.23	0.054	2.06
9	1.390	1.207	0.030	0.95	0.054	1.81
10	1.135	1.237	0.005	1.25	0.055	1.87
11	1.080	1.228	0.134	1.76	0.060	1.74
12	1.179	1.113	0.070	0.59	0.064	2.26
13	0.987	1.117	0.068	1.43	0.061	2.35
14	1.152	0.854	0.117	0.85	0.060	2.25
15	1.064	1.035	0.055	1.59	0.061	2.03
16	1.080	1.026	0.108	1.40	0.065	2.08
17	1.264	1.052	0.120	2.59	0.063	1.71
18	1.077	1.110	0.100	1.88	0.058	1.89
19	1.034	1.016	0.042	2.98	0.055	2.14
20	0.994	1.069	0.013	2.67	0.058	2.07
21	1.044	1.021	0.136	1.53	0.062	2.08
22	1.013	1.110	0.100	2.71	0.058	2.02
23	1.034	0.951	0.051	1.26	0.058	1.84
24	1.145	1.008	0.087	1.18	0.068	2.17
25	0.941	1.323	0.115	1.09	0.063	2.36
26	1.134	1.328	0.083	2.32	0.069	2.42
27	1.096	1.178	0.045	1.84	0.071	1.77
28	1.062	1.278	0.042	1.00	0.064	2.19
29	1.088	1.071	0.052	1.50	0.056	1.86
30	1.240	1.328	0.098	1.57	0.047	1.89
31	1.169	1.024	0.035	1.52	0.058	2.04
32	0.954	1.057	0.148	0.89	0.061	2.18
33	0.866	1.461	0.033	1.26	0.060	2.16
34	0.776	0.809	0.074	0.95	0.058	1.89
35	0.923	1.475	0.074	0.95	0.059	2.00
36	0.984	1.214	0.135	0.88	0.057	2.04
37	1.012	1.068	0.040	1.00	0.058	1.82
38	0.775	0.835	0.062	0.54	0.061	1.86
39	1.117	0.865	0.050	0.88	0.070	2.11
40	1.013	1.428	0.014	0.99	0.065	2.11
Mean	1.071	1.129	0.078	1.64	0.061	1.96
S.D.	0.134	0.185	0.041			

Table 4.2 Experimental Results; 2.5 second averages;

α_0=25mm , p=25mm, L=1000m.

ID# T14F1S1-40, 6/26/87

Set #	Normalized Variance		Normalized Covariance	Wind Velocity Using ZLR (m/s)	In Situ Data	
	Channel #1	Channel #2			σ_χ at λ=632.8nm	Wind (m/s)
1	0.900	0.790	0.665	1.80	0.353	2.69
2	1.263	1.274	0.748	2.80	0.339	2.71
3	1.008	1.056	0.642	3.28	0.335	2.65
4	1.018	1.065	0.664	3.91	0.339	2.69
5	1.063	1.119	0.722	4.61	0.333	2.86
6	0.974	1.053	0.647	3.62	0.325	2.75
7	1.062	1.028	0.730	2.04	0.344	2.69
8	1.050	1.016	0.698	3.06	0.349	2.37
9	1.017	0.986	0.747	3.13	0.343	2.45
10	1.290	1.234	0.784	1.97	0.339	2.53
11	1.269	1.115	0.788	1.61	0.352	2.47
12	1.025	1.138	0.683	1.74	0.334	2.32
13	0.907	1.063	0.689	1.57	0.324	2.28
14	0.930	0.825	0.707	1.56	0.347	2.36
15	1.007	1.010	0.715	1.91	0.355	2.22
16	1.051	1.030	0.723	3.31	0.351	1.96
17	1.111	1.244	0.793	2.17	0.349	2.04
18	1.086	1.142	0.642	1.74	0.375	2.06
19	1.282	1.289	0.748	2.09	0.359	1.97
20	1.610	1.532	0.852	2.16	0.369	2.20
21	1.331	1.210	0.713	2.33	0.348	2.15
22	1.311	1.139	0.747	2.02	0.369	2.13
23	1.378	1.123	0.706	3.24	0.350	2.08
24	0.921	0.934	0.622	2.17	0.374	2.05
25	1.015	0.958	0.678	1.41	0.382	2.12
26	0.990	1.075	0.685	1.63	0.368	1.85
27	0.834	1.078	0.579	1.34	0.350	1.82
28	1.121	1.217	0.679	1.73	0.406	1.76
29	0.783	0.892	0.658	2.13	0.351	1.88
30	1.004	1.118	0.679	2.01	0.386	1.70
31	0.902	0.930	0.727	2.82	0.371	1.85
32	0.879	0.854	0.749	1.46	0.363	1.72
33	0.954	0.915	0.695	1.66	0.392	1.56
34	1.104	1.053	0.678	1.81	0.383	1.68
35	1.023	1.128	0.727	1.95	0.371	1.42
36	1.148	1.032	0.752	1.59	0.411	1.42
37	1.008	1.078	0.644	1.25	0.361	1.56
38	1.182	1.275	0.732	1.68	0.367	1.51
39	0.961	0.977	0.686	1.40	0.380	1.47
40	1.021	0.949	0.692	1.70	0.374	1.61
Mean	1.070	1.073	0.705	2.19	0.359	2.09
S.D.	0.164	0.142	0.051			

Table 4.3 Experimental Results; 2.5 second averages;

α_0=25mm , p=8.6mm, L=1000m.

The mean values of the quantities averaged over forty measurements are shown in these tables. The standard deviation defined by $<(S-\bar{S})^2>$ have also been computed, where S represents the measured normalized variances and covariances. The wind measurements corresponding to these tables are shown in figures (4.11), (4.16) and (4.13) respectively.

The data of table (4.1) was collected at an intermediate turbulence level measured by the Campbell unit to be $C_n^2=1.8\text{x}10^{-14}$ $m^{-2/3}$. This is obtained from the measured log-amplitude variance of $(0.321)^2$ at the HeNe laser wavelength of 632.8 nm. The equivalent log-amplitude variance at 10.6 μm wavelength is then simply obtained to be 0.0038. It can be seen that the mean values of the normalized variance are larger than unity predicted by the jointly gaussian assumption. This is believed to be caused by the combined effects of the angle of arrival fluctuations (see sec. 3.4), log-amplitude covariance of the turbulence C_χ (see sec. 2.2) and nonuniform diffuse reflectivity of the target surface. These effects tend to raise the variance as the turbulence becomes stronger.

The measurements of table (4.2) were made at much lower turbulence strength ($C_n^2=6.5\text{x}10^{-16}$ $m^{-2/3}$) show that the means of the normalized variance for both channels are closer to one than those of table (4.1). At such a low turbulence level, the effect of the angle of arrival fluctuations and C_χ are negligible. The effect of the nonuniform diffuse reflectivity is also insignificant, since the beam does not wander much over the target surface.

The data presented in table (4.3) were obtained using the low

magnification receiver optics explained in sec. 3.4 which would suppress the effect of the angle of arrival fluctuations. These results show a lower normalized variance as compared to table (4.1), even though the strengths of turbulence are compatible in both cases. The mean values of the normalized variance obtained from the data of table (4.3) agree extremely well with the complete theory predictions shown in figure (2.1). The normalized variance using the complete theory gives a numerical value of about 1.02 which is within the measurement error (see ch. 5) of the estimated value at 1.07.

A great deal of effort was devoted to obtaining consistent T-D covariance curves from the received signals that would agree with the theoretical predictions. However, the success was limited and as a result, the windsensing techniques utilizing the T-D covariance did not produce satisfactory results.

As discussed earlier, the effect of the turbulence on the T-D covariance function is rather small at the 10.6 μm wavelength. Having to find this small effect in a fully developed speckle pattern makes the estimation of the time delayed covariance difficult.

The covariances (zero time delay) of the received intensities are listed in tables (4.1)-(4.3) which are consistently smaller than the theoretical values for the given spacings between the detectors. The results of table (4.2) show an unusual low covariance due to the very low turbulence level and high humidity of the air at the time of measurements. Figures (4.2) and (4.3) show two T-D covariance curves obtained with two different wind speeds and

opposite directions. Each curve consists of eighty measurements over 2.5 seconds. These figures clearly show the shift of the peak of the T-D curves with the wind.

Unfortunately, obtaining such curves with clear shift of the peaks and proper slopes in a consistent manner was not always accomplished. The overall results indicated that about 70% of the time, the correct direction of the wind velocity could be obtained using the slope of the T-D covariance curve at zero time delay.

For much of the experimental data, the time delay to the peak was smaller than $\tau_p = p/2V$ obtained by the independent paths jointly gaussian assumption. For others, the peak was found to be on the wrong side of the zero time delay axis. The low magnification imaging receiver optics did not appear to improve the results, indicating that the angle of arrival fluctuations was not the cause.

The shift of the peak of the T-D covariance curve toward the zero time delay axis may be attributed to the dependent effect of the turbulence on the outgoing and return paths. This effect is discussed in detail in section 2.3 where the time delayed statistics are formulated as a function of transmitter-receiver spacing.

For the results presented here, the separation between the transmitter and receiver is about 15 cm. Figures (2.6) and (2.7) show the extent of the dependence effect on the time delayed statistics for such spacing.

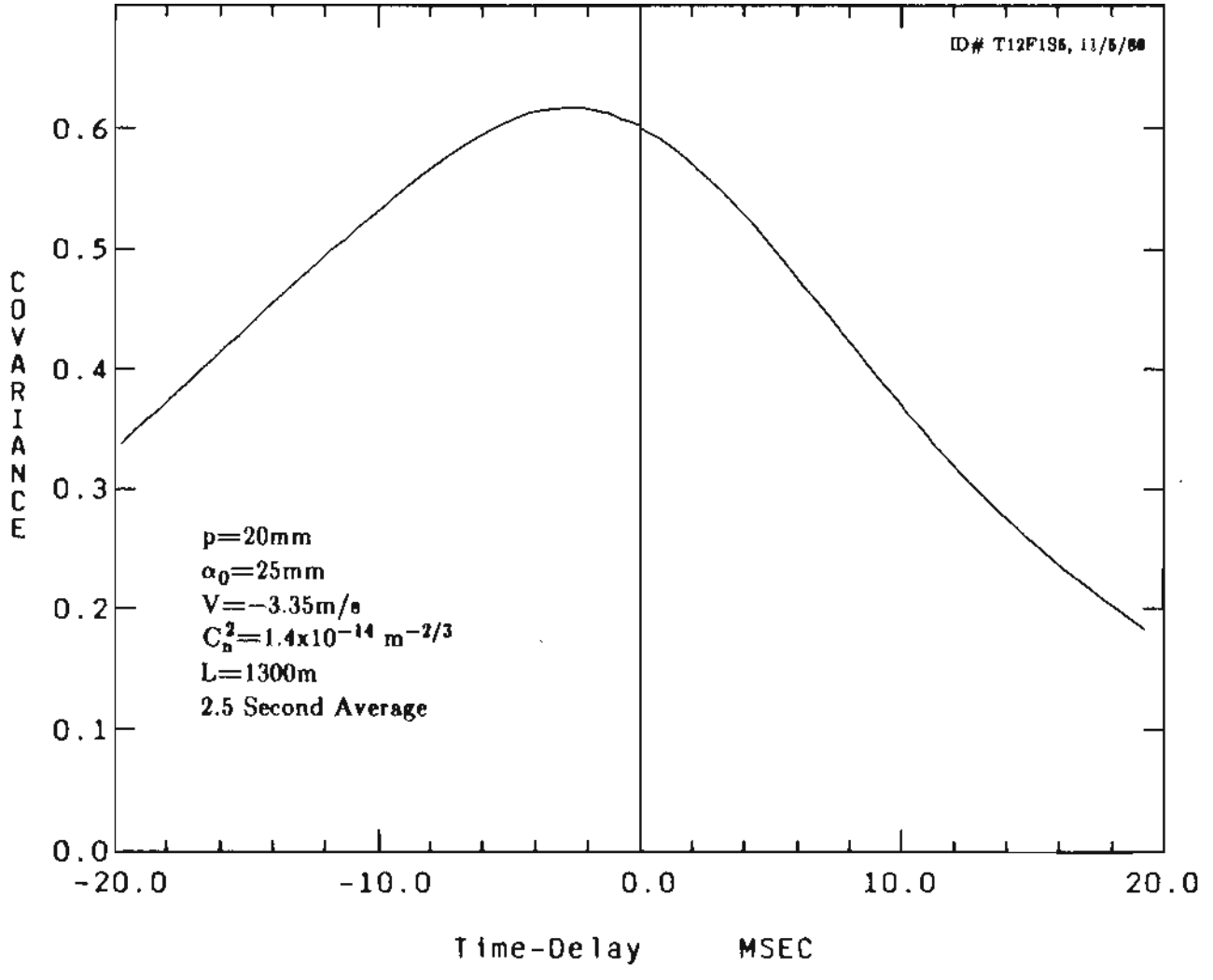

Figure 4.2 Time-Delayed Covariance Measurement.

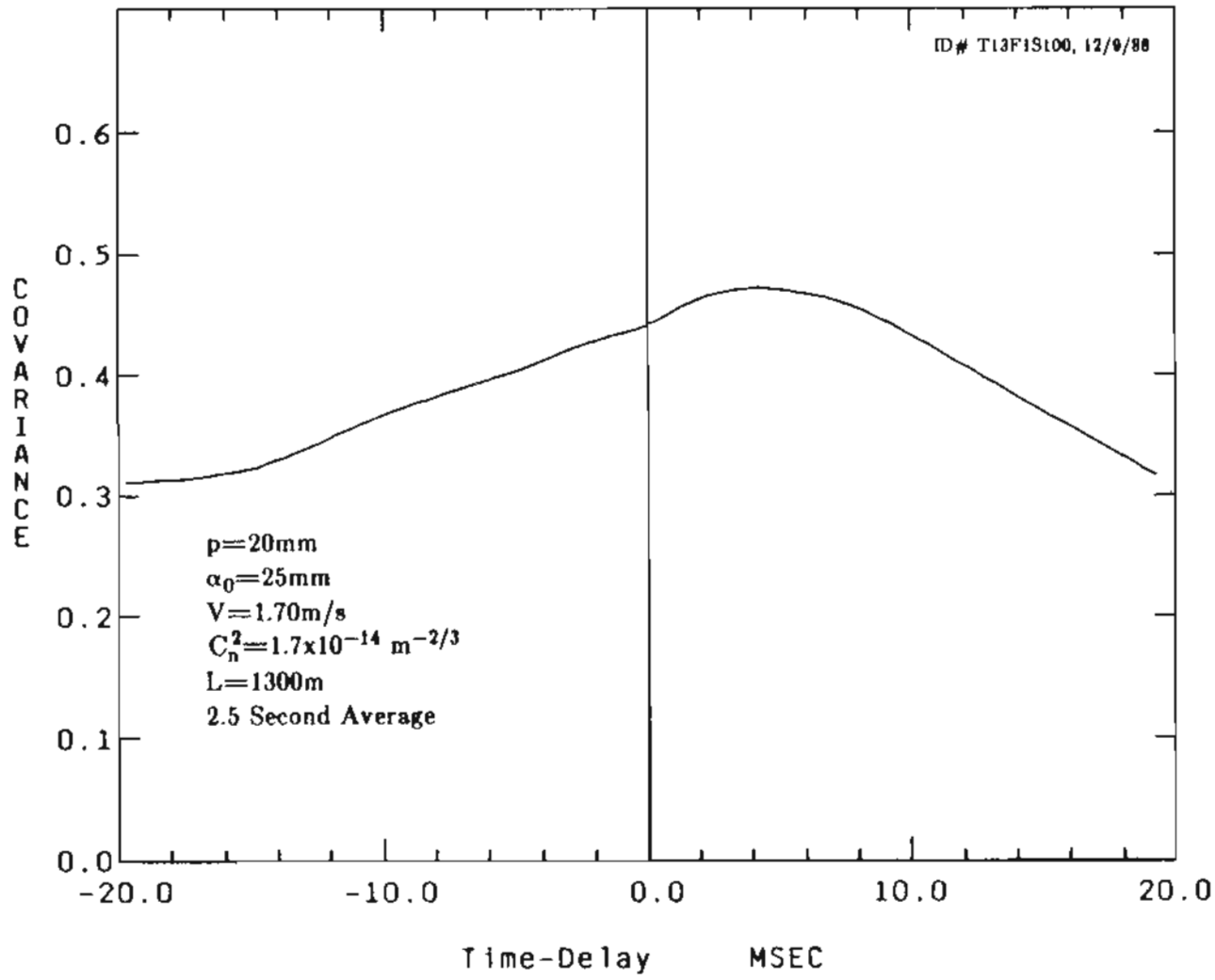

Figure 4.3 Time-Delayed Covariance Measurement.

A sample of shift of the peak from one side to the other is demonstrated in figure (4.4) where two consecutive sets of data of 2.5 second duration are shown. It appears that the peaks in both cases occur at almost the same time delay with opposite signs.

Time delayed covariance curves with double peaks were also occasionally encountered with the peaks almost symmetrical with respect to the zero time delay axis. It is interesting that the double peak occurs consistently when the transmitter beam expander adjusted to either focus the beam closer to the transmitter-receiver end than the target or diverge the beam considerably. An example of this is shown in figure (4.5) where the beam expander lenses were moved further away from each other by 0.5 millimeters from their original positions. The transmitter beam expander consists of two lenses with 38.0 mm and 375.7 mm focal lengths. Simple calculations show that by increasing the lenses separation by 0.5 mm, the focal point of the beam can move from 1000 m to 250 m. Similar results were obtained by decreasing the spacing between the lenses to diverge the transmitter beam. It should be noted that the dual modulators system with the focusing receiver optics was utilized for the data of figures (4.2)-(4.5).

Based on these observations, the author believes that the focusing of the transmitter beam as well as the fields of view and lines of sight of the detectors can significantly influence the behavior of the T-D covariance curve. However, more theoretical and experimental works are required to fully understand the effects of such alignment factors on the statistics of the received signals.

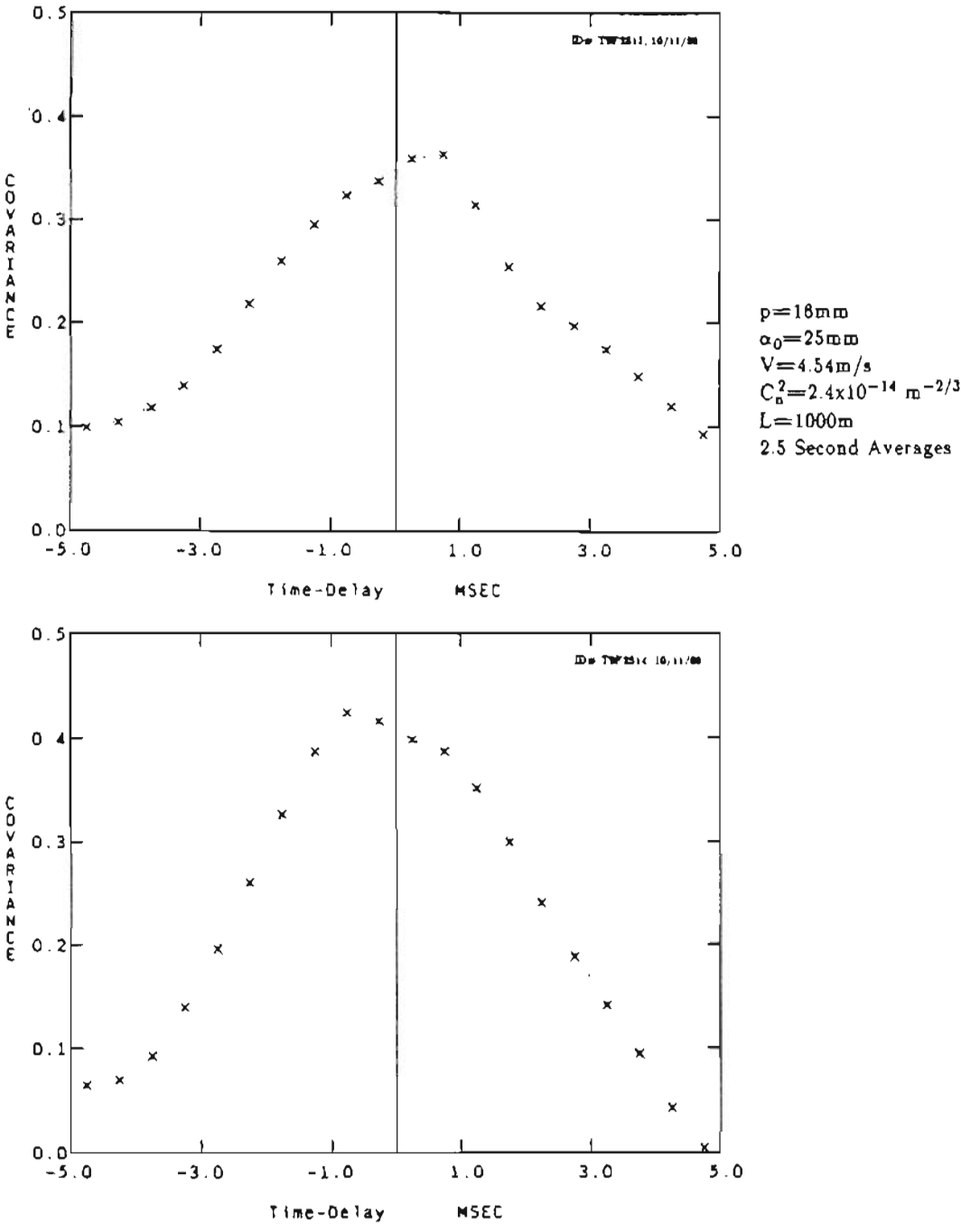

Figure 4.4 Experimental T-D covariance curves with the shift of peaks.

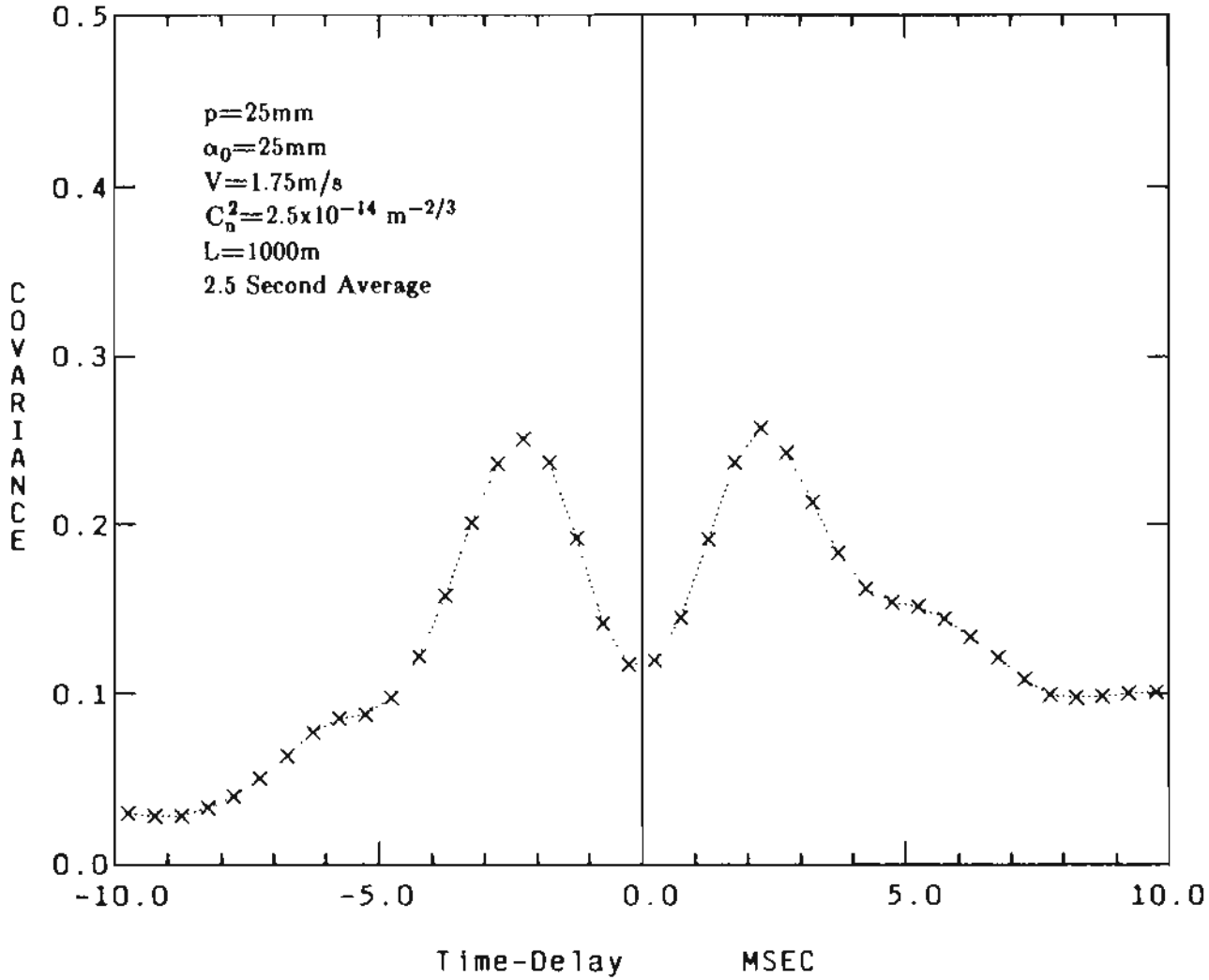

Figure 4.5 Experimental T-D covariance curve, with the transmitter beam focused closer to the transmitter-receiver end than the target.

The results of the autocovariance measurements were quite satisfactory when used in conjunction with the ZLR techniques to determine the wind velocity. A typical autocovariance measurement with the usual sampling time of 2.5 seconds is shown in figure (4.6). Also shown for comparison reasons, are the plots of the analytical expressions obtained using the jointly gaussian assumption for both dependent and independent paths cases. The curve corresponding with dependent paths uses the actual spacing of ten centimeters between the transmitter and receiver in Eq. (2.49).

As can be seen from figure (4.6), the measured autocovariance drops faster with time than the theoretical curves. Nonuniform winds along the path (see figure (2.3)) and target vibrations can contribute to faster decorrelation. It should also be noted that the calibration of the Campbell unit performed in the past had shown that C_n^2 is under estimated by a factor of about 0.64. Considering all these factors, the measured autocovariance may satisfactorily agree with the dependent paths theoretical curve. Similar results were obtained using the low magnification receiver optics indicating that the angle of arrival fluctuations had not contributed to the faster decorrelation of the data obtained using the focusing receiver optics.

Despite this deviation from the joint gaussian theory, when used with the measured covariance in the ZLR methods, good results were obtained for the wind velocity. As noted earlier, the magnitude of the measured covariance is also smaller than the theoretical value which seems to be somewhat correlated with the autocovariance.

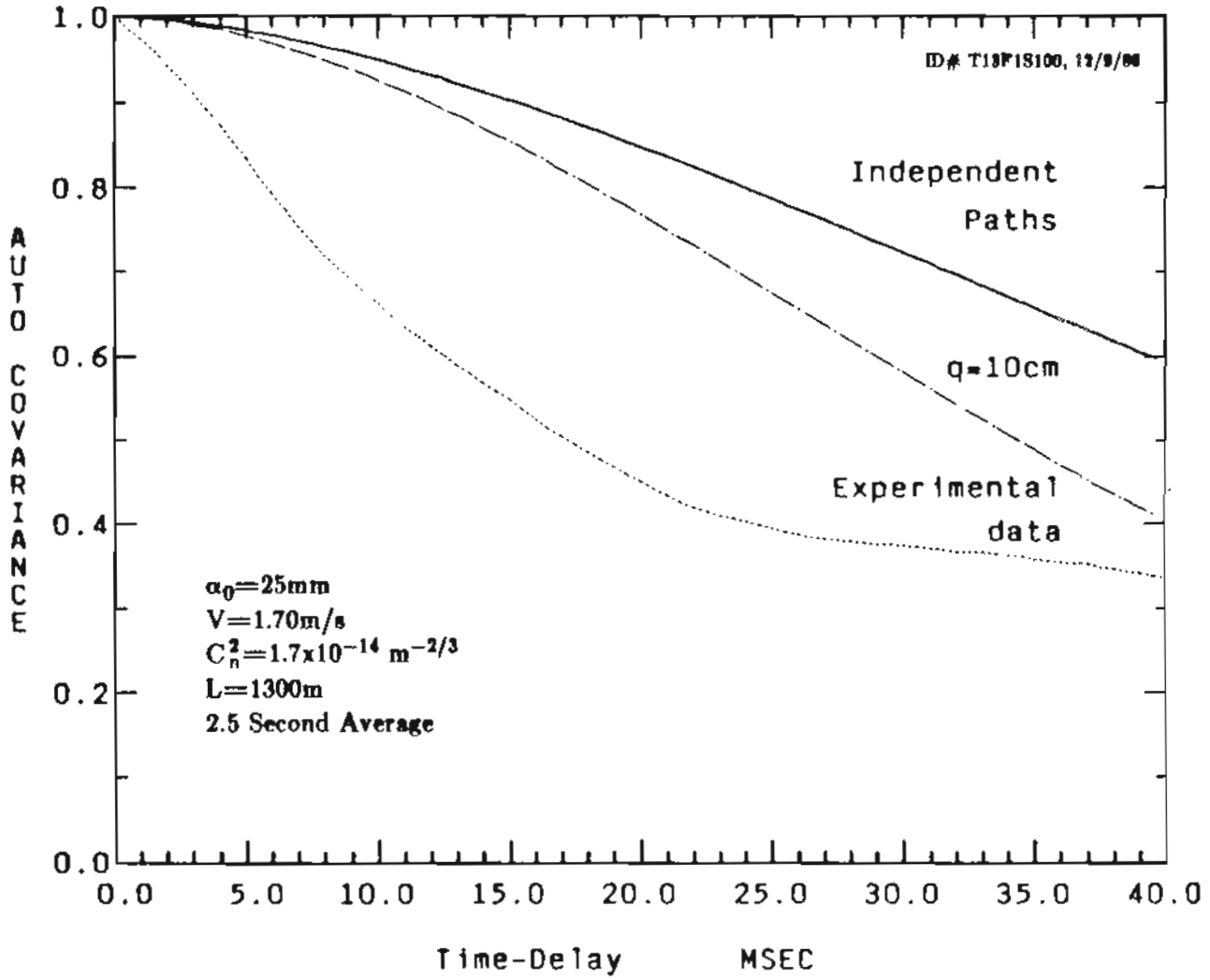

Figure 4.6 Experimental and theoretical autocovariance curves.

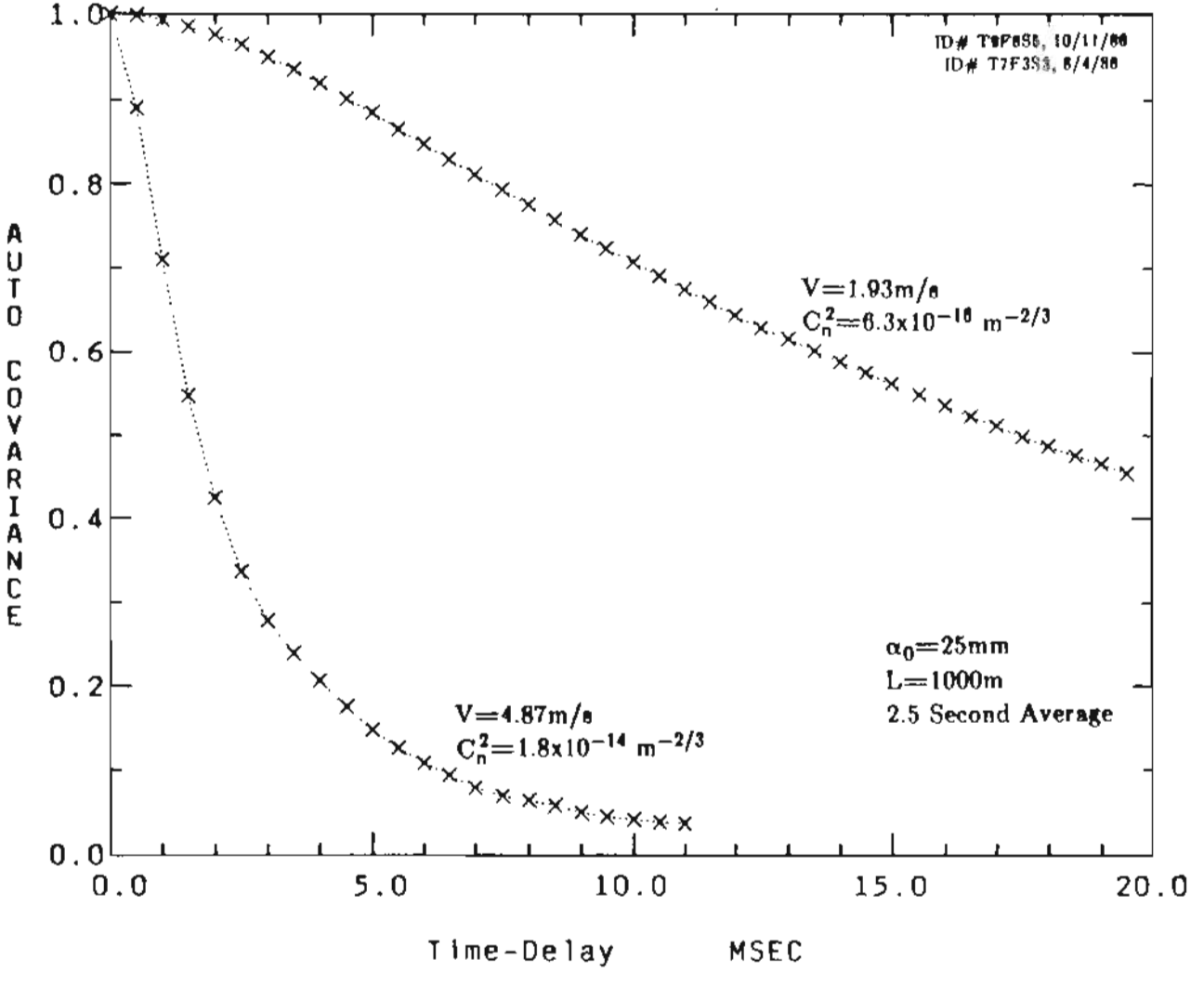

Figure 4.7 Two experimental autocovariance curves obtained over different atmospheric conditions.

Figure (4.7) shows how well the measured autocovariance are indicative of the wind velocity and the strength of turbulence. Two experimental autocovariance curves are shown in figure (4.7) which were obtained at different turbulence levels and wind velocities.

4.2 Results Of The Wind Measurements

A representative set of wind measurement results using the systems described in the previous chapter with different parameters at various atmospheric conditions are presented in this section. As discussed earlier, the conventional windsensing techniques were not adequate for our purpose, leading to the development of new techniques. The wind measurements using these techniques namely ZLR, MMSE-ZLR and B-ZLR are presented and compared with each other.

Attempts have been made to avoid presenting an excess number of wind data while representing these results as completely as possible. Some of the data obtained by different heterodyne systems were processed using the ZLR method and the results shown in figures (4.8)-(4.13). As previously stated, the transmitter beam radius α_0 is 25 mm for the dual AO modulators systems and 34 mm for the other two systems.

Figure (4.8) was obtained using the optical heterodyne system described in section 3.1 over a 500 m path length. The problem of insufficient optical isolation between the local oscillator and transmitter beams limited the

performance of this system considerably (see page 46). A limited amount of data could be collected using this system at the shorter target range of 500 m. This was accomplished by frequent adjustment of quarter wave plates and a Brewster window placed at the output of the laser to minimize the optical feedback. When averaged over the fifty measurements shown in figure (4.8), the wind velocity differs from that of the Campbell unit by 22.4% (0.8 m/s). This is mostly attributed to the optical feedback which produces random amplitude homodyne beats at the detectors. The RMS error obtained using the definition of Eq. (4.1) is 1.18 m/s.

Figure (4.9) shows a set of measurements obtained by the synchronous heterodyne detection system (sec. 3.2) also at the 500 m target range. The synchronous detection scheme increased the optical isolation by a factor of 25. By comparing figures (4.8) and (4.9), the extent of this improvement becomes obvious, where the systems and atmospheric parameters are similar.

Figure (4.10) shows another set of measurements with the same system but a longer path length of 1000 m. The RMS errors associated with the data of figures (4.9) and (4.10) are 0.46 m/s and 1.56 m/s, and the average values of the in situ measurements are about 2.0 m/s and 4.5 m/s, respectively.

Figures (4.11) and (4.12) show the results of two sets of data taken over 1000 m and 1300 m path lengths using the dual AO modulators system of section 3.3.

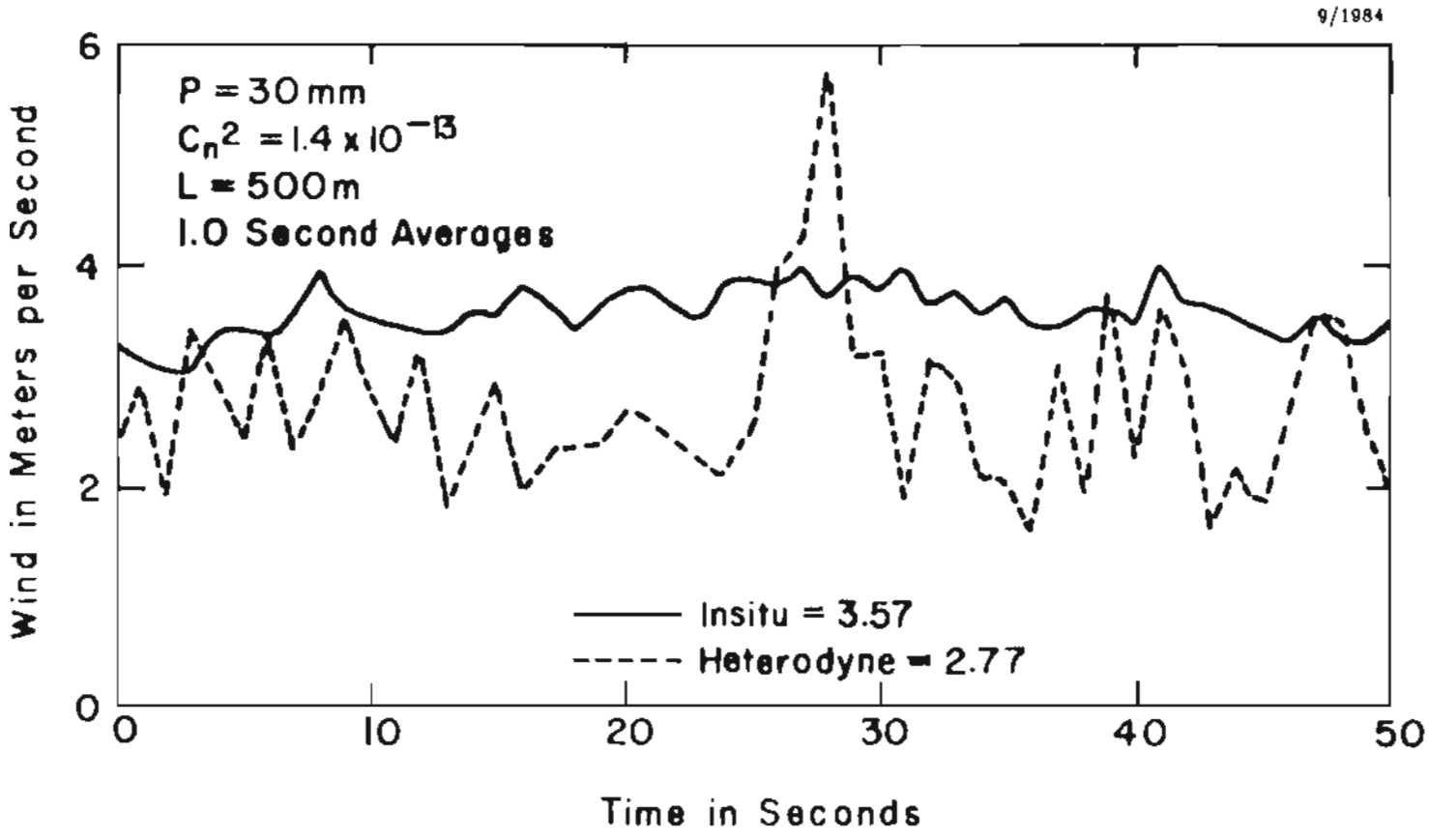

Figure 4.8 Wind measurement using the set-up of sec. 3.1, 500m target.

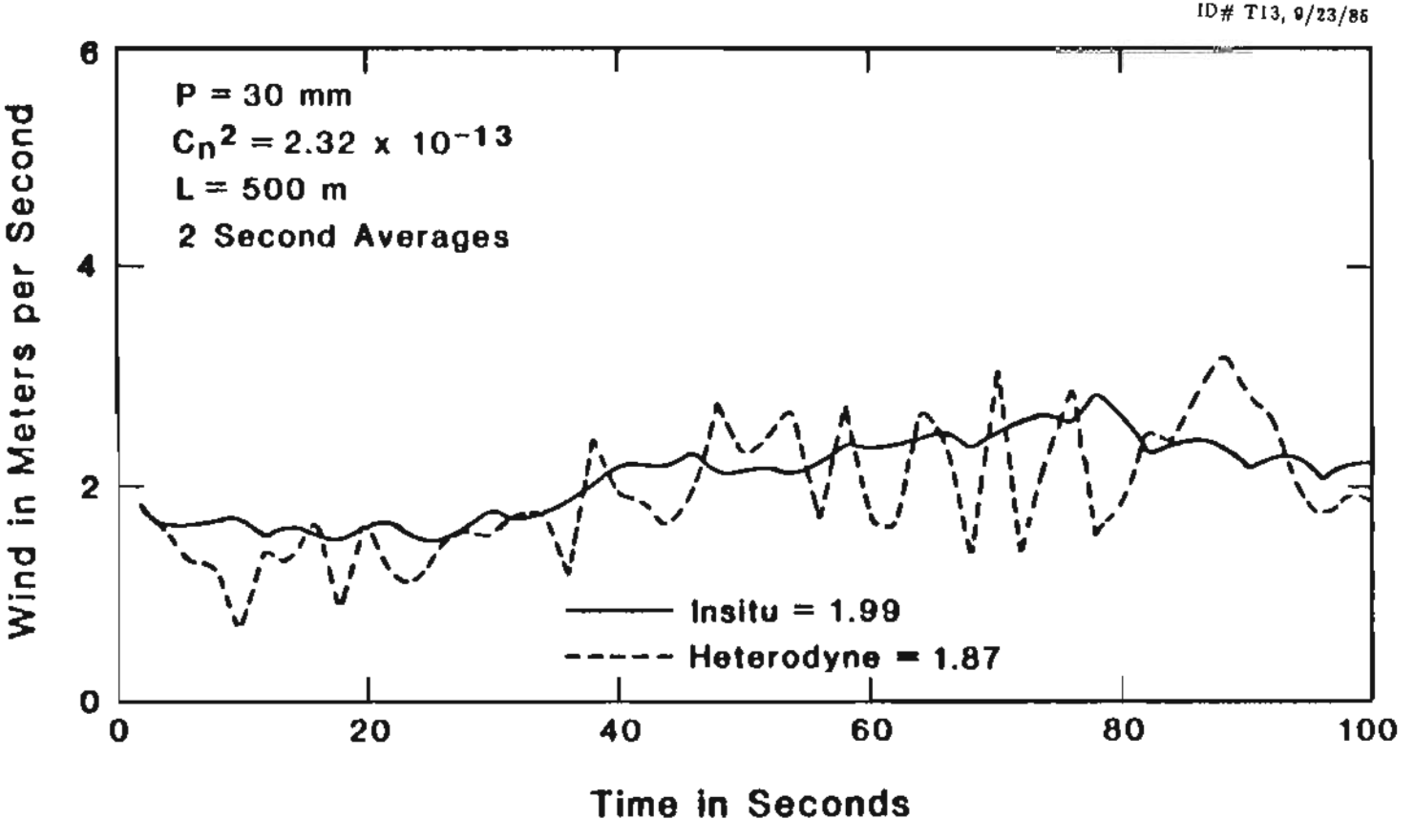

Figure 4.9 Wind measurement using the set-up of sec. 3.2, 500m target.

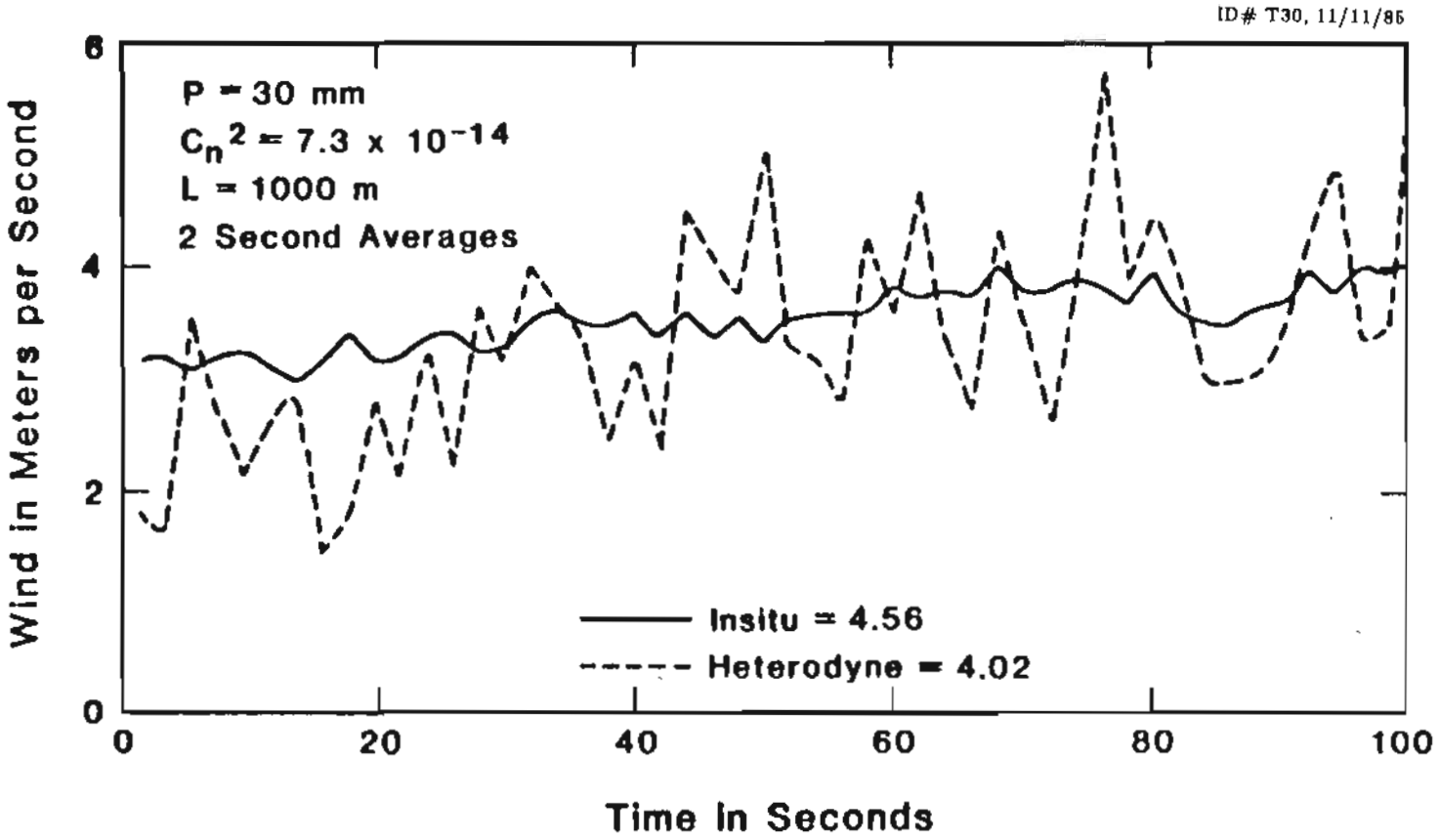

Figure 4.10 Wind measurement using the set-up of sec. 3.2, 1.0km target.

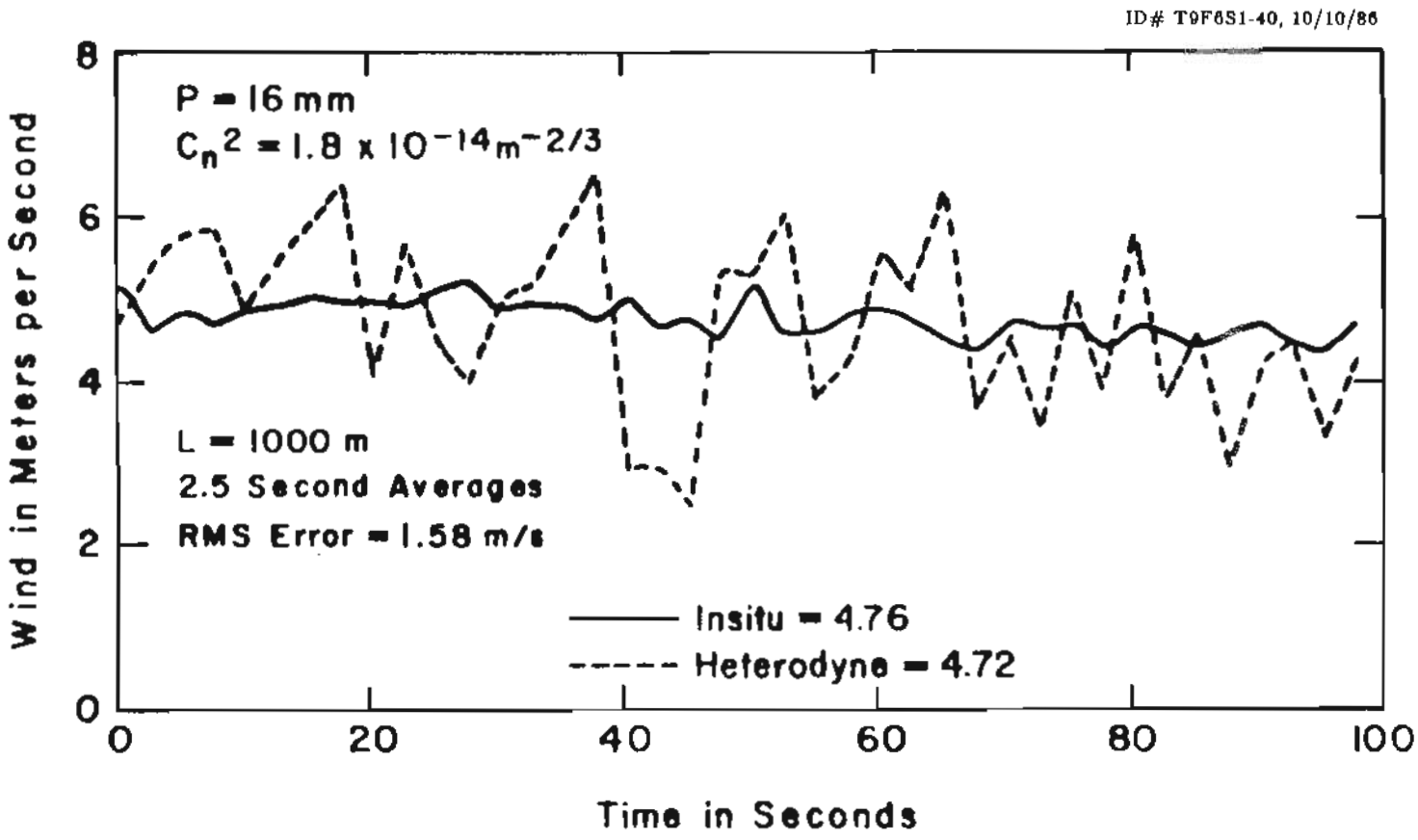

Figure 4.11 Wind measurement using the set-up of sec. 3.3, 1.0km target.

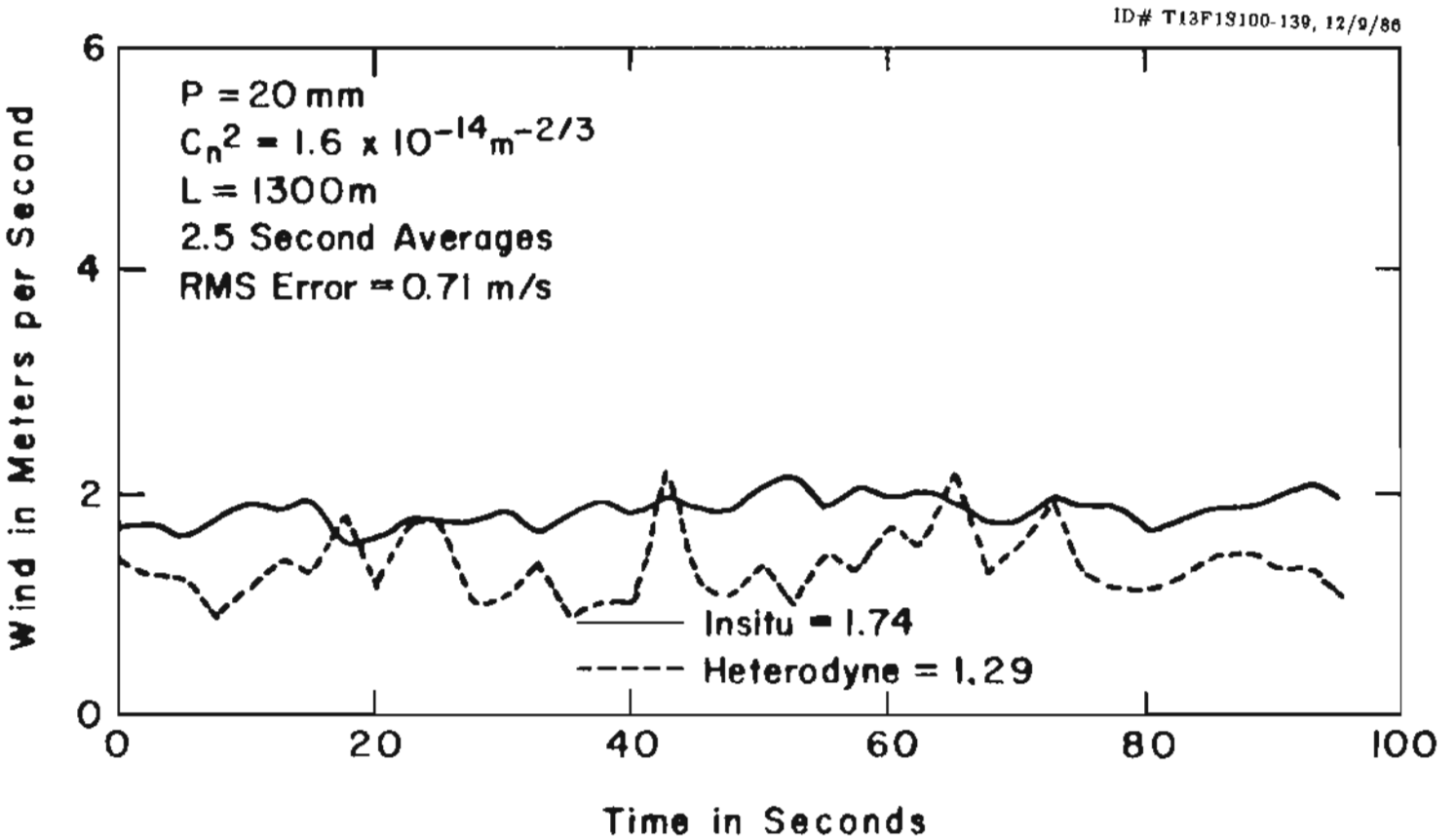

Figure 4.12 Wind measurement using the set-up of sec. 3.3, 1.3km target.

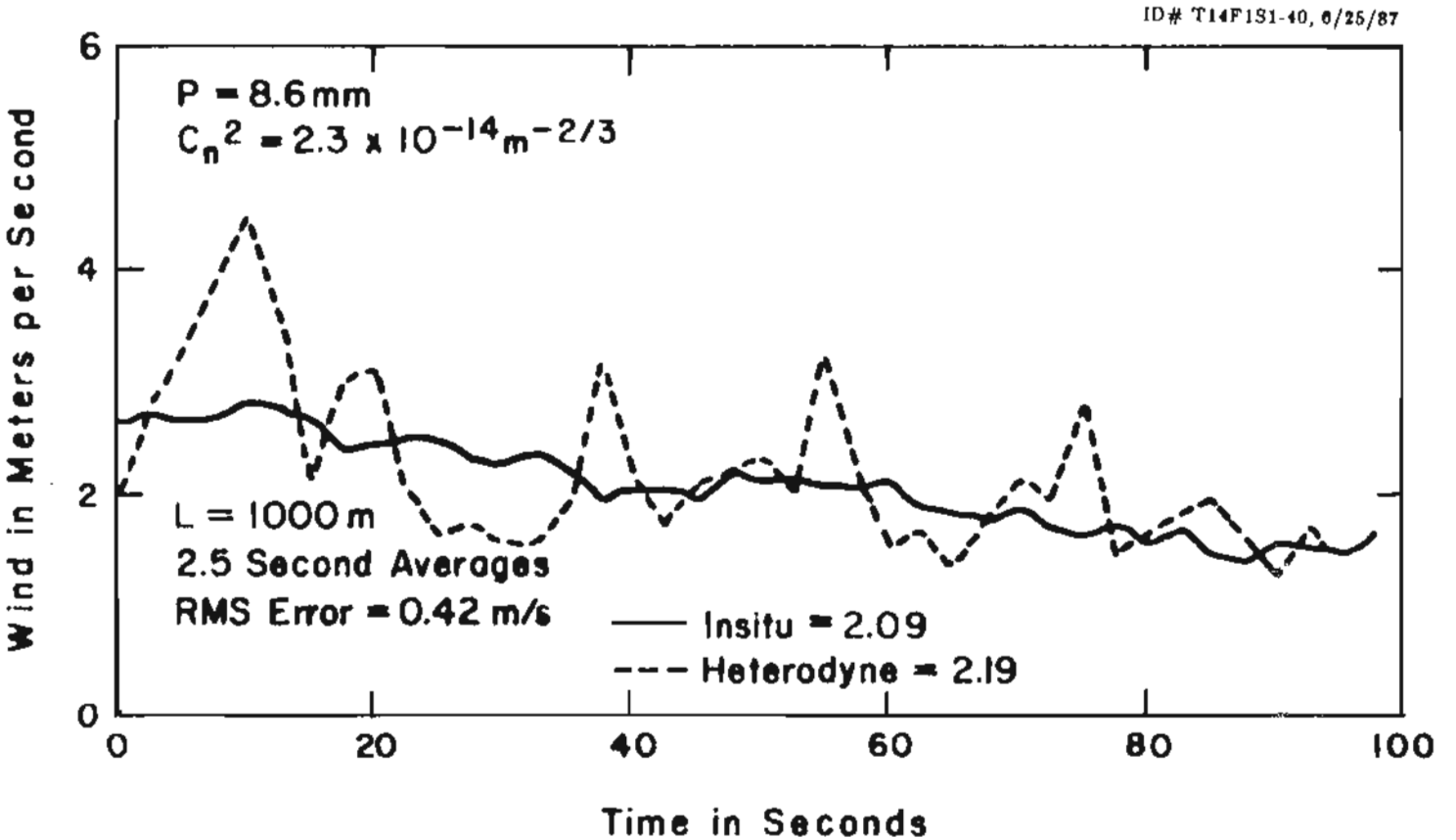

Figure 4.13 Wind measurement using the set-up of sec. 3.4, 1.0km target.

This system was found to be very reliable with extremely high optical isolation of over 200 db. Because of the use of a single laser to provide both the transmitter and LO beams and the high isolation between the two, the dual AO modulators systems are very stable.

Figure (4.13) is a set of wind measurements using the dual AO modulators system with low magnification imaging receiver optics (see sec. 3.4) over the 1000 m path. Such receiver optics would eliminate any possible effect of the angle of arrival fluctuations. However, no noticeable change could be observed between the wind results of this system and the one with focusing receiver optics. This can be seen by comparing figure (4.13) with figures (4.11) and (4.12). The rate for which the correct direction of the wind could be predicted is the same for both systems. The level of the fluctuations of the measured wind about the mean is also more or less the same. However, these statistical fluctuations are essentially due to the speckle and short averaging time. Figures (4.14)-(4.16) clarify this point where the same set of data collected by using the system of section 3.3 is processed over 1.25, 2.5 and 10 seconds, respectively. The fluctuations about the mean ($\sqrt{(V_i-\bar{V})^2}$) for the example shown in these figures are about 1.24 m/s, 1.03 m/s and 0.39 m/s, respectively; showing that the statistical fluctuation is reduced by increasing the averaging time. The averaging times of ten seconds or even one minute are quite realistic for most applications, since the atmospheric winds do not vary much over such time intervals.

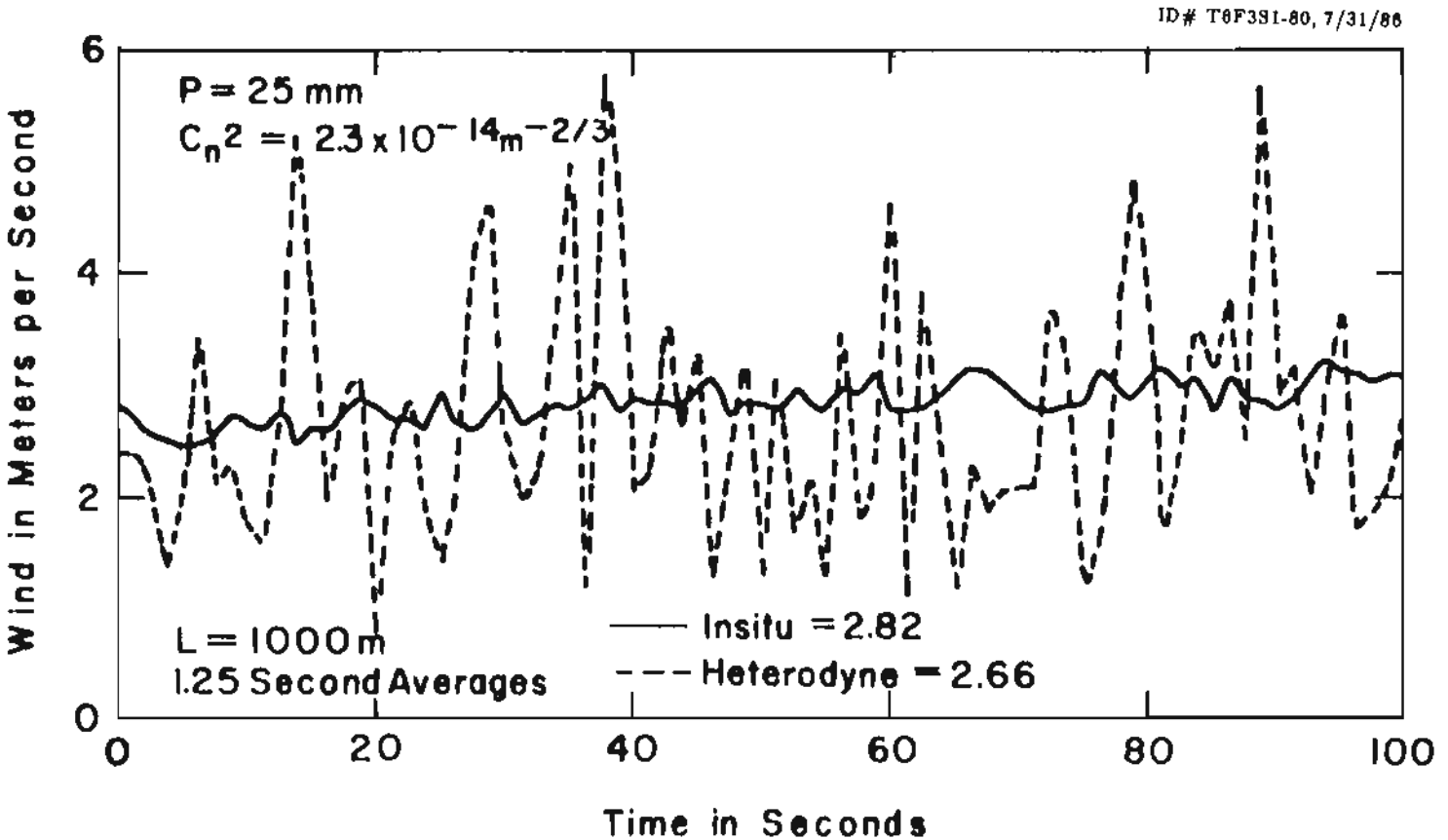

Figure 4.14 Wind measurement, ZLR processed, 1.25 second averages.

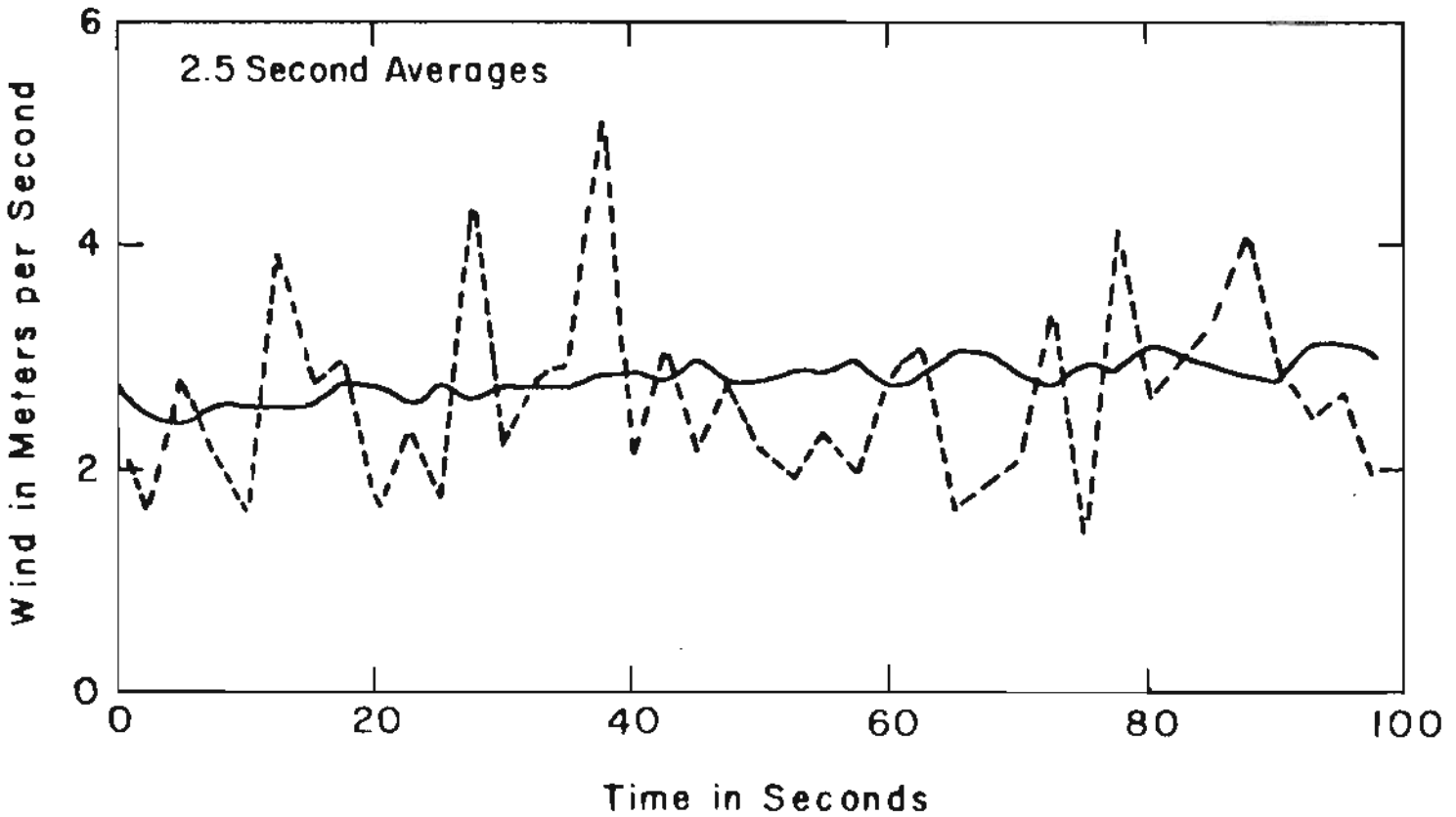

Figure 4.15 Wind measurement, ZLR processed, 2.5 second averages.

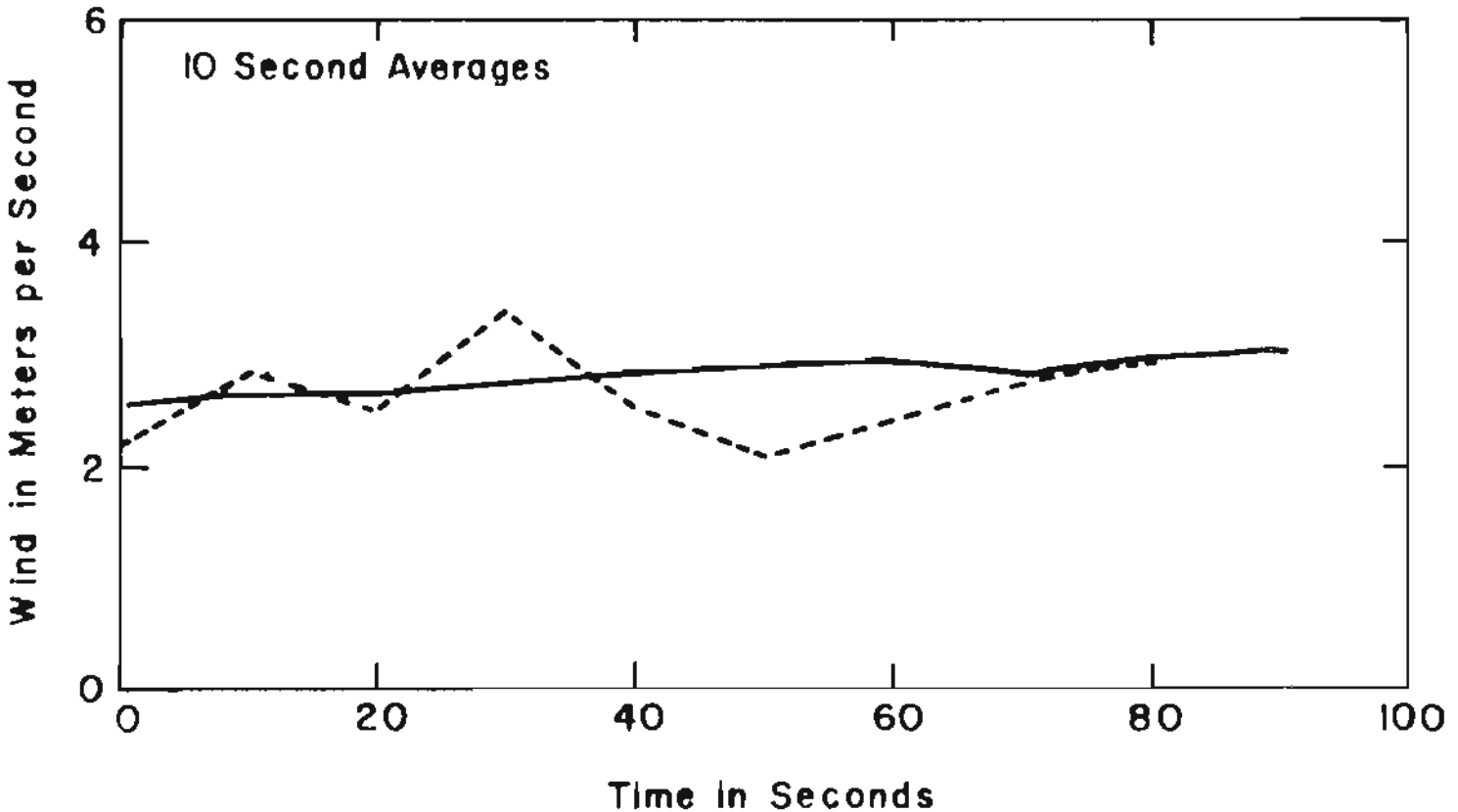

Figure 4.16 Wind measurement, ZLR processed, 10.0 second averages.

The fluctuations can also be reduced by using additional detectors and/or spatial averaging. Moreover, as will be demonstrated later in this section, the use of MMSE-ZLR and B-ZLR methods reduce the fluctuation due to speckle.

Some of the differences between the heterodyne measurements and the in situ data may be attributed to the difference in their wind weighting functions (WWF's). The Campbell unit which is a double ended sensor has a cosine-like WWF, while the heterodyne system utilizing the ZLR method of processing has a uniform WWF. Therefore, the nonuniform wind along the path is averaged differently by the two systems and results in a discrepancy between the two measurements.

An important consideration in using speckle-turbulence interaction for measuring crosswinds is operation at low turbulence levels. An estimate of the lower limit of the turbulence strength at which this type of system should operate can be made by considering Eq. (2.26). The slope of the T-D covariance curve at zero time delay given by Eq. (2.26) is directly proportional to C_n^2. Therefore as C_n^2 decreases the slope decreases and eventually a limit will be reached below which the system will not respond. Also, there are deterministic (as opposed to random) errors such as gain drifts for the two optical channels that do not average to zero. Consequently, it is doubtful that the system can measure the received intensity normalized by the mean to better than one-tenth of one percent. This translates to no more than four-tenths of one percent on the normalized slope. Using this lower limit for the slope in Eq. (2.26), it is found that

$$C_n^2 \geq \frac{1.741 \times 10^{-5} \lambda^2}{C_I(p,0) L p^{2/3} V_p} \tag{4.2}$$

It can be seen that as the wavelength decreases and the path length increases, the sensitivity improves. For the experimental systems under consideration with p=25 mm, with L=1000 m and V_p=1 m/s , Eq. (4.2) gives

$$C_n^2 \geq 3 \times 10^{-17} \ \ m^{-2/3} \tag{4.3}$$

The condition above covers all typical turbulence conditions. It is expected then, that the heterodyne system utilizing the speckle-turbulence interaction should provide good measurements at C_n^2 levels around ten times the level predicted by Eq. (4.3), *i.e.*, 3×10^{-16} $m^{-2/3}$.

Figure (4.17) demonstrates the sensitivity of the dual AO modulators experimental system, where a set of data corresponding to $C_n^2 = 6.5 \times 10^{-16}$ $m^{-2/3}$ is shown. The mean value of 1.64 m/s averaged over 100 seconds of data processed with the ZLR method is less than the mean value of 1.96 m/s measured by the Campbell unit. This reduction in mean value is believed to be indicative of the system just beginning to lose sensitivity.

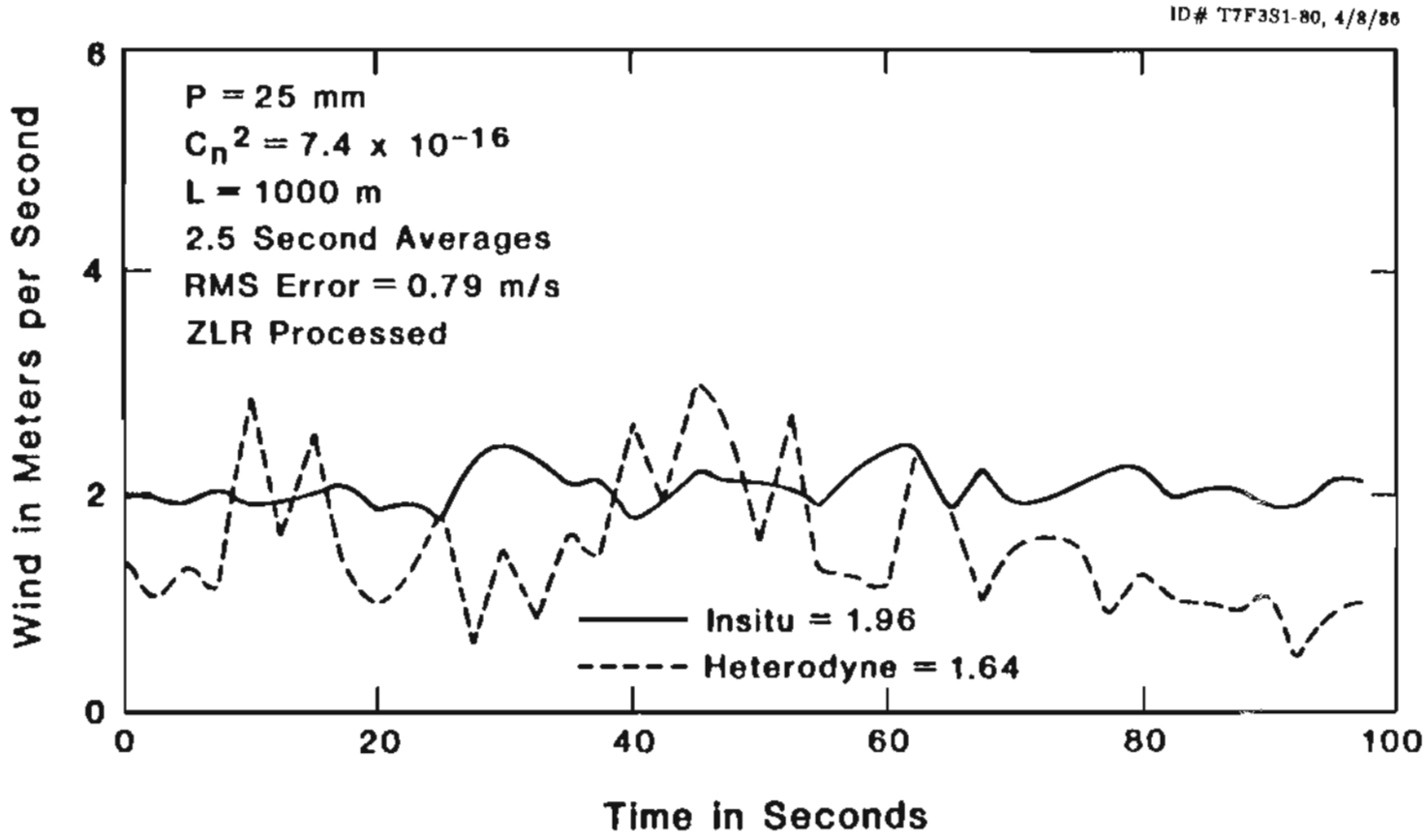

Figure 4.17 Low Turbulence Wind measurement, ZLR processed.

As noted earlier, the statistical fluctuation is reduced when MMSE-ZLR and B-ZLR methods are used to process the data. The RMS error of the results shown in figure (4.17) is 0.79 m/s and when the same set of data is processed using MMSE-ZLR method, the RMS error is reduced to 0.56 m/s. This is shown in figure (4.18) and it can be seen that the error in the mean is only slightly larger than that of the ZLR method (figure (4.17)).

The results of processing this data using B-ZLR method are shown in figure (4.19). There is a substantial reduction in error and fluctuation as compared to the results obtained by the ZLR technique. The mean error was only 0.15 m/s and the RMS error only 0.35 m/s. The reason why the B-ZLR method produces less fluctuation is not completely understood. However, SNR is unity due to the speckle, and consequently, the one bit resolution does not substantially affect the accuracy. Since the B-ZLR method only processes the mean crossings, it is effectively an FM processing method. This being the case, the amplitude fluctuations are ignored, and this may possibly be why the fluctuations of the measured wind about the mean are reduced.

The MMSE-ZLR method required more processing than the other two methods and its overall results were not any better. Also, processing the data using the binary data and the MMSE method did not show any improvement over the B-ZLR method. In addition, the B-ZLR method reduces the processing time and requires less complex processing instrumentation making it the most attractive method.

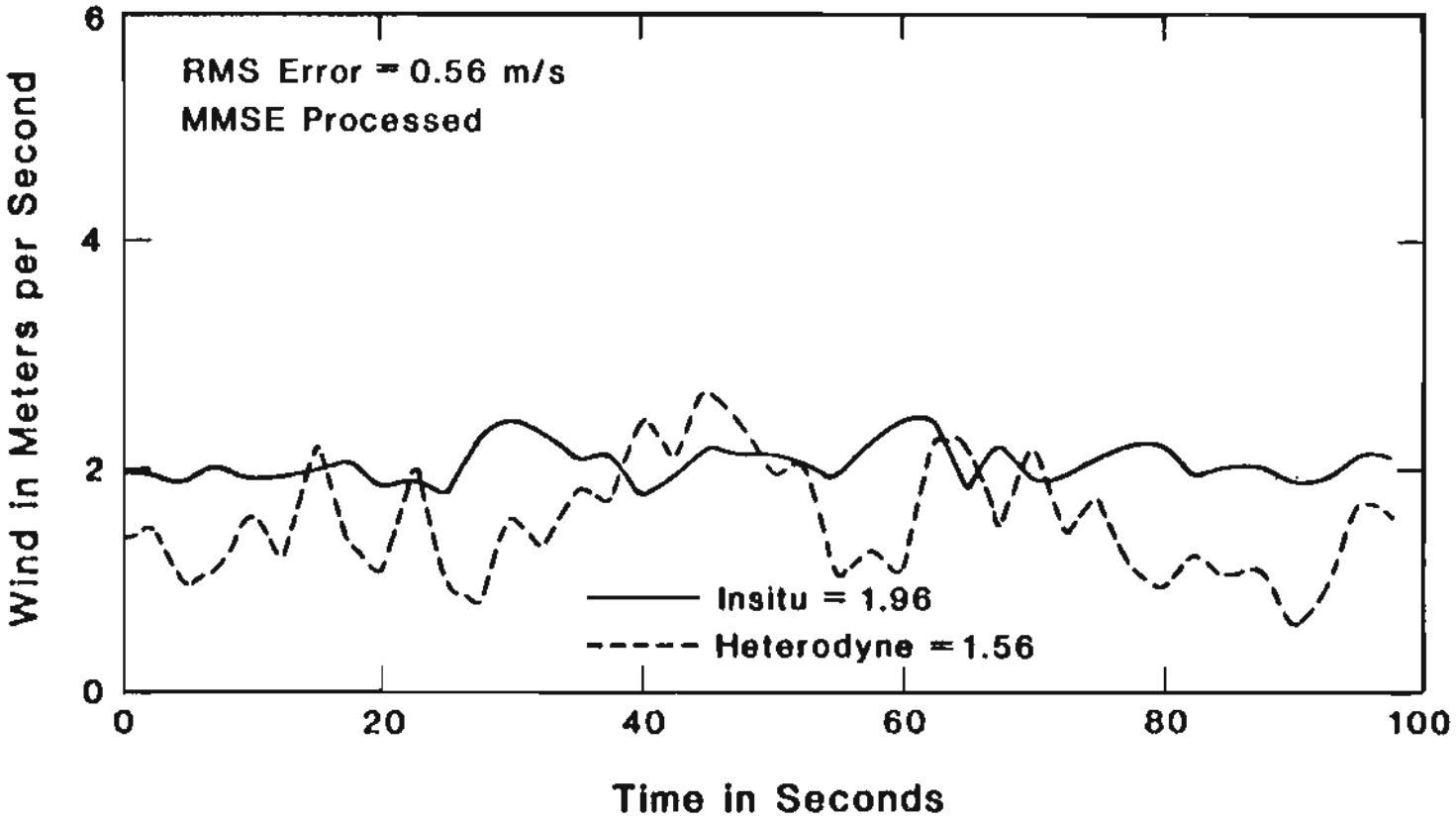

Figure 4.18 Low Turbulence Wind measurement, MMSE-ZLR processed.

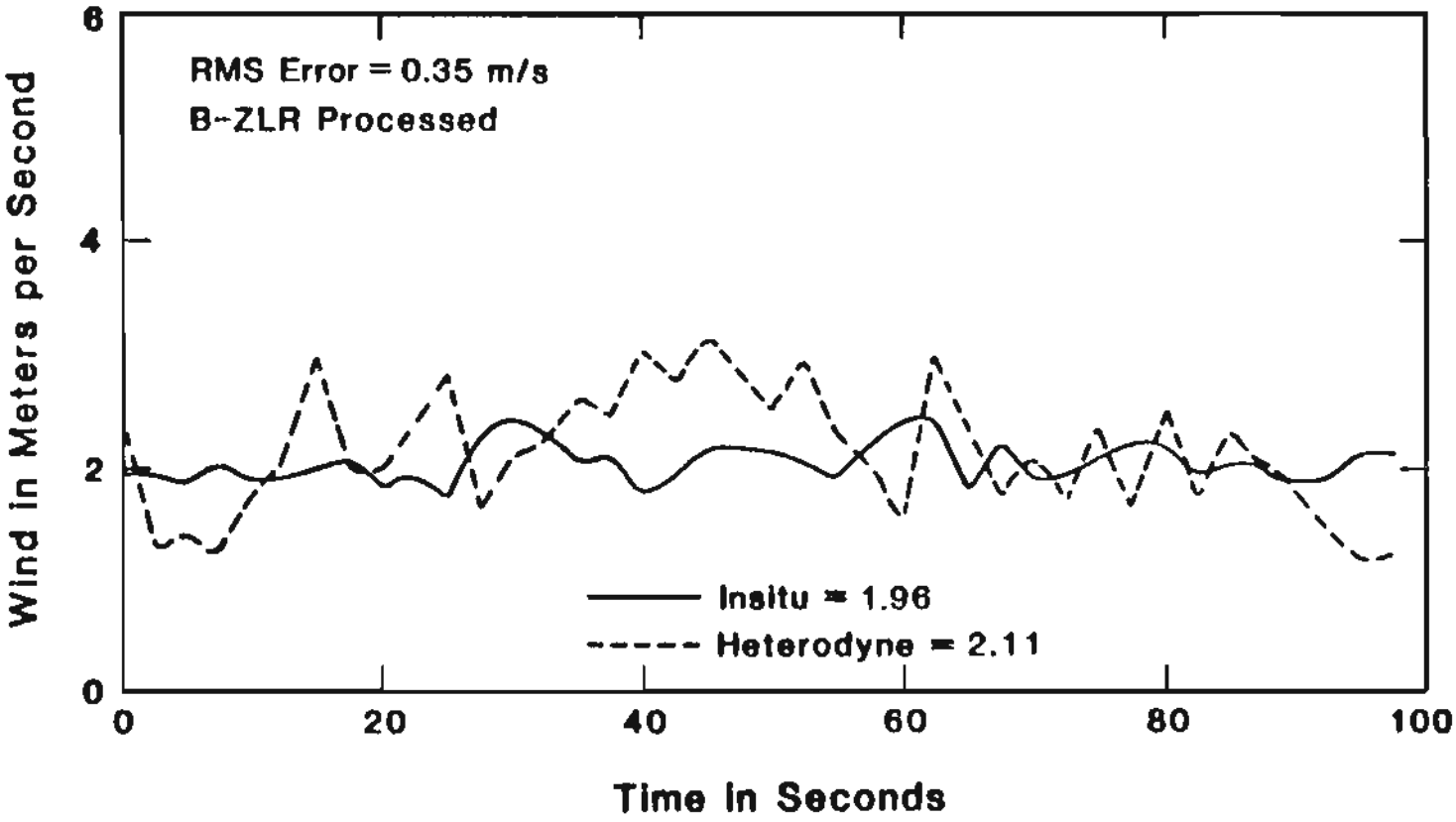

Figure 4.19 Low Turbulence Wind measurement, B-ZLR processed.

CHAPTER 5

ERROR ANALYSIS

The accuracy of the crosswind measurements is limited to the estimation error of the statistical parameters used. This is usually the case for the remote measurements of atmospheric parameters such as the turbulence strength and the concentration of molecular species, using the statistical and temporal properties of the return intensities. The reason is the temporal correlation of the returns induced by the turbulence[39–41,59,60]. The other sources of error are the detectors or the receivers noise, digitization error and finite dynamic range of the signals.

The statistical parameters required for the remote sensing of crosswinds must be estimated by a finite number of samples. The accuracy of these estimations are limited by the constraints on the duration of the measurements and the number of samples.

The Root-Mean-Square (RMS) error associated with the statistical parameters have been derived using the independent paths jointly gaussian formulations. The analytical results are presented for various atmospheric, system and processing parameters. The effect of the estimation errors on the wind measurements is demonstrated and shown that the measurements can be optimized by selecting proper spacing between the detectors and time

delay between the samples of intensity. The most general versions of the computer source programs used to generate the results presented in this chapter are listed in appendix D.

5.1 Mean Intensity

The mean of the return intensity is the normalizing factor of the other statistical parameters. The sample mean intensity is simply obtained by averaging individual intensity samples

$$I_s=\frac{1}{N}\sum_{n=1}^{N} I(nT) \tag{5.1}$$

where I denotes the return intensity and T is the sampling period. The mean square (MS) error is given by

$$\begin{aligned}\sigma_{I_s}^2&=<I_s^2>-<I_s>^2\\&=\frac{1}{N^2}\sum_{m=1}^{N}\sum_{n=1}^{N}<I(nT)I(mT)>-\left[\frac{1}{N}\sum_{n=1}^{N}<I(nT)>\right]^2\end{aligned} \tag{5.2}$$

The MS error can be written in terms of the autocovariance of the intensity as

$$\sigma_{I_s}^2=\frac{1}{N^2}\sum_{m=1}^{N}\sum_{n=1}^{N}C_I(0,(n-m)T)=\frac{1}{N^2}\sum_{k=-(N-1)}^{N-1}(N-|k|)C_I(0,kT) \tag{5.3}$$

Making use of the jointly gaussian formulation given by Eq. (2.14), the nor-

malized RMS error is obtained.

$$\frac{\sigma_{I_s}}{<I>} = \left[\frac{1}{N^2} \sum_{k=-(N-1)}^{N-1} (N-|k|) \exp\left(-\frac{32}{3\rho_0^{5/3}} |VkT|^{5/3} \right) \right]^{1/2} \qquad (5.4)$$

The expression above is plotted in figure (5.1) for different turbulence strengths as a function of the total number of samples. It should be remembered that the complete theory must be applied for higher path integrated turbulence[26] (see section 2.1). However, in this case the error analysis of second order statistics of intensity is probably impossible.

The results of figure (5.1) is shown for a sampling period of 0.5 msec and uniform wind velocity of 5 m/s over 1000 m path. As can be seen, due to correlation between the samples the RMS error deviates from $1/\sqrt{N}$ behavior and the error decreases as the total averaging time increases. It should be noted that, for sampling periods much longer than the turbulence coherence time (τ_c), the samples become independent from each other and the RMS error decreases as $1/\sqrt{N}$. This is demonstrated in figure (5.2), where the RMS errors corresponding with different sampling periods are compared to $1/\sqrt{N}$.

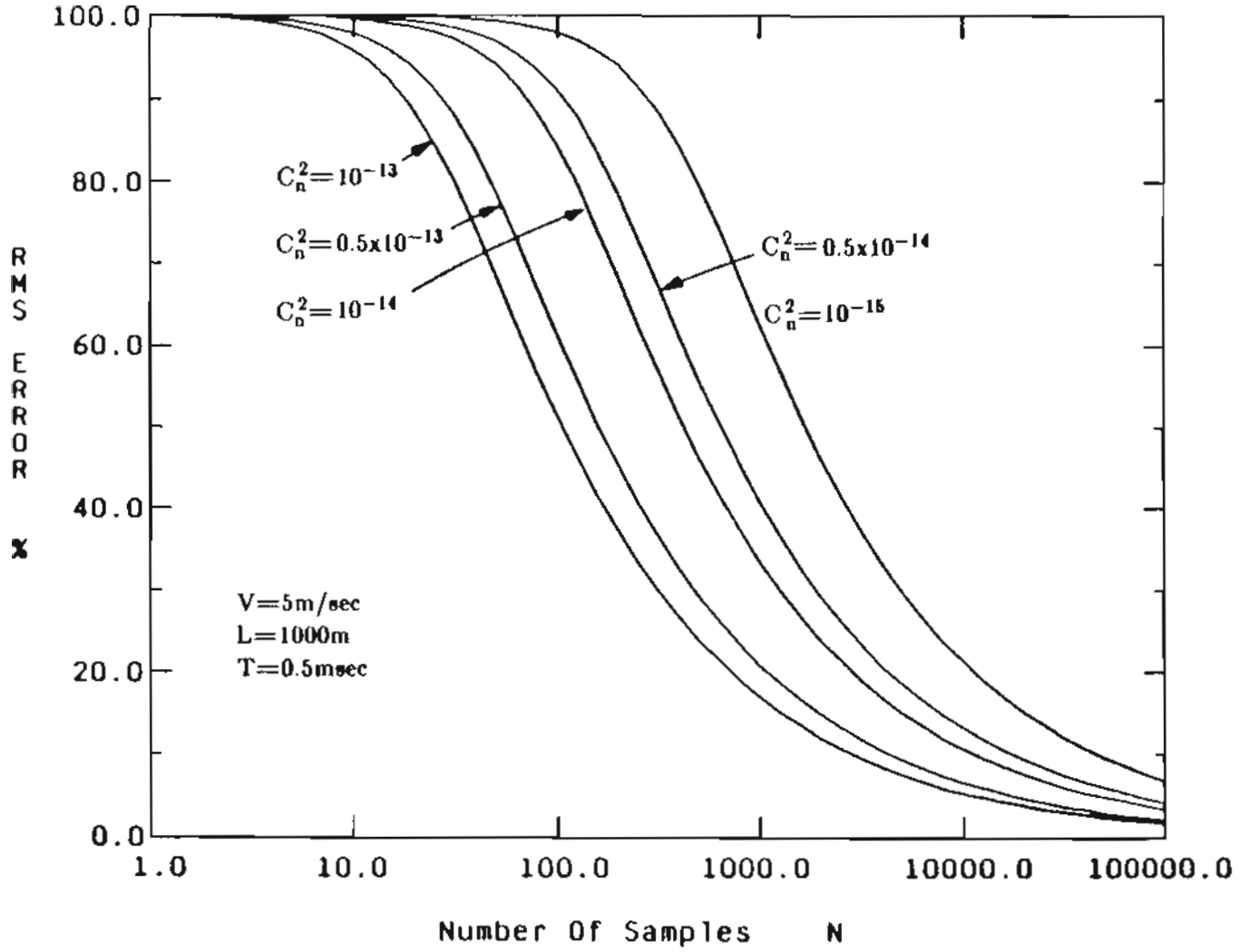

Figure 5.1 RMS error of sample mean intensity for various turbulence strengths.

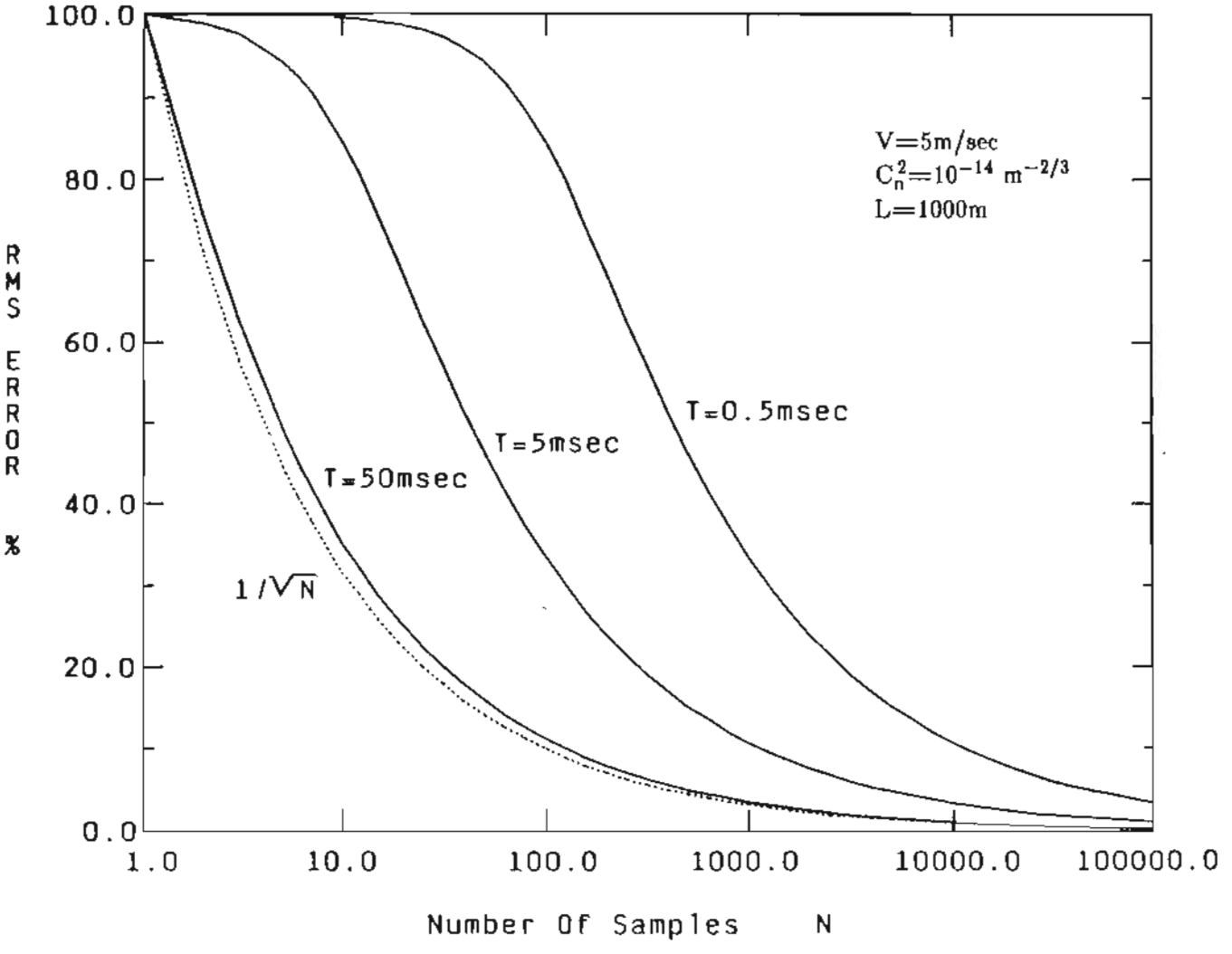

Figure 5.2 RMS error of sample mean iotensity for different sampling periods.

5.2 Variance

The sample variance of intensity can be formulated as

$$\sigma_s^2 = \frac{1}{N}\sum_{n=1}^{N} I^2(nT) - \left[\frac{1}{N}\sum_{n=1}^{N} I(nT)\right]^2 \tag{5.5}$$

Its corresponding normalized mean square error is defined by

$$\sigma_s^2 \text{ MS error} = \frac{<(\sigma_s^2-\sigma_I^2)^2>}{(\sigma_I^2)^2} = \frac{<(\sigma_s^2)^2>}{(\sigma_I^2)^2} - \frac{2<\sigma_s^2>}{\sigma_I^2} + 1 \tag{5.6}$$

Using the properties of the jointly gaussian fields in Eq. (5.5), the first and second moments of sample variance can be obtained. The mean of the sample variance is given by

$$\begin{aligned} <\sigma_s^2> &= \frac{1}{N}\sum_{n=1}^{N} <I^2(nT)> - \frac{1}{N^2}\sum_{m=1}^{N}\sum_{n=1}^{N} <I(nT)I(mT)> \\ &= <I>^2 - \frac{1}{N^2}\sum_{k=-(N-1)}^{N-1} (N-|k|)C_I(0,kT) \end{aligned} \tag{5.7}$$

The mean square of sample variance can be written as follows

$$\begin{aligned} <(\sigma_s^2)^2> &= \frac{1}{N^2}\sum_{m=1}^{N}\sum_{n=1}^{N} <I^2(nT)I^2(mT)> - \frac{2}{N^3}\sum_{j=1}^{N}\sum_{m=1}^{N}\sum_{n=1}^{N} <I^2(nT)I(mT)I(jT)> \\ &+ \frac{1}{N^4}\sum_{i=1}^{N}\sum_{j=1}^{N}\sum_{m=1}^{N}\sum_{n=1}^{N} <I(nT)I(mT)I(jT)I(iT)> \end{aligned} \tag{5.8}$$

The following equality for the fourth order moment of intensity exists when the fields are jointly gaussian.

$$<I_1I_2I_3I_4> = <I>^4 + <I>^2 \left(\Gamma_{12}^2+\Gamma_{23}^2+\Gamma_{34}^2+\Gamma_{41}^2+\Gamma_{24}^2+\Gamma_{13}^2\right)$$

$$+2<I> \left(\Gamma_{12}\Gamma_{23}\Gamma_{31}+\Gamma_{12}\Gamma_{41}\Gamma_{24}+\Gamma_{23}\Gamma_{34}\Gamma_{24}+\Gamma_{31}\Gamma_{41}\Gamma_{34}\right)$$

$$+2 \left(\Gamma_{12}\Gamma_{23}\Gamma_{34}\Gamma_{41}+\Gamma_{12}\Gamma_{24}\Gamma_{34}\Gamma_{31}+\Gamma_{41}\Gamma_{23}\Gamma_{24}\Gamma_{31}\right)$$

$$+\Gamma_{12}^2\Gamma_{34}^2+\Gamma_{13}^2\Gamma_{24}^2+\Gamma_{14}^2\Gamma_{23}^2 \qquad (5.9)$$

where $\Gamma_{ij} = <U_iU_j^*>$ is the mutual intensity function. Using Eq. (5.9) in Eq. (5.8), and substituting its result along with Eq. (5.7) in Eq. (5.6) and performing the algebra, the normalized MS error of the sample variance is obtained.

$$\sigma_s^2 \text{ MS error} = \frac{6}{N^2} + \left(\frac{4}{N^2}+\frac{6}{N^3}\right) \sum_{k=-(N-1)}^{N-1} (N-|k|)\Gamma_N^2(0,kT)$$

$$+\frac{4}{N^2} \sum_{k=-(N-1)}^{N-1} (N-|k|)\Gamma_N^4(0,kT) + \frac{3}{N^4} \left[\sum_{k=-(N-1)}^{N-1} (N-|k|)\Gamma_N^2(0,kT)\right]^2$$

$$-\frac{8}{N^3} \sum_{j=1}^{N}\sum_{m=1}^{N}\sum_{n=1}^{N} \left[\Gamma_N(0,(n-m)T)\Gamma_N(0,(m-j)T)\Gamma_N(0,(j-n)T)\right.$$

$$\left.+\Gamma_N^2(0,(n-m)T)\Gamma_N^2(0,(m-j)T)\right] + \frac{6}{N^4} \sum_{i=1}^{N}\sum_{j=1}^{N}\sum_{m=1}^{N}\sum_{n=1}^{N}$$

$$\Gamma_N(0,(n-m)T)\Gamma_N(0,(m-j)T)\Gamma_N(0,(j-i)T)\Gamma_N(0,(i-n)T) \qquad (5.10)$$

where the normalized mutual intensity Γ_N is defined as $\Gamma/<I>$.

The numerical evaluation of the expression above can be quite time consuming for large values of N, because of the triple and quadruple

summations. However, considerable simplification can be achieved when the number of samples is very large. Let N′ be the number of samples for which

$$\Gamma_N(0,nT) \ll 1 \qquad \text{for} \qquad n \geq N' \tag{5.11}$$

Then the order of magnitude of each term as appear in Eq. (5.10) can be listed as

$$\frac{1}{N^2} \qquad (\frac{N'}{N}+\frac{N'}{N^2}) \qquad (\frac{N'}{N}) \qquad (\frac{N'}{N})^2 \qquad (\frac{N'}{N})^2 \qquad (\frac{N'}{N})^3$$

Neglecting the terms with $(N'/N)^2$ and $(N'/N)^3$ orders of magnitude, in addition to $1/N^2$ and N'/N^2 terms, Eq. (5.10) simplifies to

$$\sigma_s^2 \text{ MS error} \simeq \frac{4}{N^2} \sum_{k=-(N-1)}^{N-1} (N-|k|) \left(C_{I_N}(0,kT)+C_{I_N}^2(0,kT)\right)$$

$$\text{for} \qquad N >> N' \tag{5.12}$$

where $\Gamma_N^2(0,kT)$ is replaced by $C_{I_N}(0,kT)$. The normalized RMS error for the sample variance have been numerically evaluated using Eqs. (5.10) and (5.12) and the result is plotted in figure (5.2) versus number of samples. It should be noted that the inequality of Eq. (5.11) holds when $N' >> \tau_c/T$.

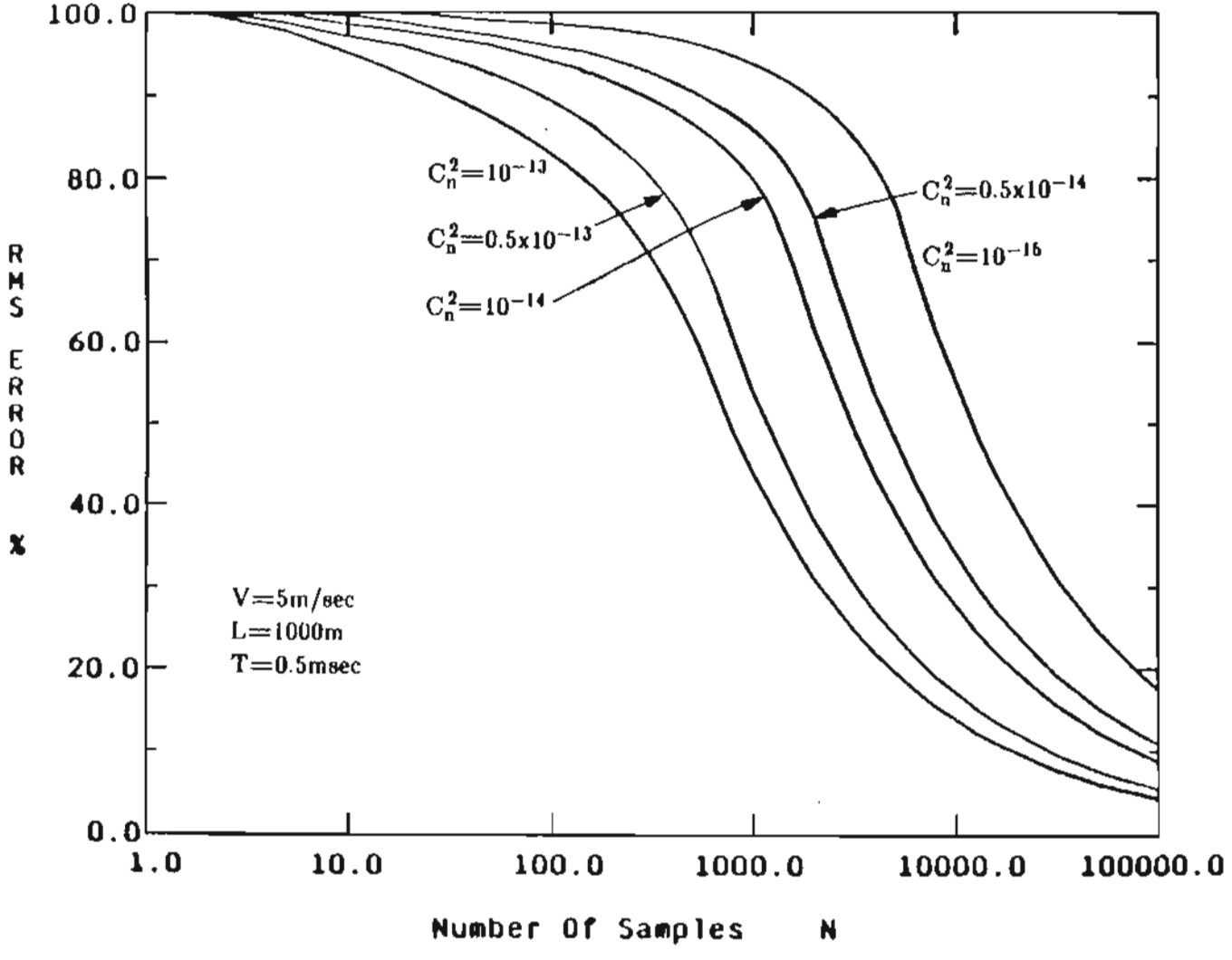

Figure 5.3 RMS error of sample variance for various turbulence strengths.

5.3 Time-Delayed Covariance

The formulations of the previous section is now extended to derive the RMS error for the sample T-D covariance for which the variance is a special case. The sample T-D covariance and its associated mean square error are given by the following expressions

$$C_s(p,\tau)=\frac{1}{N}\sum_{n=1}^{N} I(p_1,nT)I(p_2,nT+\tau)-\frac{1}{N^2}\sum_{m=1}^{N}\sum_{n=1}^{N} I(p_1,nT)I(p_2,mT+\tau) \quad (5.13)$$

and

$$C_s(p,\tau)\text{ MS error } = \frac{<\left(C_s(p,\tau)-C_I(p,\tau)\right)^2>}{C_I^2(p,\tau)}$$

$$=\frac{<C_s^2(p,\tau)>}{C_I^2(p,\tau)}-\frac{2<C_s(p,\tau)>}{C_I(p,\tau)}+1 \quad (5.14)$$

From Eq. (5.13), the mean of the sample T-D covariance can be obtained.

$$<C_s(p,\tau)>=C_I(p,\tau)-\frac{1}{N^2}\sum_{k=-(N-1)}^{N-1}(N-|k|)C_I(p,kT+\tau) \quad (5.15)$$

The mean square of the sample T-D covariance is equal to

$$<C_s^2(p,\tau)>=\frac{1}{N^2}\sum_{m=1}^{N}\sum_{n=1}^{N}<I(p_1,nT)I(p_2,nT+\tau)I(p_1,mT)I(p_2,mT+\tau)>$$

$$-\frac{2}{N^3}\sum_{j=1}^{N}\sum_{m=1}^{N}\sum_{n=1}^{N}<I(p_1,nT)I(p_2,nT+\tau)I(p_1,mT)I(p_2,jT+\tau)>$$

$$+\frac{1}{N^4}\sum_{i=1}^{N}\sum_{j=1}^{N}\sum_{m=1}^{N}\sum_{n=1}^{N}<I(p_1,nT)I(p_2,mT+\tau)I(p_1,jT)I(p_2,iT+\tau)> \quad (5.16)$$

Using the equality of Eq. (5.9), Eq. (5.16) can be evaluated in terms of the mutual intensity function.

$$
\begin{aligned}
<C_s^2(p,\tau)> = C_j^2(p,\tau) + \frac{1}{N^2}\sum_{k=-(N-1)}^{N-1}(N-|k|) \\
&\Big[\Big(\Gamma(p,kT+\tau)\Gamma(p,-kT+\tau)+\Gamma^2(0,kT)\Big)^2+2\Gamma^2(p,\tau) \\
&\Big(\Gamma(p,kT+\tau)\Gamma(p,-kT+\tau)+\Gamma^2(0,kT)-\Gamma^2(p,kT+\tau)\Big)\Big] \\
&+\frac{2}{N^4}\left[\sum_{k=-(N-1)}^{N-1}(N-|k|)\Gamma^2(p,kT+\tau)\right]^2 \\
&+\frac{1}{N^4}\left[\sum_{k=-(N-1)}^{N-1}(N-|k|)\Gamma^2(0,kT)\right]^2+\frac{1}{N^3}\sum_{j=1}^{N}\sum_{m=1}^{N}\sum_{n=1}^{N} \\
&\Big[\Gamma(0,(n-m)T)\Gamma(0,(j-n)T)+\Gamma(p,(n-m)T+\tau)\Gamma(p,(j-n)T+\tau)\Big]^2 \\
&+\frac{2}{N^3}\Gamma(p,\tau)\sum_{j=1}^{N}\sum_{m=1}^{N}\sum_{n=1}^{N}\Gamma(p,(j-m)T+\tau) \\
&\Big[\Gamma(0,(n-m)T)\Gamma(0,(j-n)T)+\Gamma(p,(n-m)T+\tau)\Gamma(p,(j-n)T+\tau)\Big] \\
&+\frac{2}{N^4}\sum_{i=1}^{N}\sum_{j=1}^{N}\sum_{m=1}^{N}\sum_{n=1}^{N} \\
&\Big[\Gamma(p,(m-n)T+\tau)\Gamma(p,(m-j)T+\tau)\Gamma(p,(i-j)T)\Gamma(p,(i-n)T)+ \\
&\Gamma(0,(m-i)T)\Gamma(0,(n-j)T)\Gamma(p,(i-j)T+\tau)\Gamma(p,(m-n)T+\tau)+ \\
&\Gamma(0,(n-j)T)\Gamma(p,(m-i)T)\Gamma(p,(i-n)T+\tau)\Gamma(p,(m-j)T+\tau)\Big] \qquad (5.17)
\end{aligned}
$$

Substituting Eqs. (5.15) and (5.17) in Eq. (5.14) gives the normalized MS error for the sample T-D covariance. However, a great deal of simplification can be achieved for large number of samples as described in previous section. The simplified result is given below.

$$C_s(p,\tau) \text{ MS error} \simeq \frac{1}{N^2} \sum_{k=-(N-1)}^{N-1} (N-|k|)(A^2+2A) \quad \text{for} \quad N >> N' \tag{5.18}$$

where

$$A = \left[\Gamma_N(p,kT+\tau)\Gamma_N(p,-kT+\tau)+\Gamma_N^2(0,kT)\right]/\Gamma_N^2(p,\tau) \tag{5.19}$$

It should be noted that the time-delay τ is assumed to be much smaller than the measurement time, *i.e.*, $\tau << NT$. Eq. (5.18) reduces to MS error of sample variance given by Eq. (5.12) by setting $p=\tau=0$. The normalized MS error for the sample covariance and autocovariance can be obtained from Eq. (5.18) by setting τ and p equal to zero, respectively.

The results of Eq. (5.18) are shown in figures (5.3)-(5.6). Figure (5.3) shows the normalized RMS error of the sample covariance for various turbulence strengths versus the number of samples. As can be seen, the error can be quite substantial for weaker turbulence levels. The error of the sample autocovariance is plotted in figure (5.4), showing an increase in error with the time delay.

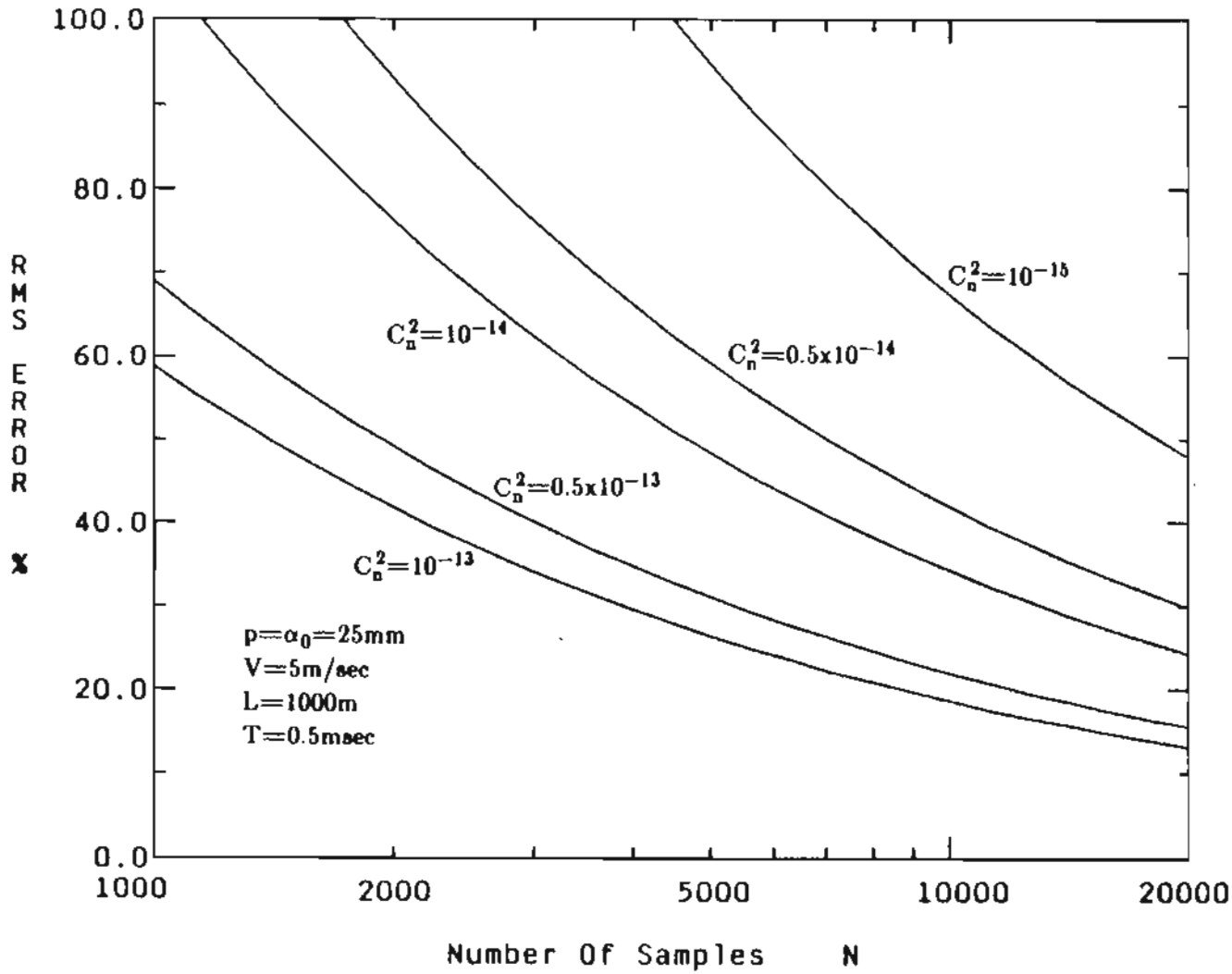

Figure 5.4 RMS error of sample covariance for various turbulence strengths.

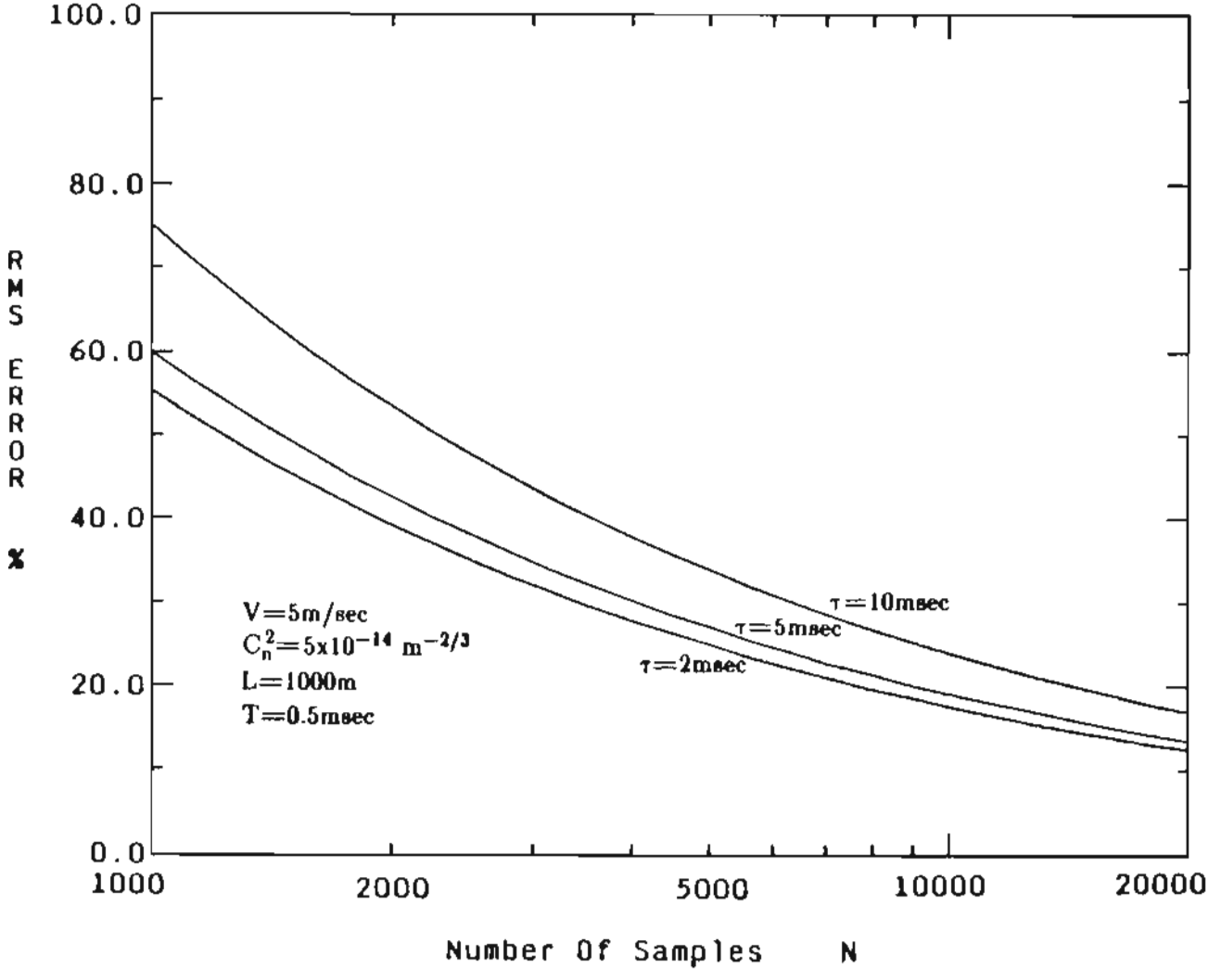

Figure 5.5 RMS error of sample autocovariance with different time delays.

Figure (5.5) shows the normalized RMS error for the sample T-D covariance as a function of time delay for three different averaging times. A moderate turbulence level of $C_N^2=5x10^{-14}$ $m^{-2/3}$ is used with a wind velocity of 5 m/s for the results of figure (5.5). It can be seen that the error is minimum at the time delay for which T-D covariance curve peaks, *i.e.*, at $\tau_p=p/2V$.

It is obvious that longer averaging times produces smaller estimation errors. However, given the averaging time, fewer number of samples can be used to achieve the same level of accuracy as long as the sampling period is smaller than the turbulence coherence time. This is shown in figure (5.6) where the error associated with the sample covariance is plotted as a function of sampling period for several averaging times. For the atmospheric parameters used in figure (5.6), the turbulence coherence time τ_c (e^{-1} point) is about 12 msec.

Figure (5.6) shows that the error remains almost constant for sampling periods smaller than τ_c and as the sampling period increases beyond τ_c, the normalized RMS error increases approaching $1/\sqrt{N}$ behavior for the longer averaging times. The use of fewer number of samples can reduce the processing time and simplify the processing instrumentation.

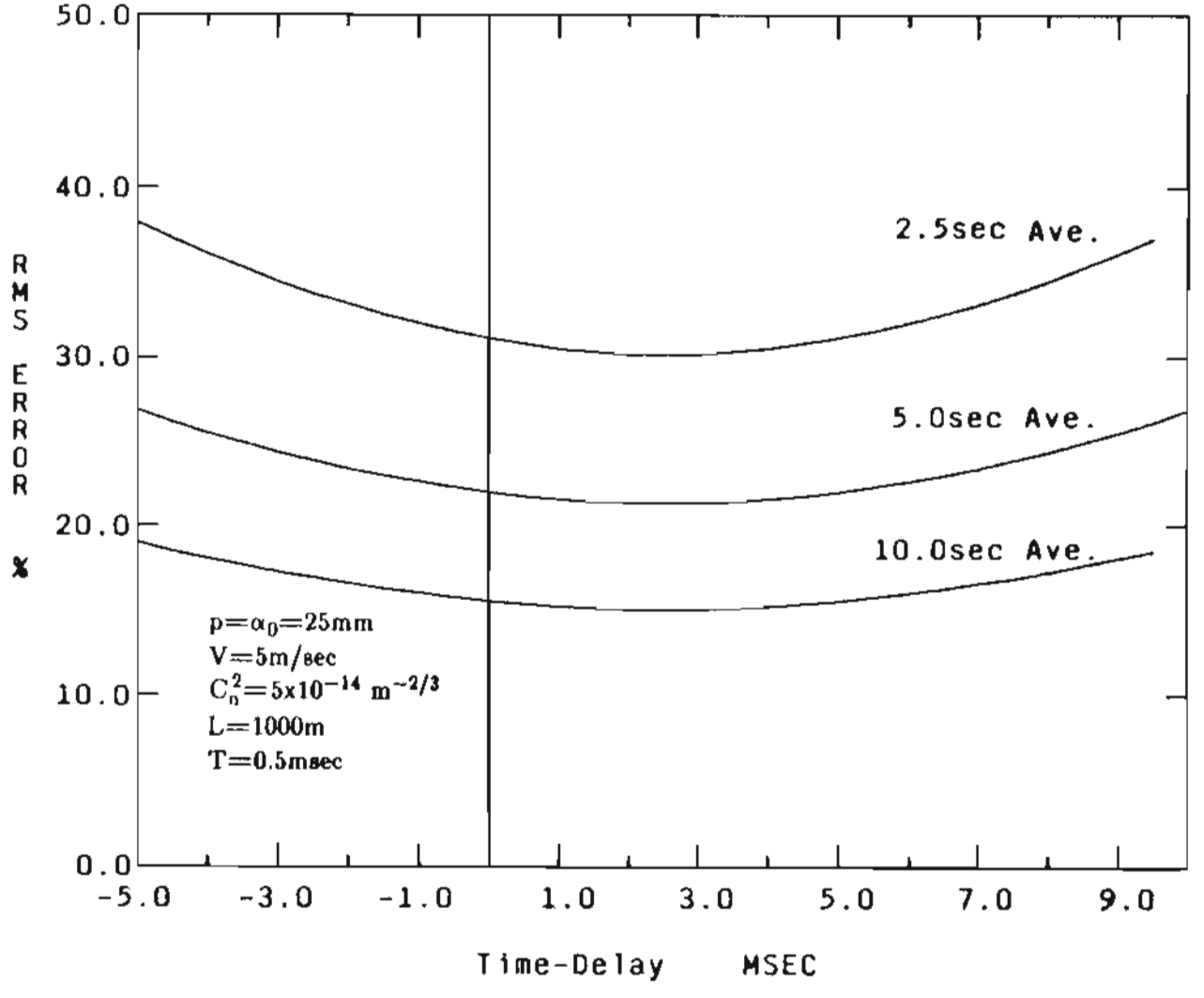

Figure 5.6 RMS error of sample T-D covariance as a function of time delay.

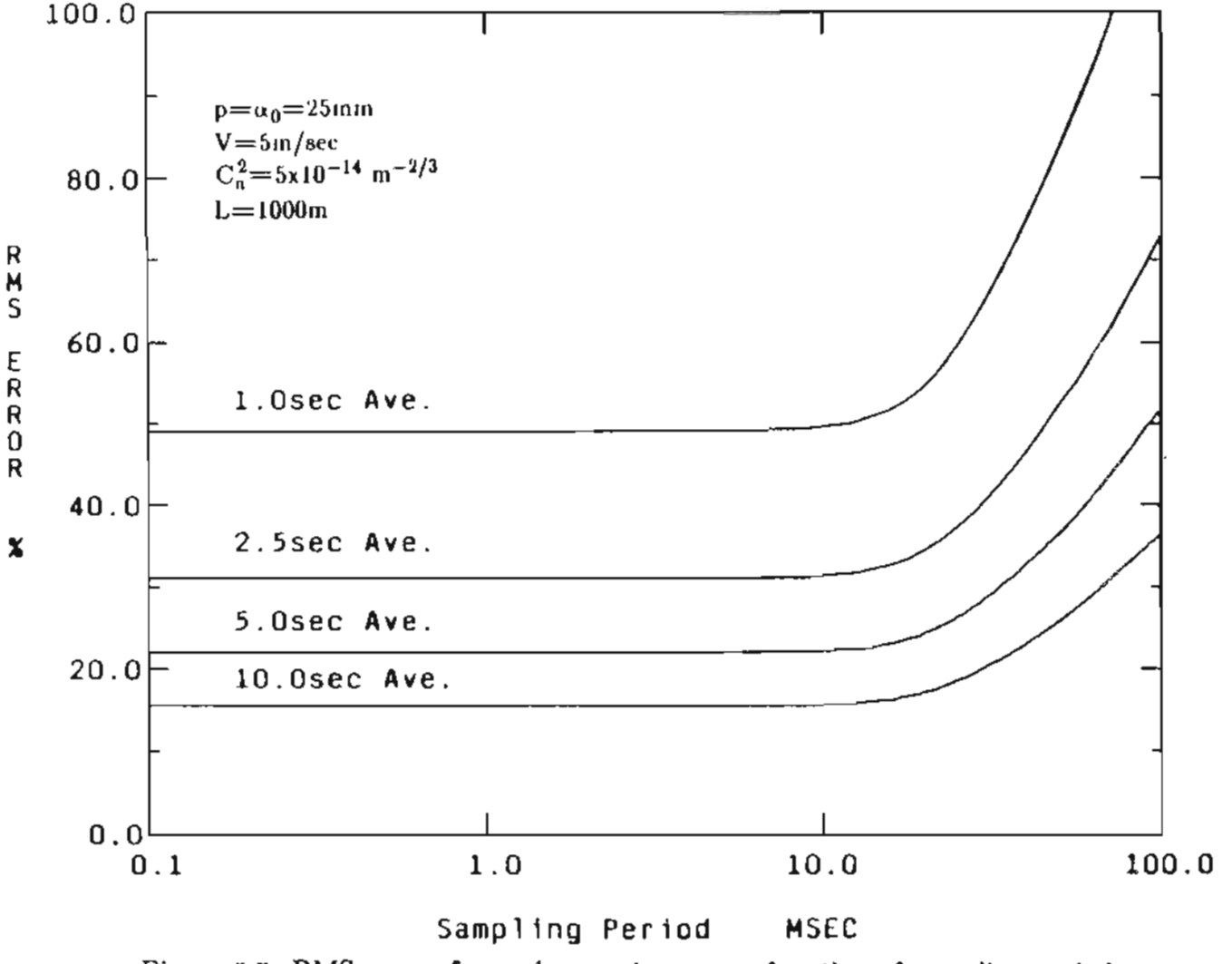

Figure 5.7 RMS error of sample covariance as a function of sampling period.

5.4 Slope Of The Time-Delayed Covariance Curve

The determination of the slope of the T-D covariance curve at zero time delay is of great importance for remote sensing of the atmospheric crosswinds and turbulence strength (see sec. 2.2). Let us write the sample slope of the T-D covariance as

$$S_s = \frac{C_s(p,\tau) - C_s(p,-\tau)}{2\tau} \tag{5.20}$$

The normalized MS error of the sample slope is equal to

$$S_s \text{ MS error} = \frac{<(S_s - S_I)^2>}{S_I^2} = \frac{<S_s^2>}{S_I^2} - \frac{2<S_s>}{S_I} + 1 \tag{5.21}$$

Using Eq. (5.15) in Eq. (5.20), the mean sample slope can simply be written as

$$<S_s> = S_I - \frac{1}{N^2} \sum_{k=-(N-1)}^{N-1} (N - |k|) \left(C_I(p, kT+\tau) - C_I(p, kT-\tau) \right) / 2\tau \tag{5.22}$$

The mean square of the sample slope can be written in terms of the sample T-D covariance function as

$$<S_s^2> = \frac{1}{4\tau^2} \left(<C_s^2(p,\tau)> + <C_s^2(p,-\tau)> - 2<C_s(p,\tau)C_s(p,-\tau)> \right) \tag{5.23}$$

In the expression above, the mean square of the sample T-D covariances have already been evaluated and given by Eq. (5.17) and the cross correlation term can be obtained similarly. Using the large number of samples

approximation, the normalized MS error can be written as

$$S_s \text{ MS error} \simeq \frac{1}{N^2\left(\Gamma_N^2(p,\tau)-\Gamma_N^2(p,-\tau)\right)} \sum_{k=-(N-1)}^{N-1} (N-|k|)$$

$$\left(A^2+B^2-2C^2+2\Gamma_N^2(p,\tau)A+2\Gamma_N^2(p,-\tau)B\right.$$

$$\left.-4\Gamma_N(p,\tau)\Gamma_N(p,-\tau)C\right) \quad \text{for} \quad N >> N' \tag{5.24}$$

where A is given by Eq. (5.19),

$$B=\left[\Gamma_N(p,kT-\tau)\Gamma_N(p,-kT-\tau)+\Gamma_N^2(0,kT)\right]/\Gamma_N^2(p,-\tau) \tag{5.25}$$

and

$$C=\left[\Gamma_N(p,kT)\Gamma_N(p,-kT)+\Gamma_N(0,kT-\tau)\Gamma_N(0,kT+\tau)\right]/\Gamma_N(p,\tau)\Gamma_N(p,-\tau) \tag{5.26}$$

The square root of Eq. (5.24) is plotted as a function of the number of samples in figure (5.7) for three different time delays and typical atmospheric and system parameters. Because of the correlation between the sample T-D covariances, the RMS error for the slope is considerably smaller than that of the T-D covariances and as τ decreases the corresponding error decreases.

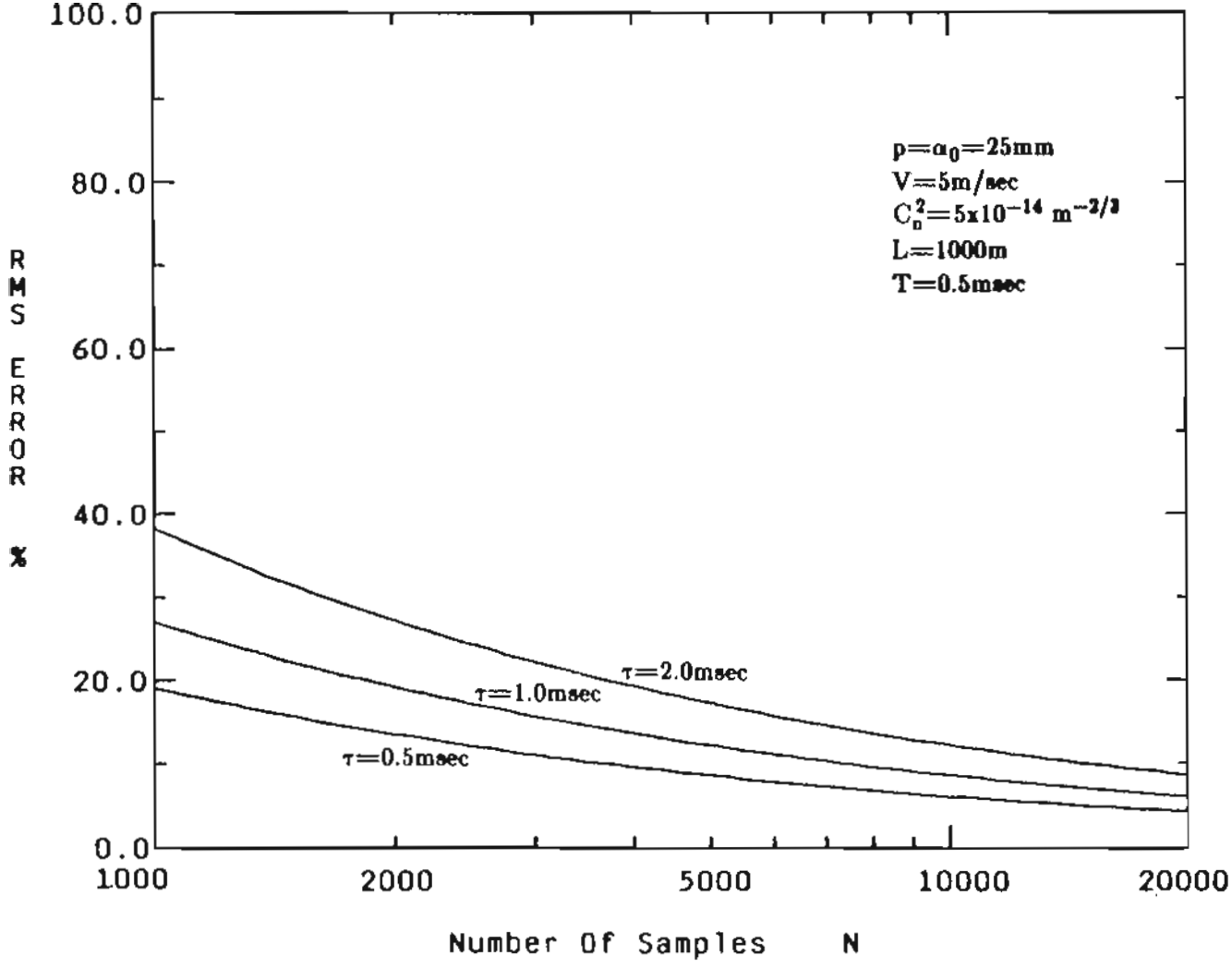

Figure 5.8 RMS error of sample slope for three different time delays.

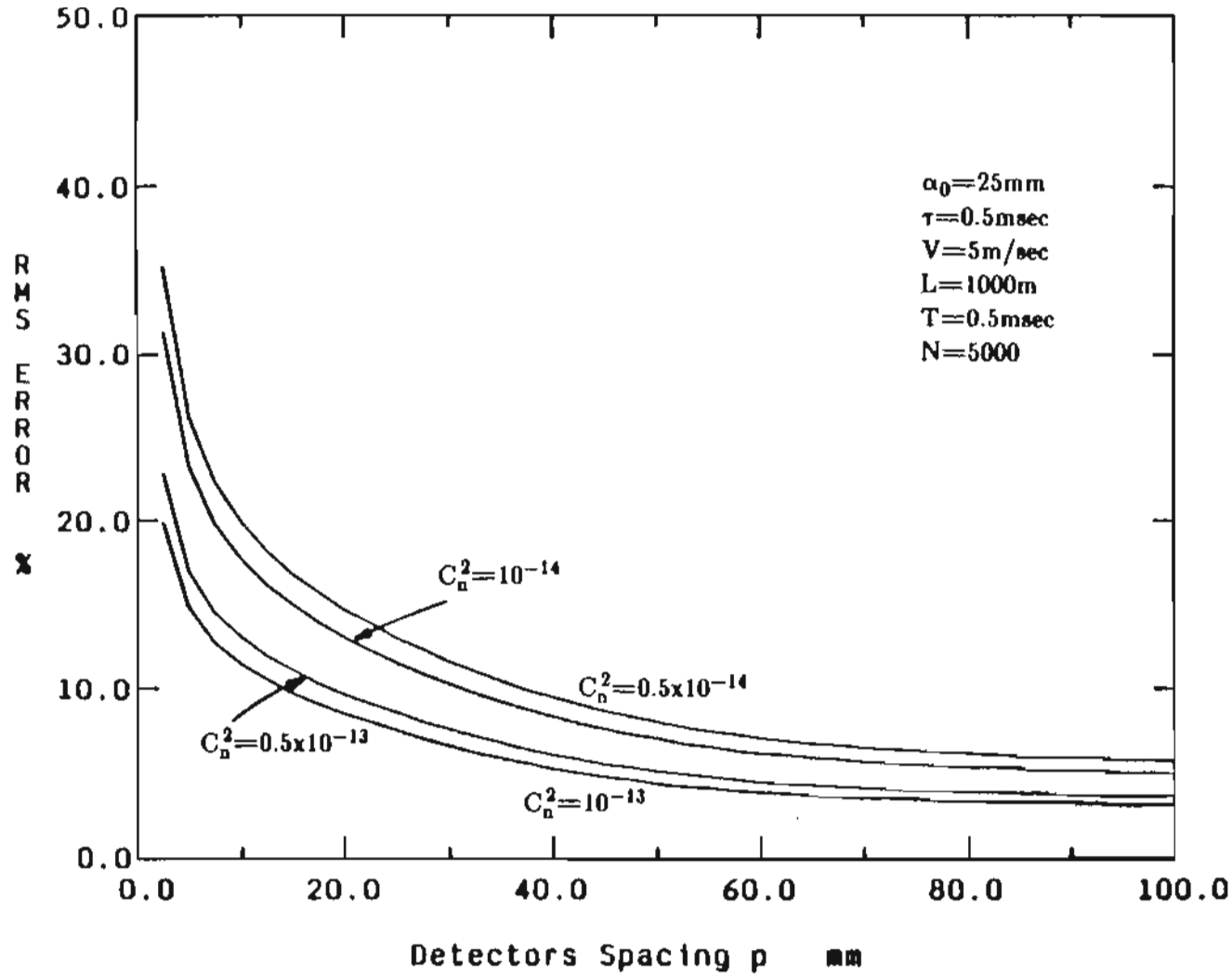

Figure 5.9 RMS error of sample slope as a function of detectors spacing.

The normalized RMS error of the slope is shown in figure (5.8) for various turbulence strengths as a function of the detectors spacing. Figure (5.8) shows that the error decreases with the detectors spacing before starting to level off at about 40 mm. It will be shown in the next section that further increase in the spacing between the detectors makes the estimation of the wind velocity more difficult.

5.5 Wind Velocity

The primary technique used for determining the magnitude of the wind velocity is the ZLR method of processing. The sample wind velocity using this method can be written as

$$V_s=(3/8)^{3/5}\frac{p}{|\tau|}\left(\frac{\ln C_{N_s}(0,\tau)}{\ln\left(e^{p^2/2\alpha\tilde{\delta}}C_{N_s}(p,0)\right)}\right)^{3/5} \tag{5.27}$$

The normalized RMS error associated with the sample wind is given by

$$\frac{<(V_s-V)^2>}{V^2}=\frac{<\left(f(X_s,Y_s)-f(X,Y)\right)^2>}{f^2(X,Y)} \tag{5.28}$$

where $f(X,Y)=\left(\frac{\ln X}{\ln Y}\right)^{3/5}$, $X=C_N(0,\tau)$ and $Y=e^{p^2/2\alpha\tilde{\delta}}C_N(p,0)$.

Using Taylor series, $f(X_s,Y_s)$ can be expanded about $X_s=X$ and $Y_s=Y$, giving

$$f(X_s,Y_s)=f(X,Y)+(X_s-X)\frac{\partial f}{\partial X_s}+(Y_s-Y)\frac{\partial f}{\partial Y_s}+\frac{1}{2}\left[(X_s-X)^2\frac{\partial^2 f}{\partial X_s^2}\right.$$

$$\left.+2(X_s-X)(Y_s-Y)\frac{\partial^2 f}{\partial X_s\partial Y_s}+(Y_s-Y)^2\frac{\partial^2 f}{\partial Y_s^2}\right]+\ \ldots\ . \qquad (5.29)$$

Neglecting the higher order terms, we get

$$<f(X_s,Y_s)>\simeq f(X_s,Y_s) \qquad (5.30)$$

$$\frac{<\left[f(X_s,Y_s)-f(X,Y)\right]^2>}{f^2(X,Y)}\simeq(3/5)^2\left[\frac{\sigma^2_{X_N}}{(\ln X)^2}-2\frac{C_{X_NY_N}}{(\ln X)(\ln Y)}+\frac{\sigma^2_{Y_N}}{(\ln Y)^2}\right] \qquad (5.31)$$

where

$$\sigma^2_{X_N}=\frac{<(X_s-X)^2>}{X^2} \qquad (5.32)$$

$$\sigma^2_{Y_N}=\frac{<(Y_s-Y)^2>}{Y^2} \qquad (5.33)$$

$$C_{X_NY_N}=\frac{<(X_s-X)(Y_s-Y)>}{XY} \qquad (5.34)$$

Eqs. (5.32) and (5.33) have already been evaluated and are given by Eq. (5.18) for large values of N and Eq. (5.34) can be derived in a similar fashion, giving

$$C_{X_NY_N}\simeq\frac{1}{N^2}\sum_{k=-(N-1)}^{N-1}(N-|k|)(D^2+2D)\qquad\text{for}\qquad N>>1 \qquad (5.35)$$

where

$$D=\left[\Gamma_N(0,kT)\Gamma_N(p,kT-\tau)+\Gamma_N(p,kT)\Gamma_N(0,kT-\tau)\right]/\Gamma_N(0,\tau)\Gamma_N(p,0) \tag{5.36}$$

It should be noted that only the first order term of the infinite series is included in Eqs. (5.30) and (5.31). Using Eq. (5.29), it can be shown that the truncation error[40,41] associated with these expressions is negligible when the following inequalities hold

$$\sigma^2_{X_N} << (\ln X)^2$$

$$\sigma^2_{Y_N} << (\ln Y)^2$$

$$C_{X_N Y_N} << (\ln X)(\ln Y)$$

In order for $\sigma^2_{X_N}$ and $\sigma^2_{Y_N}$ to be small, the number of samples or the measurement time must be sufficiently large. In addition to that, for lnX and lnY to be large, p and τ must be sufficiently large for a given turbulence strength and wind velocity.

The normalized RMS error of the sample wind is plotted in figure (5.9) for 10 second averaging time versus spacing between the detectors. The turbulence strength is set to $C_N^2=10^{-13}\ m^{-2/3}$ to ensure that lnX and lnY are large enough and the time delay is chosen to be 5 msec. As can be seen from figure (5.9) the best result is obtained for detector spacings between 20 and 40 millimeters. The optimum spacing can be made smaller by decreasing the time delay which in turn increases the error.

Smaller values of p and τ make it more difficult to deduce informations about V and ρ_0; other words, the magnitudes of lnX and lnY become smaller. At the same time, larger values of p and τ reduce the correlation between the numerator and denominator, producing larger errors. The analysis of Eq. (5.31) has shown that the best results for typical wind speeds (from 1 to 10 m/s) are obtained when

$$2 \text{ msec} \leq \tau \leq 10 \text{ msec}$$

$$20 \text{ mm} \leq p \leq 40 \text{ mm}$$

As previously shown, the estimation of the slope of the T-D covariance does not improve for spacings larger than 40 mm. Therefore, it can be concluded that an optimum spacing would be about 40 mm.

For the results of the wind measurements presented in previous chapter, each measurement is an average of several sample wind velocities obtained at different time delays between two and ten milliseconds. This would reduce the error, even though the samples are not independent.

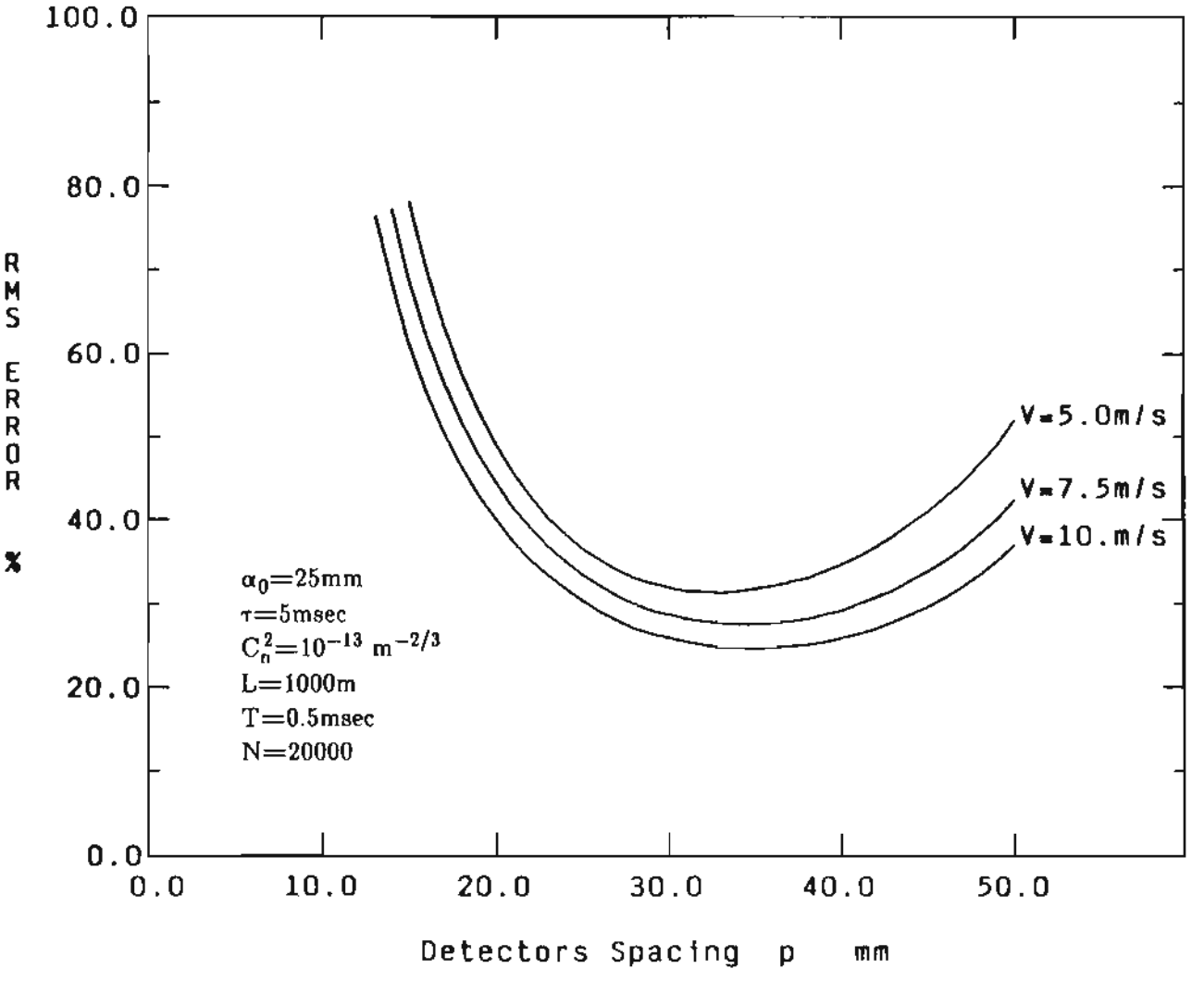

Figure 5.10 RMS error of sample wind velocity as a function of detectors spacing.

5.6 Independent Samples Approximation

The expression derived for the RMS error of the sample T-D covariance can be greatly simplified if the samples are independent. As a result, the error analysis of the quantities of interest such as the slope and wind velocity also become simpler. As can be seen from figure (5.6), over long enough measurement times, the estimation of the T-D covariance function can be accomplished using sampling periods longer than the turbulence coherence time to provide the same level of accuracy. In this case, the samples can be assumed to be independent from each other. Even for actual sampling periods shorter than the coherence time, the results presented here can be quite useful for error analysis of various quantities due to their simple forms, given a long total measurement time.

For a sampling period T much longer than the turbulence coherence time τ_c, we can write

$$\Gamma(\mathbf{p},(n-m)T+\tau)=\begin{cases}\Gamma(\mathbf{p},\tau) & \text{for} \quad n=m \\ 0 & \text{for} \quad n\neq m\end{cases} \tag{5.37}$$

Using the relationship above, Eqs. (5.15) and (5.17) can be greatly simplified.

$$<C_s(\mathbf{p},\tau)>=(1-\frac{1}{N})C_I(\mathbf{p},\tau) \tag{5.38}$$

and

$$<C_s^2(\mathbf{p},\tau)>=(1+\frac{1}{N}-\frac{4}{N^2}+\frac{2}{N^3})\Gamma^4(\mathbf{p},\tau)$$
$$+(\frac{4}{N}-\frac{8}{N^2}+\frac{4}{N^3})<I>^2\Gamma^2(\mathbf{p},\tau)+(\frac{1}{N}-\frac{1}{N^2})<I>^4 \tag{5.39}$$

Substituting Eqs. (5.38) and (5.39) in Eq. (5.14), the normalized MS error can be written as

$$C_s(p,\tau)\text{ MS error } = \left(\frac{3}{N}-\frac{4}{N^2}+\frac{2}{N^3}\right)+\left(\frac{4}{N}-\frac{8}{N^2}+\frac{4}{N^3}\right)/\Gamma_N^2(p,\tau) + \left(\frac{1}{N}-\frac{1}{N^2}\right)/\Gamma_N^4(p,\tau) \qquad (5.40)$$

For large numbers of samples ($N>>1$), Eq. (5.40) reduces to Eq. (5.18) with non zero k terms neglected.

The following correlation of the sample T-D covariance functions has been derived in a similar manner as Eq. (5.39).

$$\begin{aligned}<C_s(p,\tau)C_s(p,-\tau)> = &\left(1-\frac{2}{N}+\frac{1}{N^2}\right)\Gamma^2(p,\tau)\Gamma^2(p,-\tau)\\ &+\left(\frac{2}{N}-\frac{4}{N^2}+\frac{2}{N^3}\right)\Gamma^2(p,0)\Gamma^2(0,\tau)+\left(\frac{1}{N}-\frac{1}{N^2}\right)\left(\Gamma^4(p,0)+\Gamma^4(0,\tau)\right)\\ &+\left(\frac{2}{N}-\frac{4}{N^2}+\frac{2}{N^3}\right)\Gamma(p,\tau)\Gamma(p,-\tau)\left(\Gamma^2(p,0)+\Gamma^2(0,\tau)\right) \qquad (5.41)\end{aligned}$$

Substituting Eqs. (5.39) and (5.41) in Eq. (5.23), the MS error for the sample slope can be obtained.

Using the independent samples assumption, the quantity of Eq. (5.34) has been evaluated, giving

$$\begin{aligned}C_{X_N Y_N} = &\left(\frac{3}{N}-\frac{4}{N^2}+\frac{2}{N^3}\right)+4\left(\frac{1}{N}-\frac{2}{N^2}+\frac{1}{N^3}\right)\Gamma(p,-\tau)/\Gamma(p,0)\Gamma(0,\tau)\\ &+\left(\frac{1}{N}-\frac{1}{N^2}\right)\Gamma^2(p,-\tau)/\Gamma^2(p,0)\Gamma^2(0,\tau) \qquad (5.42)\end{aligned}$$

Eqs. (5.39) and (5.42) can be used in Eq. (5.31) to obtain the MS error associated with the sample wind velocity.

CHAPTER 6

CONCLUSION

The primary goal of this research project was the use of speckle-turbulence interaction in conjunction with optical heterodyne detection for single-ended remote sensing of the atmospheric winds. This was accomplished by using a continuous wave (cw) CO_2 waveguide laser of moderate power operating at 10.6 μm wavelength as the source. Using the experimental apparatus, wind measurements were made in the atmosphere over a flat and featureless terrain. The analysis of the experimental data demonstrated the potentials of a coherent speckle-turbulence system for real world applications.

A great deal of effort was devoted to the development of a coherent lidar system that can fully exploit the speckle-turbulence interaction. In achieving this task, two major advances were made that can benefit other applications as well. One was the achievement of ultrahigh optical isolation between the transmitter and local oscillator beams. Obtaining an adequate level of isolation is the major difficulty in designing cw optical heterodyne systems that use a single laser source. A technique was devised, using multiple acoustooptic modulators and frequency diversity, to obtain a degree of isolation which was sufficient to prevent degradation of the extreme sensi-

tivity of optical heterodyne detection. The other advancement was the realization of an optimum local oscillator power for which the SNR is maximum when using photoconductors as optical heterodyne detectors. The application of an optical local oscillator to a photoconductor can modify its conductance sufficiently to have a considerable effect on both the effective responsivity of the detector and its interaction with the external circuitry. Taking this effect into account and realizing the nonlinear nature of problem, an analytical approach was taken to formulating the SNR as a function of the detector parameters, local oscillator power and terminating load conductance. It was found that for both constant voltage bias and current bias cases, the SNR peaks at a finite local oscillator power.

Various techniques were used to process the experimental windsensing data gathered over a wide range of atmospheric conditions and different target ranges. The conventional processing methods developed in the past for the line of sight case did not produce satisfactory results. This was because of the small effect of the turbulence on the fully developed speckle pattern at 10.6 μm wavelength which makes the processing for wind velocity quite difficult. However, the use of the ZLR method that was developed for the speckle-turbulence measurements showed a significant improvement. As described in chapter 2, the ZLR method uses the measured values of the autocovariance of an arbitrary time delay to determine the wind velocity. In this method, the error can be reduced by measuring the autocovariance at several time delays and averaging the results. It was shown that averaging over five to ten terms is sufficient to produce good results. In an attempt to

further improve the results, the B-ZLR and MMSE-ZLR methods were developed by modifying the ZLR method. The use of these methods resulted in a reduction in error and statistical fluctuations as compared with the results obtained by ZLR processing method. However, the B-ZLR method is favored, since it requires less processing than the MMSE-ZLR method.

By comparing the experimental results obtained using the set-ups of sections 3.3 and 3.4, it was concluded that the effect of the angle of arrival fluctuations on the wind measurements is insignificant. The experimental set-up described in section 3.4 uses imaging receiving optics with low magnification required for suppressing the angle of arrival fluctuations, while the set-up of section 3.3 uses focusing lenses with high optical magnification. Considering that the angle of arrival is of no concern, the set-up of section 3.3 is preferable for the speckle-turbulence measurements, since it has a simpler optical design and more flexibility in selecting the spacing between the detectors.

The accuracy of the wind measurements is limited to the estimation error due to turbulence-induced temporal correlation between the samples of returns and finite averaging time rather than the detectors or the amplifiers noise. For this reason, an analysis was performed to predict the error associated with the statistical parameters required to determine the wind velocity. The error associated with the wind measurements was then estimated and shown that there is an optimum spacing between the detectors for which the error is minimum.

An analytical investigation of the effect of the turbulence-induced correlation between the outgoing and return paths on the measurements was performed. Analytical expressions were obtained describing the time delayed statistics as a function of separation between the transmitter and receiver. It was shown that the effect of this correlation on the wind measurements can be significant and should be taken into account when designing a coherent lidar system.

As discussed in chapter 4, there were deviations between the measured statistical parameters and the theoretical predictions that created some difficulty in determining the wind velocity and the strength of turbulence. Additional theoretical and experimental work is necessary to explain these deviations and further improve the measurements. Such a work can include the effects of the target vibrations and atmospheric constituents such as water vapor on the time delayed statistics of the return intensity. The author believes that the effects of the focusing of the transmitter beam, the fields of view and lines of sight of the detectors on the time delayed covariance curve are also worth further investigations.

As mentioned earlier, part of the deviation from the theory can be attributed to the small effect of turbulence at 10.6 μm wavelength. For this reason, the use of a laser source operating at a shorter wavelength in the near infrared region is recommended that will increase the speckle-turbulence interaction making the processing easier.

In the future work, the use of diode lasers must be considered. By using

optical heterodyne detection, only a watt or two of optical power is needed, and consequently, diode lasers could be used as the transmitter source. This can improve the portability and reliability of the sensor.

The other areas of this work that can be extended, include topics such as the effects of partially developed speckle pattern, aperture averaging, moving target and/or source. It will also be beneficial to conduct a feasibility study on potential methods, such as crossed beams and multiple detectors, for achieving path resolved wind measurements using a speckle-turbulence system.

REFERENCES

1. R. S. Lawrence and J. W. Strohbehn, "*A survey of clean-air propagation effects relevant to optical communications,* " Proc. IEEE 58, 1523, October 1970.

2. R. L. Fante, "*Electromagnetic beam propagation in turbulent media,* " Proc. IEEE 63, 1669, December 1975.

3. R. W. Lee and J. C. Harp, "*Weak scattering in random media, with applications to remote probing,* " Proc. IEEE 57, 375, April 1969.

4. D. L. Fried, "*Remote probing of the optical strength of atmospheric turbulence and wind velocity,* " Proc. IEEE 57, 415, April 1969.

5. R. S. Lawrence, G. R. Ochs, and S. F. Clifford, "*Use of scintillations to measure average wind across a light beam,* " Appl. Opt. 11, 239, February 1972.

6. G. R. Ochs, S. F. Clifford, and Ting-i Wang, "*A feasibility study of an optical crosswind monitor,* " NOAA Technical Memorandum ERL-WPL-10, U.S. Department of Commerce, National Oceanic and Atmospheric Administration, Wave Propagation Laboratory, Boulder, Colorado 80302, September 1973.

7. G. R. Ochs and G. F. Miller, "*Pattern Velocity Computers - Two types developed for wind velocity measurements by optical means,* " Rev. of Sci. Instrum., 43, 879, 1972.

8. T. H. Pries and E. T. Young, "*Evaluation of a laser crosswind system,* " U.S. Army Electronics Command, Research and Development Technical Report ECOM-5546, 1974.

9. G. R. Ochs, S. F. Clifford, and Ting-i Wang, "*Laser Wind Sensing: the effect of saturation of scintillation,* " Appl. Opt. 15, 403, February 1976.

10. P. Beckmann and A. Spizzichino, "*The scattering of electromagnetic waves from rough surfaces,* " Pergaman/Macmillan, London, New York, 1963.

11. J. W. Goodman, "*Statistical properties of laser speckle patterns,* " in Laser Speckle and Related Phenomena, J. C. Dainty, Springer, Berlin 1975.

12. J. F. Holmes and J. R. Kerr, "*Pulsed laser, remote crosswind measurement system -- Feasibility study and design,* " U.S. Army Electronics Command, Research and Development Technical Report ECOM74-0094-1, Atmospheric Sciences Laboratory, White Sand Missile Range, New Mexico 88002, July 1974.

13. J. F. Holmes, J. R. Kerr, M. E. Fossey, R. L. Jacob, and M. H. Lee, "*Experimental pulsed laser, remote crosswind measurement system -- Feasibility study and design (part II),* " U.S. Army Electronics Command, Research and Development Technical Report ECOM75-1, Atmospheric Sciences Laboratory, White Sand Missile Range, New Mexico 88002, January 1975.

14. J. F. Holmes, J. R. Kerr, M. H. Lee, M. E. Fossey, and R. L. Jacob, "*Experimental pulsed laser, remote crosswind measurement system -- Feasibility study and design (part III),* " U.S. Army Electronics Command, Research and Development Technical Report ECOM75-4, Atmospheric Sciences Laboratory, White Sand Missile Range, New Mexico 88002, September 1975.

15. J. F. Holmes, J. R. Kerr, M. H. Lee, and M. E. Fossey, "*Experimental pulsed laser, remote crosswind measurement system -- Feasibility study and design (part IV),* " U.S. Army Electronics Command, Research and

Development Technical Report FA-TR-76065, Frankford Arsenal, Philadelphia, Pennsylvania 19137, November 1976.

16. J. F. Holmes, J. R. Kerr, R. A. Elliott, M. H. Lee, P. A. Pincus, and M. E. Fossey, "*Experimental pulsed laser, remote crosswind measurement system -- Feasibility study and design (part V),* " U.S. Army Electronics Command, Research and Development Technical Report ARSCD-CR-79-007, Fire Control and Small Caliber Weapon Systems Laboratory, Dover, New Jersey, June 1978.

17. S. F. Clifford, G. R. Ochs, and Ting-i Wang, "*Optical wind sensing by the scintillations of a random scene,* " Appl. Opt. 14, 2844, December 1975.

18. D. L. Walters, "*Passive remote crosswind sensing,* " Appl. Opt. 16, 2625, October 1977.

19. S. F. Clifford, G. R. Ochs, and Ting-i Wang, "*Theoretical analysis and experimental evaluation of a prototype passive sensor to measure crosswinds,* " NOAA Technical Report ERL312-WPL-35, U.S. Department of Commerce, National Oceanic And Atmospheric Administration, Environmental Research Laboratories, Boulder, Colorado 80302, September 1974.

20. G. R. Ochs and Ting-i Wang, "*Infrared passive wind sensing- A feasibility study,* " NOAA Technical Memorandum ERL-WPL-34, U.S. Department of Commerce, National Oceanic And Atmospheric Administration, Wave Propagation Laboratory, Boulder, Colorado 80302, October 1977.

21. W. M. Farmer and D. B. Brayton, "*Analysis of atmospheric laser doppler velocimeters,* " Appl. Opt. 10, 2319, October 1971.

22. R. T. Menzies, "*Doppler lidar atmospheric wind sensors: a comparative performance evaluation for global measurement applications from earth orbit,* " Appl. opt. 25, 2546, August 1986.

23. H. H. Yura, "*Optical heterodyne signal power obtained from finite sized source of radiation,* " Appl. Opt. 13, 150, January 1974.

24. F. Amzajerdian and J. F. Holmes, "*Time delayed statistics for a bistatic coherent lidar operating in the atmospheric turbulence,* " in preparation for submission to J. Opt. Soc. Am.

25. M. H. Lee, J. F. Holmes, and J. R. Kerr, "*Statistics of speckle propagation through the turbulent atmosphere,* " J. Opt. Soc. Am. 66, 1164, November 1976.

26. J. F. Holmes, M. H. Lee, and J. R. Kerr, "*Effect of the log-amplitude covariance function on the statistics of speckle propagation through the turbulent atmosphere,* " J. Opt. Soc. Am. 70, 355, April 1980.

27. R. F. Lutomirski and H. T. Yura, "*Propagation of a finite beam in a inhomogeneous medium,* " Appl. Opt. 10, 1652, July 1971.

28. H. T. Yura, "*Mutual coherence function of a finite cross section optical beam propagating in a turbulent medium,* " Appl. Opt. 11, 1399, June 1972.

29. V. S. R. Gudimetla and J. F. Holmes, "*The use of reciprocity in lidar type optical propagation problems involving time lagged statistics,* " submitted for publication.

30. N. George and A. Jain, "*Space and wavelength dependence of speckle intensity,* " Appl. Phys. 4, 201, August 1974.

31. P. A. Pincus, M. F. Fussey, J. F. Holmes, and J. D. Kerr, "*Speckle propagation through turbulence:Experimental,* " J. Opt. Soc. Am. 68, 760, June 1978.

32. Ting-i Wang, S. F. Clifford, and G. R. Ochs, "*Wind and refractive-turbulence sensing using crossed laser beams,* " Appl. Opt. 13, 2662,

November 1974.

33. Ting-i Wang, G. R. Ochs, and R. S. Lawrence, "*Wind measurements by the temporal cross-correlation of the optical scintillations,* " Appl. Opt. 20, 4073, December 1981.

34. J. F. Holmes, F. Amzajerdian, V. S. R. Gudimetla, and J. M. Hunt, "*Remote sensing of atmospheric winds using speckle-turbulence interaction, a CO_2 laser and optical heterodyne detection,* " Appl. Opt. 27, June 15, 1988.

35. J. F. Holmes, "*Optical remote sensing wind measurements using speckle-turbulence interaction,* " Proc. of the Opt. Soc. Am. conference on Optical and Millimeter Wave Propagation and Scattering, May 27-30, 1986, Florence, Italy.

36. V. P. Aksenov, V. A. Banakh, and V. L. Mironov, "*Fluctuations of retroreflected laser radiation in a turbulent atmosphere,* " J. Opt. Soc. Am. 1, 263, March 1984.

37. R. M. Measures and G. Pilon, "*A study of tunable laser techniques for remote mapping of specific gaseous constituents of the atmosphere,* " Opto-Electronics 4, 141, 1972.

38. N. Menyuk and D. K. Killinger, "*Temporal correlation measurements of pulsed dual CO_2 lidar returns,* " Opt. Lett. 6, 301, June 1981.

39. D. K. Killinger and N. Menyuk, "*Effect of turbulence-induced correlation on laser remote sensing,* " Appl. Phys. Lett. 38, 968, June 1981.

40. N. Menyuk, D. K. Killinger, and C. R. Menyuk, "*Error reduction in laser remote sensing: combined effect of cross correlation and signal averaging,* " Appl. Opt. 24, 118, January 1985.

41. F. Amzajerdian and J. F. Holmes, "*The effect of speckle and atmospheric*

turbulence on dial measurements utilizing coherent detection, " in preparation for submission to Appl. Opt.

42. S. F. Clifford and S. Wandzura, "*Monostatic heterodyne lidar performance: the effect of the turbulent atmosphere,* " Appl. Opt. 20, 514, February 1981.

43. M. C. Teich, "*Infrared heterodyne detection,* " *Proc. IEEE 56, 37, January 1968.*

44. R. H. Kingston, "*Detection of optical infrared radiation,* " Springer-Verlag, New York, 1978.

45. D. L. Fried, "*Optical heterodyne detection of an atmospherically distorted signal wave front,* " Proc. IEEE 55, 57, January 1967.

46. J. H. Shapiro, "*Correlation scales of laser speckle in heterodyne detection,* " Appl. Opt. 24, 1883, June 1985.

47. M. H. Lee and J. F. Holmes, "*Effect of the turbulent atmosphere on the autocovariance function for a speckle field generated by a laser beam with random pointing error,* " J. Opt. Soc. Am. 71, 559, May 1981.

48. A. Men and M. Rosenberg, "*Acoustooptical device with extremely high contrast ratio,* " Appl. Opt. 22, 873, March 1983.

49. B. Furch, A. L. Scholtz, and W. R. Leeb, "*Isolation and frequency conversion properties of acoustooptic modulators,* " Appl. Opt. 21, 2344, July 1983.

50. U. P. Oppenheim and R. T. Menzies, "*Aligning the transmitter and receiver telescopes of an infrared lidar: a novel method,* " Appl. Opt. 21, 174, January 1982.

51. M. Bass and J. S. Whittier, "*Beam divergence determination and collimation using retroreflectors,* " Appl. Opt. 23, 2674, August 1984.

52. J. F. Holmes, J. M. Hunt , F. Amzajerdian, and V. S. R. Gudimetla, *An optical system for remote wind sensing using speckle-turbulence interaction,* " Proc. of the conference on Lasers and Electrooptics, June 9-13, 1986, San Francisco, California.

53. J. F. Holmes, F. Amzajerdian, and J. M. Hunt, "*Improved optical local-oscillator isolation using multiple acousto-optic modulators and frequency diversity,* " J. Opt. Soc. Am. 12, 637, August 1987.

54. V. I. Tatarskii, "*The effect of the turbulent atmosphere on wave propagation,* " Springfield, Va.: U.S. Dep. Commerce, Ch.3, 1971.

55. M. C. Teich, R.J. Keyes, and R. H. Kingston, "*Optimum heterodyne detection at* $10.6\mu m$ *in photoconductive Ge:Cu,* " Appl. Phys. Lett. 9, 357, November 1966.

56. R. J. Keyes, "*Optical and infrared detectors,* " Springer-Verlag, New York, 1977.

57. N. A. Penin, N. Sh. Khaykin, and B. V. Yurist, "*Investigation of the noise factor of an optical heterodyne receiver with an extrinsic photoresistor,* " Radiotekhn. I Elektron. (USSR), translated in Radio Eng. and Electron. Phys. (USA), 792, May 1972.

58. J. M. Hunt, J. F. Holmes, and F. Amzajerdian, "*Optimum local oscillator levels for coherent detection using photoconductors,* " Appl. Opt. 27, August 1, 1988.

59. N. Menyuk and D. K. Killinger, "*Limitations of signal averaging due to temporal correlation in laser remote-sensing measurements,* " Appl. Opt. 21, 3377, September 1982.

60. M. J. Milton and P. T. Woods, "*Pulse averaging methods for a laser remote monitoring system using atmospheric backscatter,* " Appl. Opt. 26, 2598, July 1987.

APPENDIX A

This appendix lists the computer source programs used to evaluate the time-delayed covariance and SNR reduction factor for the bistatic coherent lidars. The NAG library routines (installed on a Digital Equipment Corp.'s Micro Vax II computer) were used to perform the integrations. Brief descriptions of these routines and the related references can be found in the NAG library manual published by Numerical Algorithms Group Inc., Downers Grove, Illinois, 1984.

```
c-------------------------------------------------------------
c---------------------- bist1.f ------------------------------
c-------------------------------------------------------------
c---------     The T-D Covariance function is evaluated
c---------   for the dependent outgoing and returning paths
c---------   as a function of transmitter-receiver spacing.
c-------------------------------------------------------------


        external p1,p2,fun,fh
        double precision t21,t22,cov1,t24
        common alpha,p,v,rh,q,tau
        open(2,file='vr1')

        write(5,*)'enter  turb. coh. length and wind velocity'
        read(5,*)rho,v

        write(5,*)'enter beam radius, detectors spacing and
    +   transmitter-receiver spacings'
        read(5,*)alpha,p,q

        rh=rho**(5./3.)
        t21=exp(-(p/(2.*alpha))**2.)
        write(2,*)'---------------------------------------'
        write(2,*)'alpha=',alpha,'rho=',rho,'V=',v,'p=',p,'q=',q
        write(2,*)

        ifail=0
        nlimit=0
        tau=-10.0e-3

            do 10 k=1,40
            tau=tau+5.0e-4
c--
c--- A NAG library integration routine
c--- is called to evaluate the wave structure function.
c--
            t22=d01ahf(0.0,1.0,1.0e-4,in,abserr,fun,nlimit,ifail)
            t24=16./3.*t22/rh

            ifail1=0
            abs=1.0e-3
            py1=0.0
            py2=6.283185

c--- The following NAG library routine performes the double
c--- integration over vector R.

            call d01daf(py1,py2,p1,p2,fh,abs,ans,npts,ifail1)
            cov1=(t21*exp(-t24))**2.
            cov=(ans/3.141593)**2.*cov1
c--
c-- cov1 is the TD-COV for the independent paths case and cov
c-- is the corresponding dependent paths case.
c--
            write(2,*)tau,cov,cov1

  10        continue

        stop
        end


c-------------------------------------------------------------
```

```
      double precision function fh(x,y)
      external fun1
      common alpha,p,v,rh,q,tau
      common /as/xx,yy
      double precision t11,t12,t13
      ifail2=0
      nlimit=0
      xx=alpha*x
      yy=y

c--- A NAG library integration routine
c--- is called to evaluate the wave structure function.

      t11=d01ahf(0.0,1.0,1.0e-5,in1,absel,fun1,nlimit,ifail2)
      t12=(abs((q+p)**2.+xx*xx-2.*xx*(q+p)*cos(y)))**(5./6.)
      t13=(abs((q-p)**2.+xx*xx-2.*xx*(q-p)*cos(y)))**(5./6.)
      fh=x*exp(-8./3.*t11/rh+(t12+t13)/rh-x*x)
      return
      end

c-------------------------------------------------------

      double precision function fun(w)
      common alpha,p,v,rh,q,tau

      fun=(abs((1.-w)*p-v*tau))**(5./3.)
      return
      end

c-----------------------------------------------

      double precision function fun1(w)
      common alpha,p,v,rh,q,tau
      common /as/xx,yy
      double precision tt1,tt2,ttt1,ttt2

      tt1=q*q+xx*xx-2.*q*xx*cos(yy)
      tt2=v*tau*(q-xx*cos(yy))
      ttt1=(abs((1.-w)**2.*tt1+2.*(1.-w)*tt2+(v*tau)**2.))**(5./6.)
      ttt2=(abs((1.-w)**2.*tt1-2.*(1.-w)*tt2+(v*tau)**2.))**(5./6.)
      fun1=ttt1+ttt2
      return
      end

c-----------------------------------------
      double precision function p1(y)
      p1=0.0d0
      return
      end

c-----------------------------------------
      double precision function p2(y)
      p2=3.0d0
      return
      end

c-------------------------------------------------------------
c-------------------------------------------------------------
```

```
c-------------------------------------------------------
c--------------------------- bist2.f ---------------------
c-------------------------------------------------------
c--------  Heterodyne SNR reduction factor is evaluated
c--------  as a function of the receiving aperture size
c--------  given a transmitter-receiver spacing.
c-------------------------------------------------------


        double precision ans,d01fbf,q,al,alpha
        double precision abc(32),wrk(32)
        dimension npt(4)
        external fh,d01baz,d01baw
        common al,q
        open(2,file='ht1')

        write(6,*)' enter the transmitter-receiver spacing'
        read(5,*)q

        write(2,*)' alpha ',' reduction factor'
        write(2,*)'----------------------------------------'
        write(2,*)'q=',q

         npt(1)=8
         npt(2)=8
         npt(3)=8
         npt(4)=8

         itp=1
         if1=0
c--
c-- The NAG library routine is called that returns the weights and
c-- abscissae for use in the Gauss-Hermite quadrature.
c--
       call d01bbf(d01baw, 0.0d0, 0.5d0, itp, npt(1),
     * wrk(1), abc(1), if1)
       call d01bbf(d01baw, 0.0d0, 0.5d0, itp, npt(2),
     * wrk(9), abc(9), if1)
       call d01bbf(d01baw, 0.0d0, 0.5d0, itp, npt(3),
     * wrk(17), abc(17), if1)
       call d01bbf(d01baw, 0.0d0, 0.5d0, itp, npt(4),
     * wrk(25), abc(25), if1)

              do 10 ia=1,20
              alpha=10.0d0**(1.0-float(ia)/10.0)
              al=alpha**(5./3.)

              if2=0
              ndim=4
              lwa=32
c--
c-- The following NAG library routine uses the Gaussian weights
c-- to evaluate the four-folded integral.
c--
              ans=d01fbf(ndim,npt,lwa,wrk,abc,fh,if2)
              sig=ans/(39.48)

              write(2,*)alpha,sig,if

  10          continue

        stop
        end

c-------------------------------------------------------
```

```
      double precision function fh(ndim,x)
      double precision x(ndim)
      double precision x1,x2,x3,x4,q,al
      double precision t1,t2,t3,dexp,fh1
      common al,q

      x1=x(1)
      x2=x(2)
      x3=x(3)
      x4=x(4)

     fh1=dexp(-0.5d0*(x1*x1+x2*x2+x3*x3+x4*x4))
     t1=((x3-x1-q)**2.0+(x2-x4)**2.0)**(5./6.)
     t2=((x3+x1-q)**2.0+(x2+x4)**2.0)**(5./6.)
     t3=2.0d0*((x1*x1+x2*x2)**(5./6.)+((x3-q)**2.0+x4*x4)**(5./6.))
 60  fh=fh1*dexp(-al*(t3-t1-t2))

      return
      end

c-------------------------------------------------------------
c-------------------------------------------------------------
```

APPENDIX B

The schematic of the electronics designed and built for the experimental set-ups are provided in this appendix. The first schematic is the receiver used in the systems described in sections 3.1 and 3.3. The second schematic is the receiver utilized in the system of section 3.2 followed by the logic and switching circuits that achieved the gating of the transmitter and receiver. The last schematic is the receiver used in conjunction with the PC detectors in the set-up of section 3.4.

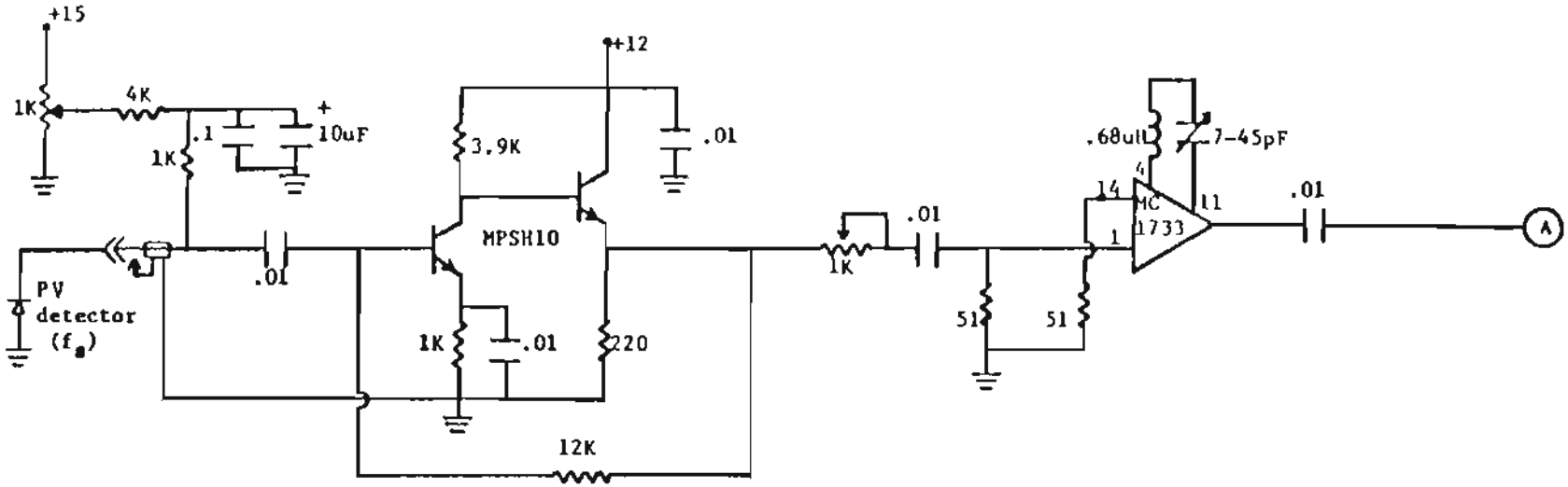

f_s=37.5MHz for single modulator system

f_s=5MHz for dual modulator system

Receiver Electronics for the
Single and Dual AO Modulator Systems
(Page 1 Of 4)

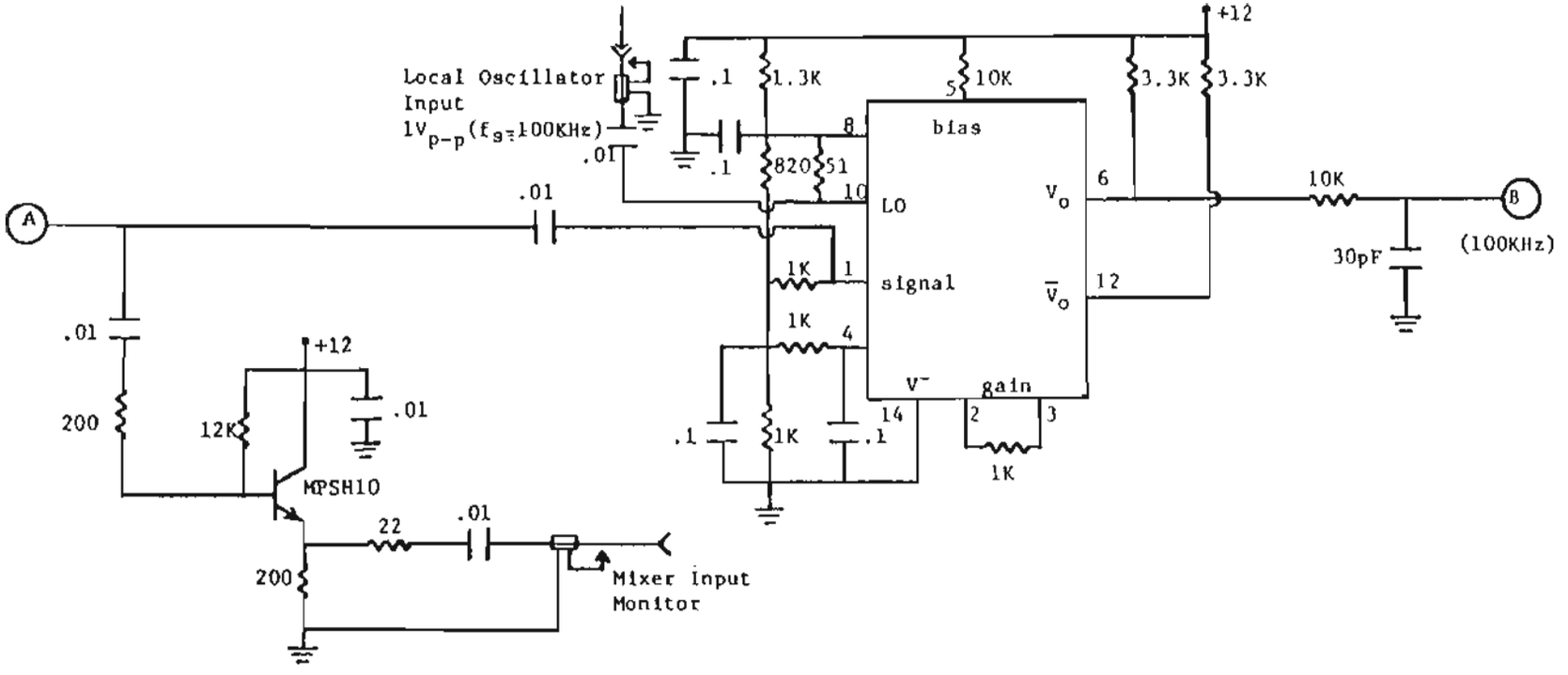
Local Oscillator Input
$1V_{p-p}(f_s=100KHz)$
.01
.1
1.3K
.1
820
51
10K
3.3K
3.3K
+12
bias
LO
signal
V_o
$\overline{V}_o$
V^-
gain
10K
30pF
(100KHz)
A
B
.01
1K
1K
1K
.1
1K
.1
1K
.01
200
12K
+12
.01
MPSH10
22
.01
200
Mixer Input Monitor

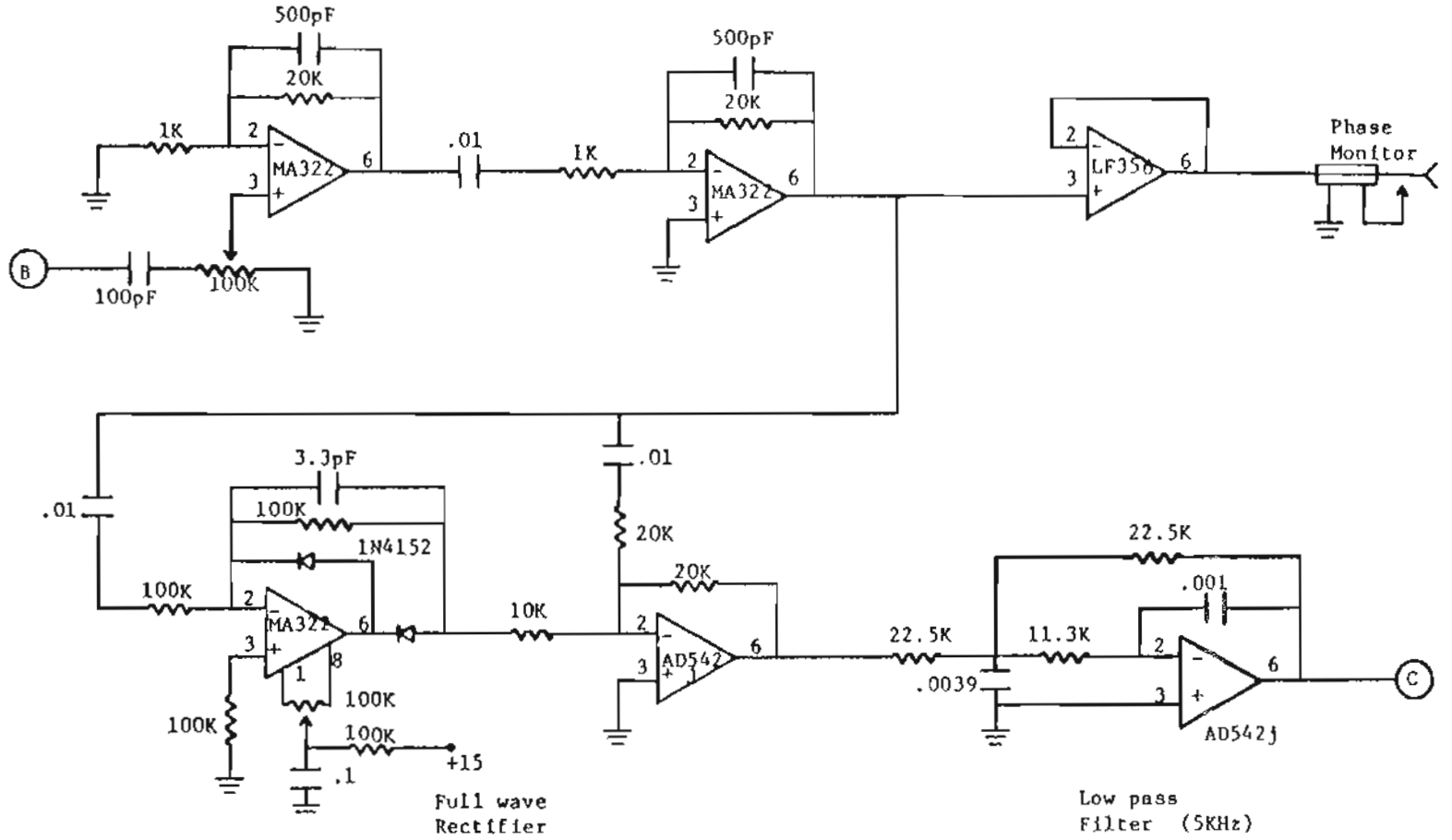
500pF
20K
1K
2
3
MA322
6
.01
1K
500pF
20K
2
3
MA322
6
2
3
LF356
6
Phase
Monitor
B
100pF
100K
.01
3.3pF
100K
1N4152
100K
2
3
MA322
6
8
1
100K
100K
100K
.1
+15
10K
.01
20K
20K
2
3
AD542
6
22.5K
.001
22.5K
11.3K
.0039
2
3
6
AD542j
C
Full wave
Rectifier
Low pass
Filter (5KHz)

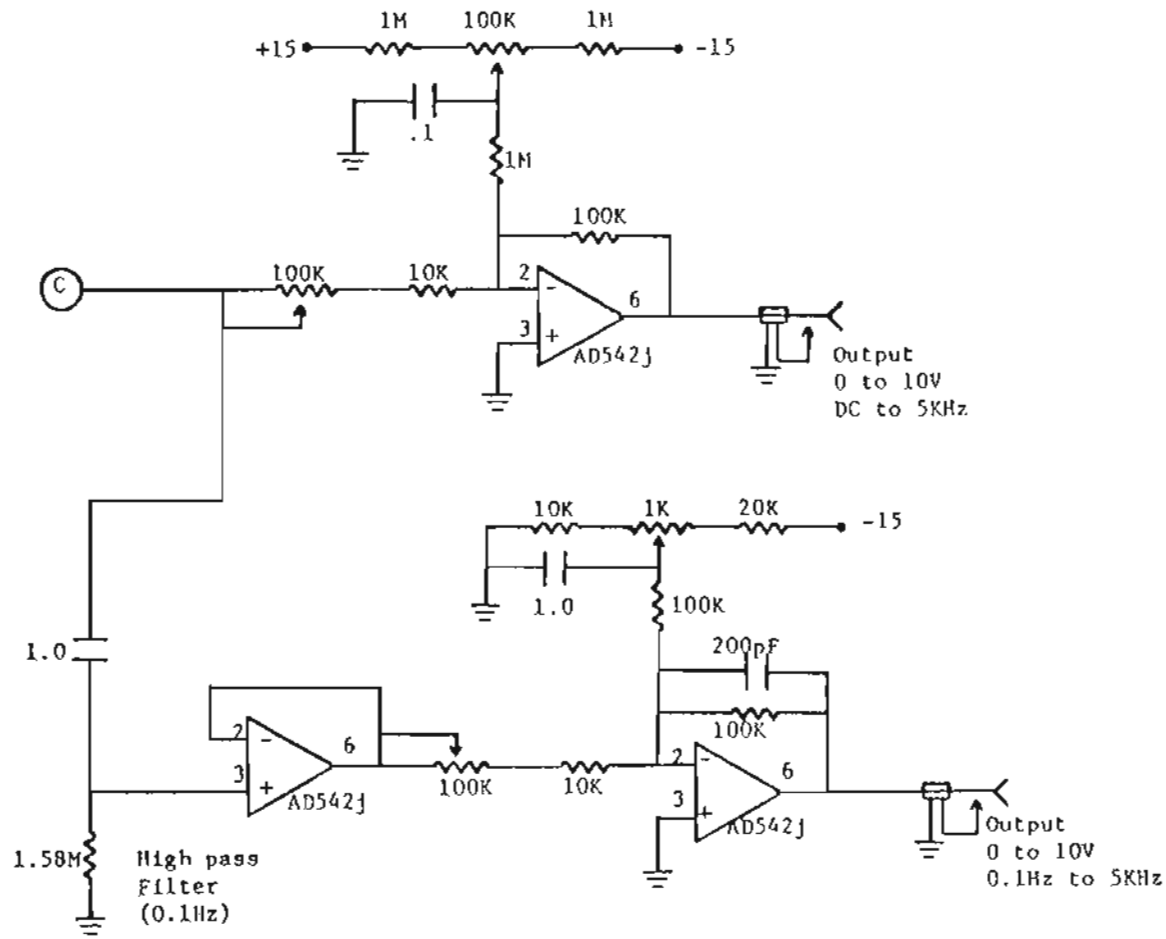
1M
100K
1M
+15
-15
.1
1M
100K
100K
10K
C
2
6
3
AD542j
Output
0 to 10V
DC to 5KHz
10K
1K
20K
-15
1.0
100K
200pF
1.0
100K
2
6
3
AD542j
100K
10K
2
6
3
AD542j
1.58M
High pass
Filter
(0.1Hz)
Output
0 to 10V
0.1Hz to 5KHz

(Page 4 of 4)

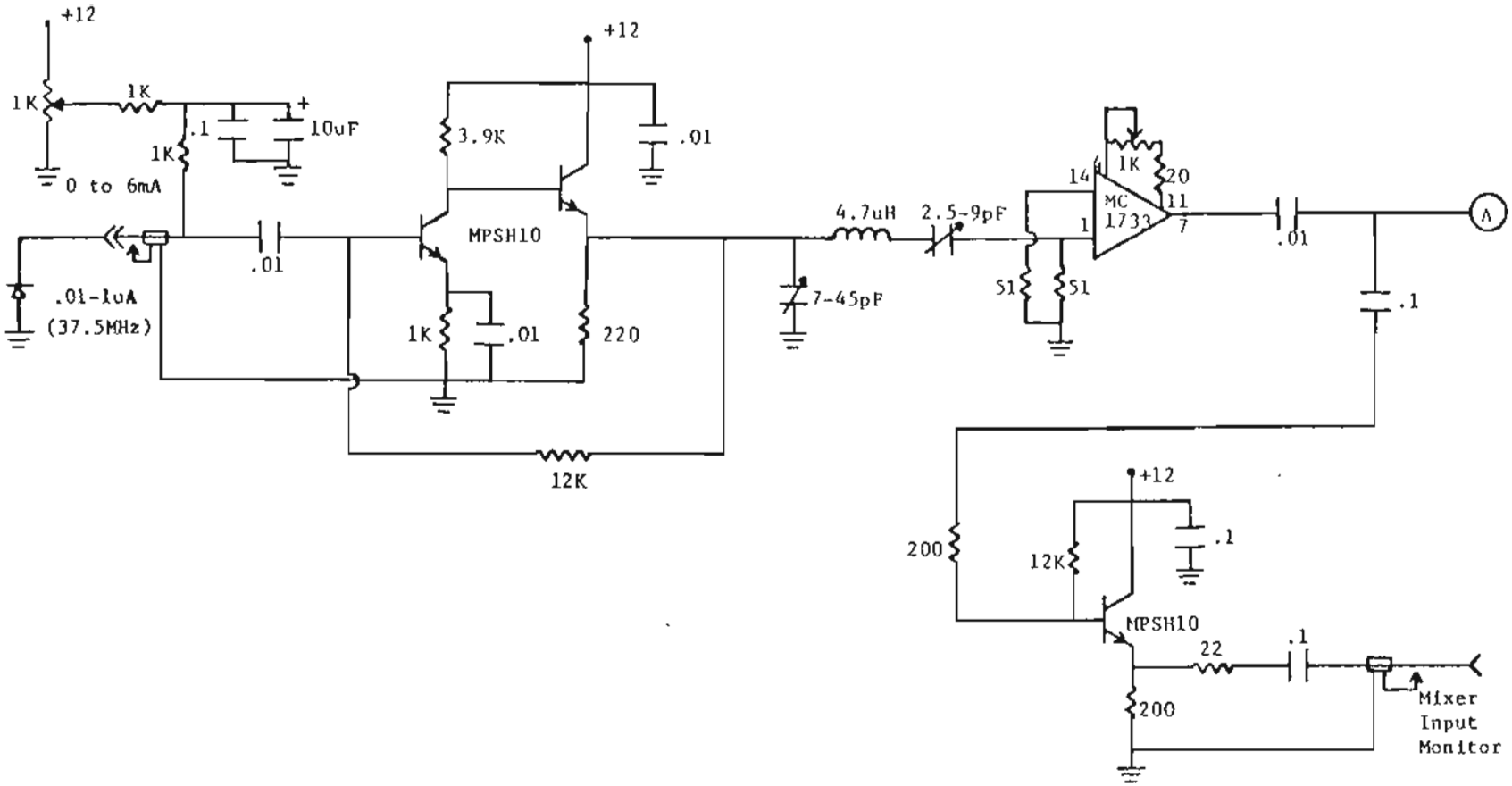

Receiver Electronics for the
Synchronous Heterodyne Detection System
(Page 1 of 3)

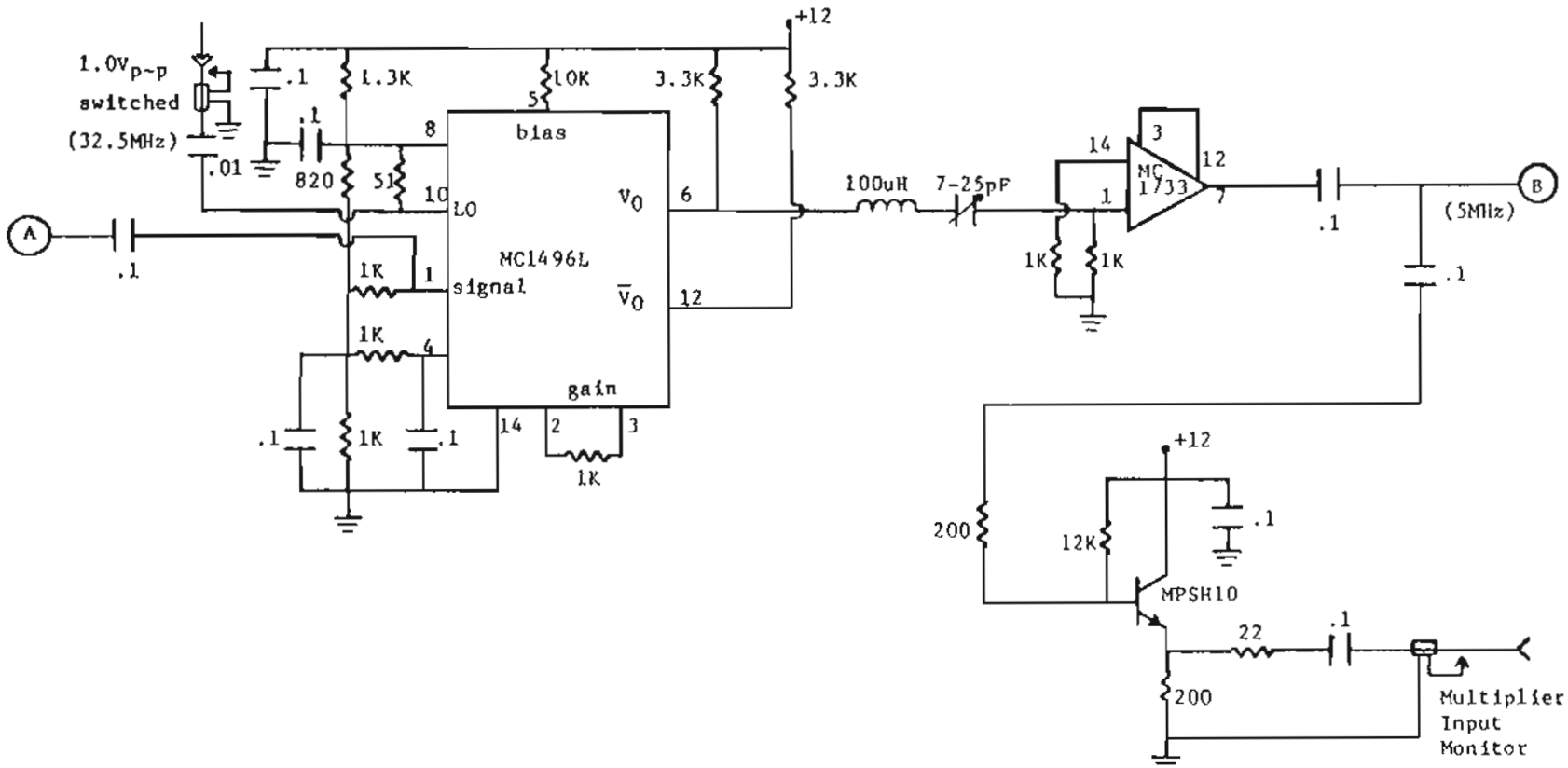
1.0Vp-p
switched
(32.5MHz)
.01
.1
1.3K
.1
820
51
10K
5
8
10
bias
LO
MC1496L
signal
gain
V_O
$\overline{V}_O$
6
12
14
2
3
1K
.1
1K
1K
1K
1K
.1
.1
+12
3.3K
3.3K
100uH
7-25pF
14
3
12
1
MC
1733
7
1K
1K
.1
.1
(5MHz)
A
B
+12
200
12K
.1
MPSH10
22
.1
200
Multiplier
Input
Monitor

(Page 2 of 3)

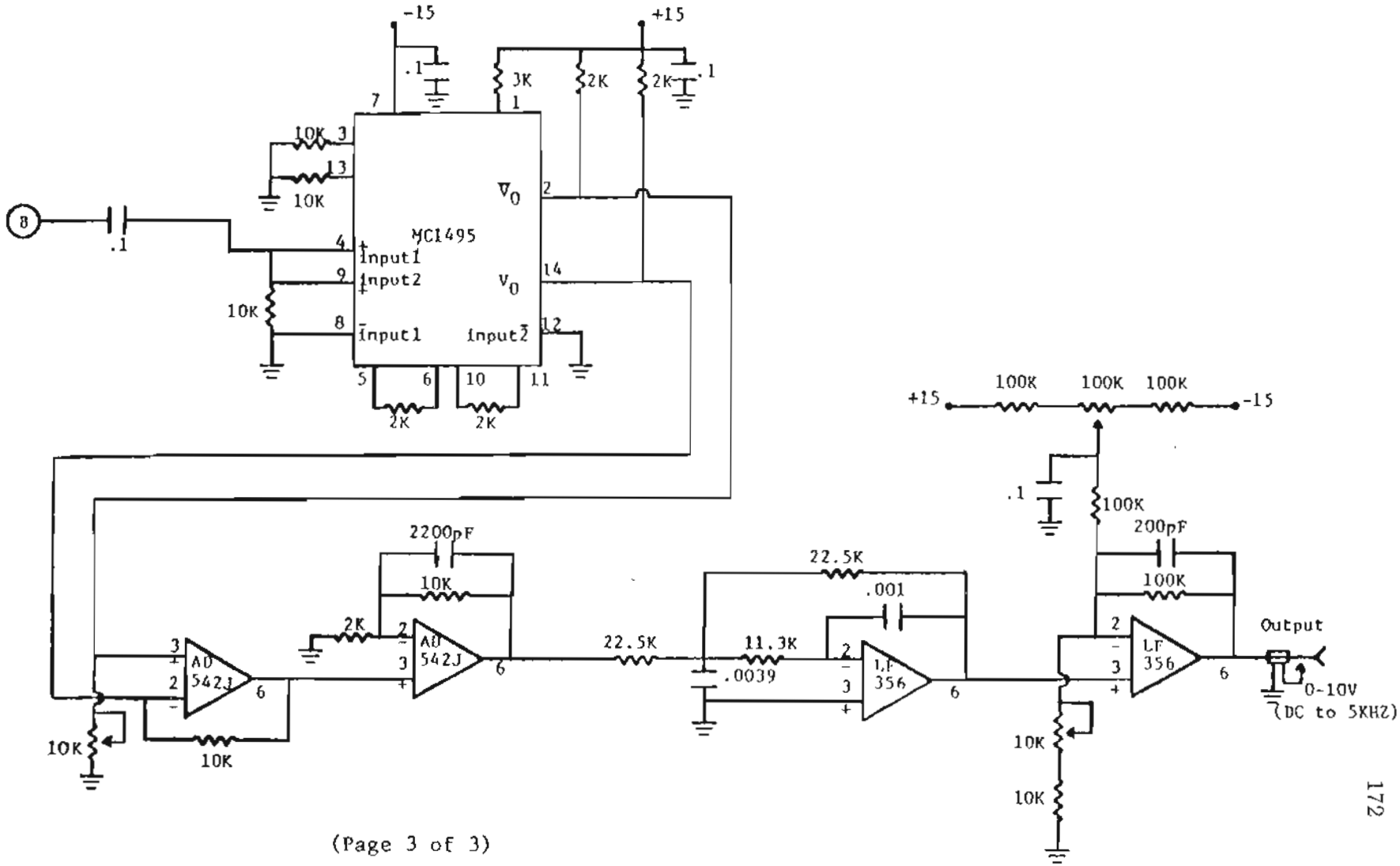
-15
+15
.1
3K
2K
2K
.1
7
1
10K
3
13
10K
MC1495
V_0
2
8
.1
4
Input1
9
Input2
V_0
14
10K
8
Input1
Input2
12
5
6
10
11
2K
2K
100K
100K
100K
+15
-15
.1
100K
2200pF
200pF
22.5K
.001
10K
100K
2K
Output
AD
542J
AD
542J
22.5K
11.3K
.0039
LF
356
LF
356
0-10V
(DC to 5KHZ)
10K
10K
10K
10K

(Page 3 of 3)

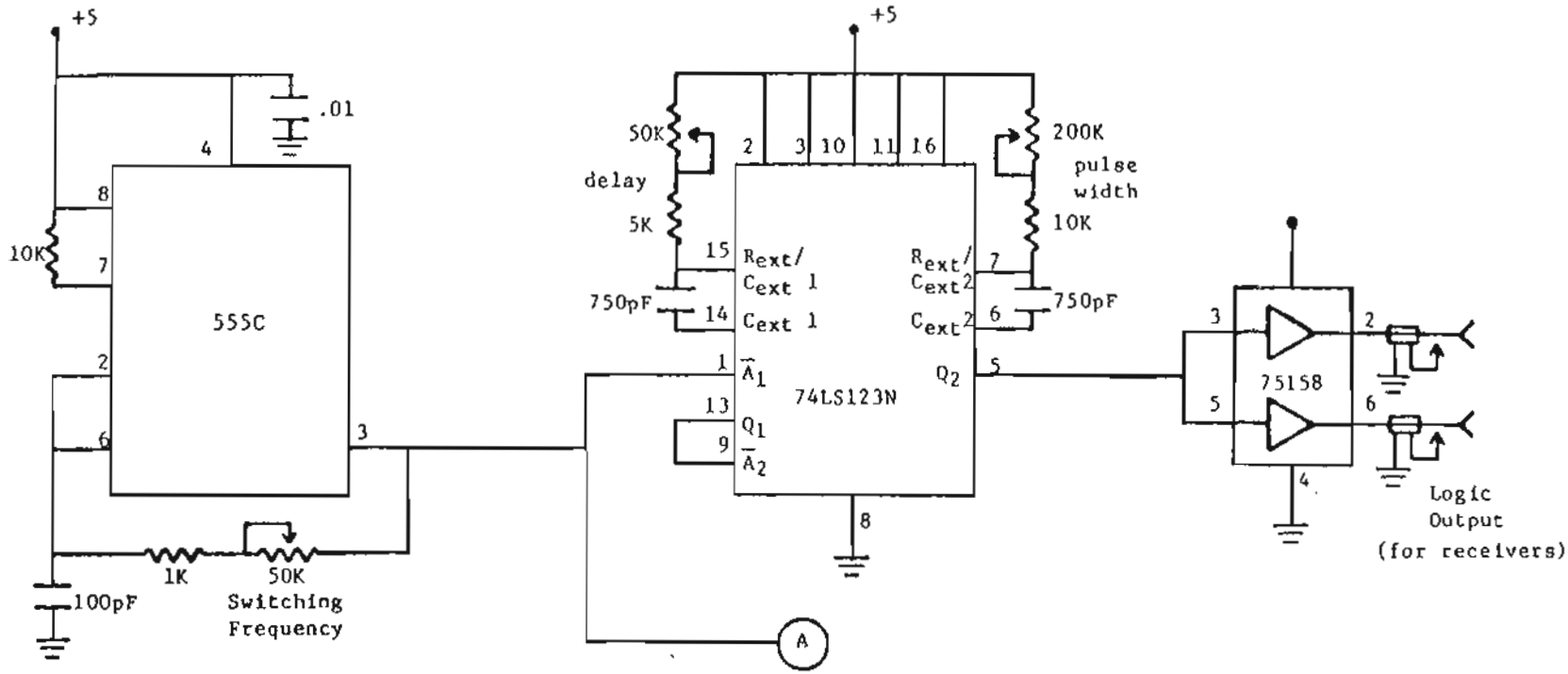

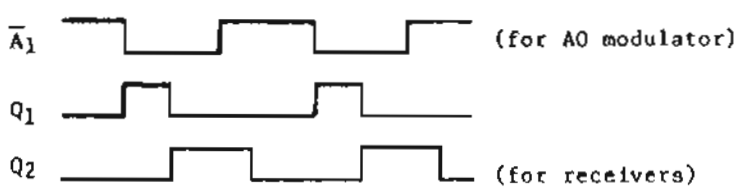

Logic and AO Modulator Switching Circuits for
the Synchronous Heterodyne Detection System
(Page 1 of 2)

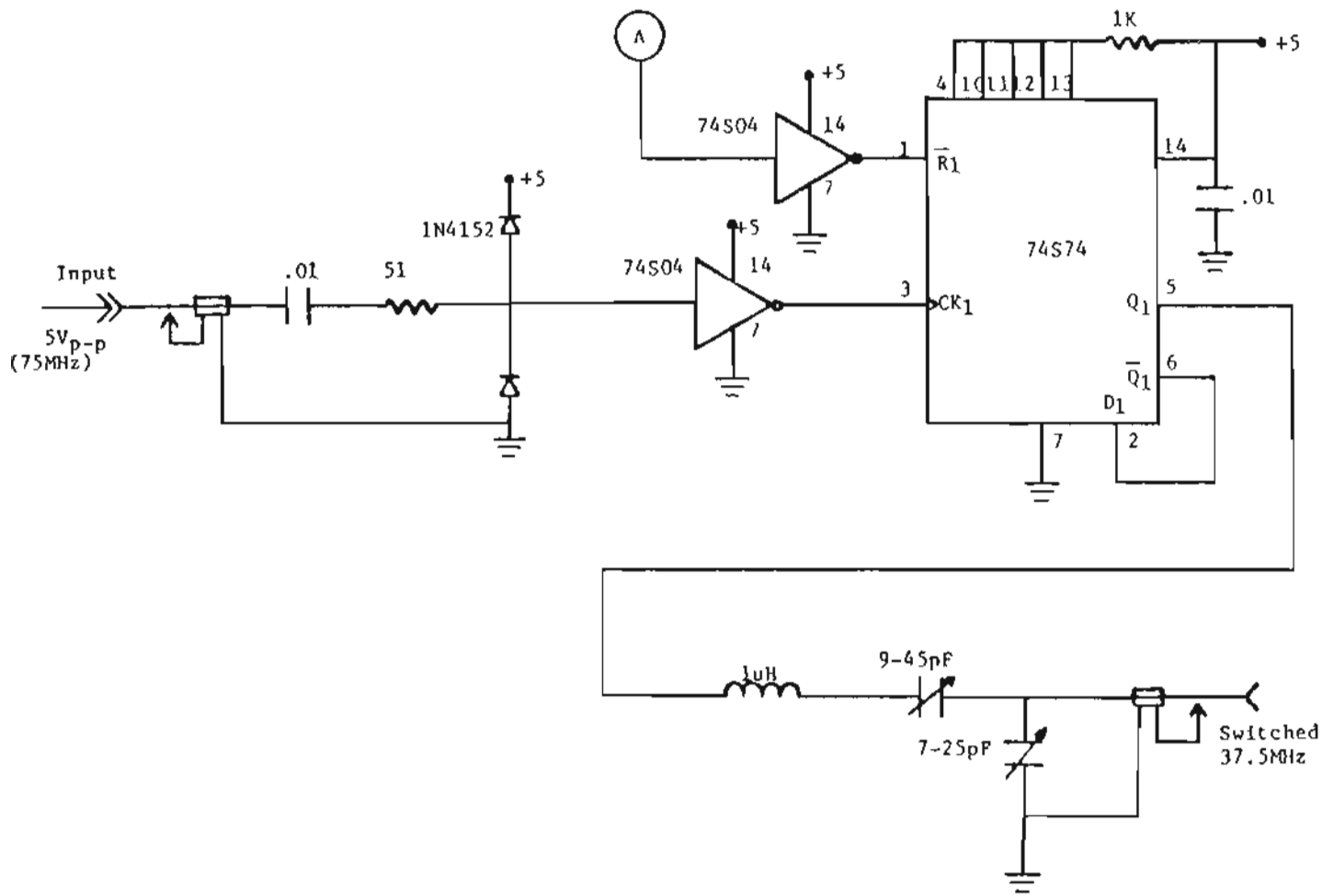
A
1K
+5
74S04
14
7
1
$\overline{R}_1$
4
10
11
12
13
14
.01
74S74
+5
1N4152
Input
.01
51
74S04
14
7
3
CK_1
Q_1
5
$\overline{Q}_1$
6
D_1
2
7
$5V_{p-p}$
(75MHz)
1uH
9-45pF
7-25pF
Switched
37.5MHz

(Page 2 of 2)

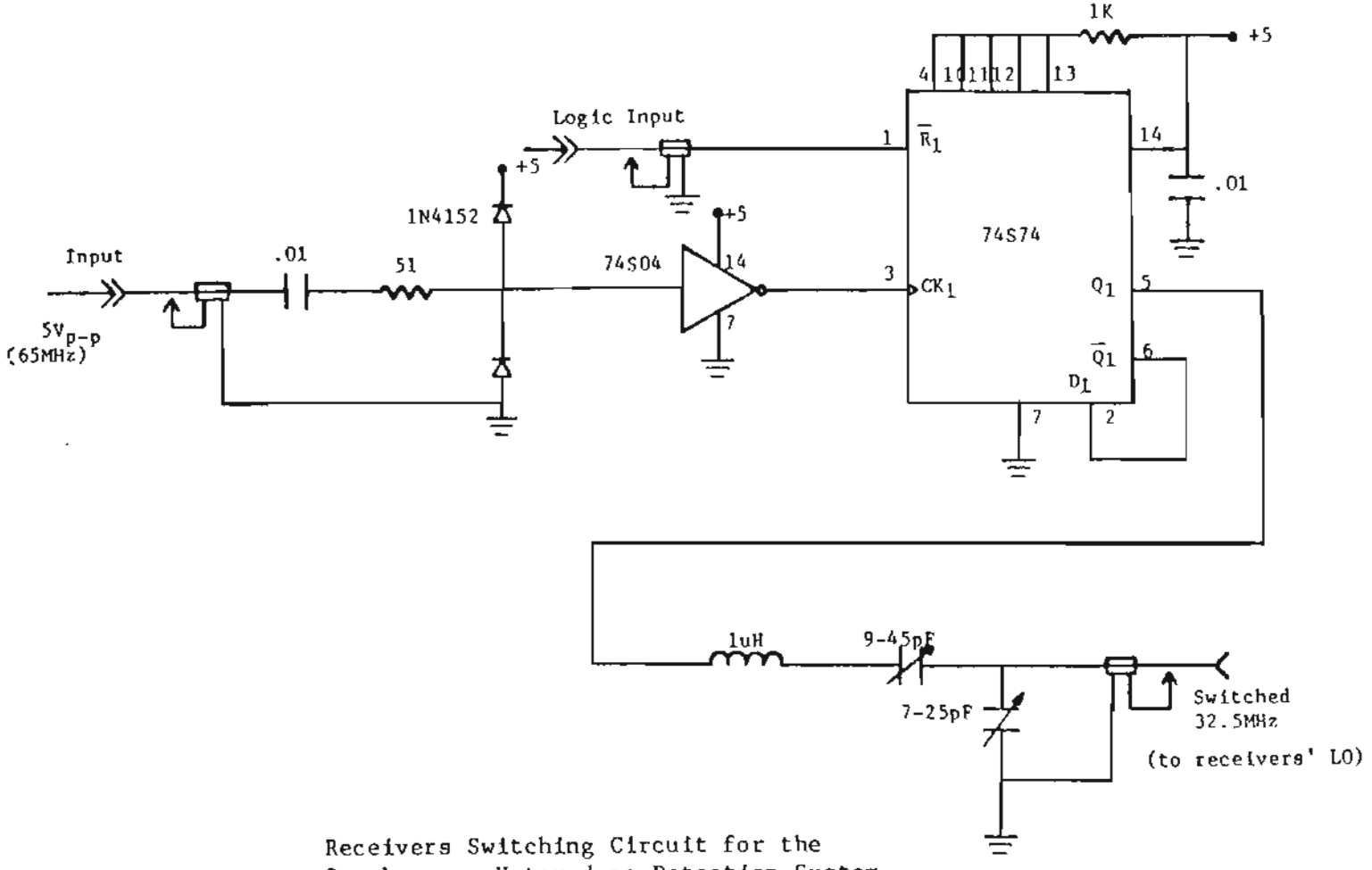

Receivers Switching Circuit for the
Synchronous Heterodyne Detection System
(Page 1 of 1)

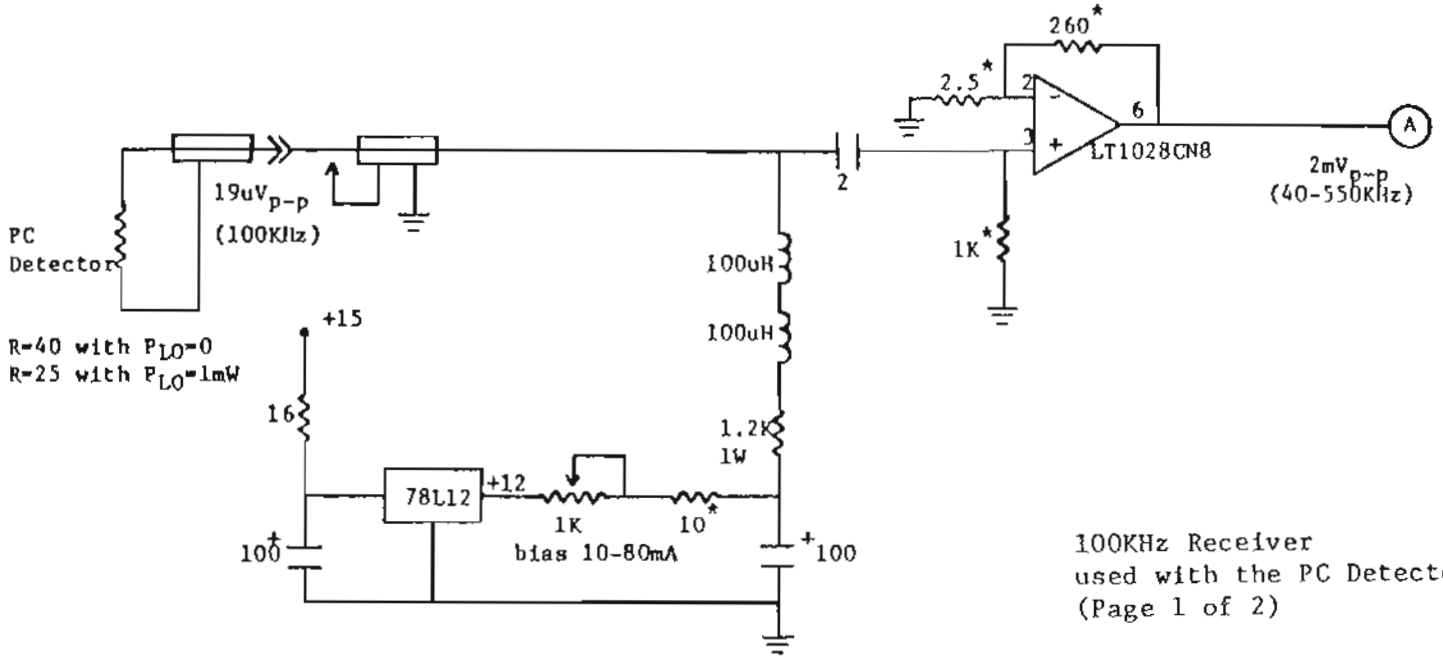

100KHz Receiver
used with the PC Detectors
(Page 1 of 2)

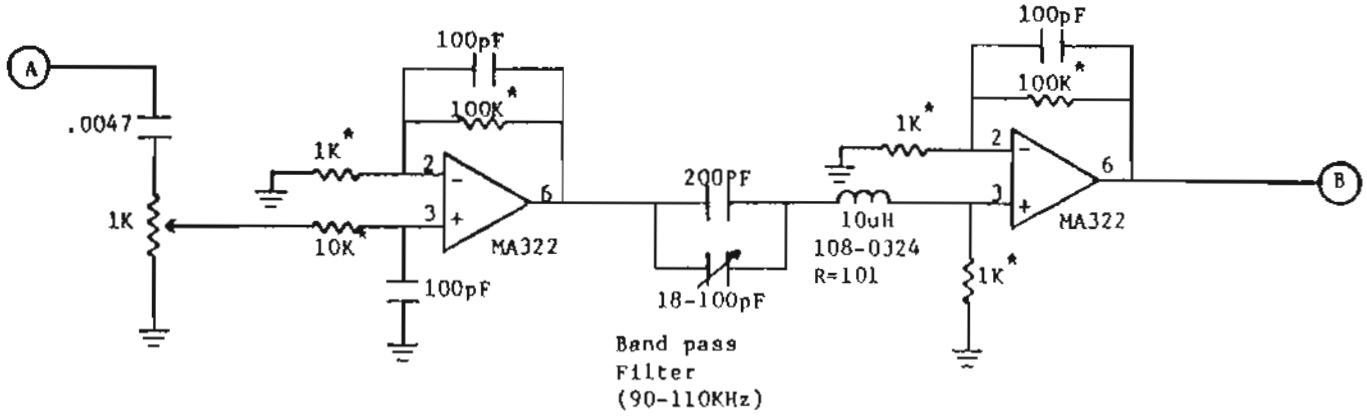

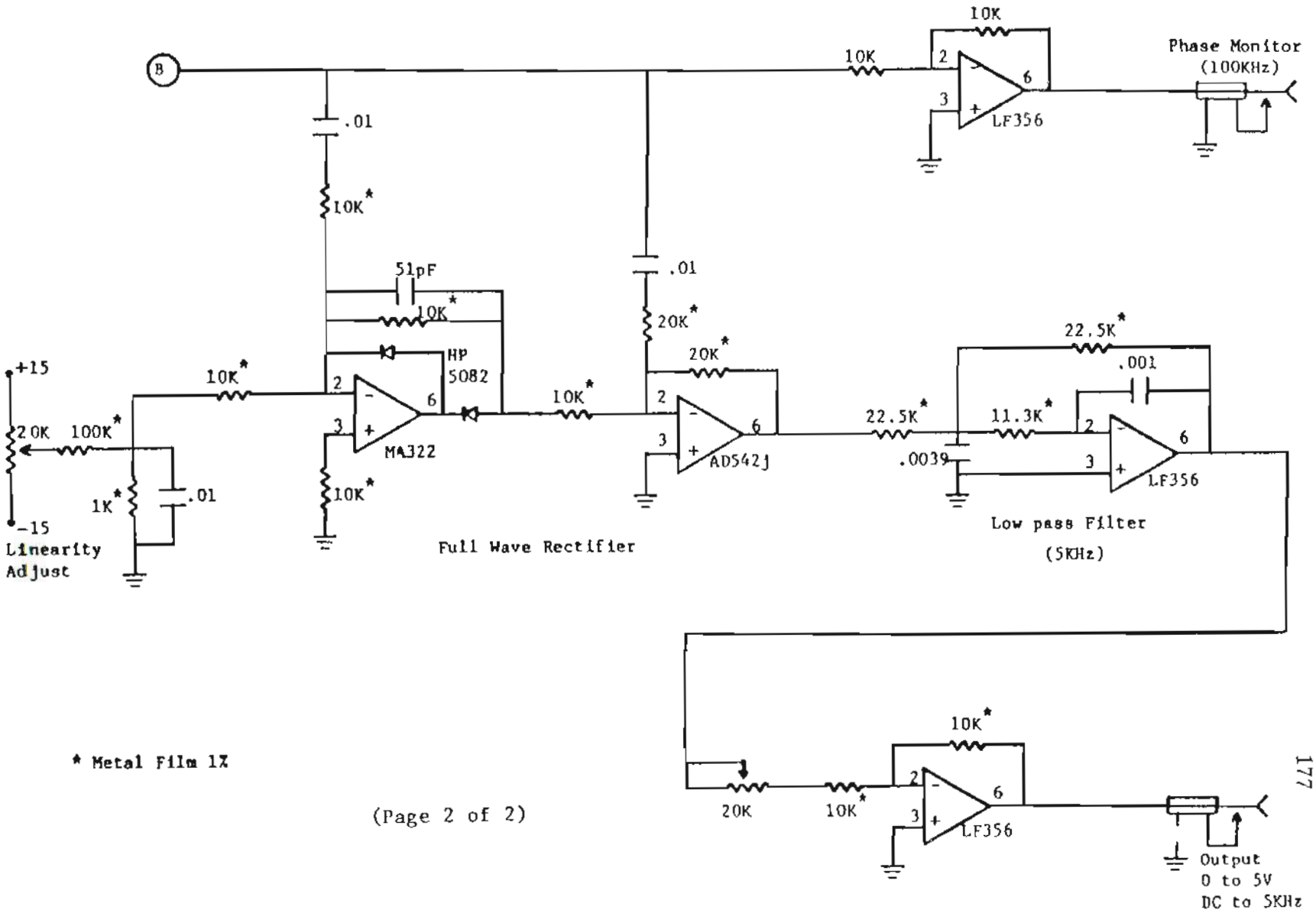
B
.01
10K*
10K
10K
2
3
6
LF356
Phase Monitor
(100KHz)
51pF
10K*
HP
5082
10K*
2
3
6
MA322
10K*
.01
20K*
20K*
10K*
2
3
6
AD542J
22.5K*
.001
22.5K*
11.3K*
.0039
2
3
6
LF356
Low pass Filter
(5KHz)
+15
20K
100K*
1K*
.01
-15
Linearity
Adjust
Full Wave Rectifier
10K*
20K
10K*
2
3
6
LF356
Output
0 to 5V
DC to 5KHz

* Metal Film 1%

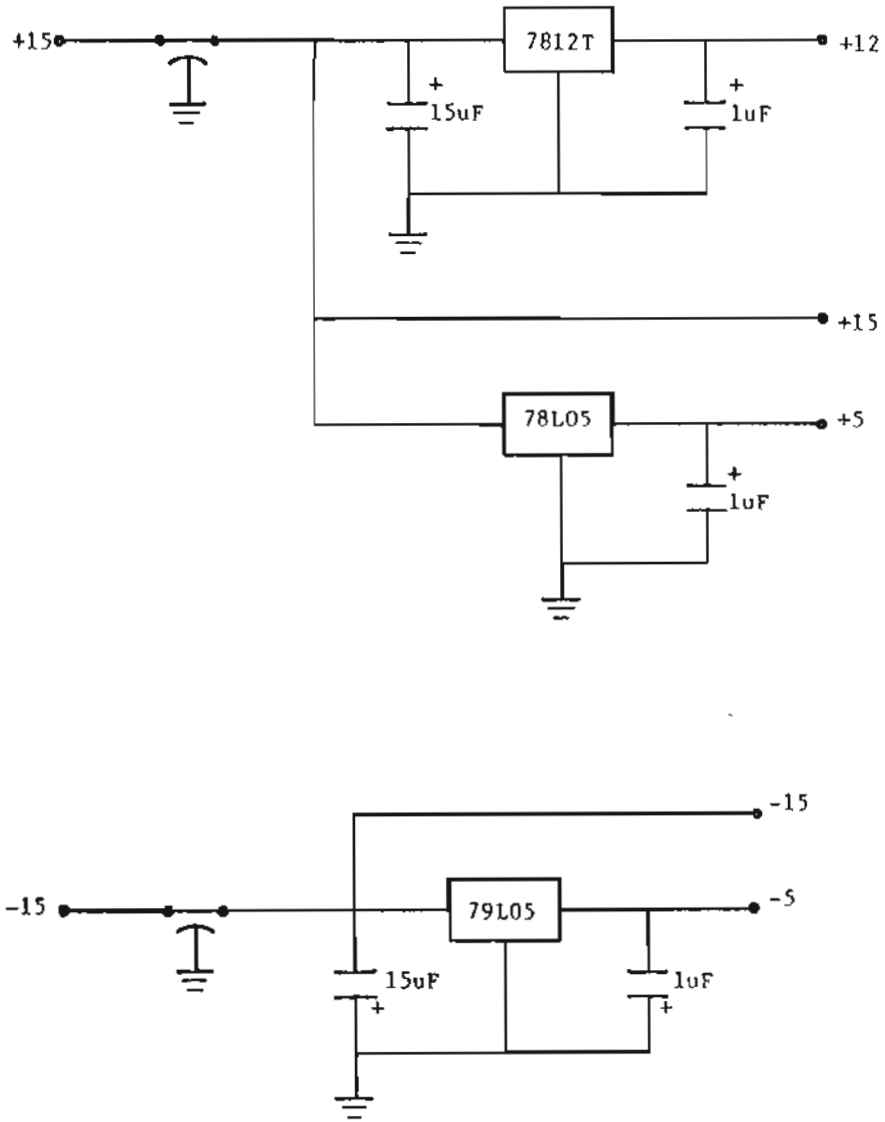

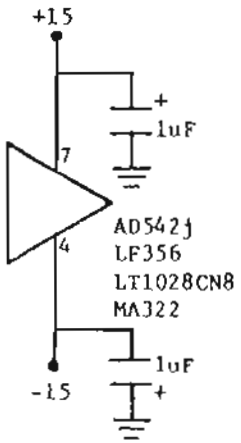

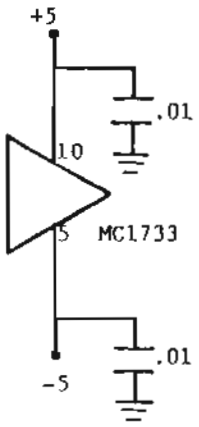

Power Supplies

APPENDIX C

A DEC PDP11/73 computer with a ADV11-A a/d board and a KWV11-C pacer clock board was used to digitalize, store and process the data. Data were stored on magnetic tapes using a DEC TK50 tape drive for processing and future reference.

Data were collected from four a/d channels in blocks of 2048 bytes (1024 words). Each block holds eight words of parameters specifying the number of data sets, number of blocks per set, sampling period and time. The next eight words are the in situ data (σ_χ) from channel 2 followed by eight words of channel 3 in situ data (V). Then 1000 words of data that are read from channels 0 and 1 alternately, starting with channel 0. Over a data set (usually consists of ten blocks), the channels 0 and 1 data are collected continuously from one block to another.

The source program listed in this appendix reads the data from a magnetic tape (one set at a time) to be processed for the statistical parameters required for wind measurement. Then the wind velocity and turbulence strength are determined using different processing techniques. In the following program the array IBUFF contains a block of data and IDATA is the array containing a set of channels 0 and 1 data.

```
*-------------------------------------------------
*-------------------- PROCESS ---------------------
*-------------------------------------------------

*---- The following segment is used to scan the magnetic tape and to
*---- locate the desired data for processing.  It then reads and stores
*---- the data in appropriate arrays, set by set, for processing.


        DIMENSION ISX(8),IWIND(8)
        dimension isb(2), iprl(6) , itime(8)
        dimension ibuf(2048), iibuf(8)
        byte temp(16)
        byte text(16)
        equivalence (iibuf,temp)

        INCLUDE 'COMMON.FTN'
 10     inumr=1
        ihead=0

        write(5,*) 'enter 1 for help, 2 read'
12      write(5,*) '5 status, 6 rewind, 7 space blocks, 8 space files'
        write(5,*) '9 process'
15      read(6,1010, err=10)icmd
        if (icmd .eq. 1)goto 100
        if (icmd .eq. 2)goto 200
        if (icmd .eq. 5)goto 500
        if (icmd .eq. 6)goto 600
        if (icmd .eq. 7)goto 700
        if (icmd .eq. 8)goto 800
        if (icmd .eq. 9)goto 850
        goto 10

1010    format(i5)

| ******************************************************

100     write(5,*)'tk50 function code commands:'
        write(5,*)'1360          get tk50 status (returned in ids(2) )'
        write(5,*)'1536          write end-of-file gap'
        write(5,*)'note:  2 end-of-file gaps = end of volume'

        goto 10


 200    ihead=1
        write(5,*)'0 for summary, 1 for full display'
        read(6,1010)ircmd
        go to 230

 850    write(5,*)'type 1 to store the results in data file,0 otherwise'
        read(6,1010)isto
        if(isto.eq.1)go to 851
        ispc=5
        isto=0
        go to 852
 851    write(5,*)'number of data sets to PROCESS'
        read(6,1010,err=10)knum
        ispc=2
        OPEN(2,FILE='DATA',STATUS='NEW')
 852    write(5,*)'number of data blocks to  PROCESS'

        read(6,1010,err=10)inumr
        KCON=1
```

```
*-- Reading the data from the magnetic tape.

230     ifnc = 512
        N=inumr

258     do 290 jnum=1,inumr

                call getadr(iprl(1),ibuf(1))
                iprl(2) = 2048          ! read 2048 byte blocks
                goto 900                ! read the block from tk50

260             iend = 1017             ! last line for summary
                WRITE(6,1015)IBUF(2),IBUF(1)
1015            format(' reading block',i4,' of',i4)

                IF(JNUM.EQ.1.AND.IHEAD.EQ.1)GO TO 265
                IF(JNUM.EQ.1)GO TO 286
                GO TO 287
286             SMPRT=IBUF(3)*1.0E-06
                IHOUR=IBUF(4)
                MIN=IBUF(5)
                DO 288 I=1,8
                ISX(I)=IBUF(I+8)
                IWIND(I)=IBUF(I+16)
288             CONTINUE
287             DO 285 I=1,1000
                IDATA(I+(JNUM-1)*1000)=IBUF(I+24)-2048
285             CONTINUE
                GO TO 290

265             do 280 j=1, iend, 8     ! index into ibuf
                        if (j .lt. 33)goto 270  ! print 3 lines
                        if (j .eq. iend)goto 270        ! print last line
                        if (ircmd .eq. 0)goto 280       ! skip print if summary

270                     jj =j   ! get next 8 words to print
                        do 272 k=1,8
                                iibuf(k) = ibuf(jj)
                                jj=jj+1
272                     continue

!       temp(16) is equivalent to iibuf

                        do 274 k=1,16
                                text(k) = temp(k)
274                     continue

!       set any unprintable ascii codes to ascii .
                        do 278 k=1,16
                                if(text(k) .lt. 32)goto 276
                                if(text(k) .gt. 126)goto 276
                                goto 278
276                             text(k) = 46    ! ascii .
278                     continue

279             write(6,1300)iibuf, text        ! integer display
280             continue

290     continue

        IF(ICMD.EQ.9.AND.KCON.EQ.1)GO TO 1060
        IF(ICMD.EQ.9)GO TO 13
        GO TO 10

1300    format (1h ,4(i6,1x), 2x, 4(i6,1x), 3x, 8a1,2x,8a1 )
```

```
! ******************************************************

500     ifnc = 1360             ! read tk50 status
        goto 900

600     ifnc = 1280             ! rewind
        goto 900

700     ifnc = 1296             ! space blocks
        write(5,*)'enter number of blocks to space (-32000 to 32000)'
        read(6,1010, err=700)iprl(1)
        goto 900

800     ifnc = 1312             ! space files
        write(5,*)'enter number of files to space (-32000 to 32000)'
        read(6,1010, err=700)iprl(1)
        goto 900

! ******************************

900     call wtqio(ifnc,1,1,0,isb,iprl,ids)

        if(ids .eq. 1) goto 960 ! good directive status (qio call ok)
950     write(6,1020)ids
1020    format(' problem in wtqio call for tape:  ids= ',i6)

960     write(6,1030)isb(1)
1030    format(' isb(1)', i6)

        if(isb(1) .eq. 240)goto 10240
        if(isb(1) .eq. 243)goto 10243
        if(isb(1) .eq. 245)goto 10245
        if(isb(1) .eq. 246)goto 10246
        if(isb(1) .eq. 252)goto 10252
        if(isb(1) .eq. 253)goto 10253
        goto 20000


10240   write(5,*)'privilege violation (probably need to mount tape)'
        goto 20000
10243   write(5,*)'data overrun (tape block bytes > requested bytes)'
        goto 20000
10245   write(5,*)'end of volume (2 tape marks) encountered'
        goto 20000
10246   write(5,*)'end of file (tape mark) encountered'
        goto 20000
10252   write(5,*)'parity error on tape'
        write(5,*)'(probably due to nothing recorded in this block)'
        goto 20000
10253   write(5,*)'tk50 drive not ready'
        goto 20000


20000   write(6,1040)isb(2)
1040    format(' isb(2)', i6)

        if (icmd.eq.2.or.icmd.eq.9) goto 260
        goto 10
```

```
*-----------------------------------------------
*-----------------------------------------------
*---------   THE PROCESSING SEGMENT   ----------
*-----------------------------------------------

*-- The system parameters are read and the subroutines are called
*-- to determine the statistical parameters and determine the turbulence
*-- coherence length and the wind velocity using different techniques.

1060    WRITE(5,*)'ENTER THE BACKGROUND NOISE (VOLTS), WITH 2F5.3 FORMAT'
        READ(6,97)DC1,DC2

        WRITE(5,*)'ENTER THE BEAM RADUIS AT THE TRANS. END IN METERS'
        READ(6,98)ALPH0
        WRITE(5,*)'ALPH0=',ALPH0

        WRITE(5,*)'ENTER THE RECEIVERS SPACING IN METERS'
        READ(6,98)P
        WRITE(5,*)'P=',P

 97     FORMAT(2F5.3)
 98     FORMAT(F7.4)
        DC1=DC1*2047/5.1175
        DC2=DC2*2047/5.1175
        IF(ISTO.NE.1)GO TO 13
        WRITE(ISPC,*)'ALPH0=',ALPH0,'SPACING=',P
        WRITE(ISPC,*)'----------------------------------------'
        WRITE(ISPC,17)
        WRITE(ISPC,18)
 17     FORMAT(1X,'VARN1',1X,'VARN2',2X,'COV',3X,5X,'RHO',4x,'slope')
 18     FORMAT(1X,2X,'CAMPBELL wind   sx    cn2',',   het cn2')
        WRITE(ISPC,*)'========================================'

 13     CALL STAT1

        WRITE(5,*)'varn1=',varn1,'varn2=',varn2,'cov.=',cov

*-- SX and WIND are the log-amplitude variance and wind velocity insitu data.

        SX=0.0
        WIND=0.0
        DO 14 JD=1,8
        SX=SX+(FLOAT(ISX(JD))-2048.0)*5.1175/2047.0/8.0
        WIND=WIND+(FLOAT(IWIND(JD))-2048.0)*25.6/2047.0/8.0
  14    CONTINUE

        WRITE(5,*)'CAMPBELL READINGS    SX=',SX,'WIND=',WIND
        IF(ISTO.EQ.1)GO TO 21

  19    WRITE(5,*)'TYPE 1 TO COMPUTE WIND VELOCITY, OTHERWISE TYPE 0 '
        READ(6,99,ERR=10)R1
        IF(R1.EQ.1)GO TO 21
        GO TO 31

  21    CALL STAT2
        CALL STAT3
        CALL SLOPE
        CALL WIND1
        CALL WIND2
        CALL WIND3
        CALL WIND4
        CALL WIND5
        CALL WIND6

*-- The turbulence coherence length and strength are obtained using
*-- the width of the autocovariance method and the ZLR method.
```

```
*-- cn2 is the calculated value and CCN is the insitu value.

        CL=WIN5*tau1/0.1395
        cn2=1./(1.918e14*CL**(5./3.))
        CCN=(SX/2.388E6)**2.
        WRITE(ISPC,*)'SET#',IBUF(1)
        WRITE(ISPC,22)VARN1,VARN2,COV,CL,SLP
  22    FORMAT(1X,3(F5.3,1X),5X,F7.3,f6.2)
        WRITE(ISPC,23)WIND,SX,CCN,CN2
        WRITE(ISPC,*)WIN11,WIN12,WIN2,WIN3,WIN4
        WRITE(ISPC,*)WIN5,WIN6,ERR6
  23    FORMAT(1X,3X,F5.3,3X,F5.3,5X,E9.2,3X,E9.2)
        WRITE(ISPC,*)

        KCON=KCON+1
        IF(KCON.LE.KNUM.AND.ISTO.EQ.1)GO TO 230
        IF(ISTO.EQ.1)GO TO 43

   31   WRITE(5,*)'TYPE 1 FOR FURTHER PROCESSING OPTIONS,OTHERWISE TYPE 0'
        READ(6,99)K4
        IF(K4.EQ.0) GO TO 38
        WRITE(5,*)'ENTER 1 FOR LISTING OF AUTO-COV.'
        WRITE(5,*)' "    2  "    "         TIME-DELAYED COV.'
        WRITE(5,*)' "    3  "    "         SLOPE AND COHERENCE LENGTH'
        READ(6,99)K5

        IF(K5.EQ.0) GO TO 38
        CALL STAT2
        CALL STAT3
        CALL SLOPE
        IF(K1.EQ.1)GO TO 35

  35    IT=ID1+ID2
        IF(K5.EQ.1)GO TO 32
        IF(K5.EQ.2)GO TO 33
        IF(K5.EQ.3)GO TO 34
        GO TO 31

  32    WRITE(5,*)'TIME DELAY    AUTO-COV.1    AUTO-COV.2'
        DO 41 IA=1,99
        IF(AUTO1(IA).EQ.0.0)GO TO 31
  41    WRITE(5,*)ATD(IA),AUTO1(IA),AUTO2(IA)
        GO TO 31

  33    WRITE(5,*)'TIME DELAY    TIME-DELAYED COV.'
        DO 42 IA=1,IT
  42    WRITE(5,*)CTD(IA),TDCOV(IA)
        GO TO 31

  34    WRITE(5,*)'SLOPE=',SLP,'RHO1=',CL1,'RHO2=',CL2

  38    WRITE(5,*)'TYPE 1 TO CONTINUE, 2 TO TRY ANOTHER SET,0 IF DONE'
        READ(6,99)K0
        IF(K0.EQ.0)GO TO 39
        IF(K0.EQ.1)GO TO 31
        IF(K0.EQ.2)GO TO 10
  99    FORMAT(I5)

  43    CLOSE(2,DISPOSE='SAVE')


  39    STOP
9999    end
```

```
*------------------------------ STAT1 ------------------------------
*-------------------------------------------------------------------
* THIS SUBROUTINE COMPUTES  THE AVERAGE,VARIANCE AND THE COVARIANCE.
*-------------------------------------------------------------------
*                                  INPUTS
* IDATA(I)= ARRAY CONTAINING THE DATA
* N= NUMBER OF BLOCKS OF DATA
* DC1 AND DC2 = BACKGROUNDS OF CH.1 AND CH.2
*-------------------------------------------------------------------
*                                  OUTPUTS
* AVG1= AVERAGE VALUE OF CH.1 SAMPLES
* AVG2= AVERAGE VALUE OF CH.2 SAMPLES
* VAR1 AND VAR2 ARE THE CH.1 AND CH.2 VARIANCES
* VARN1 AND VARN2 ARE THE CH.1 AND CH.2 NORMALIZED VARIANCES
* COV= COVARIANCE
*-------------------------------------------------------------------

        SUBROUTINE STAT1
        INCLUDE 'COMMON.FTN'

        T=0.0
        SUM1=0.0
        SUM2=0.0
        SUM11=0.0
        SUM22=0.0
        JB1=N*1000

        DO 220 I=1,JB1,2
        X1=(FLOAT(IDATA(I))-DC1)**2.0
        X2=(FLOAT(IDATA(I+1))-DC2)**2.0
        SUM1=SUM1+X1
        SUM2=SUM2+X2
        SUM11=SUM11+X1*X1
        SUM22=SUM22+X2*X2
        T=T+1.0
 220    CONTINUE

        AVG1=SUM1/T
        AVG2=SUM2/T
        VAR1=SUM11/T-AVG1*AVG1
        VAR2=SUM22/T-AVG2*AVG2
        VARN1=VAR1/(AVG1**2.0)
        VARN2=VAR2/(AVG2**2.0)

* THIS SEGMENT COMPUTES THE COVARIANCE
*-------------------------------------

        SUM=0.0
        T=0.0
        JB2=JB1-3
        X=SQRT(VAR1*VAR2)
        DO 230 I=1,JB2,2
        X1=((FLOAT(IDATA(I+2))-DC1)**2.0+(FLOAT(IDATA(I))-DC1)**2.0)/2.0
        X2=(FLOAT(IDATA(I+1))-DC2)**2.0
        SUM=SUM+(X1-AVG1)*(X2-AVG2)
        T=T+1.0
 230    CONTINUE

        COV=SUM/(T*X)

        RETURN
        END

*-------------------------------------------------------------------
```

```
*------------------------------- STAT2 ---------------------------------
*-----------------------------------------------------------------------
* THIS SUBROUTINE COMPUTES  THE AUTO-COVARIANCE OF EACH CHANNEL
* ----------------------------------------------------------------------
*                                 INPUTS
* IDATA(I)= ARRAY CONTAINING THE DATA.
* AVG1,AVG2= MEAN OF CH.1 and CH.2 .
* VAR1,VAR2= VARIANCES OF CH.1 AND CH.2 .
* DC1 AND DC2 = BACKGROUND NOISE.
* N= NUMBER OF DATA BLOCKS.
* SMPRT= SAMPLING PERIOD.
*-----------------------------------------------------------------------
*-----------------------------------------------------------------------
*                                 OUTPUTS
* AUTO1(I)= ARRAY CONTAINING THE AUTO-COV. OF CH.1
* AUTO2(I)=                                 CH.2
* ATD(I)= CONTAINS THE CORRESPONDING TIME DELAYS
*-----------------------------------------------------------------------
*-----------------------------------------------------------------------

        SUBROUTINE STAT2
        INCLUDE 'COMMON.FTN'

        ID=1

  235   J=2*ID
        SUM1=0.0
        SUM2=0.0
        JB1=N*1000-1
        T=0.0


                DO 240 I=1,JB1,2
                IF(I+J.GE.JB1) GO TO 241
                X11=(IDATA(I)-DC1)**2.0
                X12=(IDATA(I+J)-DC1)**2.0
                I1=I+1
                X21=(IDATA(I1)-DC2)**2.0
                X22=(IDATA(I1+J)-DC2)**2.0
                SUM1=SUM1+X11*X12
                SUM2=SUM2+X21*X22
                T=T+1.0
  240           CONTINUE

  241   AUTO1(ID)=(SUM1/T-AVG1**2.0)/VAR1
        AUTO2(ID)=(SUM2/T-AVG2**2.0)/VAR2
        ATD(ID)=J*SMPRT
        if(auto1(id).lt.0.01.or.auto2(id).lt.0.01)go to 245

        IF(ID.GE.80) GO TO 245
        ID=ID+1

        GO TO 235

 245    RETURN
        END

*-----------------------------------------------------------------------
*-----------------------------------------------------------------------
```

```
*------------------------------ STAT3 ------------------------------
*-------------------------------------------------------------------
* THIS SUBROUTINE COMPUTES THE TIME-DELAYED COVARIANCE
*-------------------------------------------------------------------
*
*                                 INPUTS
* IDATA(I)= ARRAY CONTAINING THE DATA
* AVG1,AVG2= MEAN VALUES OF INDIVIDUAL CHANNELS
* VAR1,VAR2= VARIANCES
* COV= COVARIANCE
* DC1 AND DC2 = BACKGROUND NOISE
* N= NUMBER OF DATA BLOCKS
* SMPRT= SAMPLING PERIOD
*-------------------------------------------------------------------
*
*                                 OUTPUTS
* TDCOV1(I) AND TDCOV2(I)= POSITIVE AND NEGATIVE TIME DELAYS COV.
* TDCOV(I) = TIME-DELAYED COVARIANCE
* CTD(I) = CORRESPONDING TIME DELAYS
* ID1 , ID2 = NUMBER OF ELEMENTS IN TDCOV1 AND TDCOV2
*-------------------------------------------------------------------


*            NEGATIVE TIME DELAYS
* IN THE FOLLOWING SEGMENT THE COV. IS COMPUTED FOR
* NEG. TIME DELAYS.
*
      SUBROUTINE STAT3
      DIMENSION CTD1(100),CTD2(100)
      INCLUDE 'COMMON.FTN'


      ID1=1
      JB1=N*1000
246   J=2*(ID1-1)
      SUM=0.0
      T=0.0

      DO 250 I=1,JB1,2
      I1=I+1
      IF(I1+J.GE.JB1) GO TO 251
      X1=(IDATA(I)-DC1)**2.0
      X2=(IDATA(I1+J)-DC2)**2.0
      SUM=SUM+X1*X2
      T=T+1.0
250   CONTINUE

251   TDCOV1(ID1)=(SUM/T-AVG1*AVG2)/(SQRT(ABS(VAR1*VAR2)))
      CTD1(ID1)=-(2.0*ID1-1.0)*SMPRT
      IF(ID1.GE.20) GO TO 255
      ID1=ID1+1
      GO TO 246


*-------------------------------------------------------------------
*            POSITIVE TIME DELAYS
* IN THE FOLLOWING SEGMENT THE TIME-DELAY COVARIANCE IS COMPUTED FOR
* POS. TIME DELAYS.
*
255   ID2=1
256   J=2*(ID2-1)
      SUM=0.0
      T=0.0
```

```
      DO 260 I=2,JB1,2
      I1=I+1
      IF(I1+J.GE.JB1)GO TO 261
      X1=(IDATA(I1+J)-DC1)**2.0
      X2=(IDATA(I)-DC2)**2.0
      SUM=SUM+X1*X2
      T=T+1.0
260   CONTINUE

261   TDCOV2(ID2)=(SUM/T-AVG1*AVG2)/(SQRT(ABS(VAR1*VAR2)))
      CTD2(ID2)=(2.0*ID2-1.0)*SMPRT
      IF(ID2.GE.20)GO TO 265
      ID2=ID2+1

      GO TO 256


*-----------------------------------------------------------------------
* REARRANGING TDCOV1 AND TDCOV2 IN ORDER TO START WITH THE
* LARGEST NEGATIVE TIME DELAY TO THE LARGEST POSITIVE TIME DELAY
* THE FINAL RESULT IS STORED IN TDCOV AND THE CORRESPONDING
* TIME DELAYS IN CTD .
*
265   ID=ID1+ID2+1
      IT=0.0

      DO 270 I=1,ID,1
      I1=ID1-IT
      IF(I1.EQ.0)GO TO 266
      IF(I1.LT.0)GO TO 267
      TDCOV(I)=TDCOV1(I1)
      CTD(I)=CTD1(I1)
      GO TO 268
266   TDCOV(I)=COV
      CTD(I)=0.0
      GO TO 268
267   I2=ABS(I1)
      TDCOV(I)=TDCOV2(I2)
      CTD(I)=CTD2(I2)

268   IT=IT+1

270   CONTINUE

      RETURN
      END


*-----------------------------------------------------------------------
```

```
*------------------------------ slope ---------------------------------
*----------------------------------------------------------------------
* THE SLOPE OF THE T-D COV. AND THE COHERENCE LENGTH IS COMPUTED.
*----------------------------------------------------------------------
*
*                                 INPUTS
* TDCOV1 AND TDCOV2 = THE NEG. AND POS. TIME DELAYS COV.'S
* COV = COVARIANCE
* AUTO1 AND AUTO2 = AUTO-COV.'S OF CH.1 AND CH.2
* ATD = ARRAY CONTAINING THE CORRESPONDING TIME DELAYS FOR AUTO-COV.
* ALPH0 = LASER BEAM SIZE AT THE TRANSMITTED END
* P = SPACING BETWEEN THE RECEIVING MIRRORS
* SMPRT = SAMPLING PERIOD
*----------------------------------------------------------------
*                                 OUTPUTS
* SLP= SLOPE OF THE TIME-DELAYED COV.
* CL1= COHRENCE LENGTH COMPUTED USING THE SLOPE METHOD
* CL2= COHRENCE LENGTH COMPUTED USING THE ZLR METHOD
*----------------------------------------------------------------
*
      SUBROUTINE SLOPE
      INCLUDE 'COMMON.FTN'

*
* A 5 POINTS DIFFERENTIAION METHOD IS USED TO COMPUTE THE SLOPE
* WHERE THE FOLLOWING EQUALITY HAS BEEN USED:
* F[(X1+X2)/2]=[-F(X0)+9F(X1)+9F(X2)-F(X3)]/16
*
      P1=(-TDCOV2(1)+9.0*TDCOV1(1)+9.0*TDCOV1(2)-TDCOV1(3))/16.0
      P2=(-TDCOV2(3)+9.0*TDCOV2(2)+9.0*TDCOV2(1)-TDCOV1(1))/16.
      X=P1-8.0*TDCOV1(1)+8.0*TDCOV2(1)-P2
      SLP=X/(12.0*SMPRT)

*
* THE COHERNCE LENGTH IS OBTAINED USING THE TIME-DELAYED COV.
*
      X=ALOG(ABS(COV))+0.5*(P/ALPH0)**2.0
      X=ABS(X)
      CL1=((4.0/X)**0.6)*P
*
* THE COHERNCE LENGTH USING THE ZLR METHOD
*
      X=(ABS(COV/SLP))**(1.5)
      Y=((32.0/3.0)**(0.6))*P*X
      T=0.0
      SUM1=0.0
      SUM2=0.0

      DO 280 I=4,10
      Z1=SUM1
      Z2=SUM2
      IF(AUTO1(I).EQ.0.0.OR.AUTO2(I).EQ.0.0) GO TO 280
      X1=ALOG(ABS(AUTO1(I)))
      X2=ALOG(ABS(AUTO2(I)))
      SUM1=SUM1+Y*(ABS(X1))**(0.9)/(ATD(I)**1.5)
      SUM2=SUM2+Y*(ABS(X2))**(0.9)/(ATD(I)**1.5)
      T=T+1.0
      IF(I1.EQ.0)GO TO 280
      Z11=SUM1/I-Z1/(I-1)
      Z22=SUM2/I-Z2/(I-1)
      IF(Z11.LE.0.001)GO TO 282
      IF(Z22.LE.0.001)GO TO 284
```

```
  280   CONTINUE

  282   CL2=SUM1/T
        GO TO 286
  284   CL2=SUM2/T

  286   RETURN
        END
*---------------------------------------------------------------
```

```
*----------------------- WIND1 ---------------------------
*---------------------------------------------------------
* THE WIND IS CALCULATED USING THE WIDTH OF THE AUTO-COV. METHOD.
*---------------------------------------------------------
*
*                        INPUTS
* AUTO1 ,AUTO2 = ARRAYS CONTAINING THE AUTO-COV,S FOR EACH CHANNEL.
* ATD = ARRAY CONTAINING THE CORRESPONING TIME DELAYS.
* COV = COVARIANCE.
* SLP = SLOPE OF TIME-DELAYED COV.
*---------------------------------------------------------
*
*                       OUTPUTS
* WIN11 = WIND MEASURED FROM CH.1
* WIN12 = WIND MEASURED FROM CH.2
*---------------------------------------------------------
*---------------------------------------------------------

        SUBROUTINE WIND1
        INCLUDE 'COMMON.FTN'

        DO 290 I=1,100,1
        Z1=AUTO1(I)-0.67
        IF(Z1.LE.0.0) GO TO 295
  290   CONTINUE

  295   TAU1=ATD(I)

        DO 300 I=1,100,1
        Z2=AUTO2(I)-0.67
        IF(Z2.LE.0.0) GO TO 305
  300   CONTINUE

* THE WIND VELOCITY FROM SLOPE METHOD IS USED TO CANCELL
*  OUT THE COHERENCE LENGTH .

  305   TAU2=ATD(I)
        Z=SLP/ABS(SLP)
        X=0.2534*P*Z*(ABS(COV/SLP))**1.5
        WIN11=X/(TAU1)**2.5
        WIN12=X/(TAU2)**2.5

        RETURN
        END
*---------------------------------------------------------------
```

```
*------------------------------ WIND2 ------------------------
*-------------------------------------------------------------
* THE SLOPE METHOD IS USED TO OBTAIND THE WIND VELOCITY.
*
*-------------------------------------------------------------

*                               INPUTS
* COV= COVARIANCE.
* SLP= SLOPE OF THE TIME-DELAYED COV.
* ALPH0= BEAM SIZE.
* P= SPACING BETWEEN THE RECEIVING MIRRORS.
*-------------------------------------------------------------
*
*                               OUTPUT
* WIN2= THE CALCULATED WIND VELOCITY.
*-------------------------------------------------------------
*-------------------------------------------------------------
*

        SUBROUTINE WIND2
        INCLUDE 'COMMON.FTN'

        WIN2=3.0/32.0*P*SLP/COV*(CL1/P)**(5./3.)

        RETURN
        END

*-------------------------------------------------------------
```

```
*-------------------------- WIND3 ------------------------
*---------------------------------------------------------
* IN THIS SUBROUTINE THE DELAY TO PEAK METHOD IS USED.
*---------------------------------------------------------
*---------------------------------------------------------
*                          INPUTS
* TDCOV= ARRAY CONTAINING THE TIME-DELAYED COV.
* CTD= ARRAY CONTAINING THE CORRESPONDING TIME DELAYS.
* ID1+ID2= NUMBER OF ELEMENTS IN TDCOV.
* P= DETECTORS SPACING.
*---------------------------------------------------------
*
*                          OUTPUT
* WIN3= THE WIND VELOCITY.
*---------------------------------------------------------
*---------------------------------------------------------
*

        SUBROUTINE WIND3
        INCLUDE 'COMMON.FTN'

        ID=ID1+ID2+1
        I1=1

        DO 310 I=2,ID,1
        IF(CTD(I).EQ.0.0)GO TO 310
        IF(TDCOV(I).GT.TDCOV(I1)) I1=I
  310   CONTINUE

        WIN3=P/(CTD(I1)*2.0)

        RETURN
        END

*---------------------------------------------------------
```

```
*-------------------------- WIND4 ------------------------
*---------------------------------------------------------
* THE WIND VELOCITY IS CALCULATED USING THE BRIGGS METHOD.
*---------------------------------------------------------
*
*                          INPUTS
* TDCOV1 , TDCOV2 = TIME-DELAYED COV. WITH NEG. AND POS. DELAYS.
* AUTO1 ,AUTO2 = CH.1,2 AUTO-COV'S
* ID1 ,ID2 = NUMBER OF ELEMENTS IN TDCOV1 AND TDCOV2.
* SMPRT = SAMPLING PERIOD.
*---------------------------------------------------------
*
*                          OUTPUT
* WIN4 = THE WIND VELOCITY.
*---------------------------------------------------------
*---------------------------------------------------------
*
      SUBROUTINE WIND4
      INCLUDE 'COMMON.FTN'

      I1=ID1
      IF(ID2.GE.ID1)I1=ID2

      X=EXP(0.5*(P/ALPH0)**2.0)

      DO 320 I=2,I1,1
      IF(AUTO1(I).EQ.0.0)GO TO 326
      IF(I.GE.ID1) GO TO 312
      X11=(AUTO1(I)+AUTO1(I-1))/2.0-TDCOV1(I)*X
      X12=(AUTO2(I)+AUTO2(I-1))/2.0-TDCOV1(I)*X
      IF(ABS(X11).LT.0.01.OR.ABS(X12).LT.0.01) GO TO 322
312   X21=(AUTO1(I)+AUTO1(I-1))/2.0-TDCOV2(I)*X
      X22=(AUTO2(I)+AUTO2(I-1))/2.0-TDCOV2(I)*X
      IF(I.GE.ID2) GO TO 320
      IF(ABS(X21).LT.0.01.OR.ABS(X22).LT.0.01) GO TO 324
320   CONTINUE

      GO TO 326
322   TAUB=-(2*I-1)*SMPRT
      GO TO 328

324   TAUB=(2*I-1)*SMPRT
      GO TO 328

326   WRITE(5,327)
327   FORMAT(5X,'NO INTERSECTION IS FOUND')
      GO TO 329

328   WIN4=P/(TAUB*3.1056)

329   RETURN
      END

*---------------------------------------------------------
```

```
*-------------------------- WIND5 --------------------------
*-----------------------------------------------------------
* THE Z-LOG RATIO METHOD IS UTILIZED FOR CALCULATING THE WIND VELOCITY.
*-----------------------------------------------------------
*
*                              INPUTS
* AUTO1 , AUTO2 = CH.1,2 AUTO-COV.
* ADT = TIME DELAYS CORRESPONDING TO AUTO-COV.
* COV= COVARIANCE
* SLP= SLOPE OF THE TIME-DELAYED COV.
* ALPH0=  BEAM RADIUS AT THE TRANSMITTED END.
* P = DETECTORS SPACING
*-----------------------------------------------------------
*
*                              OUTPUT
* WIN5= THE WIND VELOCITY.
*-----------------------------------------------------------
*-----------------------------------------------------------
*
      SUBROUTINE WIND5
      INCLUDE 'COMMON.FTN'

      SUM1=0.0
      SUM2=0.0
      Z=1.0
      T=0.0

      X=ALOG(ABS(COV))+0.5*(P/ALPH0)**2.0

      DO 340 I=5,10
      IF(AUTO1(I).LE.0.0)GO TO 340
      Y1=(3.0/8.0)*ALOG(AUTO1(I))/X
      Y2=(3.0/8.0)*ALOG(AUTO2(I))/X

      Z1=(ABS(Y1))**(0.6)/ATD(I)
      Z2=(ABS(Y2))**(0.6)/ATD(I)
      SUM1=SUM1+Z1
      SUM2=SUM2+Z2
      T=T+1.0

      IF(T.EQ.1.0)GO TO 340

      IF(Z1.LE.0.1) GO TO 342
      IF(Z2.LE.0.1) GO TO 344

  340 CONTINUE

  342 WIN5=Z*SUM1*P/T
      GO TO 346

  344 WIN5=Z*SUM2*P/T

  346 RETURN
      END

*-----------------------------------------------------------
```

```
*------------------------- WIND6 -------------------------------
*---------------------------------------------------------------
* MMSE-ZLR METHOD IS USED FOR COMPUTING THE WIND VELOCITY.
* THE CORRESPONDING MEAN SQUARE ERROR IS ALSO COMPUTED.
*---------------------------------------------------------------
*------------------------- INPUTS ------------------------------
* COV = COVARIANCE.
* AUTO1 =  AUTO-COV OF CH.1.
* ATD = CORRESPONDING TIME DELAYS FOR AUTO-COV.
* SLP = SLOPE OF THE TDCOV.
* P = SPACING BETWEEN THE RECEIVING MIRRORS.
* ALPH0 = BEAM RADUIS AT THE TRANSMITTER.
*---------------------------------------------------------------
*------------------------- OUTPUTS -----------------------------
* WIN6 = THE WIND CALCULATED USING MMSE-ZLR METHOD.
* ERR6 = THE MEAN SQUARE ERROR ASSOCIATED WITH THE ESTIMATED WIND.
*---------------------------------------------------------------
*---------------------------------------------------------------
*
        SUBROUTINE WIND6
        INCLUDE 'COMMON.FTN'


*---------------------------------------------------------

  52    T=0.0
        SUM1=0.0
        SUM2=0.0
        SUM3=0.0

        DO 60 I=2,10
        B=AUTO1(I)
        cov=abs(cov)
        if(b.le.0.0)go to 60
        Z=ALOG(B)/(ALOG(COV)+0.5*(P/ALPH0)**2.0)
        SUM1=Z*ATD(I)**(5.0/3.0)+SUM1
        SUM2=ATD(I)**(10.0/3.0)+SUM2
        SUM3=Z*Z+SUM3
        T=T+1.0
  60    CONTINUE

        SI=SLP/ABS(SLP)

        WIN6=SI*P*(3.0/8.0)**0.6*(ABS(SUM1/SUM2))**0.6
        ERR6=0.5*(SUM3-SUM1*SUM1/SUM2)/T

        RETURN
        END


*---------------------------------------------------------------




*--------------------------- COMMON ----------------------------
*---------------------------------------------------------------
        COMMON IDATA(10000),AUTO1(80),AUTO2(80),ATD(80),
     +TDCOV1(40),TDCOV2(40),TDCOV(82),CTD(82),ID1,ID2,AVG1,AVG2,
     +VAR1,VAR2,VARN1,VARN2,COV,SLP,CL1,CL2,N,SMPRT,ALPH0,P,
     +WIN11,WIN12,WIN2,WIN3,WIN4,WIN5,WIN6,ERR6
*------
*
```

APPENDIX D

The computer programs used to generate the curves presented in chapter 5 are listed in this appendix. Slightly different versions of these programs were used for some the curves. Since these variations are trivial, only one version of each program is listed here. The numerical method used by d01ahf subroutine to evaluate the wave structure function is described in the NAG library manual.

```
c-----------------------------------------------------
c--------------------- errm.f ------------------------
c--------  This program computes the RMS error for
c--------  the sample mean as a function of N.


         open(2,file='rms',status='new')

         write(5,*)'enter turb. strength cn^2'
         read(6,*)cn2

         write(5,*)'enter wind velocity v'
         read(6,*)v

         write(5,*)'enter sampling period t'
         read(6,*)t

           write(2,*)'cn2=',cn2,'v=',v,'T=',t

c--- n is the number of samples.

           n=0

             do 20 jj=1,60
             nt=n
             n=10.0**(float(jj)/10.)
             if(n.eq.nt)go to 20
 11          sum=0.0
             nn=n-1

                do 10 ii=1,nn
                rk=ii
                f=exp(-2.05e15*cn2*(v*rk*t)**(5./3.))
                sum=sum+(n-rk)*f
                if(f.lt.1.0e-6)go to 15
  10            continue

  15         ff=float(n)**2.0
             sum1=(n+2.0*sum)/ff

             rmserr=sqrt(sum1)          ! RMS error

             write(2,100)n,rmserr

  20         continue

 100        format(1x,5x,i10,3x,e10.3,3x,e10.3)

  90        continue

            close(2,status='save')

            stop
            end

 c-----------------------------------------------------
```

```
c-------------------------------------------------
c--------------------- errv.f ---------------------
c-------  The RMS error for the sample variance is computed
c-------  using complete formulation for diferent turb.
c-------  levels as a function of number of samples.

      external f
      common cn2,v,t
      open(2,file='verr')

      v=5.0                        ! wind velocity
      t=0.5e-3                     ! sampling period
      cn2=1.0e-15                  ! turb. strength

      do 80 ic=1,5
      if(ic.eq.2)cn2=0.5e-14
      if(ic.eq.3)cn2=1.0e-14
      if(ic.eq.4)cn2=0.5e-13
      if(ic.eq.5)cn2=1.0e-13

      write(2,*)'cn2=',cn2,'v=',v,'T=',t

      nn=0

      do 5 ii=1,15
      nt=nn
      nn=10.0**(float(ii)/5.)
      if(nn.eq.nt)go to 5

      sum1=0.0
      sum2=0.0
      sum3=0.0
      sum4=0.0
      sum5=0.0
      ff=1.0

         do 10 n=1,nn
         if(ff.lt.1.0e-4)go to 4
         ff=(f(n))**2.0
         sum1=sum1+(nn-n)*ff
         sum2=sum2+(nn-n)*ff*ff

 4       mm=n-50
         if(mm.lt.1)mm=1
         nn1=n+50
         if(nn1.gt.nn)nn1=nn

            do 20 m=mm,nn1

            iii=m-50
            if(iii.lt.1)iii=1
            nn2=m+50
            if(nn2.gt.nn)nn2=nn

                do 30 i=iii,nn2
                sum3=sum3+f(m-n)*f(i-m)*f(i-n)
                sum4=sum4+(f(m-n)*f(i-n))**2.0

                jj=i-50
                if(jj.lt.1)jj=1
                nn3=i+50
                if(nn3.gt.nn)nn3=nn

 6                  do 40 j=jj,nn3
                    ff5=f(m-n)*f(i-m)*f(j-i)*f(j-n)
                    if(j.gt.i.and.ff5.lt.1.0e-4)go to 30
```

```
                    sum5=sum5+ff5
 40                 continue

 30               continue

 20             continue

 10           continue

        an=float(nn)
        an1=an*an
        an2=an1*an
        an3=an2*an
      erms=8.0/an+3./an1+(8./an1+12./an2)*sum1+12./an3*sum1*sum1
     ++8.*sum2/an1-8./an2*(sum3+sum4)+6./an3*sum5

        rmserr=sqrt(erms)
        write(2,*)nn,rmserr

 5      continue

 80     continue

        stop
        end


          function f(k)
          common cn2,v,t
          f=exp(-1.025e15*cn2*(abs(v*k*t))**(5./3.))
          return
          end

c-------------------------------------------------------------
```

```
c-------------------------------------------------------------
c------------------------ errc.f -----------------------------
c------------  The RMS error for the sample T-D covariance
c------------  is computed for different time delays.

        dimension f(-820:820),f1(-820:820)
        external fun
        common v,t,kk,p
        double precision erms1,erms2,ff5,ff6
        open(2,file='ts')

        write(6,*)'enter the turb. level, wind velocity and
     + sampling period'
        read(5,*)cn2,v,t

        ifail=0
        nlimit=0
        a=0.0
        b=1.0
        epsrel=1.0e-5

        p=0.025                         ! spacing between the receivers

        ffc=exp(-0.25*(p/0.025)**2.0)

c-- the T-D mutual intensity function is evaluated as a
c-- function of time delay and stored in arrays f and f1.

        do 90 kk=-220,220
        f(kk)=exp(-1.025e15*cn2*(abs(v*kk*t))**(5./3.))

c-- NAG library integration routine is called

        res=d01ahf(a,b,epsrel,n,abserr,fun,nlimit,ifail)
        f1(kk)=ffc*exp(-1.025e15*cn2*res)
 90     continue

        id=1

        do 30 iid=1,3
        td=t*id
        write(2,*)'cn2=',cn2,'v=',v,'T=',t,'time-delay=',td

        nn=1

         do 5 ii=150,220
         nt=nn
         nn=10.**(float(ii)/50.)
         if(nn.eq.nt)go to 5

         sum1=0.0
         sum2=0.0
         sum3=0.0
         sum4=0.0
         sum5=0.0
         sum6=0.0
         sum7=0.0
         sum8=0.0
         sum9=0.0
         sum10=0.0
         an=float(nn)

           do 10 n=-200,200
           n1=nn-abs(n)
           ff=(f(n))**2.0
           ff1=f1(n+id)
```

```
            ff2=f1(-n-id)
            ff3=f1(n)
            ff4=f1(-n)
            sum1=sum1+n1*ff
            sum2=sum2+n1*ff*ff
            sum3=sum3+n1*ff1*ff1*ff2*ff2
            sum4=sum4+n1*ff1*ff2
            sum5=sum5+n1*ff*ff1*ff2
            sum6=sum6+n1*(f(n-id)*f(n+id))**2.
            sum7=sum7+n1*ff3*ff3*ff4*ff4
            sum8=sum8+n1*f(n-id)*f(n+id)*ff3*ff4
            sum9=sum9+n1*ff3*ff4
            sum10=sum10+n1*f(n-id)*f(n+id)

  10        continue

          ff5=f1(id)
          ff6=f1(-id)
          erms1=(ff5*ff5+ff6*ff6)*(sum1+sum4)+sum2+sum3+2.*sum5
          erms2=sum6+sum7+2.*sum8+2.*ff5*ff6*(sum9+sum10)
          rmserr=sqrt(2.*(erms1-erms2)/(ff5-ff6)*(ff5+ff6))/an

          write(2,*)nn,rmserr

  5       continue

         id=id*2

  30     continue

        stop
        end

c-----------------------------------------------

         double precision function fun(x)
         common v,t,kk,p
         fun=(abs((1.-x)*p-v*t*kk))**(5./3.)
         return
         end

c -------------------------------------------------------------
```

```
c-------------------------------------------------------
c---------------------- errs.f -------------------------
c-------  The RMS error for the sample slope is computed.

        double precision f(0:1000),f1(-1000:1000)
        double precision ff,ff1,ff2,aa,aa1,aa2,res1,res2,ffc
        double precision v,t,p,sum,sum1,sum2,sum3,sum4,sum5,s1,s2,an1

        external fun1,fun2
        common v,t,kk,p
        open(2,file='ts')

        cn2=5.0e-14             ! turb. level
        v=5.0d0                 ! wind velocity
        t=0.5d-03               ! sampling period

        ifail1=0
        ifail2=0
        nlimit=0
        a=0.0
        b=1.0
        epsrel=1.0e-5

        p=0.025                 ! receivers spacing

        ffc=exp(-0.25*(p/0.025)**2.0)
        mm=0

c--  the T-D mutual inensity function is evaluated and stored in
c--  arrays f and f1.

        do 90 kk=0,500
        f(kk)=dexp(-1.025e15*cn2*(abs(v*kk*t))**(5./3.))

c--  NAG library is called

        res1=d01ahf(a,b,epsrel,n,abserr,fun1,nlimit,ifail1)
        res2=d01ahf(a,b,epsrel,n,abserr,fun2,nlimit,ifail2)
        f1(kk)=ffc*dexp(-1.025e15*cn2*res1)
        f1(-kk)=ffc*dexp(-1.025e15*cn2*res2)
        af=f(kk)*f1(kk)
        if(af.lt.1.0e-3)go to 7
        mm=mm+1
 90     continue

 7      write(2,*)

        id=1

        do 30 idd=1,3
        td=id*t                 ! td is the time delay
        write(2,*)
        write(2,*)'cn2=',cn2,'v=',v,'T=',t,'time-delay=',td
        nn=1

        do 5 ii=150,250
        nt=nn
        nn=10.0**(float(ii)/50.)        ! number of samples

        if(nn.eq.nt)go to 5
        sum1=0.0d0
        sum2=0.0d0
        sum3=0.0d0
        sum4=0.0d0
        sum5=0.0d0
        an=float(nn)
```

```
      ff1=f1(id)
      ff2=f1(-id)

         do 10 n=-mm,mm
         na=abs(n)
         an1=nn-na
         ff=(f(na))**2.0
         aa=ff+f1(n+id)*f1(-n+id)
         aa1=ff+f1(n-id)*f1(-n-id)
         na1=abs(n-id)
         na2=abs(n+id)
         aa2=f(na1)*f(na2)+f1(n)*f1(-n)
         sum1=sum1+an1*(aa*aa+aa1*aa1)
         sum2=sum2+an1*aa
         sum3=sum3+an1*aa1
         sum4=sum4+an1*aa2
         sum5=sum5+an1*aa2*aa2
10       continue

      s1p=ff1*ff1-ff2*ff2
      s1=sum1+2.0d0*(ff1*ff1*sum2+ff2*ff2*sum3)
      s2=sum5+2.0d0*ff1*ff2*sum4
      sum=(s1-2.0d0*s2)**0.5
      rmserr=sum/((ff1+ff2)*(ff1-ff2))/an

      write(2,*)nn,rmserr

5     continue

      id=id*2

30    continue

      stop
      end


      double precision function fun1(x)
      double precision v,t,p
      common v,t,kk,p
      fun1=(abs((1.-x)*p-v*t*kk))**(5./3.)
      return
      end


      double precision function fun2(x)
      double precision v,t,p
      common v,t,kk,p
      fun2=(abs((1.-x)*p+v*t*kk))**(5./3.)
      return
      end

c -------------------------------------------------------------
```

```
c-------------------------------------------------------
c---------------------- errw.f -------------------------
c-----------  The RMS error for the sample Wind
c-----------  is computed.

        dimension f(-520:520),f1(-520:520)
        external fun
        common v,t,kk,p
        open(2,file='ver1')

        cn2=1.0e-13                !turb. level
        t=0.5e-3                   !sampling period
        td=5.0e-3                  !time delay

        ifail=0
        nlimit=0
        a=0.0
        b=1.0
        epsrel=1.0e-5

c--  v is the wind velocity

        v=2.5
        do 35 idd=1,3
        v=v+2.5
        write(2,*)'cn2=',cn2,'v=',v,'T-D=',td

c-- p is the spacing between the receivers

        p=1.1e-2
        do 30 ip=1,24
        p=p+0.2e-2
        ff=exp(-0.25*(p/0.025)**2.0)

c-- the mutual intensity functions are evaluated

        do 90 kk=-220,220
        f(kk)=exp(-1.025e15*cn2*(abs(v*kk*t))**(5./3.))

c-- NAG library is called to integrate the wave structure function

        res=d01ahf(a,b,epsrel,n,abserr,fun,nlimit,ifail)
        f1(kk)=ff*exp(-1.025e15*cn2*res)
 90     continue


        nn=20000             ! number of samples

        sum1=0.0
        sum2=0.0
        sum3=0.0
        sum4=0.0
        sum5=0.0
        sum6=0.0
        sum8=0.0
        sum9=0.0
        an=float(nn)

           do 10 n=-200,200
           n1=nn-abs(n)
           ff1=f(n+id)
           ff2=f(-n+id)
           sum1=sum1+n1*(f(n)**2.0+ff1*ff2)**2.0
           sum2=sum2+n1*(f(n)**2.0+ff1*ff2)
           sum3=sum3+n1*(f(n)**2.0+f1(n)*f1(-n))**2.0
           sum4=sum4+n1*(f(n)**2.0+f1(n)*f1(-n))
```

```
            sum5=sum5+n1*(f(n)*f1(n-id)+f(n-id)*f1(n))**2.0
            sum6=sum6+n1*(f(n)*f1(n-id)+f(n-id)*f1(n))
            sum8=sum8+n1*(f(n+id)**2.0)
            sum9=sum9+n1*(f1(n)**2.0)

 10         continue

         an1=an*an
         avx=f(id)**2.0
         avy=f1(0)**2.0
         varx=(sum1+2.0*sum2*avx)/(avx*avx*an1)
         vary=(sum3+2.0*sum4*avy)/(avy*avy*an1)
         ff7=avx*avy
         rxy=(sum5+2.*sum6*f(id)*f1(0))/(ff7*an1)

         alnx=alog(avx)
         alny=alog(avy/(ff*ff))

         erms=(varx/(alnx**2.)-2.*rxy/(alnx*alny)+vary/(alny**2.))

         rmserr=0.6*sqrt(erms)        ! RMS error

         write(2,100)p,rmserr,varx,vary,rxy,alnx,alny
 100     format(2x,f6.3,3x,6(f7.3,2x))

 30     continue

 35     continue

         stop
         end


         double precision function fun(x)
         common v,t,kk,p
         fun=(abs((1.0-x)*p-v*t*kk))**(5./3.)
         return
         end

c ------------------------------------------------------------
```

VITA

The author was born in Tehran, Iran, on November 30, 1957. He moved to Oklahoma City, Oklahoma in 1976 after finishing his high school education and there attended Oscar Rose Junior College. He then moved to Portland, Oregon in 1978 to attend Portland State University (PSU). He received his Bachelor's degree in Electrical Engineering in 1980 and his Bachelor's degree with high honors in Mathematics and Master's degree in Electrical Engineering in 1982 from PSU.

He worked as an instructor at PSU and Clackamas Community College, Oregon City, Oregon, teaching basic engineering courses, during the 1982-83 academic year.

In 1983, he began his studies at the Oregon Graduate Center (OGC) and completed all requirements for his Ph.D. degree in Electrical Engineering in 1988.

While at OGC, the author contributed to four patents that are currently in process and coauthored the journal publications and conference papers listed below.

Journal Publications

J. F. Holmes, F. Amzajerdian, and J. M. Hunt, "*Improved optical local oscillator isolation using multiple acoustooptic modulators and frequency diversity,*" Opt. Lett. 12, 637, August 1986.

J. F. Holmes, F. Amzajerdian, V. S. R. Gudimetla, and J. M. Hunt, "*Remote sensing of atmospheric winds using speckle-turbulence interaction, a* CO_2 *laser and optical heterodyne detection,*" Appl. Opt. 27, June 15, 1988.

J. M. Hunt, J. F. Holmes, and F. Amzajerdian, "*Optimum local oscillator levels for coherent detection using photoconductors,*" Appl. Opt. 27, August 1, 1988.

F. Amzajerdian and J. F. Holmes, "*Time delayed statistics for a bistatic coherent lidar operating in atmospheric turbulence,*" will be submitted to J. Opt. Soc. Am.

F. Amzajerdian and J. F. Holmes, "*The effect of speckle and atmospheric turbulence on coherent DIAL measurements,*" will be submitted to Appl. Opt.

Conference Papers

J. F. Holmes, F. Amzajerdian, V. S. R. Gudimetla and J. M. Hunt, "*Remote crosswind measurement using speckle-turbulence interaction and optical heterodyne detection,*" Annual meeting of the Optical Society of America, October 14-18, 1985, Washington, D.C.

J. F. Holmes, J. M. Hunt, F. Amzajerdian and V. S. R. Gudimetla, "*An optical system for remote wind sensing using speckle-turbulence interaction,*" Conference on Laser and Electrooptics, June 9-13, 1986, San Francisco, California.

J. F. Holmes, F. Amzajerdian, V. S. R. Gudimetla, and J. M. Hunt, "*Remote sensing of atmospheric winds using a coherent CW lidar and speckle-turbulence interaction,*" Proceeding of the International Laser Radar Conference, August 11-15, 1986, Toronto, Canada.

J. M. Hunt, J. F. Holmes, and F. Amzajerdian, "*Optimum local oscillator levels for coherent detection using photoconductors,*" Proceedings of the Topical Meeting on Laser and Optical Remote Sensing, September 28-October 1, 1987, Cape Cod, Massachusetts.

F. Amzajerdian and J. F. Holmes, "*Time delayed statistics for a bistatic coherent lidar operating in atmospheric turbulence,*" European Conference on Optics, Optical Systems and Applications, March 22-25, 1988, Birmingham, United Kingdom.

F. Amzajerdian and J. F. Holmes, "*The effect of speckle and atmospheric turbulence on DIAL measurements utilizing coherent detection,*" 14th International Laser Radar Conference, June 20-24, 1988, Innichen-San Candido, Italy.